UNIVERSIDAD NACIONAL AUTÓNOMA DE MÉXICO

PROGRAMA DE MAESTRÍA Y DOCTORADO EN INGENIERÍA
ELÉCTRICA – TELECOMUNICACIONES

HIGH-SPEED SHORT-REACH OPTICAL COMMUNICATION SYSTEMS OVER SINGLE MODE FIBER

TESIS
QUE PARA OPTAR POR EL GRADO DE:
DOCTOR EN INGENIERÍA

PRESENTA:
PABLO TORRES FERRERA

TUTOR PRINCIPAL
DR. RAMÓN GUTIÉRREZ CASTREJÓN
INSTITUTO DE INGENIERÍA, UNAM

COMITÉ TUTOR
DR. SERGIY KHOTYAINTSEV,
FACULTAD DE INGENIERÍA, UNAM

DR. JUAN ARNALDO HERNÁNDEZ CORDERO,
INSTITUTO DE INVESTIGACIONES EN MATERIALES, UNAM

DR. FRANCISCO JAVIER GARCÍA UGALDE
FACULTAD DE INGENIERÍA, UNAM

CIUDAD UNIVERSITARIA, CD. MX., MÉXICO, AGOSTO 2017

JURADO ASIGNADO:

Presidente:	DRA. CELIA ANGELINA SÁNCHEZ PÉREZ
Secretario:	DR. DANIEL CEBALLOS HERRERA
Vocal:	DR. RAMÓN GUTIÉRREZ CASTREJÓN
1er Suplente:	DR. JOSÉ ALFREDO ÁLVAREZ CHÁVEZ
2do Suplente:	DR. ROBERTO GAUDINO

Lugar o lugares donde se realizó la tesis: Instituto de Ingeniería (II), UNAM; México
Politecnico di Torino; Italia

TUTOR DE TESIS:

DR. RAMÓN GUTIÉRREZ CASTREJÓN

FIRMA

Agradecimientos / *Acknowledgements*

A mis padres, Miroslava y Pablo, por los tesoros más grandes que he recibido: su amor, su tiempo, por formarme en todos los ámbitos y darme un hogar y una familia. Mi eterna y trascendente gratitud hacia ustedes.

A mi hermana Miroslava, por su particular forma de brindarme amor, alegría y enseñanzas. Continúa siempre adelante.

A Marisol, por su amor, comprensión, apapachos y apoyo. Por transmitirme alegría y optimismo, y por todas las experiencias y aprendizajes compartidos.

A la familia Ferrera Garrido: Lupita, Felipe, María Elena, José Ignacio, Felipe, Rosalinda, Iván, Sandra, Thalía, María Elena, José Ignacio y Santiago. Por sus enseñanzas, amor, calidez y constante apoyo.

A la familia Torres de la Cruz: Coco, Pablo, Luis, Josefina, Francisco, Shoghik, Higinio, Sandra, Alfonso, Juanita, Isidro, Coco, Citlali, Xóchitl, Gladis, Ana, Giselle, Nayri, Daniela, Luis Alfonso, Itzel, Carlos, Fidel, Deni, Luisito y Camila. Por su cariño y por todos los gratos momentos vividos.

A mis amigos, Jesús, Jovas y Vladimir, por su amistad y siempre grata compañía ahora también durante esta fase académica compartida.

A mis amigos, Juan Carlos, Mario, Martha, Abigail, Sandra, Beto, Iris, Carlos, Ana S., Enrique, Nelly, Karla, Víctor L., Iván, Erasmo, Julián, Adrián, Sait, Saira y David H., por las vivencias que enriquecen la existencia.

A mi tutor, Dr. Ramón Gutiérrez, por su certera y amable guía en el camino de la investigación, por su amistad y por el impulso profesional y personal que siempre me ha brindado incluso más allá de sus funciones académicas. Gracias por todo.

A mi comité tutor, Dr. Juan Hernández, Dr. Sergiy Khotyaintsev y Dr. Francisco García, por sus enriquecedoras aportaciones tanto a mi proyecto de investigación, como a mi formación a lo largo de mis estudios de posgrado.

A mi jurado, Dra. Celia Sánchez, Dr. Daniel E. Ceballos, Dr. Ramón Gutiérrez, Dr. José A. Álvarez y Dr. Roberto Gaudino, por sus valiosas revisiones y aportaciones a la presente tesis, así como a sus consejos y apoyo.

To Dr. Ioannis Tomkos, for showing me new paths in the world of optical communications and for his constant academic support.

Al Dr. Jose Rivas, por su amistad, consejos y colaboración académica.

To Dr. Roberto Gaudino, for his academic and professional support. Thanks for trust me and give me the chance of exploring new research horizons.

To Dr. Stefano Straullu, for the experimental training in PhotonLab and the fruitful collaboration work.

Agradecimientos / *Acknowledgements*

A la Universidad Nacional Autónoma de México (UNAM), por la formación que recibí en su seno. Por abrirme las puertas a un interesante mundo de conocimientos, dentro y fuera de las aulas.
"Por mi raza, hablará el espíritu".

Al Consejo Nacional de Ciencia y Tecnología (CONACyT) por otorgarme una beca para realizar mis estudios de Doctorado y por patrocinar una parte de mi estancia de investigación en el Politecnico di Torino, mediante la asignación de una Beca Mixta.

Al pueblo de México, por sostener en pie a estas indispensables instituciones a pesar de las adversidades.
"Para todos la luz, para todos todo".

A la comunidad científica internacional, por compartir sus aportes, sobre los que aprendemos y desarrollamos nuevos proyectos.
"Todas las verdades son fáciles de entender, una vez que han sido descubiertas…" –Galileo Galilei.

A los profesores y alumnos que me han inspirado a buscar saber más.

A la Coordinación de Estudios de Posgrado (CEP), al Instituto de Ingeniería (II), y a la Dirección General de Asuntos del Personal Académico (DGAPA), por el apoyo que me brindaron para asistir a congresos y realizar estancias de investigación, a través del Programa de Movilidad Internacional, Programa de Colaboración Internacional No. 4116 y del Proyecto PAPIIT IN103416: "Sistemas de transmisión de alta eficiencia espectral con aplicación a redes locales de gran capacidad", respectivamente.

To Virtual Photonics Inc. University Program, for providing the student license of VPI Transmission Maker™ Optical Systems used in the numerical simulations presented in this work.

To Tektronix, for providing the high-speed AWG used in the experiments presented in this work.

To CISCO Photonics, for supporting the project in which I collaborated at Politecnico di Torino under the SVCF grant titled "5G-PON".

Content

Abstract **5**

Resumen **7**

List of Figures **9**

List of Tables **14**

List of Acronyms **14**

Introduction **17**

i) The data traffic explosion and the role of optical fiber communications. 17

ii) Different optical schemes for different network level applications 20

iii) Motivation of the thesis 23

iv) Objectives of the thesis 25

v) Original contributions presented in this work 25

vi) List of associated publications 26

1. Chapter one: Fundamental principles of digital IQ modulation and OFDM **29**

1.1 IQ modulation and demodulation 29

1.2 Orthogonal Frequency Division Multiplexing (OFDM) principles 32

1.3 OFDM digital implementations 35

1.3.1 RF-IQ-OFDM digital implementation 35

1.3.2 Real-valued OFDM digital implementation 39

2. Chapter two: Optical transceivers **41**

2.1 Optical transmitters and their modeling 41

2.1.1 The Mach-Zehnder modulator (MZM) 43

2.1.2 The electro-absorption modulator (EAM) 48

2.2 Optical receivers and their modeling 52

2.3 The fiber channel and its modeling 56

2.4 Directly Detected Optical OFDM (DDO-OFDM) 60

2.4.1 Intensity Modulated IM-DDO-OFDM system 60

2.4.2 Field Modulated RF-IQ-DDO-OFDM system 61

2.4.3 The cyclic prefix solution to the chromatic-dispersion induced time delay impairment 62
2.4.4 The single-tap equalizer solution to the system frequency response induced impairments 65
2.4.5 The non-linear distortion impairments and the adopted solutions 67
2.5 Coherent optical communication systems (COCS) 70
2.5.1 Dual-polarization single-carrier COCS (DP-SC-COCS) 71
2.5.2 Digital signal processing algorithms to compensate for DP-SC-COCS physical impairments 73

3. Chapter three: Experimental analysis of a WDM 4 x 23 Gb/s fronthaul system based on DSP-aggregated DDO-OFDM signals. 81

3.1 State-of-the-art and context 81
3.2 The analyzed architecture 83
3.2.1 Clipping technique 86
3.2.2 Non-linear MZM transfer function digital compensation technique 87
3.2.3 Frequency pre-emphasis technique 88
3.2.4 Spectral EVM estimation 93
3.3 Experimental setup 96
3.4 Downstream optimization results 97
3.4.1 Results for single-wavelength transmission of 96 radio channels 98
3.4.2 Results for WDM transmission of 192 radio channels per wavelength and mixed format transmission . 102
3.5 Upstream optimization results 104
3.6 The FDM DDO-OFDM system used as a high-speed optical interconnect 110
3.7 Conclusions of the Chapter 111

4. Chapter four: Numerical analysis of a 400 Gb/s optical intra-DCI based on WDM 4 x 100 Gb/s RF-IQ-DDO-OFDM Transceivers 113

4.1 State-of-the-art and context 113
4.2 Analyzed architecture and numerical setup 115
4.2.1 Electrical OFDM Signal Generation 116
4.2.2 Optical Transmission and Detection 117
4.2.3 Electrical OFDM Signal Reception 120
4.2.4 Peak-to-average power ratio (PAPR) reduction technique 120
4.3 Optimization of the EAM operation 122
4.3.1 Results for O- band operation 122

4.3.2 Results for C- band operation 125
4.3.3 Impact of PAPR reduction and frequency domain equalization 126
4.4 Technical feasibility of the DDO-OFDM EAM-based system in C- and O-bands 128
4.5 Comparison with a DDO-OFDM MZM-based system 131
4.6 Beyond 400 Gb/s 133
4.7 Conclusions of the Chapter 135

5. Chapter five: Numerical analysis of a 800 to 1600 Gb/s optical inter-DCI based on WDM multi-format coherent transceiver 137
5.1 State-of-the-art and context 137
5.2 Analyzed architecture and numerical setup 139
5.3 Tuning of the main physical parameters for 16-QAM format 140
5.3.1 MZM bandwidth and splitting ratio 141
5.3.2 MUX and DEMUX bandwidth 142
5.3.3 Power of the lasers 144
5.3.4 OSNR of the lasers 145
5.3.5 Linewidth of the lasers and frequency offset tolerance 147
5.3.6 Receiver electrical filter bandwidth 148
5.4 Maximum reach vs transmitted power and modulation format 149
5.5 Power and OSNR transmission penalties 151
5.6 Conclusion of the Chapter 154

6. Chapter six: General conclusions and future work 157
6.1 Future work 160

Appendix A. Selected topics of signal theory 161
1. Complex baseband representation of a real-valued passband signal 161
2. Condition of orthogonality among sub-channels in a multi-carrier system 163

References 165

Abstract

The bandwidth demand explosion in telecommunication networks is pushing the emergence of optical communication systems with increasing transmission capacity. In particular, the traffic in short-reach optical links has been surpassing that of long-haul networks since last few years. The research and development of high-speed short-reach optical systems is, therefore, essential nowadays.

In this contribution, three short-reach optical communication systems are proposed as higher-speed alternatives to currently available technology for two hot topic applications: mobile fronthaul and data center interconnections. The proposed systems are designed, analyzed and optimized in order to meet the required performance target under the corresponding physical constraints of their specific application.

The first two systems are implemented under the direct detection framework, while the third one, due to its very high data rate capacity and demanding reach and performance targets, required the use of optical coherent technology as a must. In all cases, the transmission medium is the conventional single mode fiber.

The three systems were designed using high-order modulation formats in order to increase the spectral efficiency and the capacity per optical channel and thus support the high data rate targets. In order to further increase the spectral efficiency, the direct detection systems also employed an orthogonal multi-carrier approach, called Orthogonal Frequency Division Multiplexing (OFDM), implemented in the digital domain. Due to multi-carrier transmission, the overall data rate is split into several lower-rate sub-carriers, each of which is less affected by channel impairments as compared to the single-carrier transmission. The OFDM technology also allows to implement simple but efficient distortion compensation algorithms in the digital domain. In contrast, the coherent system was implemented using a single-carrier approach. However, thanks to coherent detection, the amplitude, phase and polarization information of the optical field is translated into the digital domain, thus enabling the use of powerful digital signal processing algorithms for physical impairments compensation.

The first system, used as an optical fronthaul segment of a mobile network, is experimentally analyzed in Chapter 3. This system is implemented following a digital frequency aggregation approach of up to 192 20-MHz OFDM signals per optical channel using 64-QAM as modulation format. A set of digital signal processing techniques were developed and implemented in combination with optimization procedures in order to increase the capacity, reach and performance of the analyzed fronthauling system. An original analysis on the upstream link direction of this system was also performed. In particular, the functionality of a proposed received signal-to-noise ratio pre-emphasis equalization technique was demonstrated under the upstream conditions. To the best of our knowledge, it is the first time that such analysis is reported. Finally, a brief discussion on using this multi-channel OFDM system as a high-speed optical transceiver for data center interconnection is performed.

In Chapter 4, the technical feasibility of an unamplified 4 x 100 Gb/s wavelength division multiplexed direct detected optical OFDM system based on electro-absorption modulation, is numerically demonstrated for up to

10-km reach of single mode fiber in both C- and O-bands for a bit error ratio target of 3.8×10^{-5}. Based on the use of specifications of currently available (realistic) components, error-free operation, considering the use of a low-overhead forward error correction scheme, is achieved by finding optimum values for bias voltage and electrical gain in the modulator, and by employing a simple peak-to-average power ratio reduction technique. A performance comparison with a Mach-Zehnder driven system is also presented. A brief discussion about extending the analyzed system to a 16 x 100 Gb/s architecture for future 1.6 Tb/s optical interconnections is performed. The OFDM system put forward in this work can be used as an alternative for next-generation 400 Gb/s Ethernet for intra-data center optical interconnects applications and adds on the value proposition of using multi-carrier modulation schemes for Ethernet and similar short-reach wavelength division multiplexing schemes.

In Chapter 5, the third system, an eight-channel multi-format coherent optical transceiver, is proposed as an alternative to implement terabit metro inter-data center interconnects transmitting from 800 to 1600 Gb/s over conventional single mode fiber. The maximum reach of the system as a function of transmitted power and overall capacity is numerically estimated for a bit error ratio target of 1×10^{-13}, avoiding the use of optical amplification and forward error correction schemes. Design parameters of the main devices were tuned up in order to find an adequate trade-off between system performance and their current availability in the market. A maximum reach of 40 km was found for error free transmission of 1.6 Tb/s considering a laser output power of +13 dBm and using 16-QAM as modulation format. Longer reaches could be achieved with the same laser output power by decreasing the overall capacity of the system by lowering the modulation format cardinality. For instance, up to 110 km can be reached for a maximum capacity of 800 Gb/s using QPSK as modulation format.

Resumen

El crecimiento exponencial en la demanda de ancho de banda en las redes de telecomunicaciones impulsa de forma sostenida la creación de sistemas ópticos de comunicaciones con tasas de transmisión cada vez mayores. En particular, en años recientes, el tráfico en los enlaces ópticos de corto alcance ha venido superando el de los enlaces ópticos de larga distancia. La investigación y desarrollo de sistemas ópticos de corto alcance y alta velocidad es, por lo tanto, indispensable en la actualidad.

En el presente trabajo, se proponen tres sistemas ópticos de comunicaciones de corto alcance y alta velocidad, cada uno con capacidad y complejidad mayor que el anterior, como posibles alternativas para incrementar la tasa de transmisión de los sistemas actuales en dos rubros de vanguardia: el segmento de red móvil denominado "fronthaul" y las interconexiones para centros de datos. Dichos sistemas son diseñados y optimizados con el fin de garantizar el desempeño requerido por la aplicación específica en presencia de las restricciones físicas correspondientes.

Los dos primeros sistemas se implementan usando detección directa como esquema de recepción, mientras que el tercero requiere necesariamente del uso de detección coherente, debido a su gran tasa de transmisión y demandante alcance y desempeño requeridos. En todos los casos, se empleó fibra monomodo convencional como medio de transmisión.

Los tres sistemas se diseñaron empleando formatos avanzados de modulación con el fin de incrementar su eficiencia espectral y por tanto alcanzar las altas tasas de transmisión objetivo. Con el fin de incrementar aún más la eficiencia espectral, en los sistemas basados en detección directa se empleó un esquema multi-portadora, denominado Multiplexión por División de Frecuencias Ortogonales (OFDM, por sus siglas en inglés), implementado en el dominio digital. Debido a la transmisión de múltiples portadoras, la tasa total de transmisión se divide entre las sub-portadoras, con lo que cada una de ellas tiene una menor tasa de transmisión y se ve menos afectada por las perturbaciones del canal, como la dispersión cromática, en comparación con el esquema de transmisión de portadora única. La tecnología OFDM también permite implementar simples, pero eficientes, algoritmos digitales para compensar ciertas afectaciones físicas. En contraparte, el sistema basado en detección coherente se implementó usando el esquema de portadora única. No obstante, gracias a la detección coherente, la información transportada en la amplitud, fase y polarización del campo óptico se traslada al dominio digital, lo que habilita el uso de poderosos algoritmos de procesamiento digital de señales para la compensación de afectaciones debido a la transmisión de las señales a través de los componentes eléctricos y ópticos del sistema.

El primer sistema, empleado como "fronthaul" óptico en una red móvil, se analiza experimentalmente en el Capítulo 3. Este sistema se implementa siguiendo un esquema digital de agregación en frecuencia de hasta 192 señales OFDM de 20-MHz por canal óptico usando 64-QAM como formato de modulación. Se desarrolló un conjunto de técnicas de procesamiento digital de señales, que en combinación con procesos de optimización, ayudaron a incrementar la capacidad, alcance y desempeño del sistema "fronthaul" analizado. Se realizó

también un análisis original en la dirección de subida del enlace. En particular, se demostró la correcta operación de un ecualizador de la relación señal a ruido recibida, desarrollado para igualar el desempeño de todos los canales a la salida del sistema, aun cuando su desempeño sea distinto al inicio de la propagación por el sistema "fronthaul". Hasta donde sabemos, es la primera vez que se reporta este análisis en este tipo de sistemas. Finalmente, se realiza una breve discusión sobre la posibilidad de usar el sistema analizado como un transceptor óptico de alta capacidad para interconexiones en centros de datos.

En el capítulo 4, se demuestra mediante análisis numérico la viabilidad técnica de un sistema basado en la multiplexión por longitud de onda de 4 canales ópticos cada uno operando a 100 Gb/s, empleando OFDM con detección directa y moduladores de electro-absorción. El alcance de este sistema es de hasta 10 km usando fibra monomodo sin hacer uso de amplificadores, con la capacidad de operar tanto en banda C como en banda O con una tasa de bit en error menor o igual a 3.8×10^{-5}. Se logró una operación libre de errores contemplando especificaciones de componentes actualmente disponibles y el uso de sistemas de corrección de errores FEC de bajo porcentaje de encabezado, optimizando los valores del voltaje de polarización y amplitud de la señal eléctrica de entrada al modulador, así como haciendo uso de una técnica propuesta para reducir la razón de potencia pico a promedio de la señal OFDM. Se presenta también la comparación en términos de desempeño del sistema empleando moduladores de electro-absorción y moduladores de Mach-Zehnder. Así también, se realiza una breve discusión respecto a la posibilidad de extender la arquitectura analizada para implementar un sistema de 16 canales ópticos a 100 Gb/s con miras a una futura aplicación en interconexiones ópticas a 1.6 Tb/s. El sistema OFDM de cuatro canales presentado aquí puede representar una alternativa para implementar la siguiente generación de transceptores Ethernet a 400 Gb/s con aplicación en interconexiones internas entre centros de datos.

En el capítulo 5, un transceptor óptico de 8 canales empleando detección coherente y capaz de adaptar su formato de modulación y, por lo tanto, su capacidad, se propone como una alternativa para implementar la siguiente generación de interconexiones externas entre centros de datos a un nivel metropolitano con tasas de transmisión entre 800 y 1600 Gb/s. Se estima mediante análisis numérico el alcance máximo de este sistema en función de la potencia transmitida y la tasa total de transmisión, con una tasa de bit en error objetivo de 1×10^{-13}, sin usar amplificadores ópticos ni esquemas de corrección de errores FEC. Se encontró que el máximo alcance del sistema transmitiendo a 1.6 Tb/s, empleando 16-QAM como formato de modulación y una potencia a la salida del láser de +13 dBm, es de hasta 40 km. Este alcance puede incrementarse conservando la misma potencia de salida del láser pero reduciendo la máxima capacidad de transmisión al reducir la cardinalidad del formato de modulación. Por ejemplo, un alcance de hasta 110 km se puede lograr para una capacidad de 800 Gb/s usando QPSK como formato de modulación.

List of Figures

Figure i.1 Global total IP traffic (EB per month): fixed internet, managed IP and mobile data, as a function of year [2]. Historical: From 2008 to 2016. Forecasted: From 2017 to 2021. 17

Figure i.2 Record-breaking "hero" experiments in data rate transmission through a single optical fiber [5]. The improvement in fiber capacity before and after the introduction of wavelength division multiplexing (WDM) in 1992 is highlighted in blue. 18

Figure i.3 Percentage of fiber connections in total broadband fixed subscriptions per OECD country in 2016 [9]. 19

Figure i.4 Annual growth of fiber connections in fixed broadband subscriptions per OECD country between 2015 and 2016 [9]. 19

Figure i.5 Typical optical communication network scheme. Adapted from [13]. 21

Figure i.6 Data center interconnections. 21

Figure i.7 Transmission rate increase as a function of time of standardized OTN (in red with diamonds) and Ethernet (in blue with circles) commercial transceivers. GbE stands for Gigabit Ethernet. 50, 200 and 400 GbE are forthcoming standards. Adapted from [23]. 22

Figure 1.1 Block diagrams of an *IQ modulator* and *IQ demodulator.* 29

Figure 1.2 Block diagram of an *IQ coder* (16-QAM format is used as example). 30

Figure 1.3 Block diagrams of an *IQ modulator* built with a *complex coder* and a *complex modulator.* 32

Figure 1.4 General diagram of an OFDM system as a Multi-carrier transmission system. 35

Figure 1.5 Block diagram of the RF-IQ-OFDM transmitter. 37

Figure 1.6 Block diagram of the RF-IQ-OFDM receiver. 39

Figure 1.7 Block diagrams of the Real-valued OFDM transmitter and receiver. 40

Figure 2.1 Adapted from [39]: a) Diagram of a Phase Modulator; b) Diagram of a dual-drive MZM; Graphs of a MZM E-O field and power transfer functions biased at c) null point and d) quadrature point. 46

Figure 2.2 Structure of an Optical IQ modulator. 47

Figure 2.3 a) Schematic representation of an EAM, b) 3D representation of an EAM. 48

Figure 2.4 a) Normalized field $\left(\left|T_{EAM}(V)\right|\right)$, power $\left(\left|T_{EAM}(V)\right|^2\right)$, and b) chirp $\left(\alpha_{EAM}(V)\right)$ voltage-dependent transfer functions for a typical EAM. 51

Figure 2.5 Diagram of an optical coherent receiver. 56

Figure 2.6 Block diagram of the IM-DDO-OFDM transmission system. 61

Figure 2.7 Block diagram of the RF-IQ-DDO-OFDM transmission system. 61

Figure 2.8 a) Guard time insertion to prevent ISI; b) Cyclic prefix process to prevent ICI; c) Graphic representation of the effect of the CD-induced delay on an OFDM symbol. 64

Figure 2.9 Simplified representation ($H_n(f)$ is shown as real-valued) of a system response and its discrete approximation. Continuous response in blue, discrete response in red. 65

Figure 2.10 Block diagram of the single-tap frequency domain equalizer. 67

Figure 2.11 Simplified illustration of the SSBI and SSII processes at the output of the photodiode. 69

Figure 2.12 Diagram of a dual-polarization SC optical IQ transmitter. 72

Figure 2.13 Diagram of a dual-polarization SC optical coherent transmitter. 72

Figure 2.14 Set of DSP algorithms used in this work for impairments compensation. 74

Figure 2.15 Schematic operation of the OFDE for CD compensation, modified from [99]. 75

Figure 2.16 Structure of the adaptive time domain MIMO equalizer (TDE-MIMO). 76

Figure 2.17 Carrier phase estimation and correction algorithm. 78

Figure 2.18 16-QAM constellation partitioning in different QPSK constellation classes 79

Figure 3.1 a) Traditional mobile network architecture, b) C-RAN mobile network architecture (adapted from [28]). 82

Figure 3.2 Generation/detection and analogue FDM aggregation/de-aggregation of a set of electrical OFDM channels. PBF: Band Pass Filter. 83

Figure 3.3 Complex *baseband* generation/detection and digital FDM aggregation/de-aggregation of a set of electrical OFDM channels 84

Figure 3.4 FDM DSP aggregation/de-aggregation based optical fronthauling architecture. 85

Figure 3.5 EVM per channel distribution for two different cases. 86

Figure 3.6 Scheme of the amplitude clipping of a FDM-OFDM signal. 87

Figure 3.7 Normalized power transfer function of a MZM (in blue) and its linear adjust around the biasing point (in red). 88

Figure 3.8 Pre-emphasis technique and power spectra of the transmitted signal with and without pre-emphasis, the received signal using pre-emphasis and its corresponding EVM per channel graph. 89

Figure 3.9 Simplified model of the transmission in the upstream direction 89

Figure 3.10 Scheme of the SNR estimation technique aided by the electrical spectrum analyzer "embedded" into the digital FDM aggregator/de-aggregator. 94

Figure 3.11 Power spectrum obtained from the electrical spectrum analyzer "embedded" into the digital FDM de-aggregator when some channels are turned off. 95

Figure 3.12 EVM per channel graphs for three fronthauling conditions (Optical Path Loss (OPL) = 20, 25 and 29 dB respectively). In blue: obtained by spectral estimation. In red: measured using OFDM receivers. 95

Figure 3.13 Experimental setup of the analyzed fronthaul system 97

Figure 3.14 EVM of the 96 OFDM channels at a) 25 dB and b) 29 dB of OPL before and after equalization. 98

Figure 3.15 Average EVM of the 96 OFDM channels at 15 dB of OPL as a function of the clipping level and the compensation of the nonlinearity of the MZM electro-optic characteristic performed at (a) the transmitter side; (b) the receiver side; (c) at the receiver side setting the optimum parameters at the transmitter side. 100

Figure 3.16 Comparison of the EVM vs. the OPL obtained with different optimization procedures. 101

Figure 3.17 Comparison of the EVM as a function of the OPL obtained with different non-linear compensation procedures 102

Figure 3.18 Comparison of the EVM versus the OPL obtained after optimization for two cases: i) All channels employing 64-QAM, and ii) Half of the channels employing 64-QAM and half of them employing 16-QAM. 104

Figure 3.19 OPL as a function of the maximum capacity per channel expressed as the 64-QAM/16-QAM channels ratio, for different 64-QAM EVM targets 104

Figure 3.20 a) Performance per channel for a sinusoidal EVM^{W} distribution: at the antenna site and at the BBU site after 20 dB of OPL with and without pre-emphasis, and b) corresponding constraint function G_{US} versus EVM_{target}^{out} 106

Figure 3.21 Performance per channel for a sinusoidal EVM^{W} distribution: a) at the antenna site and at the BBU site after 20 dB of OPL with and without pre-emphasis, and b) at the BBU site after 20 dB of OPL with pre-emphasis for different EVM_{target}^{out} values. 107

Figure 3.22 Performance per channel for a random EVM^{W} distribution: at the antenna site and at the BBU site after 20 dB of OPL with and without pre-emphasis. 108

Figure 3.23 Performance per channel for (a) a random and (b) a uniform, EVM^{W} distribution: at the antenna site and at the BBU site after 25 dB and 20 dB of OPL, respectively, with and without pre-emphasis. 109

Figure 3.24 BER as a function of ROP graph of the optical channel 3 for the WDM transmission of 192 OFDM signals per optical channel, corresponding to an overall data rate of 92.16 Gb/s. 111

Figure 4.1 Schematic diagram of the WDM 4 x 100 Gb/s DD-OFDM transmission system. Electrical elements in blue. High-bandwidth elements in solid red. 116

Figure 4.2 Transfer function characteristics of the EAM as a function of the driving voltage for a CW input power of 0 dBm. The experimental curves were extracted from [139]. 118

Figure 4.3 Optical spectrum of the WDM signal after 10-km CSMF propagation for a C-band grid. 119

Figure 4.4 Schematic diagram of the operation of the random phase shifter block for a single optical channel. *N* stands for the number of OFDM subcarriers, $A_{mn}e^{j\phi_{mn}}$ represents the *n*-th 16-QAM symbol of the *m*-th OFDM symbol. 121

Figure 4.5 Electrical driving signal at the input of the modulator, EAM region of operation on the transmission function, and corresponding optical spectrum at the output of the EAM for representative pairs of eG and V_{bias}. The OSBNR is measured at a resolution of 12.5 GHz. 123

Figure 4.6 BER of the setup shown in Figure 4.1 operated in O-band after 10-km of fiber propagation as a function of a) the electrical gain of the amplifier placed at the input of the EAM, for a $V_b = 0.9$ and b) the bias voltage of the EAM for an eG = 2.5. The cases shown in Figure 4.5 are highlighted. 125

Figure 4.7 BER of the setup shown in Figure 4.1 operated in C-band after 10-km of fiber propagation as a function of a) the electrical gain of the amplifier placed at the input of the EAM and b) the bias voltage of the EAM. 126

Figure 4.8 a) Optical spectra at the output of the EAM for single channel transmission (Ch. 3) and two different input eRF-IQ-OFDM signals: b) when the PAPR reduction technique is used (dark blue) and c) when it is omitted (light blue). The electrical gain eG = 1.0. 127

Figure 4.9 Single-channel (SCh 3) received constellation diagrams for different transmission schemes: a) after 10-km of fiber propagation where EDC is turned off, b) after 10-km of fiber propagation where EDC is turned on, c) back-to-back case. 128

Figure 4.10 BER as a function of ROP of the system in Figure 4.1 operated in C-band for different transmission scenarios. 129

Figure 4.11 BER as a function of ROP of the system in Figure 4.1 operated in O-band for different transmission scenarios. 131

Figure 4.12 BER performance of each of the four channels of the system in Figure 4.1 operated in O-band as a function of fiber length. 131

Figure 4.13 BER as a function of ROP for BtB single-channel transmission using an EAM and a MZM. 132

Figure 4.14 Optical spectra at the output of the 40-GHz BW MZM for an optical channel running at 100 Gb/s and digitally modulated with 16- and 32-QAM. 133

Figure 5.1 System setup of the proposed COCS. Electrical modulation format-dependent elements in gray. 140

Figure 5.2 Simulated BER performance of the 40-km WDM system as a function of MZM bandwidth for different values of the MZM extinction ratio. 142

Figure 5.3 Optical spectrum at IQ modulator output, displayed with a) 5 MHz and b) 12.5 GHz (0.1 nm) resolution. 142

Figure 5.4 Simulated BER performance of the 40-km WDM system as a function of Mux and Demux filters BW. ... 143

Figure 5.5 Multiplexed optical spectrum at fiber a) input, and b) output (40-km), displayed with 12.5 GHz (0.1 nm) resolution. 144

Figure 5.6 Simulated BER performance of the 40-km WDM system as a function of power delivered by the LO for different values of Tx laser power (P_{Tx}). 145

Figure 5.7 Simulated BER performance of the 40-km WDM system as a function of the total power injected into the fiber and the Tx laser power. The dotted line corresponds to simulations where the fiber nonlinear response is not considered. 145

Figure 5.8 Simulated BER performance of the 40-km WDM system as a function of the OSNR at the LO output for different values of the OSNR at the Tx laser output. 146

Figure 5.9 Simulated BER performance of the system as a function of the OSNR measured at the input of the coherent optical receiver for different scenarios. Dotted lines were analytically calculated [115], [172]. Diamonds [173] and triangles [174] correspond to back-to-back experimental measurements. 147

Figure 5.10 Simulated BER performance of the 40-km WDM system as a function of the LO linewidth for different values of the Tx laser linewidth (Tx LW). 148

Figure 5.11 Simulated BER performance (measured at Ch. 4) of the 40-km WDM system as a function of the bandwidth of the electrical filter placed after balanced photodetector. 149

Figure 5.12 Electrical spectrum at receiver electrical filter output (after balanced photodetection), measured at Ch. 4, displayed with a) 5 MHz and b) 12.5 GHz resolution. 149

Figure 5.13 Reach of the system for each modulation format as a function of P_{TX} targeting a BER = $1x10^{-13}$. 150

Figure 5.14 Simulated BER for each modulation format as a function of fiber length for a P_{TX} = +13 dBm. 151

Figure 5.15 Simulated BER for each modulation format as a function of the ROP for a transmitter OSNR of 40 dB measured at the input of the coherent optical receiver for different scenarios. 152

Figure 5.16 Received constellations at a) 114 km (QPSK), b) 81 km (8PSK) and c) 40 km (16-QAM), measured at the X-Pol of the fourth channel. Similar Y-Pol constellations were measured in all cases.....152

Figure 5.17 Simulated BER for each modulation format as a function of the OSNR measured at the input of the coherent optical receiver for different scenarios. 153

List of Tables

Table 4.1 BER (and EVM_{RMS} [%]) for the WDM DD-OFDM system shown on Fig. 1 for L = 2 and 10 km reach.....129

Table 5.1 Standard Parameter Specifications 141

Table 6.1 Technical comparison among the optical DCI systems analyzed in this thesis work and a system analyzed in a previous contribution reported in [121] and [177]. 158

List of Acronyms

ADC	Analogue to Digital Converter
APD	Avalanche Photodiode
ASE	Amplified Spontaneous Emission
AWG	Arbitrary Waveform Generator
BBU	Base-Band Unit
BER	Bit Error Ratio
BPD	Balanced Photodiode
BPF	Band-Pass Filter
BW	Bandwidth
CAP	Carrierless Amplitude and Phase
CD	Chromatic Dispersion
CFR	Carrier Frequency Recovery
CMA	Constant Modulus Algorithm
CMOS	Complementary Metal-Oxide-Semiconductor
COCS	Coherent Optical Communication System
CP	Cyclic Prefix
CPE	Carrier Phase Estimation
CPRI	Common Public Radio Interface
CSMF	Conventional Single Mode Fiber
CSPR	Carrier Suppression Power Ratio
CW	Continuous Wave
DAC	Digital to Analogue Converter
DC	Direct Current
DCI	Data Center Interconnection
DD	Direct Detection

DFB	Distributed Feedback laser
DFT	Discrete Fourier Transform
DML	Directly Modulated Laser
DMT	Discrete Multi-Tone
DN	Dual-Nested
DP	Dual-Polarization
DS	Down-Stream
DSP	Digital Signal Processing
EAM	Electro-Absorption Modulator
EDC	Electronic Dispersion Compensator
EDFA	Erbium Doped Fiber Amplifier
EML	Externally Modulated Laser
E-O-E	Electrical – Optical – Electrical
ETSI	European Telecommunications Standards Institute
EVM	Error Vector Magnitude
FDE	Frequency Domain Equalizer
FDM	Frequency Division Multiplexing
FEC	Forward Error Correction
FFT	Fast Fourier Transform
FM	Field Modulation (or Modulator)
FPP	Fiber Power Penalty
FTF	Field Transfer Function
FWHM	Full Width at Half Maximum
FWM	Four Wave Mixing
GVD	Group Velocity Delay
ICI	Inter Channel Interference
IDFT	Inverse Discrete Fourier Transform
iFFT	Inverse Fast Fourier Transform
IM	Intensity Modulation (or Modulator)
IP	Internet Protocol
ISI	Inter Symbol Interference
IQ	In-phase and Quadrature
LH	Long-Haul
LO	Local Oscillator
LPF	Low Pass Filter
LTE	Long Term Evolution
MC	Multi-Carrier
MIMO	Multiple Input Multiple Output
MMA	Multiple Modulus Algorithm
MZM	Mach-Zehnder Modulator
NL	Non-Linear
NRZ	Non-Return-to-Zero

OBSAI	Open Base Station Architecture Initiative
ODSB	Optical Double Side-Band
OFDE	Overlapped Frequency Domain Equalizer
OFDM	Orthogonal Frequency Division Multiplexing
OFE	Optical Front-End
OOK	On-Off Keying
OPL	Optical Path Loss
OSBNR	Optical Side-Band to Noise Ratio
OSNR	Optical Signal to Noise Ratio
OSSB	Optical Single Side-Band
PAM	Pulse Amplitude Modulation
PAPR	Peak to Average Power Ratio
PBC	Polarization Beam Combiner
PBS	Polarization Beam Splitter
PD	Photodiode
PDL	Polarization Dependent Loss
PIN	P-doped, Intrinsic, N-doped semiconductor
PMD	Polarization Mode Dispersion
PON	Passive Optical Network
PRBS	Pseudo-Random Binary Sequence
PSK	Phase Shift Keying
PTF	Power Transfer Function
QAM	Quadrature Amplitude Modulation
RAN	Radio Access Network
RF	Radio-Frequency
RIN	Relative Intensity Noise
ROP	Received Optical Power
RRH	Remote Radio Head
RTO	Real-Time Oscilloscope
SC	Single-Carrier
SMF	Single Mode Fiber
SNR	Signal to Noise Ratio
SOA	Semiconductor Optical Amplifier
SR	Short-Reach
SSBI	Subcarrier to Subcarrier Beating Interference
SSII	Subcarrier to Subcarrier Intermodulation Interference
TDE	Time Domain Equalizer
TIA	Trans-Impedance Amplifier
US	Up-Stream
WDM	Wavelength Division Multiplexing
WGN	White Gaussian Noise
XTPP	Cross-Talk Power Penalty

Introduction

i) The data traffic explosion and the role of optical fiber communications.

An exponential growth in data traffic in telecommunication networks has been experienced in the last two decades. For instance, in 1992 global Internet networks carried around 100 Gigabytes (GB) of traffic per day, while only ten years later, in 2002, this traffic drastically increased to 100 GB per second [1]. In 2016, global Internet traffic increased to more than 20,000 GB per second (200 times in 14 years) while the annual rate for global IP traffic was 96 Exabytes (EB) per month [1]. According to Cisco forecast reported in [2], the annual global IP traffic will grow at a compound annual growth rate of 24% from 2016 to 2021, reaching 278 EB per month by 2021, as shown in Figure i.1. In Mexico, the IP traffic is forecasted to grow almost three-fold from 2016 to 2021, reaching 3.4 EB per month in 2021, up from 1.3 EB per month in 2016 [3].

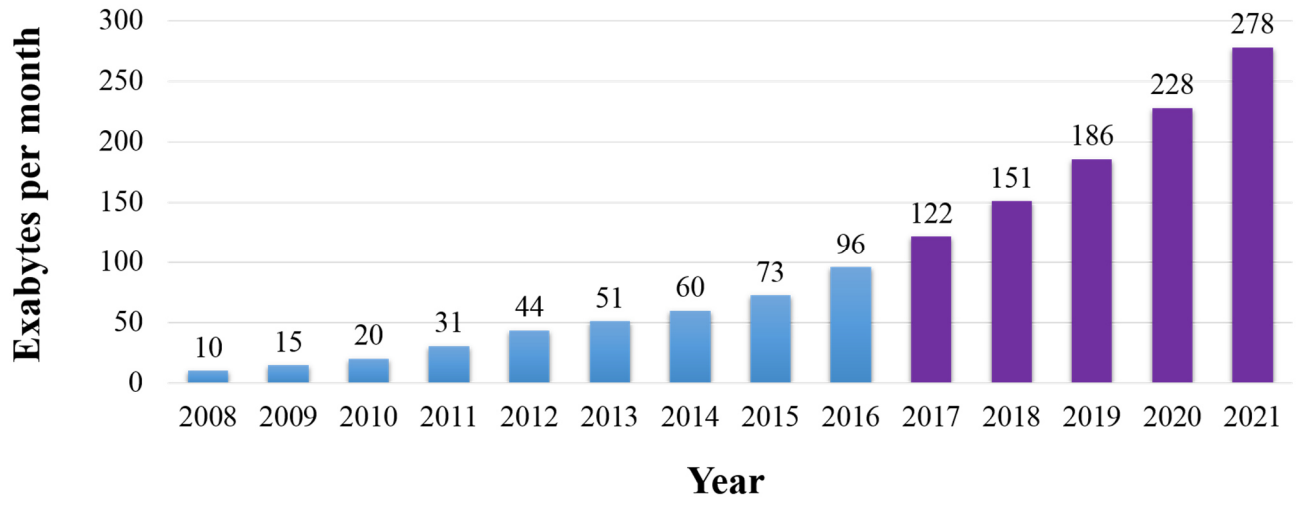

Figure i.1 Global total IP traffic (EB per month): fixed internet, managed IP and mobile data, as a function of year [2]. Historical: From 2008 to 2016. Forecasted: From 2017 to 2021.

This traffic demand explosion has been driven by both the increase of Internet users (both human and machines) and the emerging of high bandwidth-consuming applications, such as social networks, high definition video-calls, IP high definition television, the Internet of things, cloud computing, gaming, scientific computing, among others. For instance, global IP traffic per capita was 13 GB per month in 2016, up from 1 Mbyte and 1 GB in 2000 and 2007, respectively [1].

To cope with this challenging bandwidth demand, the role of optical communications has been essential [4]. Due mainly to its lower attenuation and higher bandwidth, as well as its null electrical interference sensitivity, the optical fiber has been replacing copper wire in the implementation of telecommunication networks, initially in long-distance networks and currently in shorter-reach networks.

Figure i.2 plots the overall data rate transmitted in a single optical fiber as a function of time corresponding to record-breaking experiments [5] compiled by Donald Keck, co-inventor of low-loss optical fiber. It can be observed an exponential growth of the fiber systems' capacity (note that Y-axis scale is logarithmic), motivated by the necessity of meeting the incessant bandwidth demand.

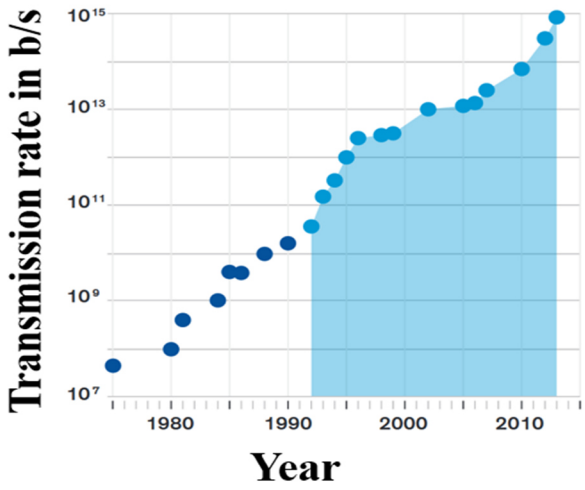

Figure i.2 Record-breaking "hero" experiments in data rate transmission through a single optical fiber [5]. The improvement in fiber capacity before and after the introduction of wavelength division multiplexing (WDM) in 1992 is highlighted in blue.

In 2015, at least 95% of all transoceanic data traffic between countries was carried through optical fiber cables [6], [7]. In 2004, more than 80% of the world's long-distance traffic was carried over optical fiber cables [8]. Regarding access networks, according to the Organization for Economic Cooperation and Development (OECD) Broadband Portal [9], in 2016 the percentage of fiber links with respect to total broadband subscriptions was still relatively low, equal to 20% in average among the OECD countries. However, an average annual growth of 18% from 2015 to 2016 was measured. Fiber subscriptions data includes fiber to the home (FTTH), fiber to the premises (FTTP) and fiber to the building (FTTB). As shown respectively in Figure i.3 and Figure i.4, the percentage of fiber links and annual growth has a strong variation among countries. For instance, Japan and Korea have more than 70% of their broadband connections set up with optical fiber, while the case of countries like Belgium Israel or Greece, is practically nil. In terms of annual growth of fiber connections, Australia and New Zealand are leaders, with more than 120%. In the case of Mexico, only 13% of broadband connections rely on optical fiber, which is a figure below the OECD average of 20 %. However, a vibrant 77% growth in the deployment of fiber links was shown between 2015 and 2016. It is important to remark, notwithstanding, that Mexico ranked last in the list of fixed broadband subscriptions per 100 inhabitants among the OECD countries. That is, only 13% of Mexican people have access to fixed broadband services. This contrasts with the situation in well-developed countries, such as Switzerland, where 51% of its inhabitants have access to these services. Therefore, there is a big room for improvement in Mexico in order

to increase this lack of broadband access among Mexican population, which will, undoubtedly, be mainly solved with the development and introduction of high-capacity optical communication technologies, such as the ones investigated in this thesis work.

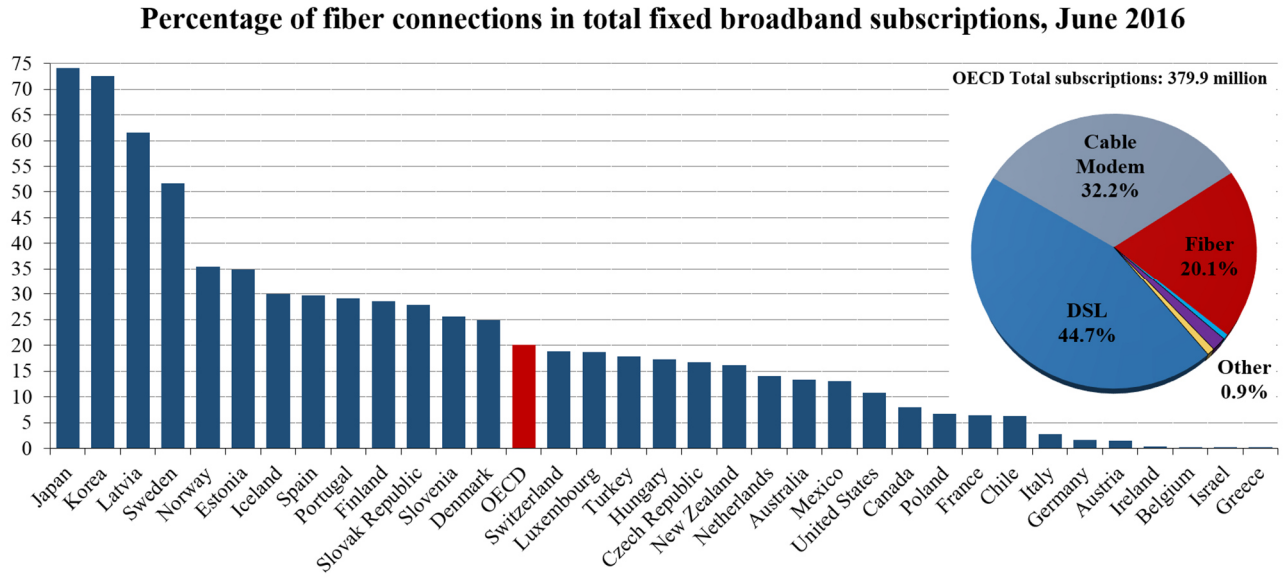

Figure i.3 Percentage of fiber connections in total broadband fixed subscriptions per OECD country in 2016 [9].

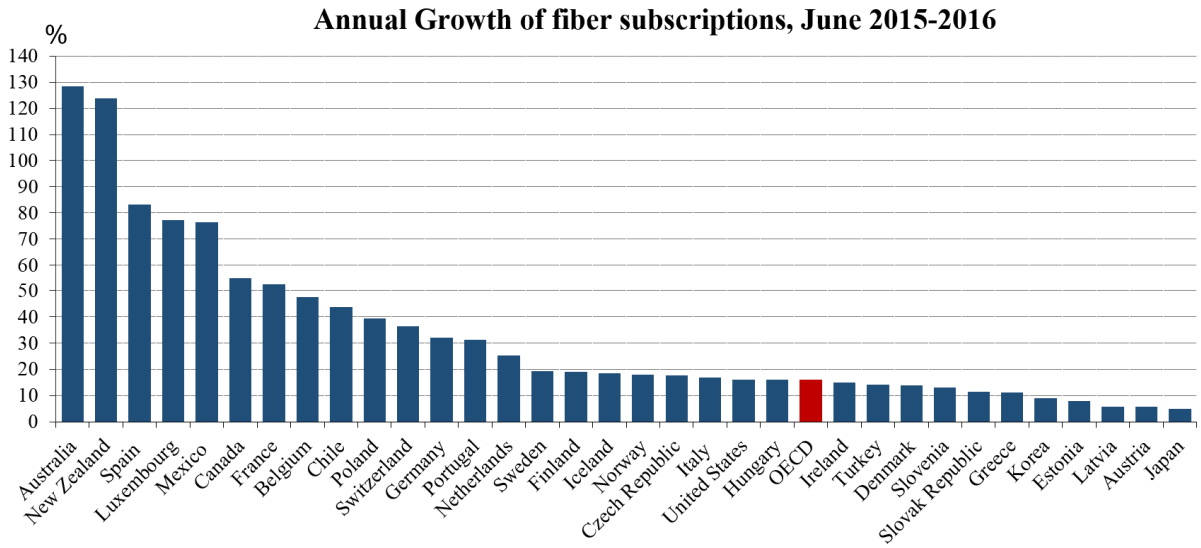

Figure i.4 Annual growth of fiber connections in fixed broadband subscriptions per OECD country between 2015 and 2016 [9].

Mobile and wireless technologies are increasingly contributing to the explosion of traffic demand. While 51% of the global IP traffic accounted for wired devices in 2016, it is predicted that wireless and mobile devices will provide 63% of traffic in 2021 [1]. Mobile data traffic has grown 18 times over the last 5 years [10]. Moreover, a compound annual growth rate of 49% of smartphone-generated IP traffic versus a lower 10% generated by personal computers, is expected from 2016 to 2021. Most of this growth will be driven by the latest technological advancements. For instance, in 2016, 69% of the mobile traffic was accounted by fourth-generation (4G) traffic. The incoming five-generation (5G) wireless and mobile networks will definitely contribute to the relentless mobile traffic increase. To achieve the demanding performance goals of 5G networks, besides the expected development of proficient wireless technologies, the deployment of high-speed optical fiber links to connect antenna sites and central offices will be a must (as detailed in section 3.1) [11]. Therefore, the huge demand of high-capacity optical communication systems is pushing engineers and scientists from several fronts.

ii) Different optical schemes for different network level applications

The optical communication networks (OCNs) are widely extended around the world, divided into segments according to their coverage, capacity and characteristics. Due to the dynamic nature of networks, there is not a unique and standardized criterion to classify the OCNs. However, there is consensus in dividing the OCNs, as well as the optical communication systems (OCSs) and the optical links, into two fundamental categories determined by their coverage: long-haul (LH) and short-reach (SR).

According to [12], the OCNs could be sub-classified into core/backbone, metropolitan, access and data center interconnections (DCI). Core and backbone networks are included in the LH category, whereas metro optical transport networks, optical access networks or other optical interconnection systems are included in the SR category. According to the author, LH links are hundreds and thousands of kilometers long, while the SR links are up to 100 km long.

The same sub-classification of the OCNs is reported in [13]. However, the author includes both core and metro networks in the LH category, and the access and DCI networks in the SR one. Metro and core networks are also considered in the referred publication as hundreds or thousands kilometers long, while access networks and optical DCIs are defined as up to several kilometers and tens of kilometers long, respectively. Figure i.5 shows a scheme of the proposed OCNs sub-classification.

Core and backbone networks connect cities and countries. Metro networks are a bridge between access and core networks. Access networks are often referred to as the “last mile connection” that links the end-users to the rest of the network. A data center consists of several computing nodes with their corresponding networking and storage subsystems, power distribution and cooling systems, housed in a building structure [14]. Data center interconnections can be divided into data center to user (through the internet or IP WAN), data center to data center (inter-DCI) and traffic that remains within data center (intra-DCI), as shown in Figure i.6.

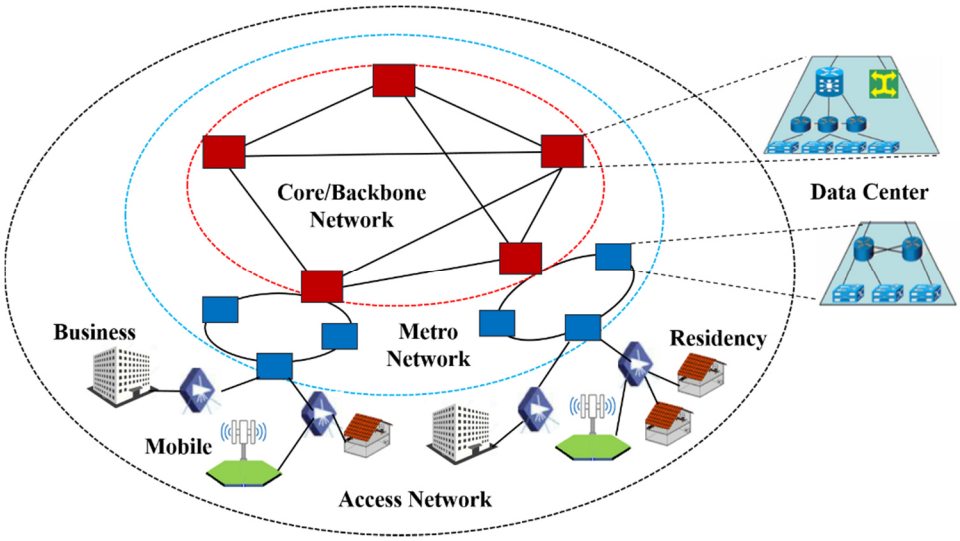

Figure i.5 Typical optical communication network scheme. Adapted from [13].

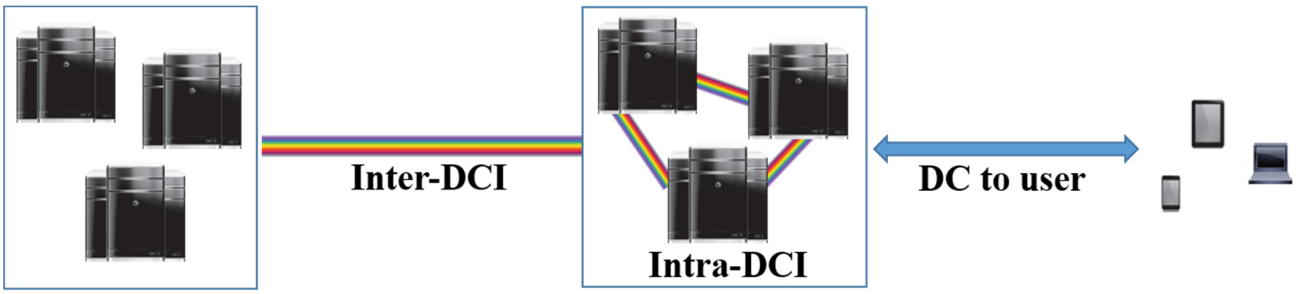

Figure i.6 Data center interconnections.

According to [15], SR-OCSs can be classified into four cases: chip to chip inter-connect, server to server inter-connect (<1km), optical inter-DCI (2km to 20km) and optical access and metro applications (>20km up to 100km). In [16] and [17], optical DCIs are classified into: intra-DCIs for link lengths up to 10 km, and inter-DCIs for link lengths higher than 10 km (up to 100 km according to [17]).

In all the above publications it is agreed that core and backbone optical networks can be categorized as LH, while optical access and optical DCIs up to 100 km are SR networks. However, there is not consensus regarding the classification of optical metro links. This stands because, in general, optical metro networks are on the cusp of many transformations, due to explosive traffic growth, changing in metro-traffic characteristics, the adoption of cloud-services with distributed computation and storage, deployment of new broadband access technologies and the emergence of new bandwidth bottlenecks in the aggregation, edge and core of the network [18]. In general, optical metro-networks are divided into metro-edge (closer to access networks) and metro-core or metro-regional (closer to the core networks) OCNs [19], [20]. A metro-access stage has been added to metro Ethernet networks between the access and the metro-edge networks [21]. Legacy metro-edge rings span lengths between 10 to 40 km (25 to 65 km according to [20]) while legacy metro-core rings cover ranges from 50 to 500 km [19], [20].

In this contribution, optical access, DCI, metro-access and metro-edge networks up to ~100 km are considered as short-reach optical communication systems. We also adopt the convention of considering optical intra-DCI as links ranging from 2 to 10 km (in process of standardization for rates of 50, 200 and 400 Gb/s by the IEEE), and inter-DCI as links extending between 10 and 100 km (not being currently standardized by any organization as far as we know).

Current standardized commercial technology for LH-OCSs transmit up to 100 Gb/s per optical channel, using dual-polarization (DP) QPSK coherent technology, propagating up to 80 optical channels over the same single mode-fiber (SMF) by means of WDM [4], [22]. Regarding SR-OCS's, the predominant standardized commercial technology is Ethernet, whose optical transceivers transmit an aggregated rate up to 100 Gb/s over the same SMF by WDM multiplexing four optical channels and using the simplest (but less spectrally efficient) optical modulation format: on-off keying (OOK) [4], [22]. In both LH and SR cases, standardization efforts are being carried out to define the next-generation of OCSs technology, targeting a data rate of 400 Gb/s per optical channel and per optical fiber in LH and SR schemes, respectively. Figure i.7 shows the evolution of commercial technology for both LH and SR schemes [23], namely, optical transport network (OTN) and Ethernet transceivers, respectively.

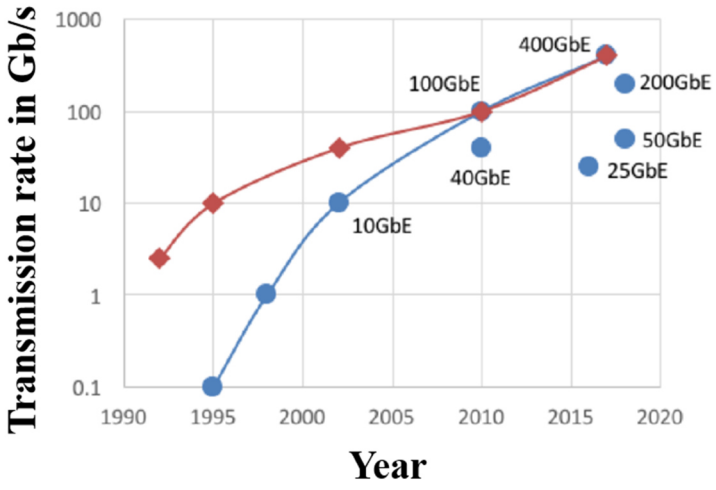

Figure i.7 Transmission rate increase as a function of time of standardized OTN (in red with diamonds) and Ethernet (in blue with circles) commercial transceivers. GbE stands for Gigabit Ethernet. 50, 200 and 400 GbE are forthcoming standards. Adapted from [23].

Apart from the evident difference in coverage, LH and SR systems have other fundamental differences [4]. On one hand, LH systems operate in C-band (to diminish losses) using a dense WDM approach, where tens of optical channels are spectrally multiplexed as close together as possible. Long distances have to be covered, therefore, the multiplexed optical channels are transmitted through several fiber spans that require the use of optical amplifiers. In this case, optical signal to noise ratio (OSNR) management becomes an important issue to be considered. For optical routing purposes, transmission across reconfigurable optical add/drop multiplexers is needed. Therefore, filter concatenation is another important impairment present in LH

transmission. In contrast, cost, complexity, size and power consumption of the LH transceivers and systems are not critical parameters in the design and implementation processes. Moreover, the use of high-overhead FEC schemes is widely extended in this kind of systems. Additionally, spectral efficiency is a key parameter due to the very high capacity targets of LH links. As a result of these considerations, high-order modulation formats and coherent technology are currently utilized in state-of-the-art commercial LH networks. Today's developments for LH systems are oriented to further increase their capacity and spectral efficiency by packing more channels together using Nyquist filtering, using spatial division multiplexing, and employing higher-order modulation formats enabled by the creation of new digital signal processing (DSP) compensation algorithms.

On the other hand, SR systems have traditionally been operated in O-band to avoid chromatic dispersion compensation, but with the incorporation of electronic dispersion compensation, this trend is now changing. Wider channel spacing plans are admitted to relax laser frequency stability requirements as well as lowering crosstalk and filter selectivity requirements. Due to the large amount of optical nodes and end-users in optical metro, access and mainly in data center networks, power consumption, cost efficiency, footprint and complexity are key consideration for SR optical communication systems [12]. SR optical transceivers were first implemented using the simplest optical features: direct modulated lasers (DML), OOK modulation format and direct detection. Although some SR systems are still implemented using DMLs, as the capacity of the SR transceivers increases, external modulation has been replacing this approach. However, even in today's higher-capacity SR commercial systems, OOK format and direct detection technology are still employed. While the OOK format is being replaced by more spectrally-efficient higher-order modulation formats in the development of new SR commercial technology, the use of non-coherent, direct detection schemes is still preserved.

iii) Motivation of the thesis

Although some years ago the main scope of optical communications was long-haul networks, the use of optical fibers in short-reach networks has gained considerable ground. Some relevant facts that demonstrate the fundamental role that short-reach optical communication systems is having in nowadays and incoming telecommunication networks are provided below:

- The bandwidth demand from SR optical networks at metro level surpassed that from LH in 2014 [24].
- The traffic exchanged over telecommunication networks is only the tip of the iceberg; there is a massive increase in internal data center network traffic [14]. For instance, in 2015 the annual global IP traffic accounted for fixed internet, managed IP and mobile data was 0.88 zettabytes (see Figure i.1) while the one exchanged among data centers was 4.7 zettabytes (5.4 times higher) [25].
- Data center traffic is forecasted to grow 27% per year from 2015 to 2020 [25].
- 75% of the overall data center traffic is exchanged within data centers (intra-DCI) while only 9% are moved from one data center to another (inter-DCI) [25]. These facts explain why standardization efforts

are focused in the intra-DCI scheme. However, the growth forecast of inter-DC traffic from 2015 to 2020 is 32%, higher than that of intra-DCI (26.8%) and DC-to-user traffic (24%).

- This growth in inter-DCI traffic is due to the fact that more datacenters are being located in metro areas, closer to the end users, to reduce latency, improve disaster resiliency and scale up the capabilities of data center operations by using a distributed architecture approach [14]. Therefore, it is clear that the development of advanced technology for both intra- and inter-DCI is becoming imperative.
- According to a Bell Labs study carried out in 2012 [26], the total traffic in metro networks was expected to increase 560% from 2013 to 2017, around two-fold faster than traffic in core networks. The main sources of this growth were: IP video, data center and cloud traffic, with a 720%, 440% and 560% of increasing over the referred period, respectively.
- The Bell Labs study also forecasted that 75% percent of total metro traffic will be terminated within the metro network in 2017, while only 2% of traffic will be transmitted through the core network [26].
- According to IHS Markit, the global optical DCI equipment market grew 49% in 2016 to reach USD 1.9 billion [27]. It is forecasted a compound annual growth rate of 18% to hit USD 4.5 billion by 2021.
- Regarding the use of optical links for mobile networks, a recently introduced segment of the network, called fronthaul, that bridges the antenna sites and the central offices, is gaining a lot of attention [28]. Due to its characteristics, this fronthaul system fits well into the short-reach optical links category. The data rate demand that should meet the current fronthauling technologies (CPRI and OBSAI) in a single link is becoming critical. For instance, to transmit five 20-MHZ long term evolution advanced (LTE-A) mobile signals, for a system configuration using 8 × 8 multiple-input and multiple-output (MIMO) and three directional sector antennas, a CPRI fronthaul link would require a data rate of about 147.5 Gb/s [29]. Then, a large number of current 10 Gb/s optical OOK transceivers are required.
- Future 5G networks may require to transport several tens of these 20-MHZ LTE-A signals per antenna site. Moreover, mobile signals with wider channel sizes of 100, 250 and up to 500 MHz are being considered for next generation 5G technology [30]. Therefore, a crash of current fronthaul systems could be envisaged, which calls for technological alternatives to upgrade the fronthauling links capacity as a fundamental requirement to achieve proper operation of the future mobile networks.

The aforementioned facts exhibit the relevance and necessity of research work to develop high-speed short-reach optical communication systems at different levels of coverage. Accordingly, in this contribution three short-reach optical schemes are proposed, designed and analyzed: optical DCIs for both intra and inter approaches, and optical fronthauling. Details of these systems and their targets are provided in the following section.

iv) Objectives of the thesis

General objective. To propose next-generation higher-speed alternatives to current available short-reach optical communication systems for two cutting-edge applications: mobile fronthaul and data center interconnections. To design and analyze the physical layer of this systems in order to meet the specific performance target of each application operating over single-mode fiber using state-of-the-art devices.

Particular objectives:

1. To design and optimize for both downstream and upstream directions a direct detection system able to transmit up to 192 20-MHz OFDM signals per optical channel (~92 Gb/s overall) over 25 km of single mode fiber for fronthauling applications using the digital signal processing frequency aggregation/de-aggregation approach. The required error vector magnitude (EVM) is 8% for 64-QAM modulated carriers and 12.5% for 16-QAM modulated carriers. An optical path loss up to 29 dB is desired to be achieved in order to meet the passive optical network (PON) requirements for class I.

2. To develop and experimentally evaluate low-complexity and low-latency digital signal processing techniques to counteract some transmission impairments of the analyzed fronthaul architecture for both downstream and upstream directions, in order to improve the performance (decrease the maximum EVM) at the output of the system.

3. To design and optimize an unamplified multi-wavelength direct detection optical OFDM transceiver, using the RF up/down conversion and optical field modulation approach, able to transmit 400 Gb/s (four wavelengths at 100 Gb/s each) up to 10-km of single mode fiber for intra-data center Ethernet optical interconnects with a target bit error ratio (BER) of 1×10^{-13} at the output of the system.

4. To develop and numerically evaluate a low-complexity and low-latency peak-to-average power ratio (PAPR) reduction technique to diminish the impact of the modulator nonlinear distortion in order to decrease the BER at the output of the 400 Gb/s direct detection optical OFDM system.

5. To design and optimize an unamplified multi-format optical IQ coherent transceiver able to transmit up to 1.6 Tb/s with a reach of 40 km (for maximum capacity) of single mode fiber for inter-data center optical interconnects with a target BER of 1×10^{-13} at the output of the system.

v) Original contributions presented in this work

- The proposal and experimental evaluation of a digital, instantaneous and low-complexity non-linear compensation technique in combination with a clipping technique to reduce the PAPR of a transmitted signal in order to counteract the system non-linear distortion effects. Its use allows to increase the optical path loss of the analyzed fronthaul system for a given target EVM on the downstream direction.
- The development of a pre-emphasis technique to equalize the received EVM per channel distribution, enabling to decrease the worst EVM obtained when the equalization is not applied. Its functionality

was experimentally demonstrated for both downstream and upstream directions of the analyzed fronthaul system. Its use in the upstream direction allows to compensate for the imbalance of received signal-to-noise ratio (SNR) between channels caused by propagation through both wireless and optical channels, thus improving the overall performance of the system.

- The proposal and numerical demonstration of a simplified technique to reduce PAPR on OFDM signals based on random phase shifting at symbol level.
- Numerical demonstration of the technical feasibility of an unamplified 4 x 100 Gb/s direct detected OFDM system using electro-absorption modulators (EAM) for transmission up to 10 km of conventional SMF that is based on the use of currently available devices. To this end, the phase shifting PAPR reduction technique was used in combination with optimization of the main modulator parameters to counteract the nonlinear distortion of the modulator. A BER of 3.8×10^{-5} at the output of the system was attained. To reach the BER target of 1×10^{-13}, the use of a low-overhead FEC scheme was found to be a must.
- Proposal of a multi-format optical coherent system designed under atypical conditions: a very low BER target of 1×10^{-13} without using forward-error correction (FEC), and no optical amplification. Its feasibility to transmit up to a very high data rate of 1.6 Tb/s along 40-km was numerically demonstrated using currently available devices. Transmission through longer reaches was shown to be possible still meeting the demanding BER target by changing the modulation format, but at expense of decreasing the data rate. Up to 110 km for a data rate of 800 Gb/s was numerically demonstrated using currently available devices.

vi) List of associated publications

The results and discussions reported in the following journal and conference proceeding publications (1, 4, 5, 8; and 2, 3, 6, 7, 9, respectively) are part of this thesis work.

Associated to Chapter 3

1. P. Torres-Ferrera, S. Straullu, S. Abrate and R. Gaudino, "Upstream and Downstream optimization in DSP-Based Channel Aggregation for Optical Fronthauling,", Optical Fiber Technology (2017) [Submitted].

2. P. Torres-Ferrera, S. Straullu, S. Abrate and R. Gaudino, "Alternative Solutions for Fronthauling based on DSP-assisted Radio-over-Fiber,", 19th International Conference on Transparent Optical Networks (ICTON), Girona, Spain, Jul. (2017).

3. P. Torres-Ferrera, S. Straullu, S. Abrate, A. Vinci, R. Gaudino, "Up to 4 x 192 LTE-A Radio Waveforms Transmission in a Point to Multipoint architecture for Massive Fronthauling Solutions," 19th Italian National Conference on Photonic Technologies (Fotonica), Padova, Italy, May. (2017).

Associated to Chapter 4

4. P. Torres-Ferrera, S.O. Vazquez, R. Gutiérrez-Castrejón, "4 x 100 Gb/s WDM DD-OFDM using EAM for next generation Ethernet transceivers over SMF," Optics Communications 365, 86-92 (2016).

5. P. Torres-Ferrera, L. Pacheco-Ramírez, R. Gutiérrez-Castrejón, "Next-generation 400 Gb/s Ethernet PMD over SMF at 1310 nm via DD-OFDM with electro-absorption modulator-based transmitters," IEEE Latin American Transactions 14 (6), 2681-2686 (2016). [Spanish version[1]].

6. P. Torres-Ferrera, R. Gutiérrez-Castrejón, "4 x 100 Gbps using MZ Modulators for Ethernet," OSA Latin America Optics and Photonics Conference (LAOP), LW4C.2, Medellin, Colombia, Aug. (2016).

7. P. Torres-Ferrera, L. Pacheco-Ramírez, R. Gutiérrez-Castrejón, "Next-generation 400 Gb/s Ethernet PMD over SMF at 1310 nm via DD-OFDM with electro-absorption modulator-based transmitters," 7th IEEE Latin-American Conf. Communications (LATINCOM), Arequipa, Peru, Nov. (2015).

Associated to Chapter 5

8. P. Torres-Ferrera, M. A. García-Yañez, R. Gutiérrez-Castrejón, I. Tomkos, "Coherent Optical WDM Systems for 1.6 Tb/s Ethernet over 40 km of Single-Mode Fiber," Optical Fiber Technology, (2017) [Submitted].

9. P. Torres-Ferrera, R. Gutiérrez-Castrejón, I. Tomkos, "Multi-Format 800 – 1600 Gb/s Coherent Transceiver for Inter-Data Centre Interconnects over SMF," 19th International Conference on Transparent Optical Networks (ICTON), Girona, Spain, Jul. (2017).

The two following journal publications report our results obtained in a previous research work. These results are not included in the present thesis document. However, the system analyzed in those publications serves as an antecedent reference for the systems presented in this thesis for comparison purposes reported in Chapter 5 ("General conclusions and future work").

10. P. Torres-Ferrera, R. Gutiérrez-Castrejón, "Impact of channel-spacing on next 400 Gb/s Ethernet 40-km PMD based on 16 x 25 Gb/s WDM architecture," Optical Fiber Technology 20, 177-183 (2014).

11. R. Gutiérrez-Castrejón, P. Torres-Ferrera, "Design and technical feasibility of next 400 GbE 40-km PMD based on 16 x 25 Gbps Architecture," Journal of Lightwave Technology 31, 2386-2393 (2013).

[1] The English version was presented in the 7th IEEE Latin-American Conference of Communications (publication number 7 of this list). An extended version translated into Spanish was required to the authors to be reviewed and published in a special volume of the IEEE Latin American Transactions journal.

1. Chapter one: Fundamental principles of digital IQ modulation and OFDM

1.1 IQ modulation and demodulation

An *IQ modulator* transforms a serial sequence of binary symbols (bits) into an analogue modulated signal, which is a real-valued *passband* signal. *Passband* signals are difficult to handle, so that they are typically represented as complex *baseband* signals (see Appendix A.1). The real *passband* output signal of an IQ modulator $x_{IQ}(t)$ can be represented as [31]

$$x_{IQ}(t) = \mathrm{Re}\left\{x(t)\exp\left(j2\pi f_c t\right)\right\} \tag{1.1}$$

where

$$x(t) = x_I(t) - jx_Q(t) \tag{1.2}$$

then,

$$x_{IQ}(t) = x_I(t)\cos(2\pi f_c t) + x_Q(t)\sin(2\pi f_c t) \tag{1.3}$$

The signal $x(t)$ is the complex *baseband* representation (or *complex envelope*) of the *passband* signal $x_{IQ}(t)$ (see Appendix A.1). The signals $x_I(t)$ and $x_Q(t)$ are real-valued *baseband* signals called the In-phase (I) and Quadrature (Q) components of $x(t)$, respectively. A typical *IQ modulator* has a block structure that follows Equation (1.3), as illustrated in the left hand side of Figure 1.1.

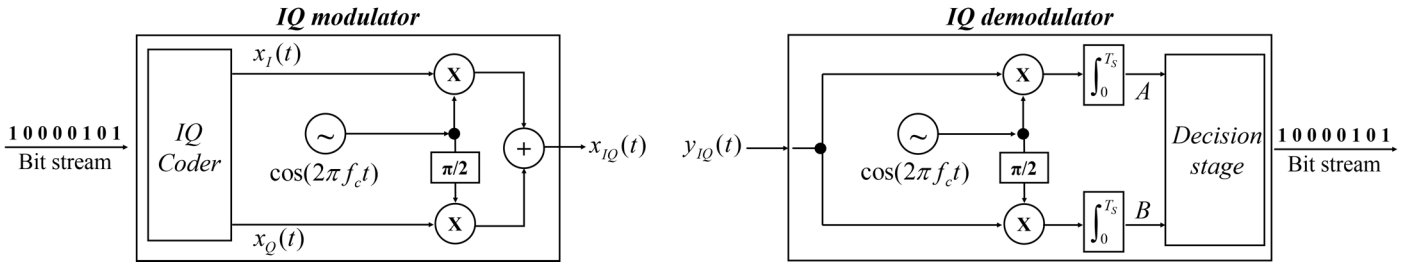

Figure 1.1 Block diagrams of an *IQ modulator* and *IQ demodulator*.

The first step in the *IQ modulation* process is the *IQ coding* performed by an *IQ coder* block, shown in Figure 1.2. An *IQ coder* transforms a serial bit stream into the pair of multi-level digital signals $x_I(t)$ and $x_Q(t)$. First, an *IQ mapper* assigns a two dimensional (2D) symbol to every block of *k* bits that inputs the coder. Each

2D-symbol is composed of a pair of real scalars α and β, i.e. $C = \{\alpha, \beta\}$. The value of the symbol components α and β (chosen from a given alphabet) depends on the decimal value of the corresponding k-size binary number. A graphical representation of an alphabet in a plane is called a *constellation*. The employed alphabet and the size of k defines the specific digital modulation format (DMF). The number $M = 2^k$ is the DMF order. The DMFs used in the present work are: QPSK (k=2), 8PSK (k=3), 16-QAM (k=4), 32-QAM (k=5) and 64-QAM (k=6). The right hand side of Figure 1.2 shows an example of a *constellation* for the 16-QAM format.

The symbol period T_s (or symbol duration) is equal to the bit period T_b multiplied by k. The bit period is the inverse of the bit rate R_b [bits/s] of the serial bit stream. The symbol rate R_s [symbol/s or *Baud* = Bd] is calculated as the inverse of T_s. Then, $R_s = R_b / k$. Since the bandwidth B of a digital signal is proportional to its data (bit or symbol) rate, it is straightforward to see that an *IQ modulation* is useful to increase the spectral efficiency of a communication system, especially for higher values of M.

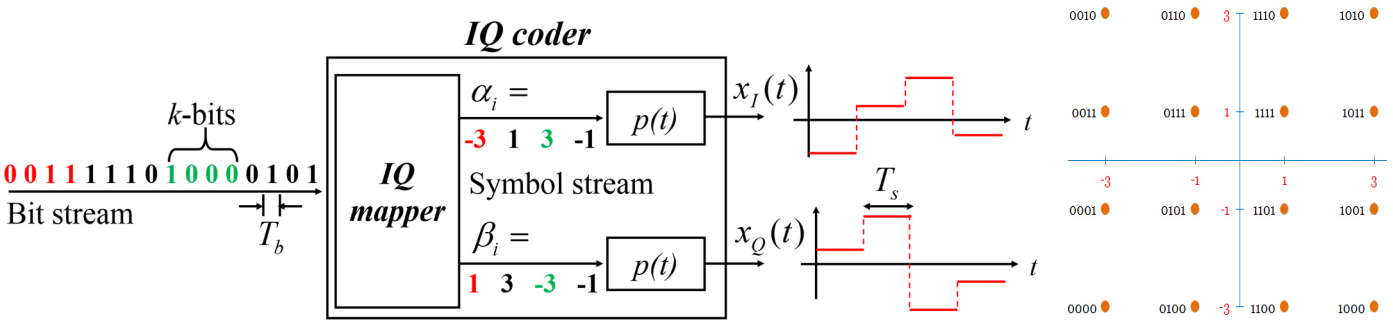

Figure 1.2 Block diagram of an *IQ coder* (16-QAM format is used as example).

After bit-to-symbol transformation, the symbols are pulse-shaped by an analogue function $p(t)$. This function can be a rectangular pulse defined as in equation (1.4) (non-return to zero (NRZ) pulse-shaping), a rectangular pulse in "on" state only half of T_s (return-to-zero (RZ) pulse shaping) or a *sinc* pulse (Nyquist pulse-shaping), among others. In the rest of the present work a NRZ pulse-shaping will be assumed.

$$p(t) = \begin{cases} 1, & (0 < t \le T_s) \\ 0, & (0 < t \le T_s) \end{cases} \qquad (1.4)$$

The pulse-shaping consists of multiplying the two parallel streams α_i and β_i, which conforms the 2D-symbol stream C_i, by the signal $p(t)$. The whole pulse-shaped symbol stream generates the pair of real-valued *baseband* analogue signals $x_I(t)$ and $x_Q(t)$, which output the *IQ coder*, as follows

$$\{x_I(t), x_Q(t)\} = \sum_{i=-\infty}^{\infty} C_i \cdot p(t - iT_s) = \left\{ \sum_{i=-\infty}^{\infty} \alpha_i \cdot p(t - iT_s), \sum_{i=-\infty}^{\infty} \beta_i \cdot p(t - iT_s) \right\} \tag{1.5}$$

The last step to generate the modulated signal $x_{IQ}(t)$, according to equation (1.3), is to multiply the signals $x_I(t)$ and $x_Q(t)$ by the 0 and π/2 branches of an oscillator having carrier frequency f_c, respectively.

After transmission through the communication system, the received signal $y_{IQ}(t)$ inputs an *IQ demodulator* whose purpose is to recover the transmitted bit stream. In order to estimate the *i*-th received symbol $\tilde{C}_i(t) = \{A_i, B_i\}$, the received signal $y_{IQ}(t)$ is projected over the two signal basis $p(t)\cos(2\pi f_c t)$ and $p(t)\sin(2\pi f_c t)$ over the *n*-th symbol period by means of the inner product, process called *matched filtering*, as follows

$$\begin{aligned} A_i &= \frac{1}{T_s}\int_0^{T_s} y_{IQ}(t - iT_s)p(t - iT_s)\cos(2\pi f_c t)dt = \frac{1}{T_s}\int_0^{T_s} y_{IQ}(t - iT_s)\cos(2\pi f_c t)dt \\ B_i &= \frac{1}{T_s}\int_0^{T_s} y_{IQ}(t - iT_s)p(t - iT_s)\sin(2\pi f_c t)dt = \frac{1}{T_s}\int_0^{T_s} y_{IQ}(t - iT_s)\sin(2\pi f_c t)dt \end{aligned} \tag{1.6}$$

Once the point $\tilde{C}_i(t) = \{A_i, B_i\}$ is obtained, a decision stage assigns a corresponding symbol within the alphabet depending on the decision region (Voronoi region) in the IQ plane to which the point belongs to. The last step of the demodulation process consists on assigning the corresponding group of bits to every estimated symbol in order to reconstruct the bit stream. A typical *IQ demodulator* block diagram is shown in the right hand side of Figure 1.1.

While the *IQ modulator* architecture presented in Figure 1.1 is useful for implementation purposes, there is a more compact representation based on the complex *envelope* $x(t)$ of $x_{IQ}(t)$ presented in equation (1.1). A *complex mapper* assigns a complex symbol *C* to every *k*-size group of bits of the input bit stream. The *i*-th symbol *C* is then represented as the complex number

$$C_i = \alpha_i - j\beta_i$$

The whole pulse-shaped complex symbol stream then becomes the complex *envelope* signal $x(t)$ as follows

$$x(t)=\sum_{i=-\infty}^{\infty} C_i \cdot p(t-iT_s)=\left\{\sum_{i=-\infty}^{\infty} \alpha_i \cdot p(t-iT_s)-j\sum_{i=-\infty}^{\infty} \beta_i \cdot p(t-iT_s)\right\}=x_I(t)-jx_Q(t) \tag{1.7}$$

where $x_I(t)$ and $x_Q(t)$ are considered as in equation (1.5). If now, $x(t)$ is multiplied by the output signal of a complex oscillator $\exp(j2\pi f_c t)$ then we have the output signal of the *complex modulator* shown in Figure 1.3. The output signal of an *IQ modulator* is the real part of the output signal of this *complex modulator*, as indicated in equation (1.1). Therefore, an *IQ modulator* could be represented in a more compact form as a *complex modulator* followed by a real-part operator, as shown in Figure 1.3.

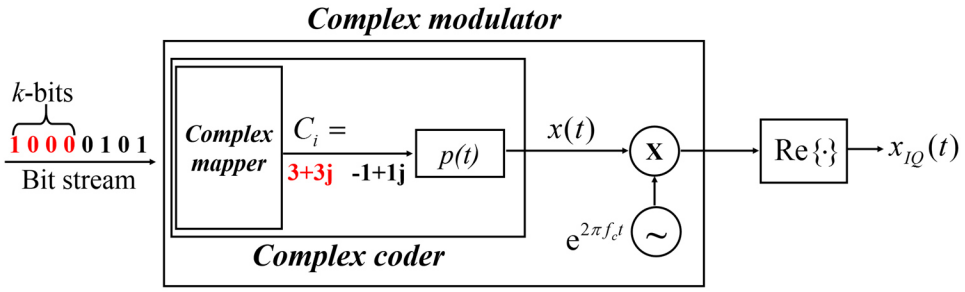

Figure 1.3 Block diagrams of an *IQ modulator* built with a *complex coder* and a *complex modulator*.

At the receiver side the *n*-th received complex symbol $\tilde{C}_i(t) = A_i - jB_i$ is estimated as follows (see Equation (1.6)):

$$\tilde{C}_i = A_i - jB_i = \frac{1}{T_s}\int_0^{T_s} y_{IQ}(t-iT_s)\exp(-j2\pi ft)\,dt \tag{1.8}$$

1.2 Orthogonal Frequency Division Multiplexing (OFDM) principles

The output signal of an *IQ modulator* $x_{IQ}(t)$ transmits information with a bit rate R_b in a *single-carrier* (SC) transmission scheme. The bandwidth B of this signal is proportional to the symbol rate R_s ($B = R_s$ in the Nyquist case). For high R_s values, B could exceed the flat response range of the devices and the channel that conforms the communication system. As a result, $x_{IQ}(t)$ will experience a frequency selective fading [32]. In the time-domain, the transmission through a dispersive channel (as the fiber channel) induces a time delay t_D. To reduce as much as possible the inter-symbol interference (ISI), the symbol period $T_s >> t_D$ [32]. This condition is difficult to be satisfied for high R_s values (i.e. short T_s values).

One solution to the previous problem is the use of *multi-carrier* (MC) transmission schemes (or *multi-carrier* modulation, MCM). In this approach the serial bit stream is divided into *N* parallel bit streams each having a much lower (especially for larger values of *N*) bit rate $\hat{R}_b = R_b / N$. Each parallel bit stream inputs an *IQ modulator*, each with a different carrier frequency f_i (called *sub-carrier*). The output signal of the every *IQ modulator*, $\hat{x}_{IQ}(t)$ (called *sub-channel*), has a symbol rate $\hat{R}_s = R_s / N$, then the bandwidth of the i-th $\hat{x}_{IQ}(t)$ signal is $B_i = \mathrm{B} / N$. Even though the communication system bandwidth is not flat in the entire frequency range $f_c \pm \mathrm{B}/2$, since B_i is much narrower than B (especially for large values of *N*), the *sub-channels* experience an almost flat system response in the frequency range $f_i \pm B_i / 2$. Similarly, the *sub-channel* symbol period $\hat{T}_s = T_s \bullet N$ becomes larger, thus satisfying the condition $\hat{T}_s >> t_D$ and therefore reducing ISI.

However, the MC systems have the following drawbacks:

I. The filters used to separate the *sub-channels* at the receiver side are not ideal. Therefore, a guard band (*GB*) between *sub-channels* is needed. As a consequence, the *sub-carrier* spacing Δf , defined as the frequency difference between any adjacent *sub-carriers*, should be $\Delta f = B_i + GB$. The total bandwidth of the MC signal will then be greater than B, i. e. $N \cdot \Delta f = N \cdot B_i + N \cdot GB = \mathrm{B} + N \cdot GB$, thus reducing the spectral efficiency of the system.

II. A large number of *IQ modulators* and *demodulators* are needed to operate the system since many *sub-channels* are required to exploit the MC system advantages. This is neither practical nor feasible.

Both issues could be avoided by using the OFDM approach for MC systems [33]. OFDM has a fundamental characteristic: all *sub-channel* waveforms are orthogonal to each other. Any two *sub-channels* are orthogonal to each other if the condition

$$f_k - f_l = m\frac{1}{\hat{T}_s} = m\hat{R}_s \tag{1.9}$$

is satisfied (see Appendix A.2), where *m* is any natural number and f_k and f_l are the *sub-carrier* frequencies of each *sub-channel*. This condition establishes that provided that the Δf between any pair of *sub-carriers* (note necessarily adjacent) is an entire multiple of $\hat{R}_s$, the whole set of *sub-carriers* is orthogonal. Under this condition, the *sub-channels* could be, in principle, fully recovered without inter-channel interference (ICI) by using a match correlator in spite of being strongly overlapped in the frequency domain [33]. Therefore, if Δf is equal to $\hat{R}_s$, then the total bandwidth of the multi-carrier OFDM signal becomes $N \cdot \hat{R}_s$, that is R_s. This results

in a good spectral efficiency of 1 [Bd/Hz] (Nyquist case). The first drawback of MC systems is then solved by using OFDM. The solution to the second concern is discussed in the next section.

A general diagram of an OFDM MC transmission system is shown in Figure 1.4. The transmitted OFDM signal $x_{OFDM}(t)$ is represented as

$$x_{OFDM}(t) = \sum_{n=1}^{N} x_{IQ,n}(t) = \mathrm{Re}\left\{ \sum_{i=-\infty}^{\infty} \sum_{n=1}^{N} C_{ni}\, p\left(t - i\hat{T}_s\right) \exp\left(j2\pi f_n t\right) \right\} \tag{1.10}$$

where $x_{IQ,n}(t)$ is the *sub-channel* waveform that outputs the *n*-th *IQ Modulator*, C_{ni} is the *n*-th complex symbol at the *n*-th *sub-carrier* and f_n is the frequency of the *n*-th *sub-carrier*.

At the receiver side, the received OFDM signal $y_{OFDM}(t)$ is split and sent to all the IQ demodulators (due to spectral overlap, typical *passband* filtering frequency demultiplexing becomes useless). The *i*-th detected complex symbol at the output of the matched correlator of the *n*-th *IQ Demodulator* $\tilde{C}_{ni}$ (see Equation (1.8)) can be expressed as

$$\tilde{C}_{ni} = \frac{1}{\hat{T}_s} \int_0^{\hat{T}_s} y_{OFDM}\left(t - i\hat{T}_s\right) \exp\left(-j2\pi f_n t\right) dt \tag{1.11}$$

Assuming an ideal linear transmission system with impulse response $h(t) = \delta(t)$,

$$y_{OFDM}(t) = \sum_{n=1}^{N} y_{IQ,n}(t) = \sum_{n=1}^{N} x_{IQ,n}(t) * \delta(t) \tag{1.12}$$

where $y_{IQ,n}(t)$ is the *n*-th received *sub-channel* and $*$ stands for convolution. Since all the received *sub-channels* are still orthogonal to each other (due to ideal transmission), then

$$\tilde{C}_{ni} = \begin{cases} \dfrac{1}{\hat{T}_s}\int_0^{\hat{T}_s} y_n\left(t-i\hat{T}_s\right)\exp\left(-j2\pi f_k t\right)dt = \dfrac{1}{\hat{T}_s}\int_0^{\hat{T}_s} x_n\left(t-i\hat{T}_s\right)\exp\left(-j2\pi f_k t\right)dt = C_{ni}, & n=k \\ \sum_{n\neq k}\dfrac{1}{\hat{T}_s}\int_0^{\hat{T}_s} y_n\left(t-i\hat{T}_s\right)\exp\left(-j2\pi f_k t\right)dt = \sum_{n\neq k}\dfrac{1}{\hat{T}_s}\int_0^{\hat{T}_s} x_n\left(t-i\hat{T}_s\right)\exp\left(-j2\pi f_k t\right)dt = 0, & n\neq k \end{cases} \quad (1.13)$$

Equation (1.13) makes it clear that thanks to the orthogonality among subcarriers, the matched correlator acts as an effective *sub-channel* filter. Then, assuming ideal linear transmission, the detected symbol $\tilde{C}_{ni}$ only depends on the transmitted symbol C_{ni} (as in a *single-channel IQ Demodulation* process). After symbol estimation, the decision stage follows, generating the corresponding bit sequence. Due to transmission system impairments, some bits could be wrongly estimated. The main target of system design is to reduce as much as possible the number of bit errors.

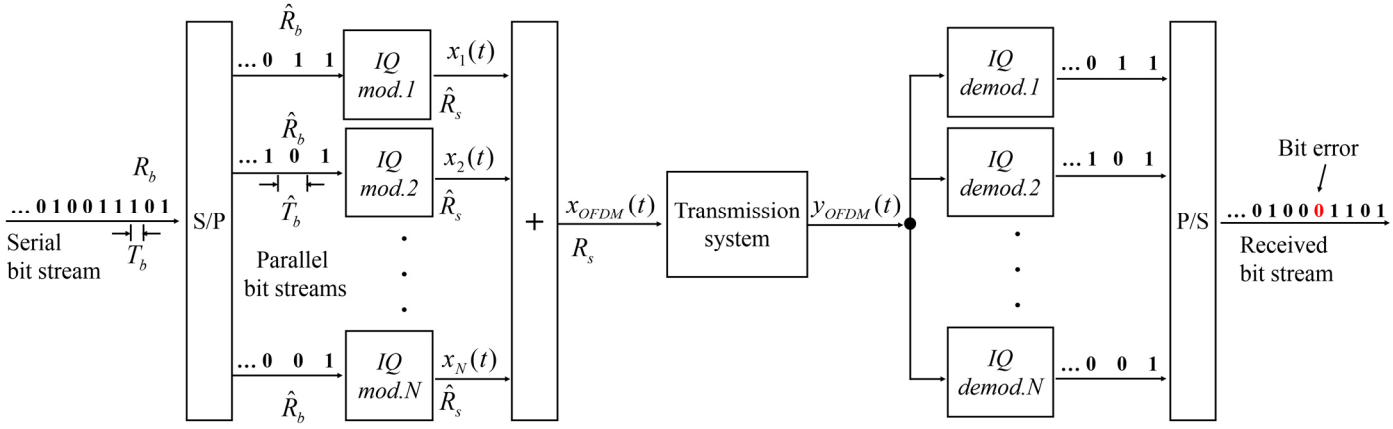

Figure 1.4 General diagram of an OFDM system as a Multi-carrier transmission system.

1.3 OFDM digital implementations

1.3.1 RF-IQ-OFDM digital implementation

Although spectrally efficient, the OFDM architecture presented in Figure 1.4 is still impractical for implementation purposes. A practical implementation approach based on signal digitizing and the use of the inverse and direct discrete Fourier Transforms (IDFT and DFT, respectively) was first proposed in [34].

The first consideration of this approach is to generate the *passband* $x_{OFDM}(t)$ as a *baseband* signal followed by a *RF-up-converter* of frequency f_{RF} equal to the frequency of the *sub-carrier* of the first *IQ Modulator*. The $x_{OFDM}(t)$ signal (for simplicity we only consider the transmission of the first symbol) then becomes

$$x_{OFDM}(t) = \mathrm{Re}\left\{\sum_{n=1}^{N} C_i \exp\left(j2\pi f_n t\right)\right\} = \mathrm{Re}\left\{\sum_{n=0}^{N-1} C_i \exp\left(j2\pi \hat{f}_n t\right)\exp\left(j2\pi f_{RF} t\right)\right\} = \\ = \mathrm{Re}\left\{\exp\left(j2\pi f_{RF} t\right)\sum_{n=0}^{N-1} C_i \exp\left(j2\pi \hat{f}_n t\right)\right\} \tag{1.14}$$

where $f_n = f_{RF} + \hat{f}_n$. The frequency $\hat{f}_n$ is the frequency of the *n*-th *sub-carrier* of the shifted OFDM *baseband* signal. So, $\hat{f}_n = n\Delta f$, where $n = 0,1,2,...,N-1$. The highest frequency of the OFDM *baseband* signal is hence $\hat{f}_{\max} = N\Delta f$.

The second consideration of the digital approach consists on generating the OFDM *baseband* signal in the digital domain and then transform it into the analogue domain. The complex signal $s(t)$ defined as

$$s(t) = \sum_{n=0}^{N-1} C_n \exp\left(j2\pi \hat{f}_n t\right) = \sum_{n=0}^{N-1} C_n \exp\left(j2n\Delta f \pi t\right) \tag{1.15}$$

is the complex representation of the OFDM *baseband* signal. The OFDM *passband* signal is then

$$x_{OFDM}(t) = \mathrm{Re}\left\{s(t)\exp\left(j2\pi f_{RF} t\right)\right\} \tag{1.16}$$

The digitized signal $s(t)$ is

$$s_m = s(t = mt_s) = \sum_{n=0}^{N-1} C_n \exp\left(j2\pi n\Delta f\left(mt_s\right)\right) \tag{1.17}$$

where t_s is the sampling period. The Nyquist sampling theorem stablishes that the minimum sampling rate to digitize a real-valued *baseband* signal to avoid ISI is twice the highest frequency of the signal ($f_{\max}$). Unlike real baseband signals, complex *baseband* signals do not have even/odd amplitude/phase symmetry, and the minimum sampling frequency to avoid aliasing becomes equal to the highest frequency of the complex signal. The maximum sampling period to digitize a complex *baseband* signal is then $t_s = 1/f_{\max}$. Note that a complex sample is actually composed of two real samples: one for the real part and one for the imaginary one. Then, two real samples are actually taken every sampling period, thus having the same Nyquist sampling rate than a

real signal with the same $f_{\max}$. If t_s is replaced by $1/\hat{f}_{\max} = 1/(N\Delta f)$ in equation (1.17) and a normalization factor $1/N$ is included, we end up with the following expression:

$$s_m = s(t = mt_s) = \frac{1}{N}\sum_{n=0}^{N-1} C_n \exp\left(j2\pi n\Delta f \frac{m}{\hat{f}_{\max}}\right) = \frac{1}{N}\sum_{n=0}^{N-1} C_n \exp\left(j\frac{2\pi}{N}nm\right) = \text{iDFT}\{C_n\} \tag{1.18}$$

Here, iDFT$\{\cdot\}$ stands for the N-points inverse Discrete Fourier Transform operator. Equation (1.18) indicates that the digitized complex *envelope* of the OFDM *baseband* signal s_m could be obtained by inverse discrete Fourier transforming the symbols C_n, where $n = 1,2,3,...,N$. The signal s_m is a stream of complex samples $s_m = I_m - jQ_m$. If the two stream of real samples I_m and Q_m are digital-to-analogue converted (DAC) then we have the real *baseband* analogue signals $I(t)$ and $Q(t)$. After DAC conversion the signal s_m becomes the complex *baseband* analogue signal $s(t) = I(t) - jQ(t)$. By replacing $s(t)$ in equation (1.16) we obtain

$$x_{OFDM}(t) = \text{Re}\{(I(t) - jQ(t))\exp(j2\pi f_{RF}t)\} = I(t)\cos(2\pi f_{RF}t) + Q(t)\sin(2\pi f_{RF}t) \tag{1.19}$$

Equation (1.19) indicates a practical approach to digitally implement the OFDM transmitter by replacing a large number of mixers, oscillators and filters with an N-points iDFT, a pair of DACs and low pass filters (LFPs), as shown in Figure 1.5. This OFDM transmitter implementation is called here as RF-IQ-OFDM transmitter.

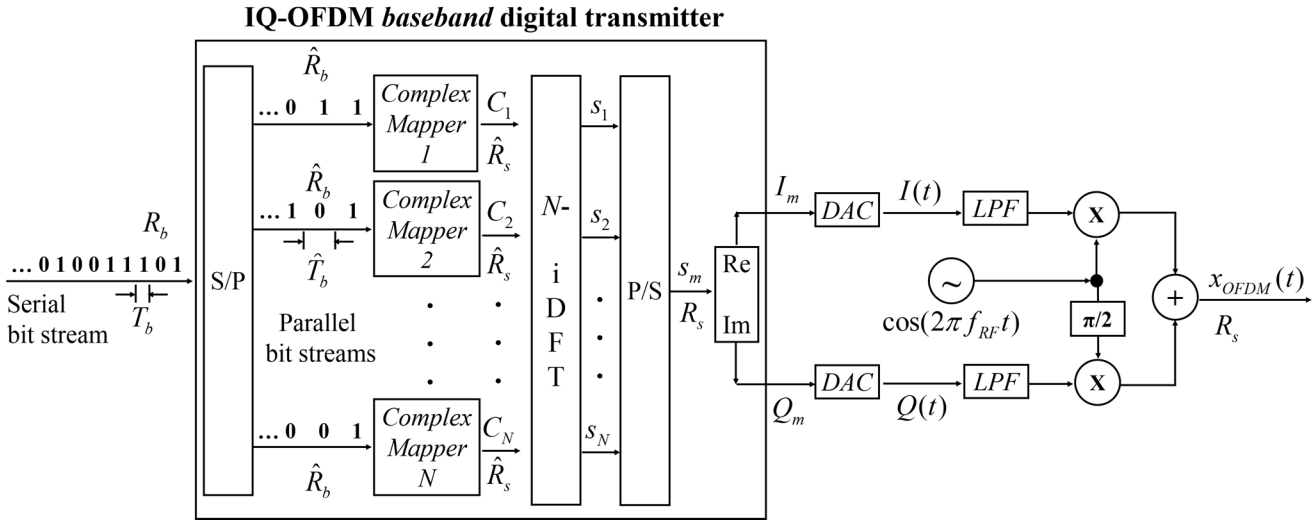

Figure 1.5 Block diagram of the RF-IQ-OFDM transmitter.

The same previous approach could be used at the receiver side. The *i*-th received symbol of the *n*-th *sub-channel* is computed by using equation (1.11). If this expression is evaluated only for the first symbol (for simplicity) and f_n is replaced by $f_n = f_{RF} + \hat{f}_n$, we have

$$\tilde{C}_n = \frac{1}{\hat{T}_s}\int_0^{\hat{T}_s} y_{OFDM}(t)\exp\left(-j2\pi f_{RF}t\right)\exp\left(-j2\pi \hat{f}_n t\right)dt = \frac{1}{\hat{T}_s}\int_0^{\hat{T}_s} \tilde{s}(t)\exp\left(-j2\pi \hat{f}_n t\right)dt \tag{1.20}$$

The signal $\tilde{s}(t)$ results after frequency-shifting the signal $y_{OFDM}(t)$ from f_{RF} to $f = 0$. This means that $\tilde{s}(t)$ is the *baseband* signal obtained after *RF-down-converting* and low-pass filtering (to remove undesired high frequencies) the signal $y_{OFDM}(t)$. After analogue-to-digital conversion (ADC) of signal $\tilde{s}(t)$ with a sampling period $t_s = 1/f_{\max} = 1/N\Delta f$, the complex digital signal $\tilde{s}_m$ is obtained. Since $\hat{T}_s = 1/\hat{R}_S = 1/\Delta f$, the signal $\tilde{s}_m = \tilde{I}_m - j\tilde{Q}_m$ has *N* complex samples in $0 \le t \le \hat{T}_s$. By replacing $\tilde{s}(t)$ by its digital version, $\tilde{s}_m$, in equation (1.20), the following expression is obtained:

$$\tilde{C}_n = \sum_{m=0}^{N-1}\tilde{s}_m \exp\left(-j2\pi \hat{f}_n m t_s\right) = \sum_{m=0}^{N-1}\tilde{s}_m \exp\left(-j2\pi n\Delta f m t_s\right) = \sum_{m=0}^{N-1}\tilde{s}_m \exp\left(-j\frac{2\pi}{N}mn\right) = \mathrm{DFT}\{\tilde{s}_m\} \tag{1.21}$$

Equations (1.20) and (1.21) indicate that the received symbols $\tilde{C}_n$ could be obtained by discrete Fourier transforming the digitized version of the *RF-down-converted* and low-pass filtered $y_{OFDM}(t)$ signal. The block diagram of this digital OFDM receiver implementation, called here RF-IQ-OFDM receiver, is shown in Figure 1.6.

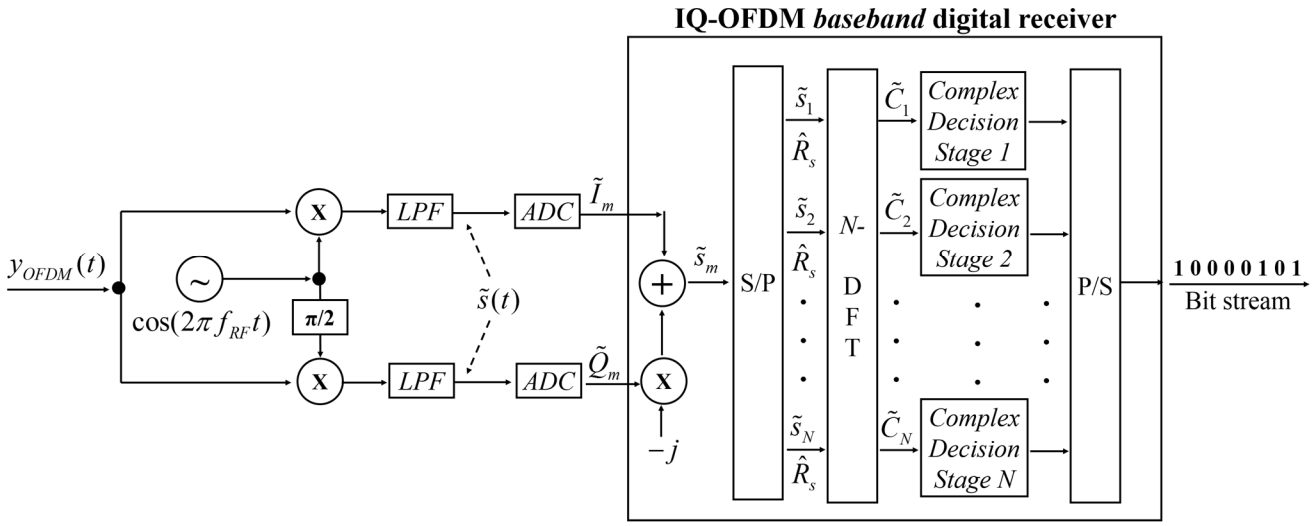

Figure 1.6 Block diagram of the RF-IQ-OFDM receiver.

1.3.2 Real-valued OFDM digital implementation

There is another digital OFDM implementation approach based on the previous one but in which the output of the iDFT is forced to be real-valued. To achieve this, the input set of symbols to the iDFT is constrained to have Hermitian symmetry [35] so that the imaginary part of the iDFT output becomes zero. The Hermitian symmetry is achieved by introducing to the iDFT the N set of symbols C_n plus a *mirror* complex conjugated replica of it. The size of the iDFT now becomes $2N$. The input ports of the iDFT $I_1,...,I_{2N}$ are *mapped* with the corresponding complex symbols $C_1,...,C_N,C_N^*,...,C_1^*$. The digital real-valued *baseband* signal that comes out from the iDFT is serialized, digital-to-analogue converted (just a single DAC is now needed) and low-pass filtered to produce the OFDM *baseband* signal. Since the signal is real-valued, the DAC should digitize it at twice its $f_{\max}$. The sampling rate then becomes $2f_{\max} = 2N\Delta f = 2R_s$. The need of a twice higher-speed DAC (and ADC at the receiver side) to transmit the same data rate is a disadvantage of this OFDM implementation approach. Note that this signal can be transmitted in *baseband* or it can be *RF-up-converted* by means of a mixer and an oscillator.

At the receiver side, after *RF-down-conversion*, if needed, the signal is low-pass filtered and analogue-to-digital converted by taking $2N$ samples every symbol period T_s. The digitized signal is 1:$2N$ parallelized and DFT converted. Only the symbols corresponding to output ports 1 to N of the $2N$-points DFT are decoded by the decision stage. Finally, the output parallel binary signal is serialized. A diagram of this transmitter and receiver implementation, named Real-valued OFDM digital implementation, is shown in Figure 1.7.

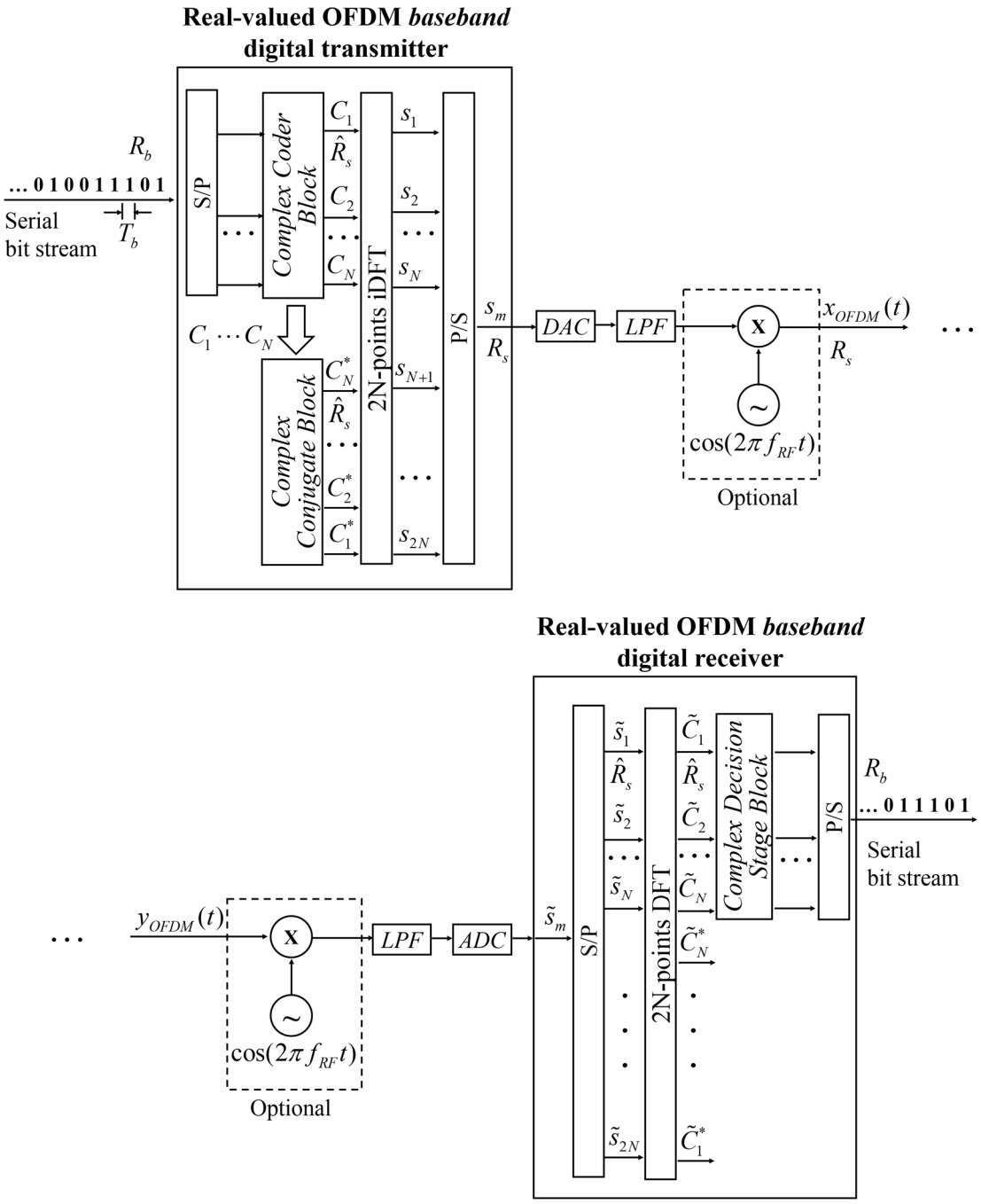

Figure 1.7 Block diagrams of the Real-valued OFDM transmitter and receiver.

The electrical signals generated in the digital and electrical domains by the Real-valued OFDM, the RF-IQ-OFDM and the IQ modulator schemes, presented in sections 1.3.2, 1.3.1 and in section 1.1, are used as the modulating signals of the optical transceivers analyzed in the present thesis work in Chapter 3, 4 and 5, respectively. The optical systems that transform these electrical signals from the electrical to the optical domain and vice versa for propagation through an optical fiber channel are described in the next Chapter.

2. Chapter two: Optical transceivers

2.1 Optical transmitters and their modeling

The function of an optical transmitter is to transfer an electrical signal that carries information into an optical signal to be transmitted through a fiber channel. There are two main schemes to perform the electro-optical (E-O) conversion: direct modulated laser (DML) and external modulated laser (EML).

In the DML approach, the electrical signal varies the driving current that pumps the laser diode, accordingly modulating its output optical power. DML is therefore the simplest alternative to implement an optical transmitter. However, under this scheme a high frequency chirp is generated, which limits the transmission bandwidth of a single-mode fiber system [36]. This scheme was not considered feasible for the reach and capacity targets of the systems analyzed in the present work.

The use of an EML scheme is an alternative to reduce, or even eliminate, frequency chirping by introducing an external modulator that proportionally modulates a continuous wave (CW) optical signal according to the variations of a driving electrical signal. The CW signal is also referred to as the optical carrier. The most used external modulators are the electro-absorption modulator (EAM) and the Mach-Zehnder modulator (MZM), described in the next two sections. Some EMLs have the modulator and the CW laser source integrated in a single chip.

The field of the optical carrier $E_c(t)$ is modeled here as [37]

$$E_c(t) = \begin{bmatrix} \sqrt{1-k} \\ \sqrt{k}\exp(j\delta) \end{bmatrix} \sqrt{P_c + P_{WGN}(t)}\exp\left(j\left(\omega_c t + \varphi_c + \varphi_c^n(t)\right)\right) = \begin{bmatrix} E_c^X(t) \\ E_c^Y(t) \end{bmatrix} \tag{2.1}$$

where $P_c = |E_c(t)|^2$ is the average output power of the transmitter laser, $\omega_c / 2\pi = f_c$ is the center frequency of the optical carrier, φ_c is the initial phase of the optical carrier, $\varphi_c^n(t)$ is the phase noise of the laser, $P_{WGN}(t)$ is the amplitude noise of the laser, k is the power ratio between the X and Y polarization components, $E_c^X(t)$ and $E_c^Y(t)$ respectively, and δ is the phase difference between them. The vector as a function of k and δ in Equation (2.1) is introduced to consider the state of polarization in order to obtain the X and Y polarization components of the laser output optical field. For simplicity, in the rest of this Chapter a single X-polarization transmission ($k = 0$, $\delta = 0$) and an initial phase $\varphi_c = 0$ of the optical carrier are considered. Equation (2.1) then becomes

$$E_c(t) = \sqrt{P_c + P_{WGN}(t)} \exp\left(j(\omega_c t + \varphi_c^n(t)) \right) \tag{2.2}$$

The phase noise $\varphi_c^n(t)$ can be modelled as

$$\varphi_c^n(t) = \int_0^t \omega(\tau) d\tau \tag{2.3}$$

where $\omega(t)$ is Gaussian white noise with a variance of $2\pi\Delta f_c$, where Δf_c is the full width at half maximum (FWHM) laser linewidth. Since the laser phase noise is caused by spontaneous emission photons with random phase and therefore the phase of the carrier changes randomly depending on a high number of independent noise events, it is a good assumption to use a Gaussian distribution to model it [38].

The amplified-spontaneous emission (ASE) noise of the CW laser is emulated by adding to $E_c(t)$ a Gaussian-distributed optical white noise with power $P_{WGN}(t)$. In a simple approach, the relative intensity noise (RIN) of the CW laser, defined as the variance of the intensity fluctuations to the squared mean power ratio, could also be modeled as optical white Gaussian noise (WGN) [39], as in this work.

The OSNR at the output of the laser after optical WGN addition expressed in dB is evaluated as [40]

$$OSNR = 10 \log\left(\frac{P_c}{B_{WGN} \cdot W_{WGN}} \right) \tag{2.4}$$

where B_{WGN} is the bandwidth for noise measurement and W_{WGN} is the power spectral density of the added optical noise in both polarizations. Unless otherwise stated, the amplitude and phase noise terms of the optical carrier are neglected in the rest of this Chapter to favor a conceptual analysis. Note however, they are indeed considered in the model of the lasers employed in the numerical analysis presented in Chapters 4 and 5.

A real-valued electrical signal, as the signals $x_I(t)$, $x_Q(t)$, $x_{IQ}(t)$ or $x_{OFDM}(t)$ described in the previous Chapter, can modulate the intensity or the field of the optical carrier, depending on the configuration of the modulator and which kind of receiver scheme is used. A complex-valued signal composed of two real signals, as the output of an IQ coder ($x(t) = x_I(t) - jx_Q(t)$) or an IQ OFDM *baseband* transmitter ($s(t) = I(t) - jQ(t)$) described in the previous Chapter, modulates the field of an optical carrier by means of an optical IQ modulator, composed by a pair of MZMs. The models of the most used optical modulators, as well as their configurations to work as an intensity, field or IQ modulators, are described below.

2.1.1 The Mach-Zehnder modulator (MZM)

A MZM is an optical device composed of a pair of phase modulators positioned within an interferometric structure. It could be used as a phase, intensity or field modulator. A pair of MZMs together with a phase modulator immersed in an interferometer conform an optical IQ modulator.

An optical phase modulator (PM) is a device that modulates the phase of an incident optical carrier proportionally to an applied external voltage by means of the Pockels effect [41]. It is fabricated by embedding an optical waveguide in an electro-optical substrate. The external voltage is applied via an electrode to modulate the refractive index of the waveguide, and thus the phase of the incoming optical carrier, as shown in Figure 2.1.a.

The modulated phase $\varphi_M(t)$ is a function of the wavelength of the optical carrier λ_c, the length of the electrode L_e and the variation of the effective refractive index $\Delta n_{eff}(t)$ as a function of the applied voltage $V(t)$ [39]. Considering only the Pockels effect, the relation between $\Delta n_{eff}(t)$ and $V(t)$ is linear, therefore, $\varphi_M(t)$ is proportional to $V(t)$. The proportionality factor between $\varphi_M(t)$ and $V(t)$ is related with the composed parameter V_π, defined as the voltage needed to achieve a π change in the phase of the incident optical carrier. The relation between $\varphi_M(t)$ and $V(t)$ is given as

$$\varphi_M(t) = \frac{2\pi L_e \Delta n_{eff}(t)}{\lambda_c} = \frac{\pi}{V_\pi} V(t) \tag{2.5}$$

The relation between the PM input $E_c(t)$ and output $E_{PM}(t)$ optical fields is then expressed as

$$E_{PM}(t) = E_c(t)\exp\left(j\varphi_M(t)\right) = E_c(t)\exp\left(j\frac{\pi}{V_\pi}V(t)\right) \tag{2.6}$$

A dual-drive MZM is constructed by placing two independently-driven optical PMs on each arm of an interferometric structure as shown in Figure 2.1.b. The incoming optical carrier is split into the two arms of the interferometer with a power splitting ratio ψ. Each replica of the optical carrier is phase modulated by different driving signals, $V_1(t)$ and $V_2(t)$, and then the modulated replicas are recombined, producing optical wave interference. The phase difference $\Delta\varphi(t)$ between the optical fields of each replica varies the interference from constructive to destructive. This enables the possibility of modulating the amplitude of the optical carrier by

means of the electrical signals $V_1(t)$ and $V_2(t)$ of each phase modulator. The relation between the dual-drive MZM input $E_c(t)$ and output $E_{MZM}(t)$ optical fields is modeled here as [42]

$$\begin{aligned} E_{MZM}(t) &= \frac{1}{\sqrt{2}\alpha_{MZM}} E_c(t)\left(\sqrt{\psi}\exp\left(j\varphi_1(t)\right)+\sqrt{1-\psi}\exp\left(j\varphi_2(t)\right)\right)= \\ &= \frac{1}{\sqrt{2}\alpha_{MZM}} E_c(t)\left(\sqrt{\psi}\exp\left(j\frac{\pi}{V_{\pi,1}}V_1(t)\right)+\sqrt{1-\psi}\exp\left(j\frac{\pi}{V_{\pi,2}}V_2(t)\right)\right) \end{aligned} \tag{2.7}$$

where $\varphi_1(t)$ and $\varphi_2(t)$ ($V_{\pi,1}$ and $V_{\pi,2}$) are the phase shifts (the V_π of the phase modulators placed) in the upper and lower arms of the dual-drive MZM, respectively, and α_{MZM} is the insertion loss of the modulator. For simplicity, let us assume a lossless device with a 50:50 power splitting ratio (ψ =0.5) and the same V_π value for both PMs. If $V_1(t)=V_2(t)=\frac{V(t)}{2}$ is set, configuration known as *push-push*, Equation (2.7) becomes

$$E_{MZM}(t)=\frac{1}{2}E_c(t)\left(\exp\left(j\frac{\pi}{V_\pi}V_1(t)\right)+\exp\left(j\frac{\pi}{V_\pi}V_1(t)\right)\right)=E_c(t)\exp\left(j\frac{\pi}{2V_\pi}V(t)\right) \tag{2.8}$$

From Equation (2.8) it could be noticed that the MZM acts as a pure phase modulator. If now we set $V_1(t)=-V_2(t)=\frac{V(t)}{2}$, configuration known as *push-pull*, Equation (2.7) becomes

$$E_{MZM}(t)=\frac{1}{2}E_c(t)\left(\exp\left(j\frac{\pi}{2V_\pi}V(t)\right)+\exp\left(-j\frac{\pi}{2V_\pi}V(t)\right)\right)=E_c(t)\cos\left(\frac{\pi}{2V_\pi}V(t)\right) \tag{2.9}$$

The dual-drive MZM *push-pull* configuration is used in the rest of the present document, and from now on will be referred to simply as MZM. The MZM E-O field transfer function (FTF), $T_{MZM}(t)$, graph in blue in Figure 2.1.c, is defined as

$$T_{MZM}(t)=\frac{E_{out}(t)}{E_{in}(t)}=\frac{E_{MZM}(t)}{E_c(t)}=\cos\left(\frac{\pi}{2V_\pi}V(t)\right) \tag{2.10}$$

The MZM E-O power transfer function (PTF), $\left|T_{MZM}(t)\right|^2$, graph in red in Figure 2.1.c, is calculated as

$$\left|T_{MZM}(t)\right|^2 = \cos^2\left(\frac{\pi}{2V_\pi}V(t)\right) = \frac{1}{2} + \frac{1}{2}\cos\left(\frac{\pi}{V_\pi}V(t)\right) \tag{2.11}$$

Equations (2.10) and (2.11) indicate a cosine relationship between the driving voltage and the field and power transfer functions, respectively. From Figure 2.1.c it could be noticed that for both, FTF and PTF vs $V(t)$ curves, there are voltage intervals in which the E-O conversion could be considered linear.

In order to use the MZM as a field modulator (FM), the driving voltage $V(t)$ should be centered in the maximally linear point of the FTF, *i. e.* $-V_\pi$ or V_π, voltage values known as *null* points (marked in Figure 2.1.c) since the PTF reaches its minimum value there. A maximum dynamic range equal to $2V_\pi$ could be achieved at the expense of operating the modulator outside its linear range. This in turn leads to unfavorable consequences (non-linear distortion) as will be discussed in section 2.4.5. A linear field modulation is achieved if the driving voltage is maintained within the FTF linear range, around the *null* point, so that

$$T_{MZM,FM}(t) \approx kV(t) \tag{2.12}$$

The MZM could also be set as an intensity modulator (IM) by centering the driving voltage $V(t)$ in the maximally linear point of its PTF, *i. e.* $-V_\pi/2$ or $V_\pi/2$, values known as *quadrature* points (pointed out in Figure 2.1.d). A maximum dynamic range of V_π could be achieved, incurring in non-linear E-O power conversion. A linear intensity modulation is achieved by keeping $V(t)$ within the PTF linear range. The PTF then becomes $\left|T_{MZM,IM}(t)\right|^2 \approx kV(t)$ around the *quadrature* point. As a consequence, around the *quadrature* point, the intensity of the optical signal at the output of the modulator is linearly proportional to $V(t)$ and can be expressed as

$$\left|E_{MZM,IM}(t)\right|^2 = \left|E_c(t)\cdot T_{MZM,IM}(t)\right|^2 = P_c\cdot\left|T_{MZM,IM}(t)\right|^2 \approx P_c kV(t) \tag{2.13}$$

The modulating signals $V_m(t)$ used in the present work ($x_{OFDM}(t)$, $x_I(t)$ and $x_Q(t)$) are zero-mean valued, therefore a DC bias (V_b) should be added to the signal in order to center the driving signal $V(t) = V_m(t) + V_b$ in the desired operational point.

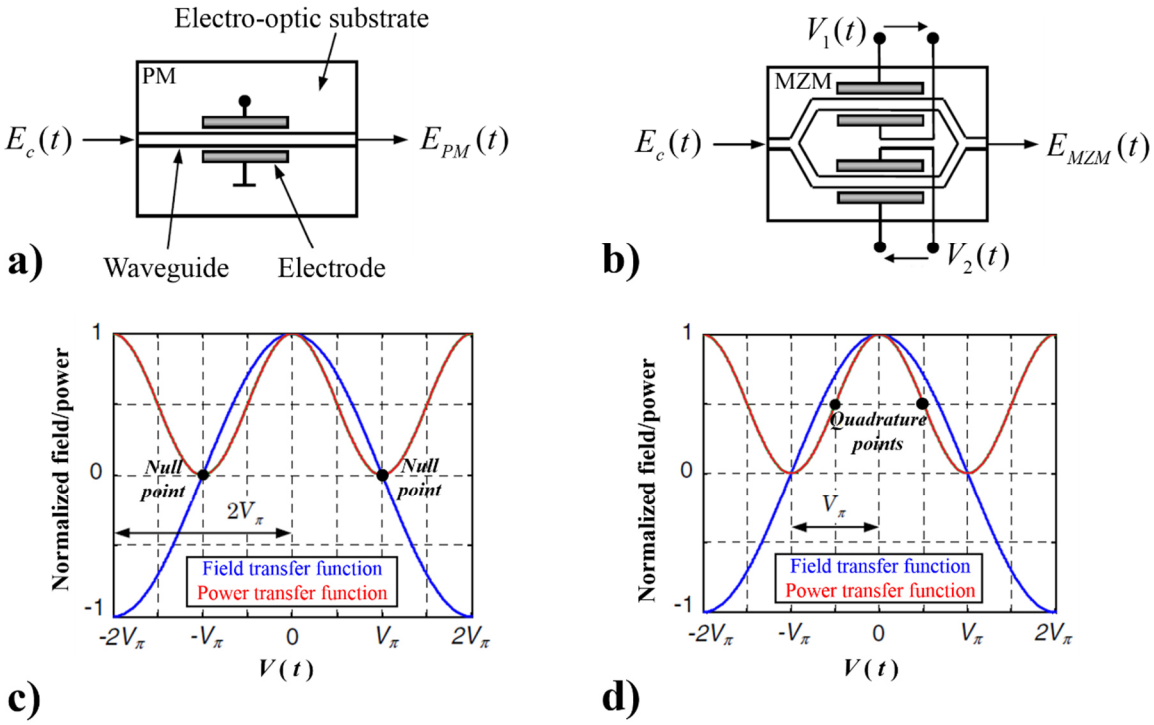

Figure 2.1 Adapted from [39]: a) Diagram of a Phase Modulator; b) Diagram of a dual-drive MZM; Graphs of a MZM E-O field and power transfer functions biased at c) null point and d) quadrature point.

The driving signal of a MZM is real-valued. There are also complex-valued driving signals composed of two real components, such as the output of an IQ coder (see section 1.1) or an IQ-OFDM *baseband* digital transmitter (see section 1.3.1), represented in general as $x(t) = x_I(t) - jx_Q(t)$. In this case, a MZM is needed to modulate the amplitude of the real component $x_{\mathrm{Re}}(t)$, and another MZM is needed to modulate a π/2 phase shifted imaginary component $x_{\mathrm{Im}}(t)$. The interferometric structure formed by the pair of MZMs and the π/2 phase shifter (a PM driven with a fixed voltage of $-V_\pi/2$) is called dual-nested MZM (DN-MZM). A CW laser that acts as an optical oscillator and a DN-MZM conform an optical IQ (oIQ) modulator, depicted in Figure 2.2.

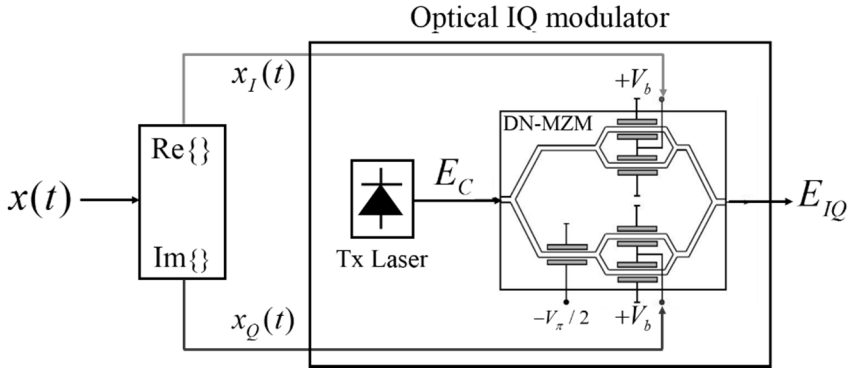

Figure 2.2 Structure of an Optical IQ modulator.

If the DN-MZM is assumed to be a lossless and perfectly balanced device conformed by identical MZMs, the optical field that outputs the oIQ modulator, $E_{IQ}(t)$, is then calculated as [39]

$$E_{IQ}(t)=\left(\frac{1}{2}T_{MZM}(t)+\exp\left(j\frac{\pi}{V_\pi}\left(\frac{-V_\pi}{2}\right)\right)T_{MZM}(t)\right)E_c(t)=\left(\frac{1}{2}\cos\left(\frac{x_I(t)}{2V_\pi}\pi\right)-j\frac{1}{2}\cos\left(\frac{x_Q(t)}{2V_\pi}\pi\right)\right)E_c(t) \quad (2.14)$$

The complex transfer function of the oIQ modulator is defined as

$$T_{IQ}(t)=\frac{E_{IQ}(t)}{E_c(t)}=\frac{1}{2}\cos\left(\frac{x_I(t)}{2V_\pi}\pi\right)-j\frac{1}{2}\cos\left(\frac{x_Q(t)}{2V_\pi}\pi\right)=T_I(t)-jT_Q(t) \quad (2.15)$$

Provided that the MZMs are used as field modulators, the real and imaginary parts of $T_{IQ}(t)$ linearly vary with the driving signals $x_I(t)$ and $x_Q(t)$, respectively, *i.e.* $T_I(t)\approx kx_I(t)$ and $T_Q(t)\approx kx_Q(t)$ around the *null* point.

If $T_{IQ}(t)$ is expressed according to Euler representation as $T_{IQ}(t)=A_{IQ}(t)\exp\left(-j\phi_{IQ}(t)\right)$, then the output of the IQ modulator can be cast as

$$E_{IQ}(t)=E_c(t)\cdot T_{IQ}(t)=E_c(t)\cdot A_{IQ}(t)\exp\left(-j\phi_{IQ}(t)\right) \quad (2.16)$$

where

$$A_{IQ}(t)=\sqrt{T_I^2(t)+T_Q^2(t)} \quad (2.17)$$

and

$$\phi_{IQ}(t) = \arg\left(T_Q(t), T_I(t)\right) \tag{2.18}$$

The operation $\arg(\cdot)$ denotes the angle of a complex value in the range between – π to π. Equation (2.16) indicates an amplitude and phase modulation of the optical carrier at the output of the oIQ modulator proportional to the amplitude and phase of the driving signal $x(t)$, respectively. Therefore, the complex symbols mapped onto the electrical signal $x(t)$ could be also mapped onto the optical field that comes out from the oIQ modulator. The receiver scheme that allows to recover the electrical complex information from the IQ modulated optical field is described in section 2.2.

The electro-optic frequency response of the MZM is modeled here as an electrical low-pass fifth-order Bessel filter with a given 3 dB bandwidth B_{MZM}. The filter is applied to the driving signal at the input of the modulator.

2.1.2 The electro-absorption modulator (EAM)

An EAM is a semiconductor device with the same structure of a laser diode that directly modulates the amplitude of an optical carrier. It is formed by a single waveguide with electrodes to apply the modulating electrical field across the waveguide; this is schematically represented in Figure 2.3. Due to the electro-absorption effect, the energy difference between the conduction and valence bands in a semiconductor are changed proportionally to an applied external electric field. Therefore, the absorption of the semiconductor, and thus the amplitude of an incident optical field, is modulated proportionally to the amplitude of the electrical driving signal $V(t)$. This effect occurs in bulk semiconductors, including both silicon and III-V materials, but it is stronger in quantum wells built in III-V semiconductors [43]. Apart from an absorption change, the applied electrical field changes the refractive index through the Kramers–Kroenig relations [44], which results in optical phase modulation along with the optical intensity modulation: frequency chirp.

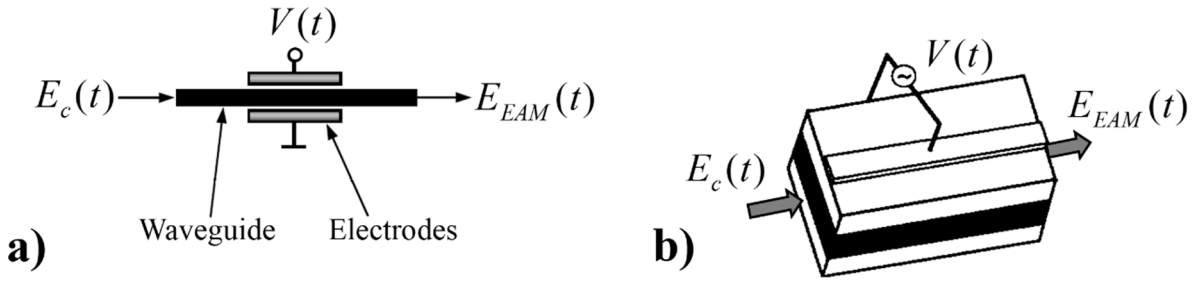

Figure 2.3 a) Schematic representation of an EAM, b) 3D representation of an EAM.

The optical field at the output of the EAM, $E_{EAM}(t)$, is modeled here according to [45] as follows

$$E_{EAM}(t) = T_{EAM}(t) \cdot E_c(t) \tag{2.19}$$

where $T_{EAM}(t)$ is the complex field transfer function of the EAM, and can be expressed as

$$T_{EAM}(t) = \left|T_{EAM}(t)\right| \exp\left(\phi_{EAM}(t)\right) \tag{2.20}$$

$\left|T_{EAM}(t)\right|$ and $\phi_{EAM}(t)$ are the transfer magnitude and transfer phase functions of the EAM, respectively. Amplitude modulation in an EAM is accompanied by phase modulation, which results in generally undesired frequency chirp. The change of phase as a function of time is modeled in this thesis according to [46] as follows

$$\frac{d\phi_{EAM}(t)}{dt} = \frac{\alpha_{EAM}}{2}\left(\frac{1}{\left|T(t)\right|^2}\right)\left(\frac{d\left|T(t)\right|^2}{dt}\right) \tag{2.21}$$

where $\alpha_{EAM} = \Delta n_R / \Delta n_I$ is the relative change of the real part Δn_R and imaginary part Δn_I of the refractive index. The parameter α_{EAM} is referred to in the literature as the α-factor, chirp factor or linewidth enhancement factor, and it is in general voltage-dependent $\alpha_{EAM} = \alpha_{EAM}(V)$ [47].

The transfer function $T_{EAM}(t)$ could be expressed in terms of the time-varying driving voltage $V(t)$ as follows

$$T_{EAM}(V(t)) = \left|T_{EAM}(V(t))\right| \exp\left(\phi_{EAM}(V(t))\right) \tag{2.22}$$

The voltage-dependent version of Equation (2.21) is then evaluated as

$$\frac{d\phi_{EAM}(V(t))}{dV} \cdot \frac{dV(t)}{dt} = \frac{\alpha_{EAM}(V(t))}{2}\left(\frac{1}{\left|T_{EAM}(V(t))\right|^2}\right)\left(\frac{d\left|T_{EAM}(V(t))\right|^2}{dV} \cdot \frac{dV(t)}{dt}\right) \tag{2.23}$$

then

$$\frac{d\phi_{EAM}(V(t))}{dV} = \frac{\alpha_{EAM}(V(t))}{2}\left(\frac{1}{\left|T_{EAM}(V(t))\right|^2}\right)\left(\frac{d\left|T_{EAM}(V(t))\right|^2}{dV}\right) \tag{2.24}$$

From Equation (2.24), the voltage-dependent phase transfer function $\phi_{EAM}(V)$ of the EAM can be calculated as

$$\phi_{EAM}(V(t)) = \int_0^{V(t)} \frac{\alpha_{EAM}(V)}{2}\left(\frac{1}{\left|T_{EAM}(V)\right|^2}\right)\left(\frac{d\left|T_{EAM}(V)\right|^2}{dV}\right)dV \tag{2.25}$$

According to [48], the voltage-dependent $\alpha_{EAM}(V)$ and $\left|T_{EAM}(V)\right|^2$ functions, using a small-signal approximation, can be recast via a Taylor series expansion about the bias voltage V_b as

$$\left|T_{EAM}(V)\right|^2 = T_0 + T_1 V + T_2 V^2 + T_3 V^3 + \ldots \tag{2.26}$$

$$\alpha_{EAM}(t) = \alpha_0 + \alpha_1 V + \alpha_2 V^2 + \alpha_3 V^3 + \ldots \tag{2.27}$$

Where T_i and α_i, $i = 0,1,2,3,\ldots$, are the i-th Taylor's series coefficients of the power $\left|T_{EAM}(V)\right|^2$ transfer functions and chirp-factor $\alpha_{EAM}(V)$, respectively. It is usual to express $\left|T_{EAM}(V)\right|^2$ and their corresponding coefficients in decibels as

$$\left|T_{EAM}(V)\right|^2_{dB} = T_{0,dB} + T_{1,dB} V + T_{2,dB} V^2 + T_{3,dB} V^3 + \ldots \tag{2.28}$$

By means of the polynomial approximation of $\alpha_{EAM}(V)$ and $\left|T_{EAM}(V)\right|^2$, the optical field at the output of the EAM can be evaluated using Equations (2.19), (2.22) and (2.25). The numerical implementation to carry out this procedure can be found in [45].

Figure 2.4.a and Figure 2.4.b show graphs of $\left|T_{EAM}(V)\right|^2$ (in red) and $\alpha_{EAM}(V)$ for a typical EAM, respectively. They are approximated as fourth-order polynomial functions with the following coefficients:

$$\{T_{0,dB}, T_{1,dB}, T_{2,dB}, T_{3,dB}\} = \{0, -2.75, -6.30, +1.50\} \qquad \{\alpha_0, \alpha_1, \alpha_2, \alpha_3\} = \{0.20, -0.30, -0.40, +0.10\} \tag{2.29}$$

The corresponding $\left|T_{EAM}(V)\right|$ function is shown (in blue) in Figure 2.4.a.

From Figure 2.4 it could be observed a region in which the power transfer function $|T_{EAM}(V)|^2$ varies linearly with respect to the driving voltage. The EAM could be operated as an intensity modulator by centering the driving voltage $V(t)$ in the maximally linear point of its PTF. As a result, the intensity of the optical signal at the output of the modulator becomes linearly proportional to $V(t)$ around V_b as follows

$$\left|E_{EAM,IM}(t)\right|^2 = \left|E_c(t)\cdot T_{EAM,IM}(t)\right|^2 = P_c\cdot\left|T_{EAM,IM}(t)\right|^2 \approx P_c kV(t) \tag{2.30}$$

To operate the EAM as a linear field modulator, the driving voltage $V(t)$ should be centered in the maximally linear point of its FTF and the driving voltage should be maintained within the FTF linear range, so that

$$\left|T_{EAM,FM}(t)\right| \approx kV(t) \tag{2.31}$$

For very low chirp values $\alpha_{EAM} \rightarrow 0$, the field transfer function of the EAM tends to become real-valued, $T_{EAM,FM}(t) \rightarrow \left|T_{EAM,FM}(t)\right|$. If in addition a linear field modulation is used, then

$$T_{EAM,FM}(t) \approx kV(t) \tag{2.32}$$

as in the case of a MZM used as a field modulator (see Equation (2.12)).

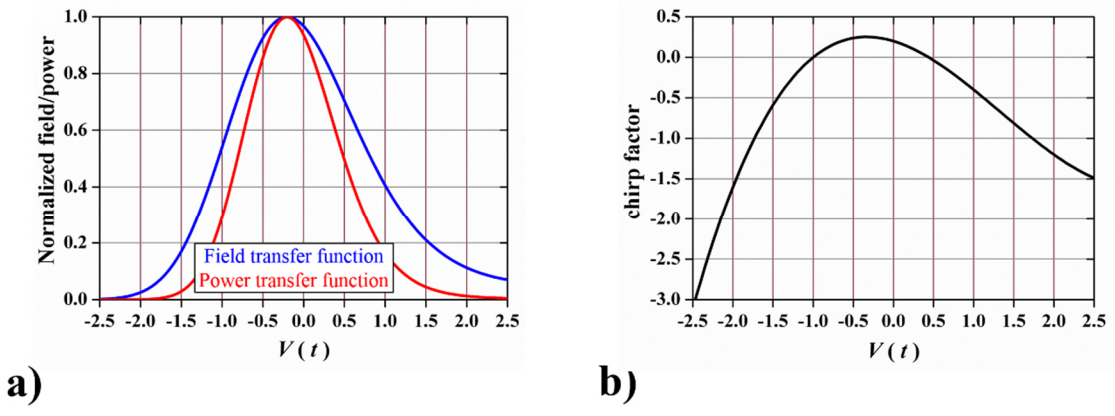

Figure 2.4 a) Normalized field $\left(\left|T_{EAM}(V)\right|\right)$, power $\left(\left|T_{EAM}(V)\right|^2\right)$, and b) chirp $(\alpha_{EAM}(V))$ voltage-dependent transfer functions for a typical EAM.

The electro-optic frequency response of the EAM is modeled here as an electrical low-pass Bessel filter of fifth-order with a given 3 dB bandwidth B_{EAM} . The filter is applied to the driving signal at the input of the modulator.

2.2 Optical receivers and their modeling

A photo-diode is the key component to perform the opto-electrical (O-E) conversion. A single photo-diode (PD) is sensible only to the intensity of light. The output current $i(t)$ of an ideal photo-diode is then proportional to the squared modulus of the incident optical field $E(t)$ in both polarizations [49], as follows

$$i(t) = R\left|E(t)\right|^2 = R \cdot E(t) \cdot E^*(t) \tag{2.33}$$

where *R*, expressed in A/W, is a proportionality factor called the *responsivity* of the PD.

Let us assume for the rest of this section a back-to-back transmission in which the optical field that outputs an optical modulator immediately inputs a single photo-diode with *R* = 1 A/W.

If intensity modulation is used, then the output current of the PD is proportional to the transmitter driving signal as follows

$$i(t) = \left|E_{IM}(t)\right|^2 = P_c\left|T_{IM}(t)\right|^2 \approx P_c k V(t) \tag{2.34}$$

This very simple receiver scheme, called direct-detection (DD), is useful enough to recover modulating signals mapped into the intensity of the optical carrier. However, if field modulation is used instead, it is not possible to recover the driving signal using the DD scheme, as can be observed from Equation (2.34).

If we now assume the transmission of a field modulated signal $E_{FM}(t)$ plus the optical carrier $E_c(t)$ (or even part of it), the output current of the PD is

$$i(t) = \left|E(t)\right|^2 = \left|E_{FM}(t) + E_c(t)\right|^2 = \left|E_{FM}(t)\right|^2 + \left|E_c(t)\right|^2 + 2\,\mathrm{Re}\{E_c^*(t)E_{FM}(t)\} \tag{2.35}$$

where

$$\mathrm{Re}\{E_c^*(t)E_{FM}(t)\} = \mathrm{Re}\left\{E_c^*(t)\cdot\left(E_c(t)\cdot T_{FM}(t)\right)\right\} = \left|E_c(t)\right|^2 \cdot \mathrm{Re}\left\{T_{FM}(t)\right\} \tag{2.36}$$

Considering the use of a MZM or a chirp-less EAM, we have

$$\mathrm{Re}\{T_{FM}(t)\} = T_{FM}(t) \approx kV(t) \tag{2.37}$$

then,

$$i(t) \approx \left|E_{FM}(t)\right|^2 + \left|E_c(t)\right|^2 + 2P_c kV(t) \tag{2.38}$$

According to Equation (2.38) it is possible, in principle, to recover the driving signal if we are able to isolate it from the other components of the PD output. This reception scheme is called self-coherent, and it is useful to recover a driving signal if field modulation is used and the optical carrier generated at the transmitter side is also sent through the transmission system. One of the main challenges of this scheme is the isolation of the desired terms from the rest of them. The spectrum of $i(t)$ is composed of a DC tone related to $\left|E_c(t)\right|^2$ (easy to filter out), the desired terms related to $V(t)$, and the undesired beating terms $\left|E_{FM}(t)\right|^2 = P_c \cdot T_{FM}^2(t)$ (difficult to filter out). As an example, if a MZM is used as field modulator the beating terms are calculated as in Equation (2.39). If the driving signal $V(t)$ is the sum of multiple sub-carriers, as in OFDM, then the power operation $V^2(t)$ results in sub-carrier beating, which is a deleterious phenomenon that should be removed or avoided as much as possible (see section 2.4.5).

$$\left|E_{FM}(t)\right|^2 = P_c \cdot \left|T_{FM}(t)\right|^2 \approx P_c \cdot k^2 V^2(t) \tag{2.39}$$

If the chirp of the EAM is now taken into account, then Equation (2.37) becomes

$$\mathrm{Re}\{T_{FM}(t)\} = \mathrm{Re}\left\{\left|T_{EAM,FM}(t)\right| \exp\left(\phi_{EAM,FM}(t)\right)\right\} = \left|T_{EAM,FM}(t)\right| \cos\left(\phi_{EAM,FM}(t)\right) \approx kV(t) \cos\left(\phi_{EAM,FM}(t)\right) \tag{2.40}$$

Therefore, the driving signal could be extracted as described before, but affected by a cosine function in terms of the modulated phase. For low chirp values this effect is diminished, and completely vanishes if no chirp is present, as stated in Equation (2.37).

The detection of an optical IQ modulated signal with a complex driving signal $x(t) = x_I(t) - jx_Q(t)$ is now analyzed. The output current of a single PD for this case is

$$i(t) = \left|E_{IQ}(t)\right|^2 = \left|E_c(t) \cdot A_{IQ}(t) \exp\left(-j\phi_{IQ}(t)\right)\right|^2 = P_c A_{IQ}^2(t) \tag{2.41}$$

From Equation (2.41) it could be observed that a loss of the signal $\phi_{IQ}(t)$ occurs after direct detection. However, $\phi_{IQ}(t)$ is needed to recover $x_I(t)$ and $x_Q(t)$. Since the modulating signal $x(t)$ is complex valued, it is not possible to fully recover it after self-coherent detection either. The imaginary part of $E_{IQ}(t)$ would still be missing.

Therefore, an alternative approach called coherent detection has to be used to recover the signal $x(t)$. Under this approach, an optical carrier is no longer required to be sent from the transmitter side. Instead, an optical carrier $E_{LO}(t)$ is generated by a local oscillator (LO) at the receiver side and added to the incoming optical signal just before photo-detection. The output current of the PD is thus

$$i_1(t) = \left|E_{IQ}(t) + E_{LO}(t)\right|^2 = \left|E_{IQ}(t)\right|^2 + \left|E_{LO}(t)\right|^2 + 2\,\mathrm{Re}\{E_{LO}^*(t)E_{IQ}(t)\} \tag{2.42}$$

where

$$E_{LO}(t) = \sqrt{P_{LO} + P_{LO,WGN}(t)}\exp\left(j\left(\omega_{LO}t + \varphi_{LO}^n(t)\right)\right) \tag{2.43}$$

and $\omega_{LO}/2\pi = f_{LO}$ is the center frequency, $\varphi_{LO}^n(t)$ is the phase noise, P_{LO} is the average output power and $P_{LO,WGN}(t)$ is the amplitude noise of the optical carrier generated by the LO, respectively. For simplicity let us assume that the LO laser is noiseless and its frequency is the same as the transmitted optical carrier, then we have

$$\mathrm{Re}\{E_{LO}^*(t)E_{IQ}(t)\} = \mathrm{Re}\left\{\sqrt{P_{LO}}\exp\left(-j\omega_c t\right)\cdot\sqrt{P_c}\exp\left(j\omega_c t\right)\cdot T_{IQ}(t)\right\} = \sqrt{P_c P_{LO}}T_I \tag{2.44}$$

Substituting the result of Equation (2.44) into Equation (2.42), we obtain

$$i_1(t) = \left|E_{IQ}(t)\right|^2 + \left|E_{LO}(t)\right|^2 + 2\sqrt{P_c P_{LO}}T_I \tag{2.45}$$

To remove the undesirable terms $\left|E_{IQ}(t)\right|^2$ and $\left|E_{LO}(t)\right|^2$, one alternative consists in applying a π-phase shift to a replica of the LO optical carrier, add this to a replica of the incoming signal and detect the resulting signal by a second PD whose output current is

$$i_2(t) = \left|E_{IQ}(t) - E_{LO}(t)\right|^2 = \left|E_{IQ}(t)\right|^2 + \left|E_{LO}(t)\right|^2 - 2\sqrt{P_c P_{LO}}T_I \tag{2.46}$$

The subtraction of current i_2 to i_1 results in $i_I(t) = i_1(t) - i_2(t) = 4\sqrt{P_c P_{LO}}T_I$ from which the signal $x_I(t)$ could be extracted provided that field modulation was employed, *i.e.* $T_I(t) \approx kx_I(t)$. In a similar way, the imaginary part of the modulated optical field could be obtained by applying phase shifts $\frac{\pi}{2}$ and $\frac{3\pi}{2}$ to replicas of the LO optical carrier, add each of them to corresponding replicas of the incoming signal and detect the resulting signals by a third and fourth PD to obtain the currents i_3 and i_4, respectively, as follows

$$i_3(t) = \left|E_{IQ}(t) - jE_{LO}(t)\right|^2 = \left|E_{IQ}(t)\right|^2 + \left|E_{LO}(t)\right|^2 + 2\,\mathrm{Im}\left\{E_{IQ}(t)E_{LO}^*(t)\right\} \tag{2.47}$$

$$i_4(t) = \left|E_{IQ}(t) + jE_{LO}(t)\right|^2 = \left|E_{IQ}(t)\right|^2 + \left|E_{LO}(t)\right|^2 - 2\,\mathrm{Im}\left\{E_{IQ}(t)E_{LO}^*(t)\right\} \tag{2.48}$$

The subtraction of current i_4 to i_3 results in $i_Q(t) = i_3(t) - i_4(t) = 4\,\mathrm{Im}\left\{E_{IQ}(t)E_{LO}^*(t)\right\} = 4\sqrt{P_c P_{LO}}T_Q$. The photo-current $i_Q(t)$, then provides access to the signal $x_Q(t)$. Therefore, under the assumed conditions, the complex driving signal $x(t)$ could be fully recovered. It is important to remark that the two pair of PD used to obtain the $i_I(t)$ and $i_Q(t)$ signals need to have ideally the same physical characteristics, so that they are called balanced photo-detectors.

The noiseless BtB case considered here is very idealistic. In the presence of noise and transmission of the signal through the fiber channel and the use of non-ideal electrical and optical devices, the reconstruction of signals $x_I(t)$ and $x_Q(t)$ requires the use of a block of DSP algorithms to estimate and compensate for distortions imposed by the transmission physical impairments. The DSP techniques used for the optical coherent system analyzed in this work are described in section 2.5.2.

In summary, the elements that conform an optical coherent receiver are: the LO that generates the optical carrier, the optical 90° hybrid that performs the split and phase shifts of the LO carrier and their addition to the incoming signal, the set of four balanced photodetectors that generates currents $i_1,...,i_4$, and two trans-impedance amplifiers (TIA) that perform the current subtraction operations and the current-to-voltage signal conversion from $i_{I,Q} \rightarrow \hat{x}_{I,Q}$. The conventional scheme of an optical coherent receiver is shown in Figure 2.5 [39].

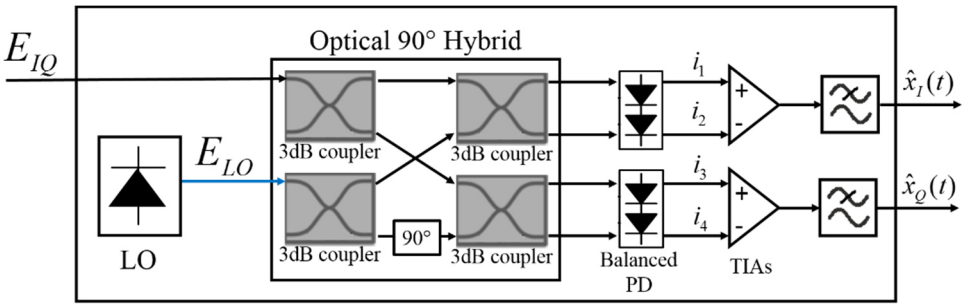

Figure 2.5 Diagram of an optical coherent receiver.

For the sake of simplicity, in the whole previous discussion the output current of the photo-diodes was considered just proportional to the square modulus of the incident optical field. However, the model of the PIN photo-diode used in the simulations presented in this work also considers some additional impairments. The actual output current of our modeled PIN photo-diode is [50]

$$i_{PIN}(t) = i(t) + i_{sh}(t) + i_{th}(t) + i_d \tag{2.49}$$

where $i(t)$ is the output current of an ideal photo-diode as defined in Equation (2.33), $i_{sh}(t)$ is the shot noise current, $i_{th}(t)$ is the thermal noise current and i_d is the dark current that are inherent to the optical detection process. The one-sided spectral noise density in $\mathrm{A}/\sqrt{\mathrm{Hz}}$ of the shot noise current is determined as follows

$$N_{sh} = \sqrt{2q\left(i_{sh}(t) + i_d\right)} \tag{2.50}$$

2.3 The fiber channel and its modeling

The aim of the E-O and O-E conversions addressed in the previous sections is the transmission of the modulated signals through a fiber channel which is known to have lower attenuation and much more capacity than copper cables. The fiber channel used in the systems analyzed in this thesis work is the conventional SMF. Propagation of optical waveforms in SMFs has been widely studied and different models with different degrees of complexity have been developed. The choice of the fiber model depends on a trade-off between the amount of detail required from the simulation results for a specific application and the computational time required to perform the simulation process [51].

For instance, by using a simple model in the frequency domain [49] which takes into account only deterministic and linear effects as well as a single-polarization propagation, the optical field at the output of a fiber channel is computed as

$$E_{FC}(f) = E_{in}(f) \cdot 10^{-\alpha_{FC} L/20} \exp\left(-j\beta(f)L\right) \tag{2.51}$$

where $E_{in}(f)$ is the frequency representation of the input optical field, α_{FC} [dB/m] is the attenuation coefficient of the fiber, L is the length of the fiber in meters and $\beta(f)$ is the frequency-dependent phase variation of the signal, which can be approximated by a third-order Taylor series expansion around 0 as

$$\beta(f) \approx \beta(0) + \frac{d\beta}{df}(0) \cdot f + \frac{1}{2}\frac{d^2\beta}{df^2}(0) \cdot f^2 + \frac{1}{6}\frac{d^3\beta}{df^3}(0) \cdot f^3 = \beta_0 + \beta_1 f + \frac{1}{2}\beta_2 f^2 + \frac{1}{6}\beta_3 f^3 \tag{2.52}$$

where β_0 is a fixed phase shift and β_1 is a linear phase shift associated with a delay in time. Coefficient β_2 stands for a frequency-dependent linear change of the group velocity whose effect is the first order group velocity dispersion (GVD) or chromatic dispersion. This dispersive effect causes that the frequency components of the propagating signal travel at different speeds. If a multi-carrier signal is sent through a chromatic dispersive channel, then a time delay between its *sub-carriers* is present at the output of the channel. The β_2 term in units of s^2/m is related with a most used parameter called chromatic dispersion coefficient D in units of s/m^2 as follows

$$\beta_2 = -\frac{\lambda_c^2}{2\pi c} D \tag{2.53}$$

where c is the speed of light in a vacuum and λ_c is the center wavelength of the propagating optical carrier.

β_3 is the second order GVD coefficient in s^3/m, related with D and the dispersion slope S (in s/m^3) coefficients in this manner:

$$\beta_3 = \left(\frac{\lambda_c}{2\pi c}\right)^2 \left(2\lambda_c D + \lambda_c^2 S\right) \tag{2.54}$$

Parameter S is used to calculate the value of parameter D corresponding to a certain wavelength.

Considering only the effect of the first order GVD in Equation (2.51), the fiber channel acts as a linear filter whose frequency response is obtained as follows

$$H_{CD}(f) = \frac{E_{FC}(f)}{E_{in}(f)} = \exp\left(-\frac{j\beta_2 f^2 L}{2}\right) \tag{2.55}$$

This simple model does not take into account relevant transmission impairments such as the fiber nonlinear response due to the Kerr effect or polarization mode dispersion (PMD). However, the derivation of Equation (2.55) was presented since a CD compensation algorithm used in the system analyzed in Chapter 5 relies on this expression (see section 2.5.2).

A more sophisticated model of the fiber channel, reported in [52], is used in the simulation analysis presented in Chapter 4 and 5 of this work. This model solves a system of two coupled nonlinear Schrödinger equations describing the propagation of two orthogonal polarization components of optical signals in a fiber channel. The model takes into account polarization-dependent loss (PDL), PMD, four-wave mixing (FWM), self-phase modulation (SPM), cross-phase modulation (XPM), first order GVD, second order GVD, and attenuation of the fiber. Adjustment factors for SPM, FWM, and XPM due to polarization evolution are included in the model.

To calculate polarization effects in the fiber the coarse-step method is used [53]. In this method, continuous variations of birefringence are approximated by series of many short-polarization-sections in which the degree of birefringence and the orientation of the principal axes are constant. The polarization state of the optical field is scattered to a new point on the Poincaré sphere at the end of each section [52]. Each scattering section is defined by frequency-dependent Jones matrix which has the eigenvectors that coincide with the rotation axis in Stokes space. The multiplication of the input field by the Jones matrix is equivalent to the rotation of polarization vector on the Poincare sphere around this rotation axis. In the employed model, the length of each polarization scattering section Δz_{scatt} is randomly selected from a Gaussian distribution, with a given mean μ_{scatt} and standard deviation σ_{scatt}. The values used in this work are 1 km and 10 m, respectively. The length of all polarization sections should be longer than the correlation length (L_c) between the X and Y polarization components. The parameter L_c is related with the variance σ_T^2 of the random time delay ΔT occurring between the X and Y polarization components during propagation of an optical pulse through a fiber with length L [54] as follows:

$$\sigma_T^2 = \left\langle (\Delta T)^2 \right\rangle = 2\left(\left(\beta_1^X - \beta_1^Y\right) L_c\right)\left[\exp\left(-L/L_c\right) + L/L_c - 1\right] \tag{2.56}$$

where β_1^X and β_1^Y describe the group velocity deviation for the X and Y polarization components, respectively. Typical values of L_c are between 10 and 300 m. The value used here is 50 m. For $L > 0.1$ km, we can use $L_c << L$ in Equation (2.26) to get the approximation [55]

$$\beta_1^X = -\beta_1^Y \approx \frac{\sigma_T}{2\sqrt{2L_c L}} = \frac{D_{PMD}}{2\sqrt{2L_c}} \tag{2.57}$$

where D_{PMD} is the PMD coefficient in $s/\sqrt{m}$, obtained statistically as $D_{PMD} = \sigma_T / \sqrt{L}$.

The mathematical model for pulse propagation within each polarization section, as mentioned before, is based on a set of coupled propagation equations for two orthogonal polarization components of the electrical field, given by Equations (2.58) and (2.59) [56]. These polarization components correspond to the principal axes of polarization in the fiber section [57].

$$\left[\frac{\alpha_{FC}}{2} + \frac{\partial}{\partial z} + \beta_1^X \frac{\partial}{\partial t} - j\frac{\beta_2}{2}\frac{\partial^2}{\partial t^2} - \frac{\beta_3}{6}\frac{\partial^3}{\partial t^3}\right] E_{FC}^X(z,t) = -j\gamma\left[\left|E_{FC}^X(z,t)\right|^2 + \frac{2}{3}\left|E_{FC}^Y(z,t)\right|^2\right] E_{FC}^X(z,t) \tag{2.58}$$

$$\left[\frac{\alpha_{FC}}{2} + \frac{\partial}{\partial z} + \beta_1^X \frac{\partial}{\partial t} - j\frac{\beta_2}{2}\frac{\partial^2}{\partial t^2} - \frac{\beta_3}{6}\frac{\partial^3}{\partial t^3}\right] E_{FC}^Y(z,t) = -j\gamma\left[\left|E_{FC}^Y(z,t)\right|^2 + \frac{2}{3}\left|E_{FC}^X(z,t)\right|^2\right] E_{FC}^Y(z,t) \tag{2.59}$$

where α_{FC} is expressed in linear units 1/m $\left(\alpha_{FC} = \alpha_{FC,dB}/4.343\right)$. It is important to remark that $E_{FC}^{X,Y}(z,t)$ denotes in Equations (2.58) and (2.59) the slowly-varying complex-envelope of the electric field of the light wave.

The fiber nonlinearity factor γ due to the Kerr effect in units of $(W \cdot km)^{-1}$ is given by

$$\gamma = \frac{2\pi n_2}{\lambda_c A_{eff}} \tag{2.60}$$

where A_{eff} in μm^2 is the fiber effective area and n_2 in m^2/W is the fiber non-linear index. n_2 is assumed to be measured with a constant linear polarization throughout the measured fiber.

Coupled Equations (2.58) and (2.59) are solved numerically by employing the well-known asymmetrically split-step Fourier method [54]. The maximum and minimum step widths allowed for the split-step method used in this work are, 1 km and 0 m, respectively, for a maximum phase change of 0.5 degrees. Polarization scattering and nonlinear effects are calculated using independent step sizes [52].

2.4 Directly Detected Optical OFDM (DDO-OFDM)

The digital implementation based on the IDFT and the DFT to modulate/multiplex and demodulate/demultiplex multiple *sub-carriers*, respectively, spurred OFDM as a popular technology for the deployment of communication systems of different kinds. In particular, the interest to use OFDM in optical communications systems has grown in the last decade, mainly because the benefits in terms of spectral efficiency and flexibility that this technology provides. Up to now, however, there are no commercial optical OFDM-based transmission systems available in the market.

There are many approaches to implement an OFDM system over a fiber channel. The first classification depends on the domain in which the OFDM signal is generated and detected. If the OFDM signal is completely modulated/demodulated and multiplexed/demultiplexed in the optical domain, the system is classified as All-Optical OFDM (AO-OFDM). If the OFDM signal is digitally generated and E-O converted and transmitted through a fiber channel and then O-E transformed to be digitally detected at the receiver side, the system is classified as Electro-Optical OFDM (EO-OFDM). In [58] six types of EO-OFDM formats are defined. However, three main implementations of EO-OFDM over a fiber channel stand out [59]. Two of them are based on the use of a single optical modulator at the transmitter side and a single photo-detector for direct detection at the receiver side (DDO-OFDM). The third one (CO-OFDM) is based on the use of an IQ-OFDM *baseband* digital transmitter (see Figure 1.5) followed by an optical IQ modulator at the transmitter side and an optical coherent receiver followed by an IQ-OFDM *baseband* digital receiver. The CO-OFDM and AO-OFDM approaches have been studied mainly to implement long-haul communication systems. AO-OFDM is out of the scope of the present work since it requires many optical transceivers to operate. This makes its use prohibitive under short-haul applications. CO-OFDM will be discussed in section 2.5.

Regarding DDO-OFDM systems, the differences between the two main existing alternatives pertain to the kind of OFDM digital implementation that is used and the way that the modulator is operated. If the RF-IQO-OFDM digital implementation is used, then we have a Field Modulated RF-IQ-DDO-OFDM system. If the Real-valued OFDM digital implementation is employed, we have the Intensity Modulated (IM)-DDO-OFDM approach. The latter architecture is used to implement the system analyzed in Chapter 4. The former one is employed to implement the system proposed and analyzed in Chapter 5. Both approaches are treated in next sections as well as the main physical impairments that affect this kind of DDO-OFDM systems.

2.4.1 Intensity Modulated IM-DDO-OFDM system

This scheme is so far the simplest and most cost-effective approach to transmit an OFDM signal over a fiber channel. A real-valued OFDM *baseband* modulating signal $V_m(t)$ is generated in the digital domain (see section 1.3.2). The electrically generated signal $x_{OFDM}(t)$ modulates the power of a CW optical signal by means of an optical intensity modulator. A DML could also be used instead of an EML (as in [60], [61]). In this case, the electrical signal $x_{OFDM}(t)$ is used to adjust the current of the laser. However, as previously stated, one major disadvantage of this scheme is the high chirp that a DML normally adds to the signal [62]. This in turn severely

limits the system's reach, especially at high transmission rates. Then, the DML alternative is not studied in the present work to transmit OFDM signals.

The optical waveform produced by the optical IM in response to the OFDM driving signal, is an optical double-side band (ODSB) signal, in which the two side OFDM bands are symmetric around the optical carrier. For some purposes (as described in section 2.4.3) one of the optical sub-bands (OSBs) is removed to obtain an optical single-side band (OSSB) signal. This operation is performed by an optical filter placed just after the OIM. The modulated signal (ODSB or OSSB) is launched into the optical fiber and, after transmission, it is directly-detected by a single photo-diode. The PD delivers an electrical signal which, after analogue-to-digital conversion, enters the corresponding OFDM electrical receiver. A general diagram of the IM-DDO-OFDM architecture is shown in Figure 2.6.

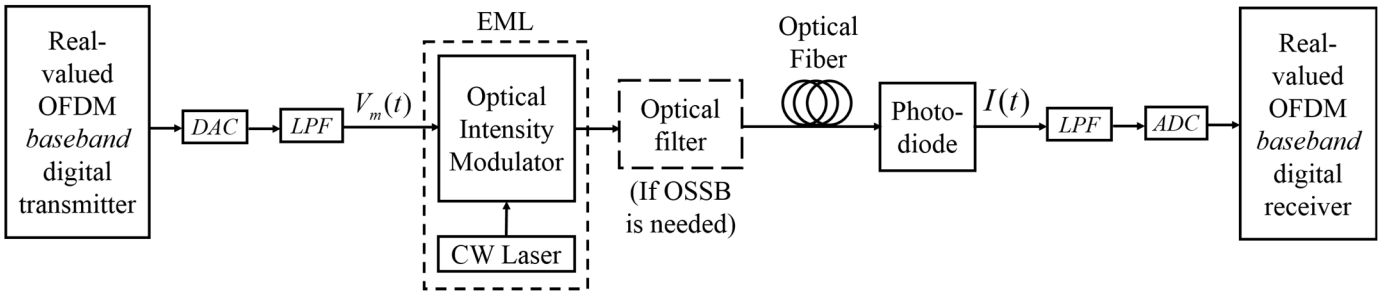

Figure 2.6 Block diagram of the IM-DDO-OFDM transmission system.

2.4.2 Field Modulated RF-IQ-DDO-OFDM system

An alternative DDO-OFDM implementation is based on the use of an RF-IQ-OFDM transmitter (see section 1.3.1) to digitally generate the electrical OFDM modulating signal $V_m(t)$ that drives the EML. The rest of the optical path is the same as in the scheme described in the previous section 2.4.1. The current signal $i(t)$ delivered by the PD now is injected into the corresponding RF-IQ-OFDM receiver. A general diagram of this architecture, named here as RF-IQ-DDO-OFDM, is shown in Figure 2.7.

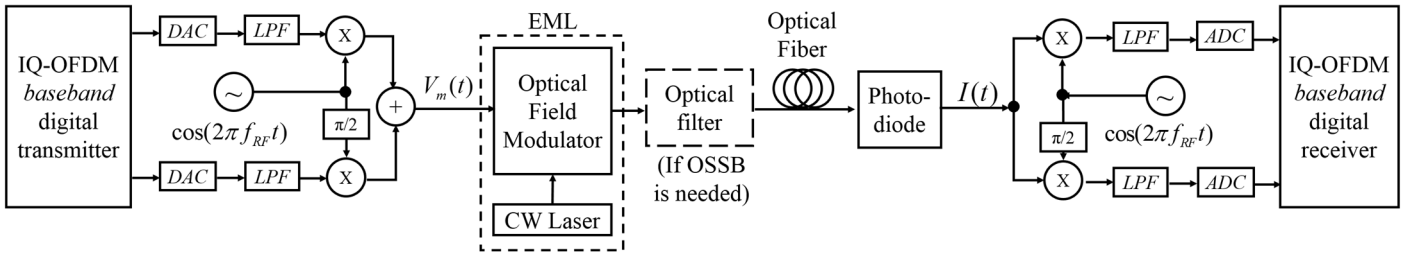

Figure 2.7 Block diagram of the RF-IQ-DDO-OFDM transmission system.

In this scheme, the complex OFDM *baseband* signal is *up-converted* to an intermediate frequency f_{RF} in the electrical domain. A frequency gap of $f_G = f_{RF} - 0.5B$ between the optical carrier and the OSB is then created

after optical modulation, where $B = R_s$ is the bandwidth of each OSB. The value of f_G is typically equal to B (see section 2.4.5), thus f_{RF} is set equal to 1.5B. The signal that outputs the optical field modulator is an ODSB signal. It is very common in the RF-IQ-DDO-OFDM approach to use the OSSB scheme (also known as Optical Vestigial Side-Band or OVSB), which is typically referred as SSB-DDO-OFDM. The optical filter that removes one side-band is also used to vary the amplitude of the optical carrier and thus control the carrier to signal power ratio (CSPR) value. It has been shown in [63] and [64] that a CSPR = 0 dB (equal power between carrier and side-band) results in the best receiver sensitivity for a given OSNR when this DDO-OFDM approach is used.

For this kind of optical OFDM implementation, unlike the previous approach, the bias voltage (V_b) of the modulator (either EAM or MZM) must be tuned to modulate the device within its linear field range (or as close as possible). For example, if a MZM is used, it should be biased at its *null* point to achieve a linear field modulation (see section 2.1.1). However, if the bias is set exactly at the *null* point, the optical carrier (needed at the receiver side for self-coherent detection) is completely suppressed. Therefore, the bias should be *close* to the *null*, to transmit a part of the carrier. Moreover, the CSPR parameter and the chirp factor of the modulator also depends on the value of V_b [64]. Therefore, it is very important to optimize the bias voltage parameter value for a specific system configuration.

In order to avoid or diminish the deleterious impact of some system impairments that affects the DDO-OFDM systems, some DSP techniques at the receiver end and the correct optimization of some key parameters become necessary at the design stage. In next sections the main impairments that affect this kind of systems are described as well as some solutions to counteract their harmful impact.

2.4.3 The cyclic prefix solution to the chromatic-dispersion induced time delay impairment

An optical fiber is a dispersive channel. Chromatic dispersion (CD) is a linear distortion that causes a frequency-dependent group velocity, thus inducing a time delay between the *sub-carriers* of the optical OFDM signals. The maximum delay between the fastest and the slowest *sub-carriers* is represented as t_D. An OFDM symbol is the sum of all the modulated *sub-carriers* over a *sub-channel* symbol period $0 \le t \le \hat{T}_s$. An OFDM signal is composed of consecutive OFDM symbols. Although in an OFDM system the *sub-channel* symbol period is much greater than the CD-induced time delay ($\hat{T}_s >> t_D$), there is still a small ISI among the adjacent OFDM symbols. To completely avoid ISI a silent (empty of data) guard time $t_G > t_D$ should then be placed between consecutive OFDM symbols as shown in Figure 2.8.a.

A disadvantage of the insertion of a guard time is the reduction of the data rate efficiency. The OFDM symbol period is $T_{OFDM} = \hat{T}_s$, then the raw data rate is $R_s = N / T_{OFDM}$. The true OFDM symbol period after guard time addition (OFDM frame) is $\tilde{T}_{OFDM} = T_{OFDM} + t_G$. Then, the true data rate $\tilde{R}_S$ is given by Equation (2.61). The data rate efficiency is $\eta = \tilde{R}_s / R_s$. It is clear that as t_G increases the data rate efficiency decreases.

$$\tilde{R}_S = \frac{N}{\tilde{T}_{OFDM}} = \frac{T_{OFDM}}{T_{OFDM} + t_G} R_s \tag{2.61}$$

According to Equation (1.13) (see section 1.2), under an ideal channel transmission condition ($h(t) = \delta(t)$) the received symbol of the *i*-th *sub-channel* only depends on its corresponding transmitted symbol. This no longer holds for transmission over a dispersive channel, where $h(t) \neq \delta(t)$, even if a silent guard time is added to every OFDM symbol. In this situation, the received symbol of a given *sub-channel* not only depends on the corresponding transmitted symbol but also on the received symbols of other *sub-channels*. This undesirable phenomenon is known as ICI among *sub-channels*. An elegant solution to avoid ICI in OFDM transmission [32], [65] consists on filling the silent guard period with a copy of the first t_G seconds of each OFDM symbol (called *cyclic prefix* or CP), as shown in Figure 2.8.b. As a result, the OFDM frame begins and ends with the same waveform, acquiring a cyclic quality (at least for a given time window). Consequently, the channel time domain dispersive effect is turned from a linear convolution into a cyclic convolution at the receiver DFT observation period (or DFT window) for each *sub-channel*. This is graphically shown in Figure 2.8.c. Therefore, as long as the CP period (t_G) is longer than the CD-induced delay and the DFT window is well synchronized, as shown in Figure 2.8.c, the data can be recovered without ICI [65]. Since the CP lasts t_G seconds, it still absorbs any residual symbol spreading (ISI).

Different algorithms have been proposed to synchronize the receiver-side DFT window with the start and end of each OFDM data frame. Since the CP is redundant data, correlation techniques could be used to identify the beginning (an ending) of the frame [32]. Another popular method based on correlation operations between two identical segments transmitted on a preamble symbol is proposed in [66]. In the present work, as explained later in section 2.4.4, pilot OFDM symbols known at the receiver side are transmitted for channel estimation purposes. By using this pilot symbols, a simple algorithm, based also on correlation techniques, was developed and it will be explained later. An improper DFT window synchronization causes that part of the previous symbol inputs de DFT. This results in ISI as well as ICI since the cyclic condition is no longer observed.

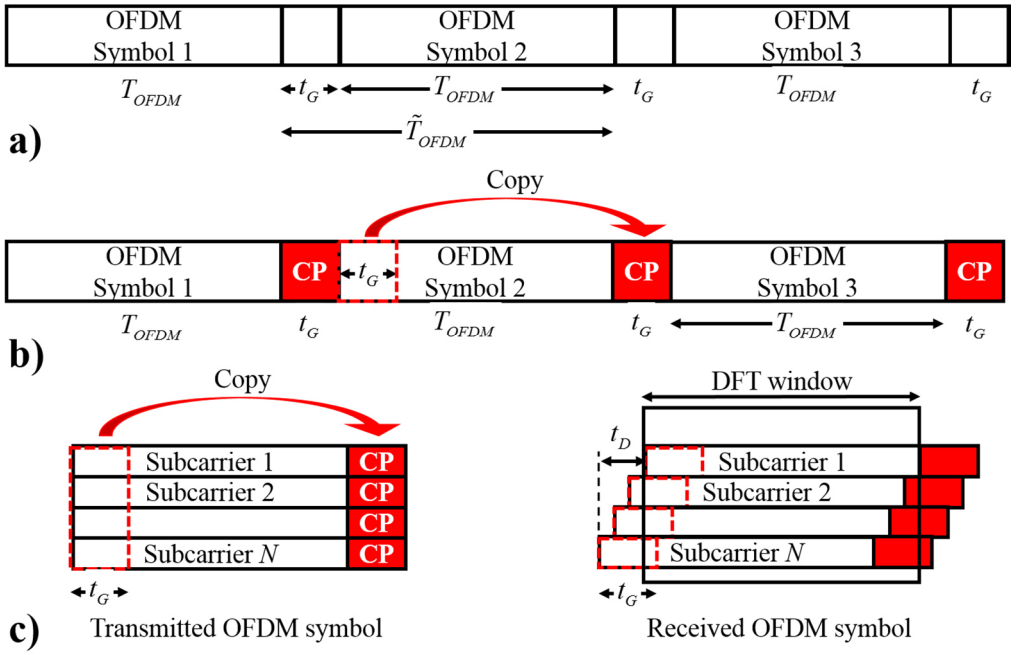

Figure 2.8 a) Guard time insertion to prevent ISI; b) Cyclic prefix process to prevent ICI; c) Graphic representation of the effect of the CD-induced delay on an OFDM symbol.

The value of t_G in seconds is estimated as [67]

$$t_G \geq \frac{c}{f_c^2}|D|LR_s \times 10^{-3} \tag{2.62}$$

where $|D|$ is the absolute value of the fiber CD coefficient in ps/nm·km, c is the speed of light in m/s, f_c is the optical carrier center frequency in Hz and L is fiber length in km. As an example, for an OFDM transmission with a symbol rate of 28 GBd, over 10 km of conventional SMF over C-band (f_c = 193.4 THz) with D = 17 ps/nm·km and N = 256 *sub-carriers*, $T_{OFDM} = 10.24ns$ and $t_G \geq 38.18ps$. If we set $t_G = 50ps$, then the data rate efficiency becomes 99.5 %.

CP insertion is typically performed digitally after the IDFT operation of the OFDM *baseband* transmitter. At the receiver side the DFT window synchronization algorithm is implemented after digitization and parallelization of the samples. Once the beginning and ending of the OFDM frame are identified, the CP removal block acts just before the signal enters the DFT stage.

2.4.4 The single-tap equalizer solution to the system frequency response induced impairments

The electrical and optical devices that as well as the fiber channel conform an optical OFDM system are band-limited systems. They act as low and band pass filters. The equivalent complex transfer function of the complete electro-optical OFDM system is called here the system frequency response.

Assuming a linear system without ISI and ICI (thanks to the CP insertion), the complex frequency response $H_n(f)$ of the *n*-th *sub-channel* centered at its *sub-carrier* frequency f_n and within a bandwidth equal to the *sub-carrier* spacing Δf, can be expressed as

$$H_n(f) = \frac{Y_n(f)}{X_n(f)}, \quad f_n - \frac{\Delta f}{2} \le f \le f_n + \frac{\Delta f}{2} \tag{2.63}$$

where $X_n(f)$ and $Y_n(f)$ are the transmitted and received complex spectra of the *n*-th *sub-channel*, respectively. At $f = f_n$ the discrete H_n coefficients are

$$H_n = H_n(f = f_n) = \frac{Y_n(f = f_n)}{X_n(f = f_n)} = \frac{\tilde{C}_n}{C_n} \quad \Rightarrow \quad \tilde{C}_n = H_n C_n \tag{2.64}$$

where C_n and $\tilde{C}_n$ are the transmitted and received symbol over the *n*-th *sub-carrier*, respectively. If the number of *sub-carriers* is large enough, a flat response could be assumed for each *sub-channel* band. Then, as shown in Figure 2.9, the system response (in blue) could be approximated as a discrete system (in red).

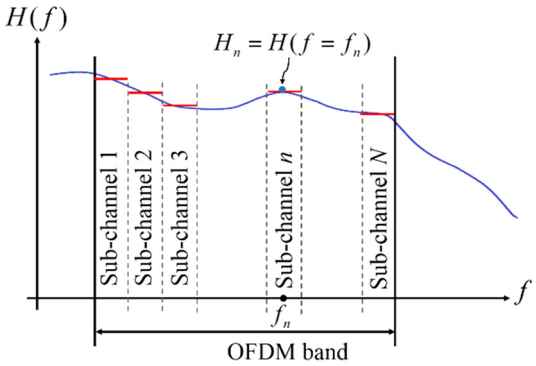

Figure 2.9 Simplified representation ($H_n(f)$ is shown as real-valued) of a system response and its discrete approximation. Continuous response in blue, discrete response in red.

After transmission, the received symbols have phase and amplitude distortion which should be reverted for a proper decoding process. Following Equation (2.64) it is possible to revert the effect of the system response by a complex multiplication between the received symbol C_n and the inverse of the coefficient H_n, as follows

$$C_n^{EQ} = H_n^{-1}\tilde{C}_n = H_n^{-1}(H_n\tilde{C}_n) = C_n \tag{2.65}$$

If now, apart from the effect of the system frequency response, noise is considered for each symbol, the previous equation becomes:

$$C_n^{EQ} = H_n^{-1}\tilde{C}_n = H_n^{-1}(H_n\tilde{C}_n + N_n) = C_n + H_n^{-1}N_n \tag{2.66}$$

where N_n is the average noise over the *n*-th *sub-channel* band. The equalized symbol C_n^{EQ} is equal to the transmitted symbol C_n, as desired, but with an extra component of noise $H_n^{-1}N_n$. This represent the general situation under which the decision block at the receiver side works (without changing the decision regions). Since the equalizer is only based on a complex multiplication for each received complex symbol $\tilde{C}_n$ (thanks to ISI and ICI cancellation enabled by CP insertion), it is known as *single-tap* frequency domain equalizer (FDE) [32].

The coefficients H_n could be estimated by sending a pilot OFDM symbol (as in this work) that is already known at the receiver side. Following Equation (2.64), H_n could be calculated by dividing the *n*-th received symbol of the pilot by the *n*-th known transmitted symbol. A pilot symbol is sent at the beginning of the transmission to train the equalizer. The same pilot OFDM symbol could be sent several *L* times to improve the estimation. The corresponding $H_{n,l}$, $l = 1 \ldots L$, are averaged to obtain the corresponding H_n value. The process of sending one or more copies of the OFDM pilot symbol to train the equalizer could be repeated from time to time, to adapt the equalizer to the dynamic system variations. If the channel changes very quickly it is even possible to send pilot symbols in all the OFDM transmitted symbols, but just in some *sub-carriers* (pilot *sub-carriers)* and then, by interpolation, estimate the rest of the H_n coefficients [68]. In the present work a slow-varying channel was assumed, then the pilot OFDM-aided FDE approach can be employed. It is important to remark that the *single-tap* pilot-aided equalizer only corrects for linear distortions.

This kind of equalizer has been shown to work well in DDO-OFDM systems [59], [63], [64] to correct for CD-induced phase shifts, linear distortions and a small amount of phase noise due to the laser linewidth. To significantly increase the *single-tap* FDE ability to correct for CD-induced phase shifts, the OSSB transmission scheme should be preferred over the ODSB scheme [63], [69]. In DSB DDO-OFDM systems with linear field modulation each electrical OFDM *sub-carrier* is translated into two conjugated optical *sub-carriers* on both

sides of the optical carrier [70]. In contrast, when OSSB is used, each OFDM *sub-carrier* is translated into a single optical *sub-carrier*. As a consequence, after fiber transmission and square-law direct photo-detection the phase shift of every single optical *sub-carrier* is translated into a phase shift of every single electrical OFDM *sub-carrier*. In contrast, when ODSB is used, the two conjugated optical *sub-carriers,* which have different phase shifts due to CD, are translated into a single electrical *sub-carrier* destroying the direct optical-electrical phase shift relationship present in OSSB [63], [69]. In addition to increase the effectiveness of the CD-induced phase shifts equalization, the use of OSSB also considerably reduces the effect of CD-induced power fading as a function of the fiber length as compared to the ODSB case [71], [72].

Figure 2.10 shows the block diagram of the *single-tap* FDE placed just after the DFT block in the OFDM *baseband* digital receiver.

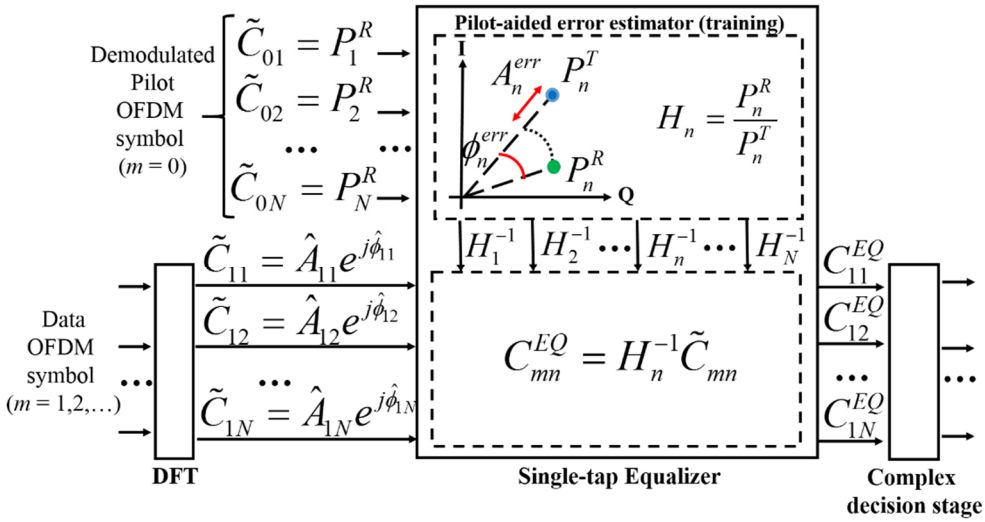

Figure 2.10 Block diagram of the single-tap frequency domain equalizer.

2.4.5 The non-linear distortion impairments and the adopted solutions

The E-O transfer function of a modulator (both EAM and MZM) has regions that could be considered linear. However, in practice, operation in part of the non-linear regions may take place (see sections 2.1.1 and 2.1.2). A linear conversion between the electrical OFDM signal and the optical field (or optical power), desired in RF-IQ (or IM) DDO-OFDM systems, could be achieved by operating the modulator into its corresponding E-O linear region. However, this limits the maximum peak to peak amplitude of the input electrical signal, which in turn limits the modulation depth (or optical modulation index, OMI). As a consequence, both the SNR and the OSNR of the electrical and optical signals, respectively, become limited to a narrower region. If we want to increase the OSNR by increasing the OMI of the modulating signal beyond the limits allowed for linear operation, the signal will be non-linearly distorted.

An OFDM signal inherently has high values of PAPR, which has been identified as one of the main drawbacks of this technology [33]. The amplitude of an OFDM signal could be accurately modelled as a Gaussian

distributed random variable [73], with zero-mean and standard deviation σ_s. Therefore, most of the amplitude of the signal (more than 99%) is concentrated within $\pm 3\sigma_s$. However, although unlikely, the signal contains some peaks that surpass this limit, named here as *high* peaks. The PAPR is the ratio between the *highest* peak power and the average power of the signal

$$PAPR = \frac{\max_t \{x_{OFDM}^2(t)\}}{\left\langle x_{OFDM}^2(t) \right\rangle} \tag{2.67}$$

One of the problems of working with signals with high PAPR is related to the quantization noise at the output of the DACs/ADCs [73]. The quantization levels N_q of a DAC/ADC, are set according to the peak-to-peak amplitude of the signal. Quantizing a signal that contains unlikely *high* peaks, results in an inefficient assignation of the quantization levels. Instead of assigning more levels to amplitude ranges in which the signal is more likely to be, some levels must be assigned for amplitude ranges in which the signal rarely exists. This in turn increases the average quantization error.

Another problem that arises from the use of high PAPR signals is related to the modulator E/O conversion. Although most of the amplitude values of an OFDM signal would fit into the linear region (to get maximum OSNR at the output of the modulator), the *high* peaks of the signal will surpass the E/O linear limits causing non-linear distortion. In contrast, if non-linear distortion is wanted to be avoided, the *high-peaks* of the signal should fit into the linear region which results in a sharp reduction of the average amplitude (and power) of the signal, with the corresponding abrupt reduction of its OSNR.

Not only the modulator may produce non-linear distortion of an OFDM signal (especially with high PAPR), but the rest of the devices involved in the E-O and O-E conversion processes, such as electrical amplifiers, square-law photo-detectors [64], [74], [75] and TIAs, may produce it as well. Other phenomena that can alter the characteristics of the non-linear distortion are the chromatic dispersion and the modulation chirp [74], [76], [77]. The non-linear distortion causes both in-band distortion and out-of-band power spreading [32]. The in-band interference deteriorates the BER performance of the received signal through warping of the signal constellation and non-linear inter-carrier interference (NL-ICI), whereas the out-of-band interference causes adjacent channel interference through spectral spreading.

In an optical OFDM scheme with linear field modulation (such as RF-IQ-DDO-OFDM), NL-ICI only comprises the *sub-carrier* to *sub-carrier* beat interference (SSBI) terms among subcarriers due to the square-law photo-detection [64], [78]. In contrast, in a linear intensity modulation optical OFDM approach (such as IM-DDO-OFDM), the NL-ICI includes the previous mentioned beating terms plus additional intermixing products caused by square-root-law intensity modulation (direct or external) and chirp-induced phase modulation [76], called *sub-carrier* to *sub-carrier* intermixing interference (SSII). Therefore, unlike SSBI, the SSII value depends on dispersion and chirp. In some references the whole NL-ICI is called SSII [74], [79],

what means that the authors considered that the SSBI terms are contained into the SSII terms. While the SSBI undesired tones are mainly concentrated in frequencies between 0 and *B* and their amplitude decrease as the frequency increases, the SSII products are distributed in a broader BW and its amplitude exhibits higher variation as a function of frequency, as shown in Figure 2.11.

In order to avoid overlapping (interference) of the sought signal frequency components and the unwanted SSBI products [64], [68], as well as some SSII tones [74], in the receiver side, DDO-OFDM systems could use a guard-band f_G with the same size as the OSBs bandwidth between the optical carrier and the OSBs (as already mentioned in section 2.4.2), as shown in Figure 2.11.b. As a consequence, the spectral efficiency of the system is reduced twice. Despite avoiding some undesired tones by using the guard-band alternative, if the amplitude of the modulating signal drives the modulator into the non-linear region, some NL-ICI products (especially SSII tones) still will fall into the signal band, thus producing residual interference.

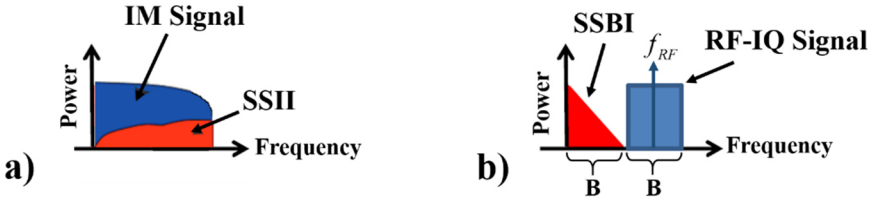

Figure 2.11 Simplified illustration of the SSBI and SSII processes at the output of the photodiode.

Unlike the CP addition and the single-tap equalizer, which are very well established solutions to the corresponding impairments, there is still not a common solution to the non-linear distortion problem in DD-OFDM systems. Many alternatives such as methods for PAPR reduction [80], [81], [82], [83], guard-band-sharing [75], SSII estimation and cancelation [70], [74], [76], [79], SSBI reconstruction and elimination [64], [78], [84], non-linear modulator compensation [85], [86], [87], [88], and combination of some of them [89], have been proposed to counteract this impairment. To reduce the impact of non-linear distortion, in the present work, we employed the following approaches:

- For the system analyzed in Chapter 3, we combine a clipping technique to reduce PAPR and a simple time-domain digital technique to compensate for the nonlinear E-O transfer function of the modulator. Further details about this techniques will be provided in the corresponding section of the referred Chapter.
- For the system analyzed in Chapter 4, we implement a simple technique based on random phase-shifting to reduce PAPR and an optimization of the modulator parameters looking for a trade-off between OMI and SSII. The architecture of the analyzed system based-on *RF-up-conversion* to shift the OFDM side-band was intentionally adopted to avoid detecting in the band in which most of the SSBI tones fall. Further details about this techniques will be provided in the corresponding section of the referred Chapter.

2.5 Coherent optical communication systems (COCS)

The previously presented DDO-OFDM systems have some inherent limitations due to the use of direct detection, such as:

- Part of the optical carrier should be transmitted for self-coherent detection purposes, which results in more power consumption and less receiver sensitivity. In addition, if a MZM is used as modulator, it could not be biased at *null* for maximum linearity, in order to preserve the optical carrier.
- A frequency gap should be placed between the optical carrier and the optical side-band to avoid the beating products due to the square-root-law photo-detection, which reduces the spectral efficiency at least twice.
- If the frequency gap is meant to be avoided, the intensity modulation approach should be used. However, the square-root-law intensity modulation generates intermixing products as well as beating tones, thus complex algorithms for SSII and SSBI estimation and cancellation are required (a maximum of 77.4% of SSII cancellation has been reported in [74]). Another disadvantages of the IM-DD approach are: due to real-valued OFDM signal generation the required transmitter's bandwidth (BW) to generate an IM-DDO-OFDM signal is approximately twice of the output optical signal BW (half of the transmitter BW has been wasted for carrying no effective information in transmission) [64]. Moreover, IM-DDO-OFDM systems are typically ODSB transmitted, thus the CD-induced power fading and a lower efficiency counteracting the CD-induced phase shifts are the main limitations of this kind of systems.

In contrast, when coherent detection is used, the transmission of the optical carrier is no longer needed since an optical carrier (generated at a LO) is added at the receiver side, increasing its receiver sensitivity. The linear region of the field modulation could then be maximized. By maximizing the linearity of the field modulation, the generation of SSII could substantially be reduced at the transmitter side. Moreover, the SSBI could be optically removed at the coherent receiver thanks to balanced photo-detection. Therefore, frequency *RF-up-conversion* to create a frequency gap is no longer needed.

Thanks to coherent detection it is also possible to modulate not only the amplitude, but the phase of the optical field since after coherent optical to electrical conversion both are translated into the electrical domain (no matter if DSB or SSB scheme is applied). This characteristic adds modulation degrees of freedom, which in turn increases the capacity of the system. Moreover, by having access to the full received optical field information, the use of powerful DSP algorithms to correct for physical impairments is enabled. Amplitude and phase optical modulation is performed by an optical IQ transmitter. The combination of an optical IQ transmitter and an optical coherent receiver conforms a coherent optical communication system (COCS).

The use of COCS solves the problems of optical OFDM transmission related to direct detection. However, some of the main drawbacks inherent to OFDM, such as its high PAPR and its sensitivity to the frequency and phase noise [33], remain even when coherent detection is employed. Some of the advantages of OFDM as a multi-carrier scheme as compared to a single-carrier scheme are related to its ability to compensate for linear system distortions, robustness against CD-induced time delay and spectrum broadening as well as CD-induced phase shifts (bandwidth and capacity flexibility are also important features). The simplicity of the DDO-OFDM

DSP algorithms to compensate for these impairments in comparison to the ability and complexity of those in DDO single-carrier schemes [90] has positioned OFDM (and one of its variants called Discrete Multi-Tone, or DMT) as a promising direct detection-based technology [91], [92]. However, if these physical impairments estimation and correction capabilities could be solved in the single-carrier scheme by DSP algorithms enabled by coherent detection, then CO-OFDM could not be superior to single-carrier COCSs anymore. For instance, the complexity of the SC-COCS transmitter is lower than the CO-OFDM one (DACs, CP insertion and iDFT are not needed). Moreover, a SC-COCS signal has a much lower value of PAPR than a CO-OFDM one. In [93], [94], [95], [96] and [97], comparisons between CO-OFDM and SC-COCS have been performed. The conclusions of all of them agree in that both schemes have similar receiver complexity and tolerance to CD-induced impairments, however, SC-COCS outperforms CO-OFDM in terms of non-linearity and receiver constraints (such as DAC/ADC resolution, samples per symbol and bandwidth) tolerances.

Based on the previous arguments, the COCS analyzed in Chapter 5 is implemented using a single-carrier scheme. Therefore, the next two sections are focused on the optical generation, detection and correction of single-carrier signals transmitted by a COCS.

2.5.1 Dual-polarization single-carrier COCS (DP-SC-COCS)

Following the same principle of the *RF-up-conversion* stage of the electrical IQ modulator presented in section 1.1, a SC optical IQ modulator directly transforms the electrical signals $x_I(t)$ and $x_Q(t)$ that outputs an IQ coder into a modulated optical field $E_{IQ}(t)$. This is accomplished by an optical oscillator (Tx laser) that generates the optical carrier and a device (the DN-MZM) that "beats" each driving signal with the 0 and $\pi/2$ phases of the optical carrier, respectively (see section 2.1.1).

In a dual-polarization multiplexing scheme, two independent DN-MZM are driven by its corresponding IQ coder. Each DN-MZM modulates orthogonal polarizations of the optical carrier, generated with a single laser source in combination with a polarization beam splitter (PBS). The modulated optical fields that outputs both DN-MZMs are then multiplexed with a polarization beam combiner (PBC) to generate the dual-polarization modulated optical field $E_{IQ}^{DP}(t)$ that is launched into the fiber channel. A schematic diagram of the described dual-polarization SC optical IQ transmitter is shown in Figure 2.12.

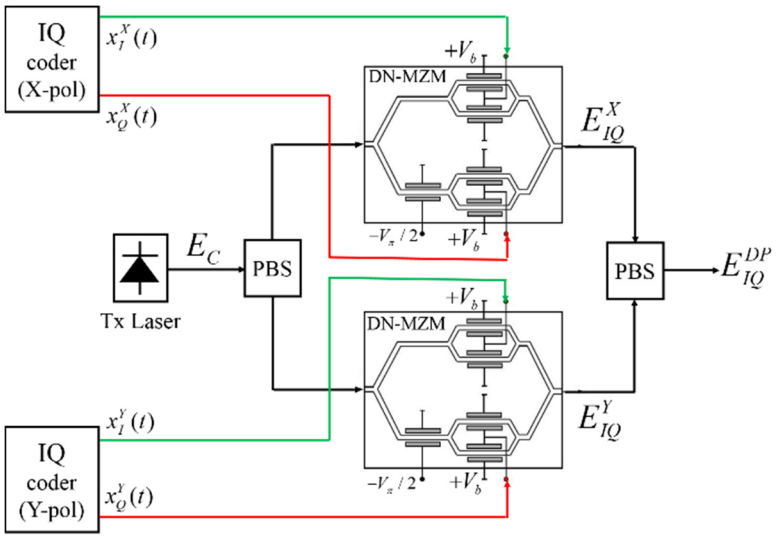

Figure 2.12 Diagram of a dual-polarization SC optical IQ transmitter.

At the receiver side, an optical coherent receiver, described in section 2.2, is needed to detect the complex information contained in the received optical field. If a dual-polarization scheme is used, the incoming signal must be split into its two orthogonal polarizations by means of a PBS. The same procedure should be carried out for the LO optical carrier. The signal of each polarization state inputs its own coherent receiver. The scheme of a dual polarization coherent receiver is shown in Figure 2.13.

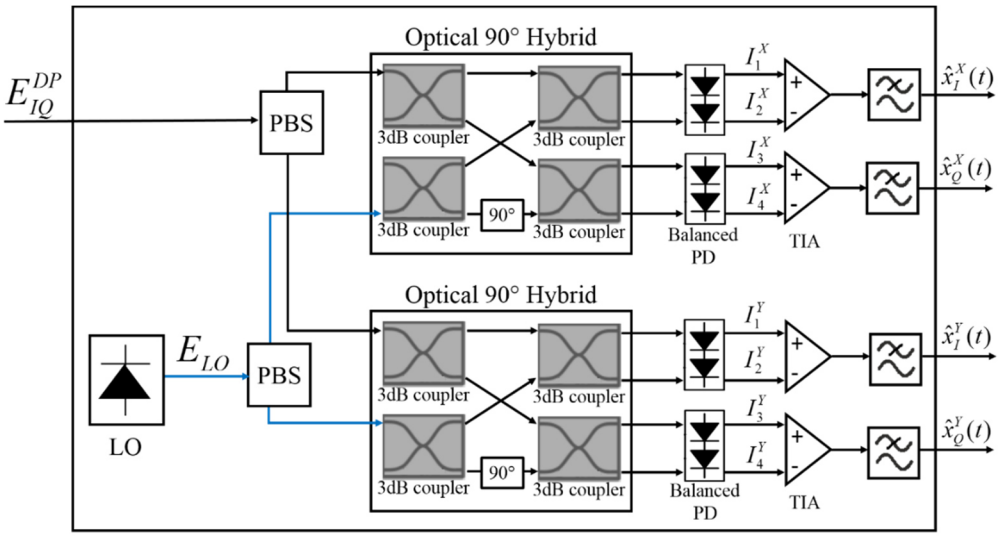

Figure 2.13 Diagram of a dual-polarization SC optical coherent transmitter.

Just after coherent detection, the I and Q signals of each polarization need to be analogue-to-digital converted in order to be equalized by estimating and correcting the distortion induced by some physical impairments, as it is discussed in the following section.

2.5.2 Digital signal processing algorithms to compensate for DP-SC-COCS physical impairments

For single-carrier transmission, the DSP algorithms developed for the multi-carrier DD-OFDM scheme that are described in previous sections of this work, are no longer useful. However, thanks to coherent detection we have a linear mapping from the full optical field into the electrical domain. Therefore, by digitizing the electrical signals that outputs the coherent receiver, it is possible to apply some DSP techniques to reverse some deleterious effects caused by the transmission. Some of this DSP techniques are adapted from those developed for wireless applications. Actually, the rebirth of optical coherent communications is largely due to the use of mature DSP algorithms and technology.

The development of DSP techniques to correct for linear and non-linear, static and dynamic, deterministic or random impairments, is a wide area of research and development that has gained a lot of attention during last years. Several alternatives have been proposed and are still being investigated. It is important to state that the DSP algorithms used here for SC-COCS were not developed by the author. Rather, they were chosen from the literature looking for a standard and well-tested set of algorithms to perform the impairment correction. It was out of the scope of the present work to develop novel DSP algorithms. Rather, the analysis and optimization of some physical characteristics of the optical devices were carried out. Notwithstanding, some of the parameters of the employed DSP algorithms were optimized as well for a short-reach SC-COCS, targeting low bit error rate values. This is detailed in Chapter 5.

The set of standard DSP algorithms used in the present work are schematically presented in Figure 2.14. After analogue-to-digital conversion with a sampling frequency F_s and a resolution m_{ADC}, a first block that performs CD compensation based on an overlapped frequency domain equalizer (OFDE) is applied. An adaptive time domain equalizer (TDE) MIMO algorithm follows; it is used to correct for polarization mode dispersion, cross-polarization and polarization rotation. In combination with this subroutine, a constant modulus algorithm (CMA) is used for M-PSK and a multiple modulus algorithm (MMA) is used for 16-QAM, to adapt the MIMO equalizer. The subsequent algorithm performs clock recovery and *slicing* of the signal. Then, a frequency-offset estimation and correction algorithm is used to eliminate the effect of the mismatch between the incoming optical carrier signal and the one generated at the LO. The last algorithm estimates and corrects for phase errors. Some of the algorithms are modulation-independent, while some others do depend on the modulation format. The latter are highlighted in gray in Figure 2.14.

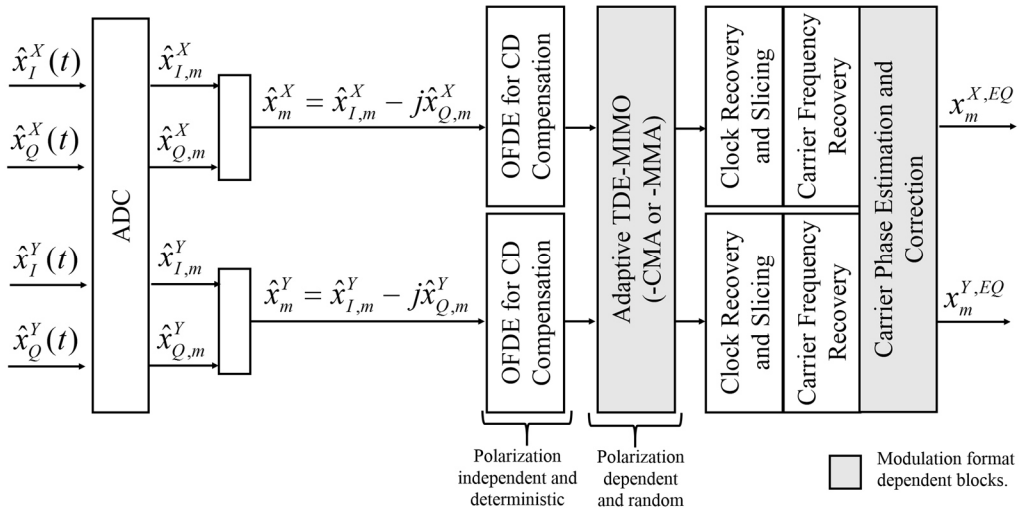

Figure 2.14 Set of DSP algorithms used in this work for impairments compensation.

According to the figure, the first DSP technique to be applied is CD compensation for each polarization. This algorithm is polarization-independent. Since CD is a deterministic effect this algorithm do not need to be adaptive. Since as a result of using a coherent receiver we have full access to the received electric field, chromatic dispersion can, in principle, be fully compensated using a linear filter with frequency response

$$G(f) = \exp\left(j\frac{\hat{\beta}_2 f^2 L}{2} \right) \tag{2.68}$$

where $\hat{\beta}_2$ is the estimation of the first order GVD dispersion parameter [98]. The frequency response of this linear equalizer is actually the inverse of that of the filter calculated using Equation (2.55). Note that f is the frequency of the baseband signal, *i.e.* the frequency of the electrical signal, not the frequency of the optical signal, and $-F_s/2 \le f \le F_s/2$. To implement the FDE, the time-domain digital received complex signal for each polarization $\hat{x}_m^{X,Y}$ has to be parallelized to form blocks of size N_{FFT}. Each of these blocks has to be transformed to the frequency domain using a Fast Fourier Transform (FFT) of size N_{FFT}. The FDE described in Equation (2.68) is then used to compute the weight coefficients that multiply the elements of each block, followed by an inverse FFT (iFFT) operation to return the blocks to the time domain. One limitation of using the FDE in single-carrier systems is the large temporal dispersion created by CD, which results in ISI. As discussed in section 2.4.3 for multi-carrier systems, a guard time addition between blocks of symbols is effective to eliminate ISI due to temporal dispersion. However, a large guard time is needed because the symbol period in a single-carrier transmission is much longer than that of every *sub-carrier* in OFDM, which results in a decrease on the transmission efficiency. Moreover, according to [99] the operation with a large block size is vulnerable for the synchronization error and increases the calculation complexity of the reception weight at

the FDE. Following [99], in order to avoid these problems, an overlap approach is used. The principle of operation of the OFDE is shown in Figure 2.15. The number of effective symbols N_{Eff} that the equalized signal takes from the total N_{FFT} symbols is an important parameter that depends on the total accumulated dispersion to be compensated.

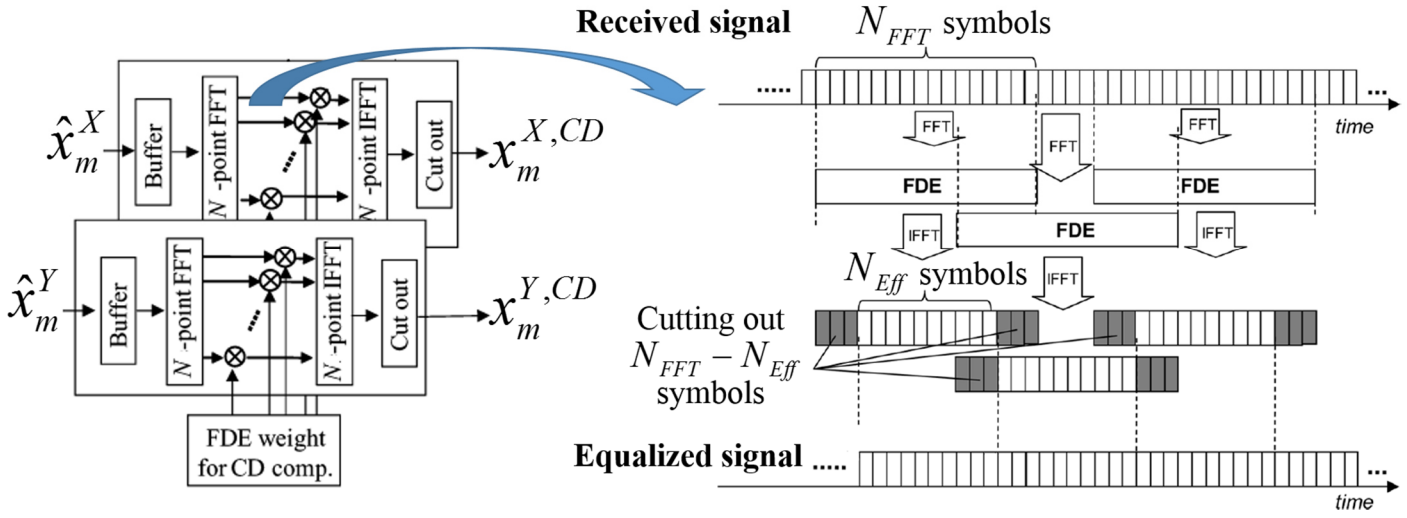

Figure 2.15 Schematic operation of the OFDE for CD compensation, modified from [99].

Although some residual ISI is present after the application of the OFDE algorithm, this is removed aided by the TDE algorithm in subsequent DSP stage.

The TDE-MIMO DSP block is a very important algorithm for dual-polarization schemes. During propagation through the fiber channel, the polarization of the optical signal is not maintained and changes unpredictably. If physical polarization tracking is not employed to orientate the PBS at the receiver side to match with the polarization axis of the incoming signal, both components of polarization affect each other. This phenomenon is known as polarization cross-talk. Since this and other polarization dependent impairments, such as PMD, are random and thus time-variant, an adaptive algorithm should then be used to compensate for their deleterious impact. The effect of polarization-dependent impairments on the signal propagation can be modeled using a the Jones matrix formalism, as follows

$$\begin{bmatrix} E_{Rx}^X \\ E_{Rx}^Y \end{bmatrix} = \begin{bmatrix} J_{11} & J_{12} \\ J_{21} & J_{22} \end{bmatrix} \begin{bmatrix} E_{Tx}^X \\ E_{Tx}^Y \end{bmatrix} \tag{2.69}$$

where $E_{Tx}^X, E_{Tx}^Y, E_{Rx}^X$ and E_{Rx}^Y are the transmitted and received X and Y components of the optical signal, respectively, and $J_{i,j}$ are the components of the Jones matrix. In general this matrix is frequency dependent due to PMD [54] and not unitary due to PDL. The goal of the DSP block is the estimation of the Jones matrix

in order to apply its inverse to compensate for the impairments incurred. The compensation for polarization rotations is a MIMO problem [100], with two inputs and two outputs. Following [101] the adaptive equalizer that compensates for these dynamic impairments is implemented using a set of four finite impulse response (FIR) filters, as shown in Figure 2.16. The functionality of this MIMO filter is to digitally perform the inverse Jones matrix of the dynamic channel after CD compensation, such that the outputs are given by

$$x_m^{X,MIMO} = h_{xx}^H x_m^{X,CD} + h_{xy}^H x_m^{Y,CD} \tag{2.70}$$

$$x_m^{Y,MIMO} = h_{yx}^H x_m^{Y,CD} + h_{yy}^H x_m^{Y,CD} \tag{2.71}$$

where h_{xx}, h_{xy}, h_{yx}, and h_{yy} are adaptive FIR filters of length N_{MIMO} representing the tap weights. There are different alternatives for adapting the equalizer in MIMO systems. For M-PSK modulation formats the constant modulus algorithm (CMA) is used in this work, while for 16-QAM format the multiple modulus algorithm (MMA) is employed. The parameters of the CMA and MMA are the number of iterations I_{MIMO} and the error weight ε_{MIMO}. Once the adaptive algorithm has converged, then the equalizer may move into a decision directed mode, using a decision directed least mean squared algorithm. The complete blind and adaptive TDE-MIMO-CMA equalizer is implemented according to [102], while the TDE-MIMO-MMA alternative is a modification of [102] implemented following [103].

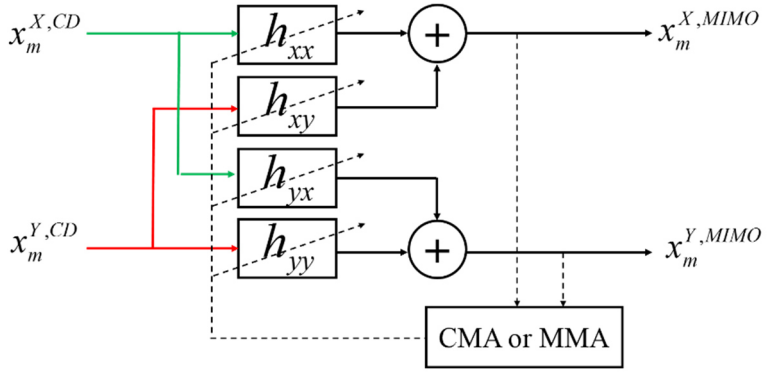

Figure 2.16 Structure of the adaptive time domain MIMO equalizer (TDE-MIMO).

Once the polarization components have been demultiplexed, a clock recovery and *slicing* algorithm is implemented. This block down-samples the signal to the symbol rate by selecting the sampling time with maximum mean power. The transmitted and received symbol clocks are in principle not synchronized. Since the ADC clock starts sampling at an arbitrary time, the obtained samples could not coincide with the optimum sampling point of the received waveform. The symbol clock recovery algorithm then finds the symbol clock frequency, selects the optimum sampling point and resamples the data accordingly. This algorithm is implemented following [104].

After clock recovery, a Carrier Frequency Recovery (CFR) technique is applied to estimate the frequency offset Δf_c between the carriers of the incoming signal and the CW signal generated by the local oscillator. The CFR used here is a blind algorithm based on [105]. Assuming a perfect compensation of CD and PMD, the received signal of each polarization component (*X* is used to exemplify) takes the following form

$$\tilde{x}_m^X = x_m^{X,MIMO} = \tilde{C}_m^X \exp\left(j2\pi\Delta f_m^{X,c} m T_s + \varphi_m^{X,n} \right) + \sqrt{P_m^{X,n}} \tag{2.72}$$

where $\tilde{C}_m^X$ is the sequence of received symbols, $\varphi_m^{X,n}$ is the digitized phase noise and $\sqrt{P_m^{X,n}}$ is the digitized amplitude noise, corresponding to the *X* polarization component. The term $\Delta f_m^{X,c} T_s$ is the discrete-time frequency offset for polarization *X* to be estimated. Following [106] the result of the operation $\left(x_m^{X,in}\right)^4$ can be decomposed as

$$\left(\tilde{x}_m^X\right)^{\mathrm{M}} = A^X \exp\left(j2\pi \mathrm{M}\Delta f_m^{X,c} m T_s + \mathrm{M}\varphi_m^{X,n} \right) + g_m^X \tag{2.73}$$

where M is the order of the modulation format if M-PSK is used or M = 4 if 16-QAM is set, $\mathrm{E}\{\cdot\}$ is the expected value operator, $A^X = \mathrm{E}\left\{\left(\tilde{C}_m^X\right)^{\mathrm{M}}\right\}$ is a constant value (independent of the data stream) and g_m^X is a discrete zero mean noise process. $\left(\tilde{x}_m^X\right)^{\mathrm{M}}$ is then a complex exponential with frequency $\mathrm{M}\Delta f_m^{X,c} T_s$ and constant amplitude embedded in a zero-mean additive noise. The $\Delta f_m^{X,c} T_s$ value can be estimated based on the maximization of the periodogram of $\left(\tilde{x}_m^X\right)^{\mathrm{M}}$, as reported in [105]. The same procedure is applied for the estimation of $\Delta f_m^{X,c} T_s$ for the *Y* polarization component. The CFR algorithm described before is independent of the modulation format.

The last DSP algorithm to apply to the signals is carrier phase estimation (CPE) and compensation. When M-PSK is employed, a Viterbi-Viterbi algorithm [107] implemented here according to [108] is used. Following a similar approach as for CFR (see Equation (2.73)), a M-PSK symbol data stream can be reduced to a single symbol through a $(\cdot)^{\mathrm{M}}$ operation, *i.e.* the phase modulation is removed from $\left(\tilde{x}_m^X\right)^{\mathrm{M}}$. A procedure to estimate $\varphi_m^{X,n}$ is shown in Figure 2.17. The estimation of the digitized phase noise is computed as follows

$$\tilde{\varphi}_m^{X,n} = \frac{1}{\mathrm{M}} \arg\left[\sum_{j=-N_{CPE}}^{N_{CPE}} \left(\tilde{x}_{m+j}^{X} \right)^{\mathrm{M}} \right] \tag{2.74}$$

where N_{CPE} is a parameter called here number of pre-symbols for CPE. The phase correction consist on subtracting the phase noise estimation $\tilde{\varphi}_m^{X,n}$ from the measured phase of $\tilde{x}_m^X$ for every sample, starting from sample $m = N_{CPE}$.

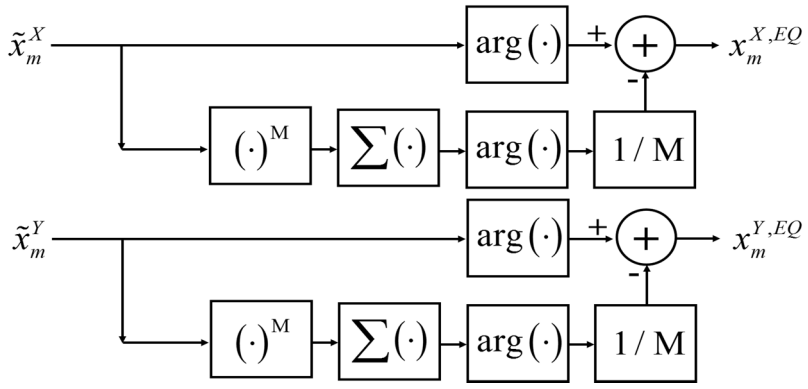

Figure 2.17 Carrier phase estimation and correction algorithm.

Due to the 1/M averaging operation, $\tilde{\varphi}_m^{X,n}$ will lie between $[-\pi/\mathrm{M}, +\pi/\mathrm{M}]$. When the trajectory of the physical phase exceeds this range, a phase jump of $\pm 2\pi / M$ occurs, resulting in a symbol error. To avoid this, $\tilde{\varphi}_m^{X,n}$ should be compared to the previous estimation $\tilde{\varphi}_{m-1}^{X,n}$. If the difference between adjacent two symbols is greater than $\pm\pi / M$, a phase of $\mp 2\pi / M$ should be added to the latter.

In the 16-QAM case, the phase modulation cannot be removed through a $(\cdot)^{\mathrm{M}}$ operation. However, the 16-QAM symbols could be treated as QPSK symbols of different classes, which is graphically represented in the constellation diagram shown in Figure 2.18. By separating the 16-QAM symbols in classes: Class I (symbols located in the inner and outer circles) and Class II (located in the central circle), and then applying the M-PSK CPE algorithm to each set of symbols after some extra adjustments, an algorithm for CPE and correction, proposed in [109], could be implemented. This algorithm is used in this work for phase correction of the16-QAM format.

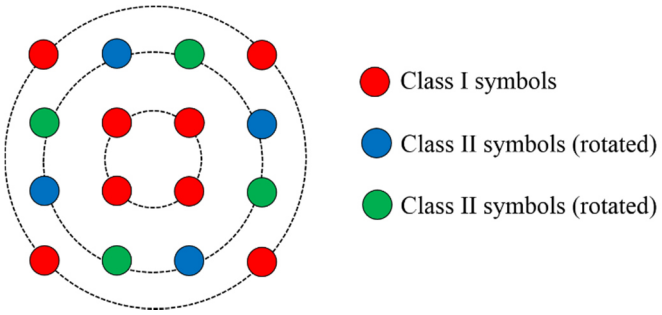

Figure 2.18 16-QAM constellation partitioning in different QPSK constellation classes

3. Chapter three: Experimental analysis of a WDM 4 x 23 Gb/s fronthaul system based on DSP-aggregated DDO-OFDM signals.

This Chapter presents a first application of a DDO-OFDM system. Many electrically generated OFDM signals are frequency division multiplexed (FDM) in the digital domain and the resulting aggregated signal drives an optical intensity modulator. After propagation through conventional SMF, the optical signal is directly detected, and frequency demultiplexed in the digital domain at the receiver. Each received OFDM signal is detected by its corresponding OFDM digital receiver.

The previously described system can be used as an optical transceiver that transforms a bit stream into an optical signal carrying a radio-waveform that is formed by multiple OFDM signals. Another attractive application of this system is mobile fronthauling, and this is actually the main rationale for this Chapter. Under this approach, each OFDM signal is assumed to be a mobile *baseband* radio signal (such as a long term evolution, or LTE, signal, actually corresponding to a baseband complex signal), which is aggregated to other radio signals. The resulting digitally aggregated bundle of signal is sent through a fiber channel. The signals are then de-aggregated and distributed to their corresponding antenna site after direct detection.

A FDM DDO-OFDM system used as an optical fronthaul segment of a mobile network architecture is experimentally analyzed in this Chapter. The digital FDM aggregation of radio waveform signals for optical fronthauling systems was first proposed by Liu in 2015 [29]. Building over this proposal, in this work we implemented a set of DSP techniques and some optimization procedures in order to increase the capacity, reach and performance of the analyzed fronthauling system in the downstream link direction. Sections 3.2.3 and 3.5 also present an original analysis on the upstream link direction. To the best of the author's knowledge, it is the first time that such upstream-transmission analysis is reported. Finally, a brief discussion about the analyzed system used as a high-speed optical transceiver for optical interconnection is performed in section 3.6. The experimental investigation presented in this Chapter has been performed in collaboration with the Optical Communications Group (OptCom) of the *Politecnico di Torino*, Italy, and the Photonics Group of the *Istituto Superiore Mario Boella* (ISMB), Italy.

3.1 State-of-the-art and context

In a traditional mobile network architecture, shown in Figure 3.1.a, a base station (BS), co-located at the antenna site, performs most of the signal processing related to the wireless protocols. A segment called backhaul links the BS and the edge of the core network.

Based on a centralization approach, a new mobile network architecture paradigm, shown in Figure 3.1.b, has emerged [28]. This paradigm is called C- Radio Access Network (C-RAN), where C could mean centralized or cloud. While the antenna site is highly simplified, most of the processing is performed by baseband units

(BBU) concentrated in a central office (CO). The CO is connected to the antenna sites (called Remote Radio Heads or RRHs) by segments of fibers called mobile fronthaul or optical fronthaul. C-RAN improves the performance and energy efficiency of a mobile network [29], and effectively enables massive MIMO, a key technology for next-generation 5G mobile networks [110]. Therefore, this new paradigm is going to be more and more common for LTE-Advanced. Moreover, it is perceived to be a must for next-generation 5G networks.

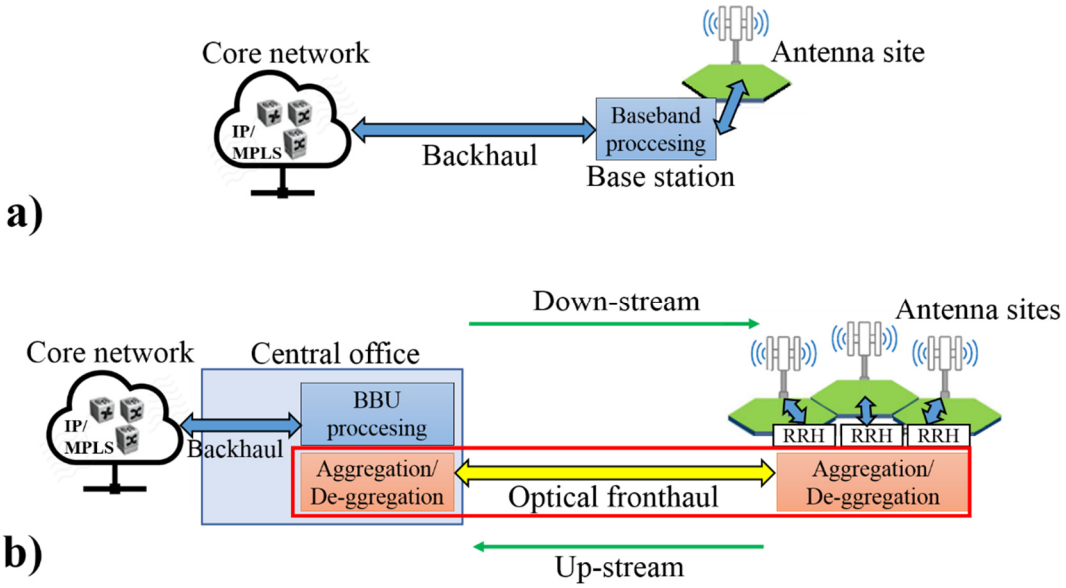

Figure 3.1 a) Traditional mobile network architecture, b) C-RAN mobile network architecture (adapted from [28]).

Today, optical fronthauling is already deployed for some LTE installations, and it is given for granted as a key enabler for future 5G networks. The current fronthauling technology, based on the so-called digitized radio-over-fiber (DRoF), using either the Common Public Radio Interface (CPRI) [111] or Open Base Station Architecture Initiative (OBSAI) de-facto standards, is suitable for today mobile network requirements. However, it does not scale well for future LTE-Advanced (LTE-A) and 5G networks since the bit rate to be transported may become exceedingly high. For instance, the actual traffic for the final user carried by one 20 MHz LTE signal is about 100 Mbit/s (when using 64-QAM). However, the transmission of this LTE signal using CPRI requires a bit rate of 921.6 Mb/s (without control words) [111]. Future 5G networks may require to transport several tens of these signals per RRH, for total bit rates that may easily go beyond the 100 Gb/s per RRH site. To overcome this bit-rate expansion problem in CPRI, alternative solutions for fronthauling have been proposed. One of the most competitive proposals is the DSP-aggregated fronthauling (DSP-AF) FDM architecture, originally proposed in [29]. The effectiveness of this technique is proven by its addition in an ITU-T document [112]. The key feature of DSP-AF is the transmission of many LTE-A (and in the future 5G) waveforms using an analogue radio-over-fibre approach, but taking advantage of a specific DSP-based aggregation/de-aggregation at the transmitter and receiver that, thanks to the well-known FFT and iFFT efficiency, allows to obtain both frequency *down*- and *up-conversion* and FDM aggregation with low latency and relatively low complexity using only DSP functionalities.

3.2 The analyzed architecture

A general FDM system operates based on the use of *RF-up/down-converters* and filters to distribute and select the aggregated channels in the frequency domain. Figure 3.2 shows a diagram of the frequency multiplexing of N_{ch} OFDM signals, digitally generated and *RF-up-converted* after pulse shaping. At the receiver side, the OFDM channels are distributed to their individual receivers. Each channel is then filtered by means of a band-pass filter (BPF), *RF-down-converted* and finally detected by its corresponding OFDM receiver. This aggregation/de-aggregation process is performed in the analogue domain. As discussed in section 1.2, for multi-carrier systems, the analogue frequency multiplexing of several channels requires a large number of oscillators, mixers and filters.

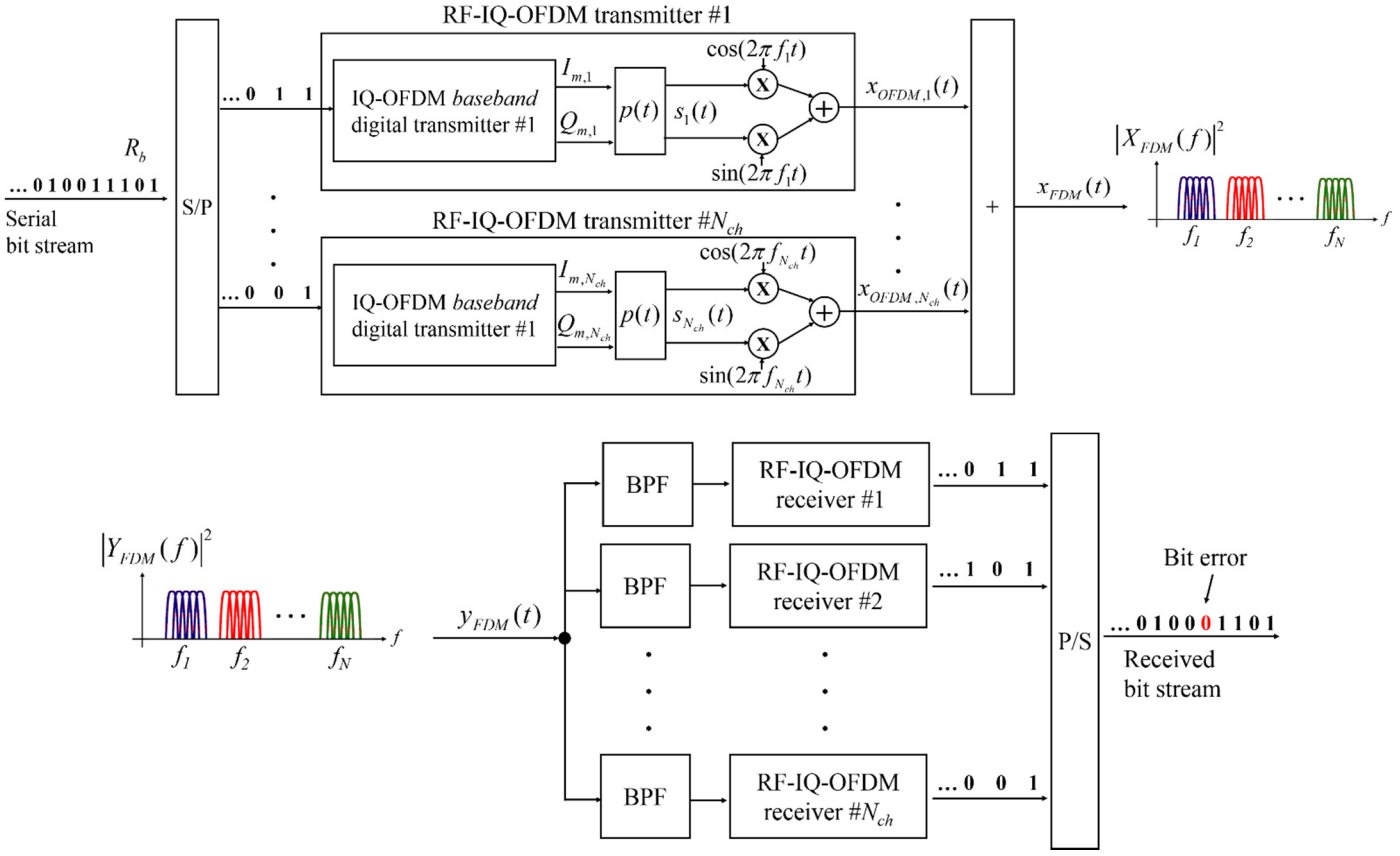

Figure 3.2 Generation/detection and analogue FDM aggregation/de-aggregation of a set of electrical OFDM channels. PBF: Band Pass Filter.

An alternative to overcome this problem is a DSP-based FDM aggregation/de-aggregation approach, shown in Figure 3.3. The OFDM signals are generated as complex *baseband* discrete-time domain signals $s_{m,i}$ (see section 1.3.1). Each digital OFDM channel is converted to the frequency domain in a block basis by means of a FFT of size N_a. The block of samples of each channel after FFT-transformation is mapped to the corresponding inputs of an iFFT of size M_a. This allocates the radio channels in their corresponding frequency band. To obtain a real-valued signal at the output of the iFFT, the Hermitian symmetry is enforced at its input,

as described in section 1.3.2. The discrete-time signal that outputs the iFFT of the FDM DSP-based aggregator is digital-to-analogue converted to finally obtain the $x_{FDM}(t)$ aggregated signal. The same approach is followed in reverse to implement the digital de-aggregation and detection stages, as observed in Figure 3.3.

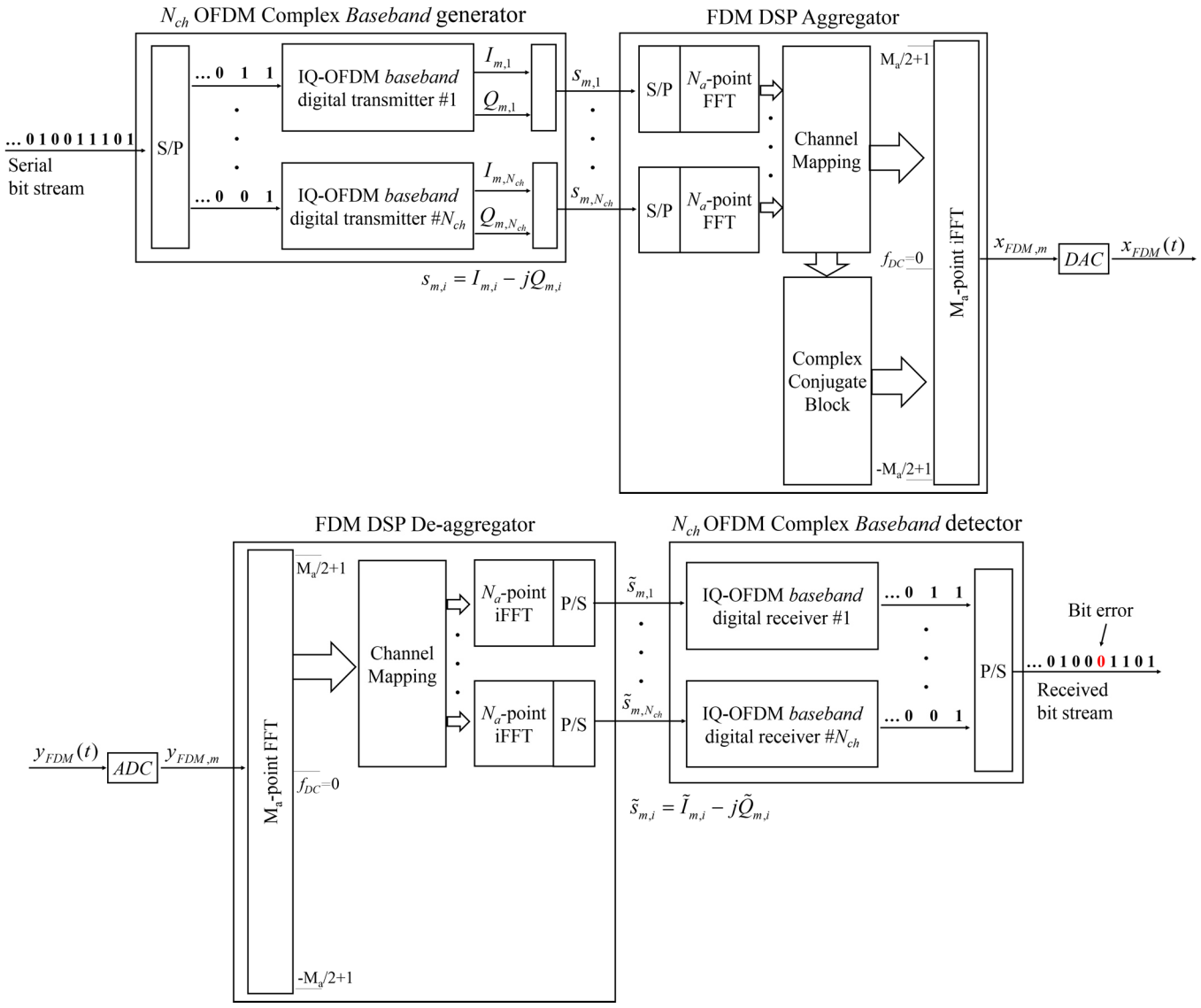

Figure 3.3 Complex *baseband* generation/detection and digital FDM aggregation/de-aggregation of a set of electrical OFDM channels.

The described architecture based on digital FDM was proposed in [29] for aggregation/de-aggregation of digitized complex *baseband* radio channels for optical fronthauling systems, and it is shown in Figure 3.4. The generation and detection of the radio channels is not performed by the fronthauling system, whose functions start with the aggregation of the channels, and end with their de-aggregation after the optical transmission. However, for our experimental purposes the radio waveforms are generated and detected as OFDM signals, as shown in Figure 3.3, emulating the generation and detection of LTE-A like signals.

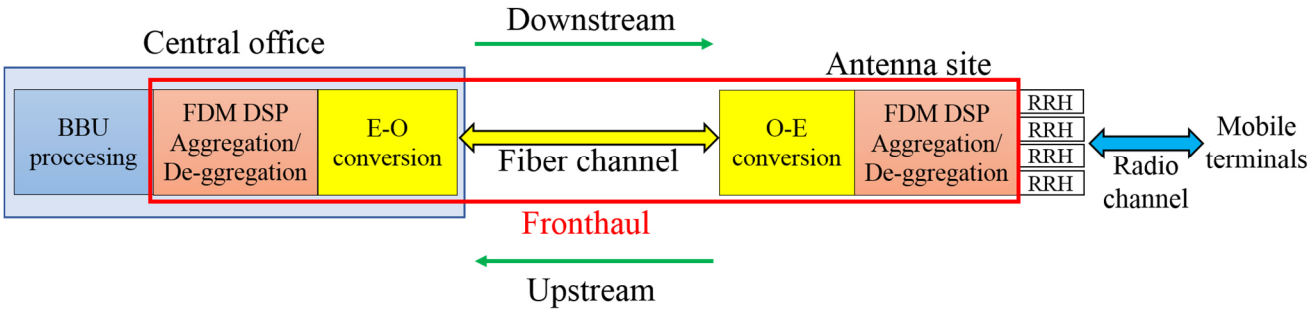

Figure 3.4 FDM DSP aggregation/de-aggregation based optical fronthauling architecture.

In a real-world implementation, the BBUs or the mobile terminals generates and detects the radio channels. In the downstream (DS) direction, the information flows from the BBUs to the RRH units that delivers the signals to the mobile terminals, while the opposite occurs in the upstream (US) direction, as illustrated in Figure 3.4. The BBUs already generate complex *baseband* digital radio signals, while the RRHs need to digitized and *RF-down-convert* the incoming analogue *passband* radio waveforms. A key difference in terms of the optical fronthauling operation exists between the DS and US situations. In the downstream case, all the radio channels generated and delivered to the fronthaul from the BBUs are "perfect" in terms of performance, *i.e.,* they are noiseless and have a same ideal performance of EVM = 0% (at least ideally, actually it can be higher due to DSP-related minor impairments). In contrast, in the upstream case, the radio channels that are delivered to the fronthaul from the RRHs are already affected by noise due to their propagation through the wireless channel from the mobile terminals to the RRHs. Moreover, in a general realistic situation, the SNR of the radio channels at the input of the fronthaul is not uniform, which results in a non-uniform EVM per channel distribution, as shown in the left-hand side graph of Figure 3.5. In both DS and US cases, the aggregation/de-aggregation processes, the E-O/O-E conversions and the transmission through the fiber channel affect the SNR level and thus the performance of the transmitted channels in a non-uniform sense. At the output of the fronthaul, however, all channels should outperform a given EVM target, irrespective of the transmission direction, as shown in the right-hand side graph of Figure 3.5. While in the DS direction the SNR penalty per channel is only caused by the fronthaul segment, in the case of the US direction, this penalty is caused by both the wireless and the fronthaul segments. This important difference could affect the procedure to optimize the EVM per channel, as it is analyzed in Sections 3.2.3 and 3.5.

In the following Sections the DSP techniques used here to counteract the impact of some deleterious impairments on the analyzed architecture are described.

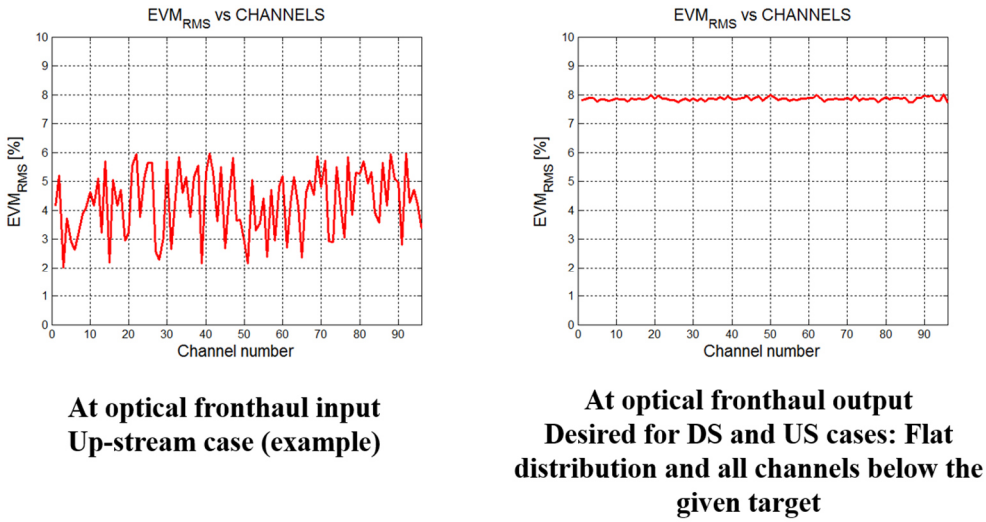

At optical fronthaul input
Up-stream case (example)

At optical fronthaul output
Desired for DS and US cases: Flat distribution and all channels below the given target

Figure 3.5 EVM per channel distribution for two different cases.

3.2.1 Clipping technique

Thanks to the central limit theorem, the FDM aggregated signal, being the sum of many OFDM properly *RF-up-converted* signals, has an amplitude distribution with a probability density function that is very well approximated by a Gaussian distribution; this is illustrated in Figure 3.6. Just as in many other similar situations, the signal should be amplitude clipped just before entering the transmitter DAC and/or before entering the receiver ADC. This reduces the PAPR of the signal, and thus counteract part of its effect in the quantization noise and the non-linear distortion. Here the clipping level is defined as

$$C_{clip} = \frac{V_{pp}}{\sigma_s} \tag{3.1}$$

and it is expressed in dB as

$$CLIP[dB] = 10\log\left(\frac{V_{pp}}{\sigma_s}\right) \tag{3.2}$$

where σ_s is the standard deviation of the DSP-aggregated and Gaussian-like signal, while V_{pp} is the peak-to-peak level of the clipped amplitude, *i.e.*, the signal after clipping assumes amplitude values in $\left[-\frac{V_{pp}}{2}, +\frac{V_{pp}}{2}\right]$.

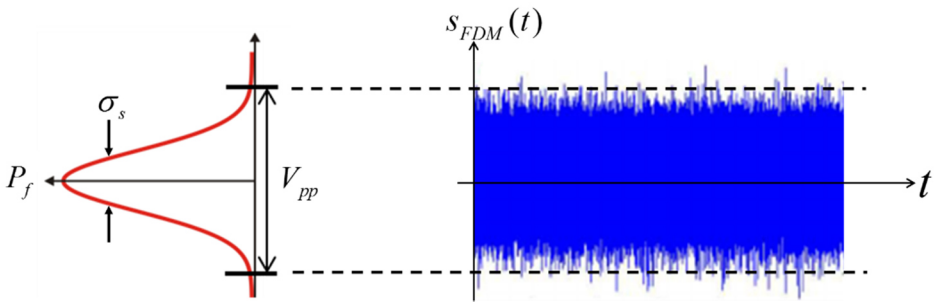

Figure 3.6 Scheme of the amplitude clipping of a FDM-OFDM signal.

The clipping level should be optimized in order to found the best trade-off between PAPR reduction and signal distortion impact on the system performance.

3.2.2 Non-linear MZM transfer function digital compensation technique

Due to the use of intensity modulation through a MZM and direct detection, the electrical received signal $i_{FDM,RX}(t)$ is proportional to the instantaneous power $P_{TX}(t)$ of the transmitted optical signal (see section 2.1.1) as follows

$$i_{FDM,RX}(t) \propto P_{TX}(t) \propto \frac{1}{2} + \frac{1}{2}\cos\left(\frac{\pi}{V_\pi}\left(x_{FDM}(t) + V_b\right)\right) \tag{3.3}$$

In order to reduce the non-linear distortion induced by the modulator when operated out of its linear region, as shown in Figure 3.7, the transmitted power (or the received current) can be linearized by applying the following transfer function to a digitized version of the $x_{FDM}(t)$ signal (or the $i_{FDM,RX}(t)$ signal) before it inputs the MZM modulator (or after it outputs the photodiode):

$$x_{m,corr} = \left(\frac{V_\pi}{\pi}\right)\arccos\left(2x_{m,FDM} - 1\right) - V_b \tag{3.4}$$

where the signal $x_{m,FDM}$ stands for either the DSP-aggregated signal before clipping (when the nonlinearity correction is applied at the transmitter side) or the signal after the photodiode and the ADC (when the correction is applied at the receiver). Since the $\arccos(\cdot)$ function might be difficult to implement in hardware and its domain is only defined from -1 to 1, a simpler nonlinearity correction technique implemented in the digital domain based on a cubic transformation of the type

$$x_{m,corr} = x_{m,FDM} + CF \cdot \left(x_{m,FDM} \right)^3 \tag{3.5}$$

is proposed here to compensate for the 3rd order term of the polynomial approximation of the function presented in Equation (3.4). The term *CF* is a correction factor that should be experimentally optimized in order to obtain a good match between the approximation given by Equation (3.5) and the actual inverse function given by Equation (3.4).

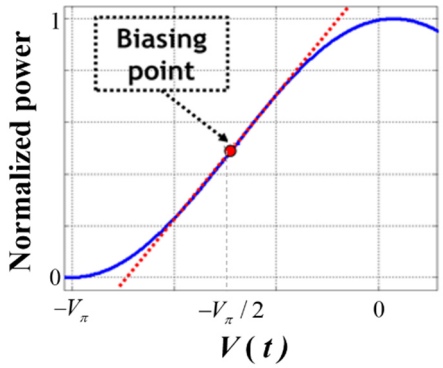

Figure 3.7 Normalized power transfer function of a MZM (in blue) and its linear adjust around the biasing point (in red).

3.2.3 Frequency pre-emphasis technique

The OFDM channels transmitted through the optical fronthauling arrive at the receiver with different SNR values, which results in a non-uniform EVM per channel distribution. A single-tap frequency domain equalizer, described in section 2.4.4, is used at each OFDM receiver to counteract the frequency response of the transmission system. However, the equalizer only acts at each individual channel. Therefore, the non-uniform EVM per channel distribution is maintained after single-tap individual equalization.

To compensate for this impairment, the aggregated channels are pre-emphasized at the transmitter side in order to obtain approximately the same EVM in all channels at the receiver side. The pre-emphasis technique consists on multiplying the amplitude of each OFDM complex digital waveform that conforms the x_{FDM} signal by a real coefficient k_i, where $i = 1,2,...,N_{ch}$, as shown in Figure 3.8. The k_i coefficients are globally optimizedin order to minimize the maximum EVM_i at the receiver side, which is equivalent to maximize the minimum received SNR_i. EVM_i and SNR_i stand for the EVM and SNR of the *i*-th OFDM channel, respectively. An algorithm to carry out this optimization is developed here as follows.

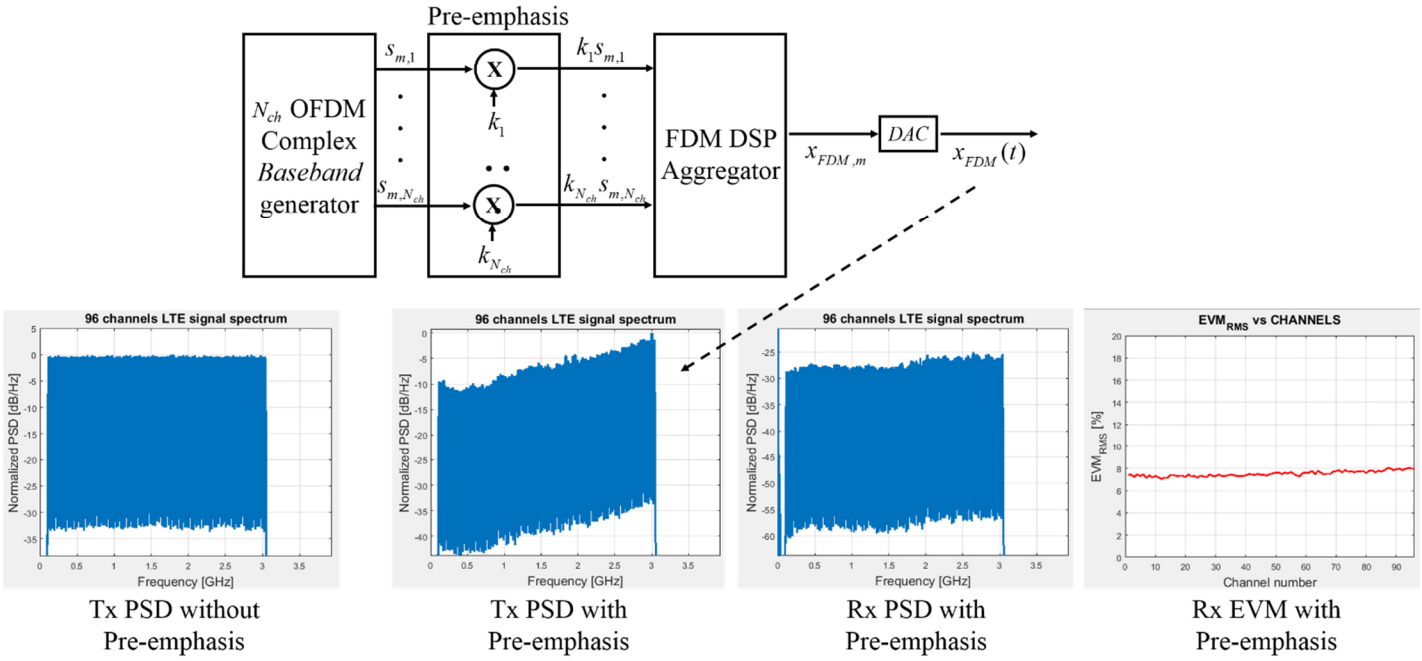

Figure 3.8 Pre-emphasis technique and power spectra of the transmitted signal with and without pre-emphasis, the received signal using pre-emphasis and its corresponding EVM per channel graph.

Let us analyze the upstream direction to generate the pre-emphasis algorithm. The downstream direction could then be considered a particular case of the upstream direction, as discussed later. A simplified model of the upstream transmission is shown in Figure 3.9. All the systems are considered linear, therefore, the propagation of each OFDM channels is assumed to be, as a first approximation, independent, in the sense that we neglect in this analysis nonlinearly generated crosstalk among channels.

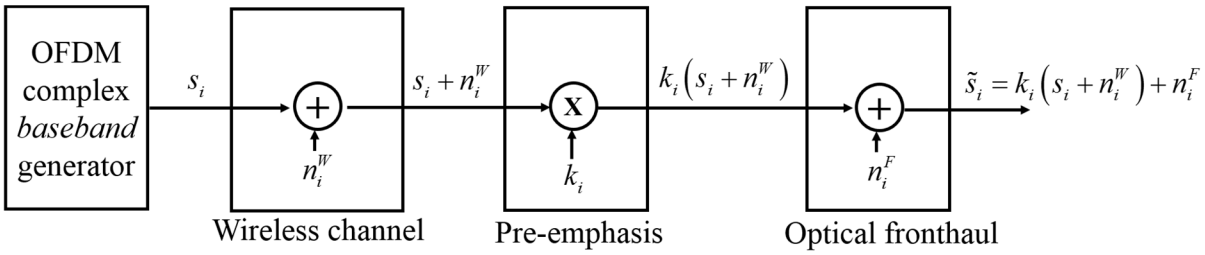

Figure 3.9 Simplified model of the transmission in the upstream direction

According to this model, the *i*-th OFDM signal at the output of the fronthaul is

$$\tilde{s}_i = k_i\left(s_i + n_i^W\right) + n_i^F \tag{3.6}$$

where s_i is the OFDM signal generated for the *i*-th mobile terminal, and n_i^W , n_i^F are noise signals, modelled as additive WGN that emulates the noise addition to s_i after transmission through the wireless channel and the optical fronthaul, respectively. The SNR at the output of the fronthaul is evaluated as follows

$$\mathrm{SNR}_i^{out} = \frac{k_i^2 P_{s,i}}{k_i^2 P_{W,i} + P_{F,i}} = \frac{1}{\frac{P_{W,i}}{P_{s,i}} + \frac{1}{k_i^2}\frac{P_{F,i}}{P_{s,i}}} \tag{3.7}$$

where $P_{s,i}$, $P_{W,i}$ and $P_{F,i}$ are the average power of the signals s_i , n_i^W and n_i^F , respectively. Equation (3.7), can be expressed as

$$\left(\mathrm{SNR}_i^{out}\right)^{-1} = \left(\mathrm{SNR}_i^{W}\right)^{-1} + \left(k_i^2 \cdot \mathrm{SNR}_i^{F}\right)^{-1} \tag{3.8}$$

where $\mathrm{SNR}_i^W = \frac{P_{s,i}}{P_{W,i}}$ and $\mathrm{SNR}_i^F = \frac{P_{s,i}}{P_{F,i}}$, are the SNR at the output of the wireless channel and the optical fronthaul, respectively, when they are considered as independent blocks with an input signal s_i . Since both, the wireless channel and the optical fronthaul, are modeled as additive WGN channels, then the SNR and the root-mean-square EVM of the signal at the output of each block are related as [113]

$$\mathrm{SNR}_i = \frac{1}{\left(\mathrm{EVM}_i\right)^2} \tag{3.9}$$

Therefore, Equation (3.8) can be express in terms of EVM as follows

$$\left(\mathrm{EVM}_i^{out}\right)^2 = \left(\mathrm{EVM}_i^{W}\right)^2 + \left(k_i^{-1} \cdot \mathrm{EVM}_i^{F}\right)^2 \tag{3.10}$$

then

$$k_i = \sqrt{\frac{\left(\mathrm{EVM}_i^{F}\right)^2}{\left(\mathrm{EVM}_i^{out}\right)^2 - \left(\mathrm{EVM}_i^{W}\right)^2}} \tag{3.11}$$

This last expression indicates a useful way to compute coefficients k_i for a given set of EVM_i^F, EVM_i^W and EVM_i^{out}. The last two terms are the EVM of the *i*-th OFDM signal at the output of the wireless channel and at the output of the optical fronthaul, respectively, and they can be measured directly at the fronthaul system. The term EVM_i^F is the EVM that would be obtained at the output of the fronthaul segment if only the signal s_i was transmitted through it. This term could not be measured directly, but could be estimated indirectly. In particular, for a given setup, a first transmission in which all coefficients k_i are equal to one is performed (no pre-emphasis situation) and then the resulting EVM_i^{out}, named $\mathrm{EVM}_i^{out,no-pre}$, is measured. The EVM_i^F is then computed as follows

$$\mathrm{EVM}_i^F = \sqrt{\left(\mathrm{EVM}_i^{out,no-pre}\right)^2 - \left(\mathrm{EVM}_i^W\right)^2} \tag{3.12}$$

Note that the fiber channel is assumed to be static, then this estimated term is considered fixed for a given setup. If the fronthaul setup changes, this procedure should be repeated. By substituting Equation (3.12) into Equation (3.11) we obtain

$$k_i = \sqrt{\frac{\left(\mathrm{EVM}_i^{out,no-pre}\right)^2 - \left(\mathrm{EVM}_i^W\right)^2}{\left(\mathrm{EVM}_i^{out}\right)^2 - \left(\mathrm{EVM}_i^W\right)^2}} \tag{3.13}$$

The objective of the pre-emphasis technique is to minimize the maximum EVM_i^{out}. An alternative to solve this optimization problem is to enforce a uniform EVM per channel distribution, *i.e.,* enforcing EVM_i^{out} to be constant, as follows

$$\mathrm{EVM}_i^{out} = \mathrm{EVM}_{\mathrm{target}}^{out} \qquad \forall i = 1, 2, ..., N_{ch} \tag{3.14}$$

Under this condition, the k_i coefficients are evaluated by means of the following expression

$$k_i = \sqrt{\frac{\left(\mathrm{EVM}_i^{out,no-pre}\right)^2 - \left(\mathrm{EVM}_i^W\right)^2}{\left(\mathrm{EVM}_{\mathrm{target}}^{out}\right)^2 - \left(\mathrm{EVM}_i^W\right)^2}} \tag{3.15}$$

The signal $x_{FDM}(t)$ at the output of the FDM aggregator when the pre-emphasis technique is applied now becomes

$$x_{FDM}(t) = \sum_{i=1}^{N_{ch}} k_i \cdot x_{OFDM,i}(t) = \sum_{i=1}^{N_{ch}} k_i \cdot \mathrm{Re}\left\{ s_i(t) \exp\left(j2\pi f_i t \right) \right\} \tag{3.16}$$

It is clear that the value of $\mathrm{EVM}_{\mathrm{target}}^{out}$, which is directly involved in the evaluation of the coefficients k_i, is not a free parameter. Instead, it is constrained to maintain the peak to peak amplitude of the signal $x_{FDM}(t)$ between the voltage range in which the MZM is driven. Since the signal $x_{FDM}(t)$ is clipped before driving the MZM, its actual V_{pp} is related to its variance before clipping as $V_{pp} = C_{clip} \cdot \sigma_s$ (see Equation (3.1)). Therefore, the $\mathrm{EVM}_{\mathrm{target}}^{out}$ value is constrained to maintain the variance of the signal $x_{FDM}(t)$ equal before and after pre-emphasis. Since the $x_{OFDM,i}(t)$ signals are properly modeled as independent random variables that are Gaussian distributed, the variance of $x_{FDM}(t)$ can be evaluated as

$$\sigma_{FDM}^2(t) = \sum_{i=1}^{N_{ch}} k_i^2 \cdot \sigma_{OFDM,i}^2 \tag{3.17}$$

If the variance of all OFDM signals is assumed to be the same, *i.e.*, $\sigma_{OFDM,i}^2 = \sigma_{OFDM}^2$ (a very reasonable assumption in the fronthauling scenario, since all OFDM channels can be properly normalized in DSP), then the variance of signal $x_{FDM}(t)$ can be computed as follows

$$\sigma_{FDM}^2(t) = \sigma_{OFDM}^2 \sum_{i=1}^{N_{ch}} k_i^2 \tag{3.18}$$

Before the pre-emphasis block, in our proposed equalization procedure, all the k_i coefficients are equal to one, therefore the variance before pre-emphasis is evaluated as follows

$$\sum_{i=1}^{N_{ch}} k_1^2 = N_{ch} \quad \Rightarrow \quad \sigma_{FDM}^2(t) = N_{ch} \cdot \sigma_{OFDM}^2 \tag{3.19}$$

In order to preserve the variance of $x_{FDM}(t)$ as the one before applying the pre-emphasis block, the choice of $\mathrm{EVM}_{\mathrm{target}}^{out}$ is constrained to satisfy the following (normalized with respect of N_{ch}) condition:

$$G_{US}(\mathrm{EVM}_{\mathrm{target}}^{out}) = \frac{1}{N_{ch}}\sum_{i=1}^{N_{ch}} k_i^2 = \frac{1}{N_{ch}}\sum_{i=1}^{N_{ch}}\left(\frac{\left(\mathrm{EVM}_i^{out,no-pre}\right)^2 - \left(\mathrm{EVM}_i^{W}\right)^2}{\left(\mathrm{EVM}_{\mathrm{target}}^{out}\right)^2 - \left(\mathrm{EVM}_i^{W}\right)^2}\right) = 1 \tag{3.20}$$

The previous equation is a very important result in the channel equalization procedure; to the best of our knowledge, this equalization procedure was never proposed before in the literature. The practical application of this equation will be practically explained in section 3.5 on experimental upstream transmission demonstration.

While in the upstream case the OFDM complex *baseband* generator block, shown in Figure 3.9, emulates the mobile terminals, in the downstream case this block emulates the BBUs. Just after the BBUs, the optical fronthaul follows in the downstream direction, *i.e.*, the wireless channel is not in the middle of them. However, all the previous analysis carried out for the upstream case are still valid for the downstream one if considering that $\mathrm{EVM}_i^{W} = 0$. Then, for the downstream situation, Equations (3.15) and (3.20) simplify to:

$$k_i = \frac{\mathrm{EVM}_i^{out,no-pre}}{\mathrm{EVM}_{\mathrm{target}}^{out}} \tag{3.21}$$

and

$$G_{DS}(\mathrm{EVM}_{\mathrm{target}}^{out}) = \frac{1}{N_{ch}}\sum_{i=1}^{N_{ch}} k_i^2 = \frac{1}{N_{ch}}\sum_{i=1}^{N_{ch}}\left(\frac{\mathrm{EVM}_i^{out,no-pre}}{\mathrm{EVM}_{\mathrm{target}}^{out}}\right)^2 = 1 \tag{3.22}$$

The functionality of the proposed pre-emphasis technique for the downstream directions is experimentally evaluated in section 3.4.

3.2.4 Spectral EVM estimation

In order to measure the EVM of each channel, at the input or output of the fronthaul, a full OFDM receiver for each of the channels is needed. While in our laboratory experiments this procedure is performed off-line via Matlab® and it is thus not problematic, in a real-world fronthaul implementation this would indeed be exceedingly complex to be carried out in the RRH units.

For this reason, a simpler approach in which the EVM_i values are estimated from measuring the SNR_i on all channels without passing from the EVM_i evaluation at the OFDM receivers is here proposed. In this approach, named here spectral EVM estimation, a direct SNR_i measurement is performed based on the parameters available in the DSP that performs channel aggregation/de-aggregation at the transmitter/receiver. In particular, each SNR_i is obtained by averaging the values at the output of the FFT that has to be performed for channel aggregation/de-aggregation, which is thus used as a form of "embedded" electrical spectrum analyzer, without requiring any further DSP complexity. This is shown in Figure 3.10. The EVM values are then estimated by means of the measured SNR_i values using Equation (3.9).

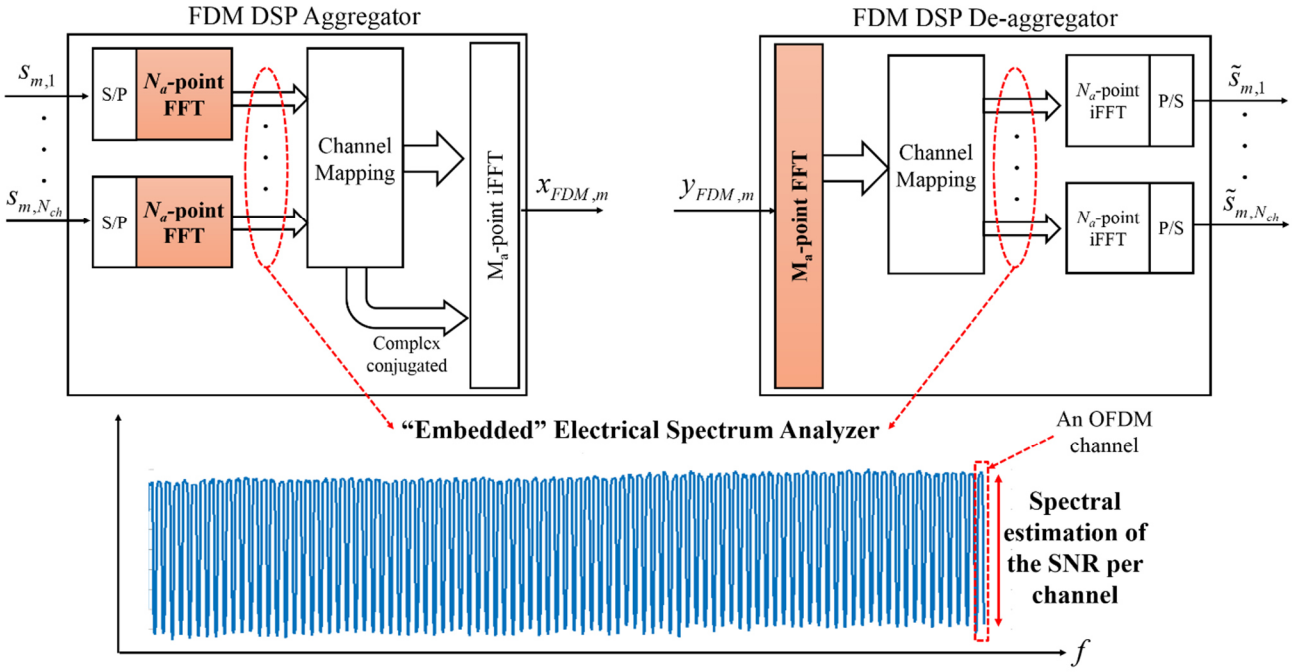

Figure 3.10 Scheme of the SNR estimation technique aided by the electrical spectrum analyzer "embedded" into the digital FDM aggregator/de-aggregator.

Unfortunately, by testing our proposed spectral EVM estimation method, we found a significant disagreement between the spectrally estimated and the actual EVM_i values measured using OFDM receivers. We thus tried to turn off some channels and repeat the SNR measurements. The corresponding power spectrum at the output of the de-aggregator's FFT is plotted in Figure 3.11. A mismatch between the noise levels measured when a channel is turned on and off was found. As depicted in Figure 3.11, the actual noise level of the channels is hidden by cross-talk. This noise level mismatch is reflected in the referred EVM disagreement between the two EVM measurement techniques.

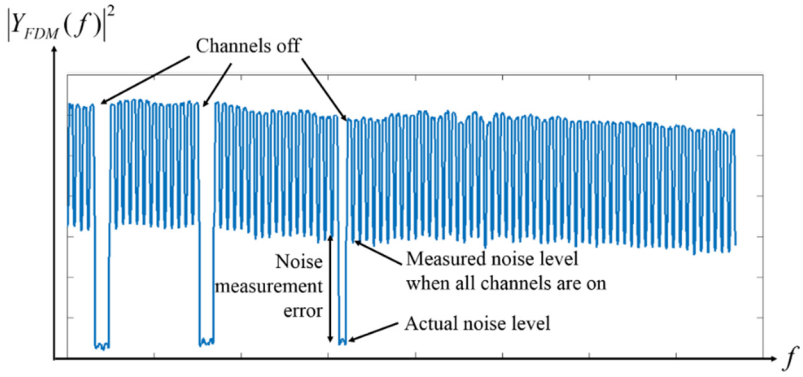

Figure 3.11 Power spectrum obtained from the electrical spectrum analyzer "embedded" into the digital FDM de-aggregator when some channels are turned off.

To overcome this limitation, one channel can be turned off at a time in a proper initial "bootstrap" phase of the optical fronthauling system, so the corresponding actual noise level of that channel can be measured and stored. This operation should be performed periodically before sending the data. The optical fronthaul system is assumed to be static under that period. Once having the complete noise per channel vector stored, the SNR can be estimated by means of the actual power of the signal per channel (measured at real-time) and its corresponding noise value (stored). If the fronthaul setup changes, the procedure to measure and store the corresponding noise per channel vector must be repeated. Figure 3.12 shows EVM per channel graphs for three experimental tests in which the EVM values obtained by using the spectral estimation technique and the ones measured using full OFDM receivers are compared. It could be observed that the difference between the results obtained using both procedures is negligible. While in a real-world fronthauling system our proposed spectral EVM estimation approach is simpler and faster to be performed, in our experimental tests the opposite occurs due to the lack of a real-time DSP. Since both approaches deliver similar results, the EVM-based measurement that relies on full OFDM decoding will be used in our experiments unless otherwise stated.

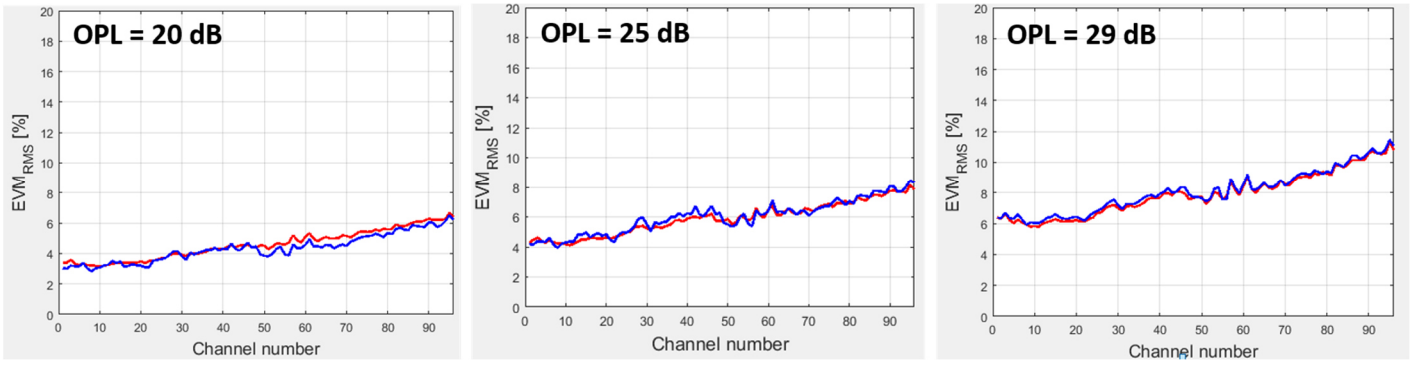

Figure 3.12 EVM per channel graphs for three fronthauling conditions (Optical Path Loss (OPL) = 20, 25 and 29 dB respectively). In blue: obtained by spectral estimation. In red: measured using OFDM receivers.

3.3 Experimental setup

The experimental setup for our emulation of a DSP-aggregated fronthauling system is shown in Figure 3.13, where both the downstream or upstream directions of a fronthauling architecture can be set. At the transmitter side, the same MZM is used to modulate the CW carrier(s) generated by the laser(s) source(s) for both single wavelength and multi-wavelength experiments. The MZM is driven (at its 3-dB point) by a FDM signal, which is off-line generated in Matlab and stored in a Tektronix Arbitrary Waveform Generator (AWG). The AWG is characterized by an analog bandwidth of 20 GHz, a vertical resolution of 10 bits and a sampling rate of 50 GS/s. Depending on the particular experiment, N_{ch} = 96 or 192 *baseband* radio channels are generated and then digitally aggregated using the approach proposed in [29] to generate the $x_{FDM}(t)$ signal. Each radio waveform is an OFDM signal using 64-QAM as digital modulation format and generated with a 30.72 MHz sampling rate, according to the specification of a 20 MHz LTE-A signal with a raw bit rate of 120 Mb/s. The resulting spectral separation between adjacent radio waveforms is exactly set at 30.72 MHz, so that the total electrical spectrum is approximately equal to 3 GHz or 6 GHz if 96 or 192 radio channels are used, respectively. This choice allows a very straightforward DSP aggregation procedure as previously explained. The aforementioned resulting signal bandwidths let us envision that a DML, instead of the external MZM, would not introduce any significant distortion to the overall performance of the system. The optical signal at the output of the modulator is amplified using an erbium doped fiber amplifier (EDFA). The transmitted output optical power (P_F) is set to +9 dBm. The transmitter output signal is launched into 25 km of SMF followed by a variable optical attenuator (VOA) for spanning different values of optical path loss (OPL). At the receiver side, an optical filter selects the desired optical channel when the WDM configuration is used. Then, an avalanche photodiode (APD) directly detects the signal. We used an APD that is today typical for next-generation Passive Optical Network architecture (such as XGS-PON or NG-PON2) that, thanks to their high sensitivity requirements, cannot use a standard PIN-based photodiode. It is followed by a transimpedance amplifier and a real-time oscilloscope (RTO) which performs analogue-to-digital conversion and stores the resulting samples. The EVM calculation is carried out in Matlab by applying the de-aggregating post-processing algorithm on the signals stored by the RTO, and then demodulating each OFDM signal. After applying the single-tap frequency domain equalizer described in section 2.4.4, the EVM per channel is obtained as the average over all the OFDM subcarriers.

In a previous work [113] on the same topics, it was found that the MZM should be operated over its maximum dynamic range in order to improve the system performance for high OPL values. This range is equal to the V_π of the modulator (see section 2.1.1). The amplitude of the driving signal is then set accordingly. This in turn results in non-linear distortion, which is counteracted by using the non-linear compensation technique described in section 3.2.2. The clipping technique to decrease the PAPR value and the pre-emphasis technique to minimize the maximum received EVM, described in sections 3.2.1 and 3.2.3, respectively, are also implemented.

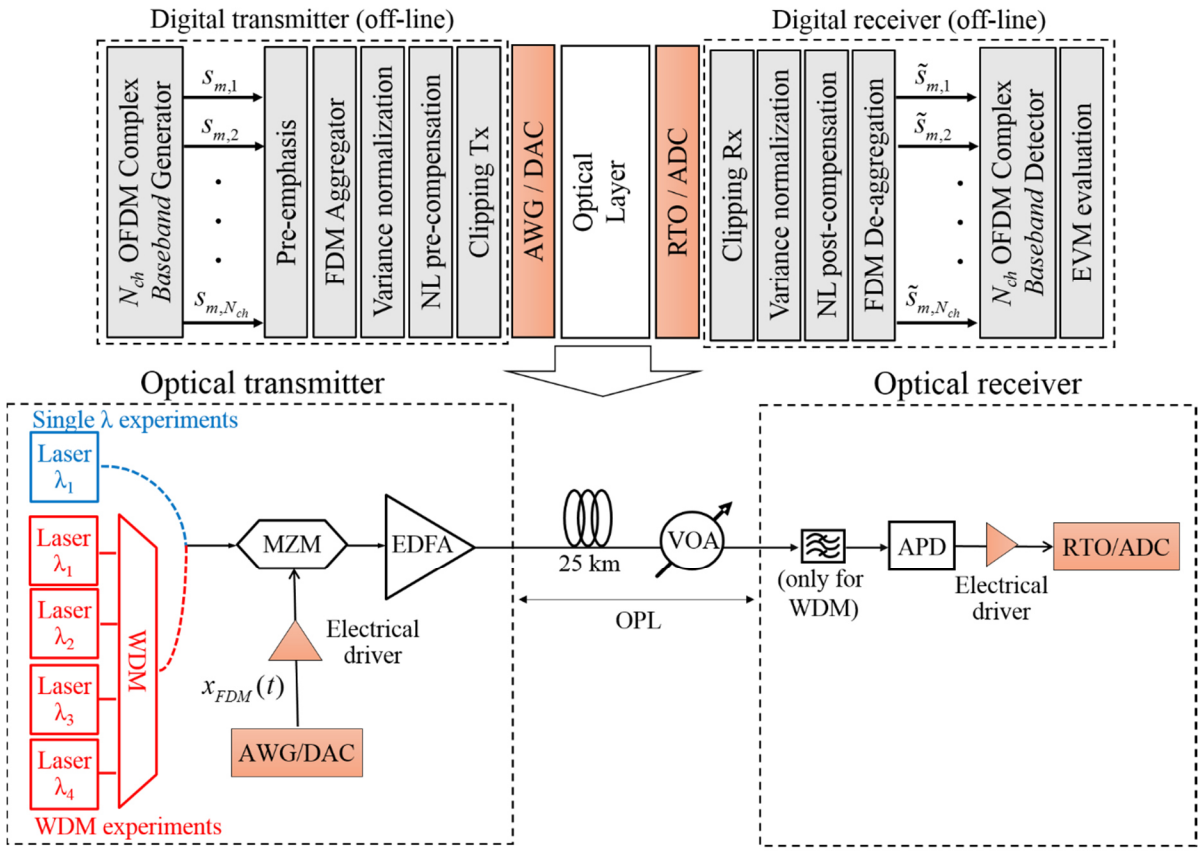

Figure 3.13 Experimental setup of the analyzed fronthaul system

3.4 Downstream optimization results

The focus of this section is the analysis of several physical layer optimization procedures of the fronthauling system in the downstream direction. The key target of this analysis is to achieve a low EVM at the output of the optical fronthauling part thanks to DSP-based optimization at the transmitter and receiver sides. We believe that dimensioning the optical segment to a low EVM target is a must if the impact of the optical fronthauling segment on the wireless part needs to be small, as it is discussed with more detail in [113]. For instance, the European Telecommunications Standards Institute (ETSI) standard requires EVM ≤ 8% for LTE-A 64-QAM signals [114]. This EVM target is specified by ETSI at the transmitter antenna connector so that, when using downstream optical fronthauling, the EVM target should be specified with at least some margin, for instance, for the small impairments introduced to the wireless frequencies by the electrical *RF-up-conversion* that is implemented in the RF electronics in the RRH units. Therefore, some optimization procedures in combination with impairment compensation techniques, which can be carried out in the DSP domain (at either the transmitter or receiver sides) with small complexity to minimize the EVM obtained at the output of the optical fronthauling segment, are implemented.

The functionality of the compensation techniques described in section 3.2 in combination with optimization procedures is experimentally demonstrated on a transmission system that uses N_{ch} aggregated radio

waveforms, each emulating a 20-MHz LTE-A signal. After implementing the referred optimizations, the EVM as a function of the system OPL has been evaluated, improving the results of a previous work reported in [113], where these optimizations were not realized.

3.4.1 Results for single-wavelength transmission of 96 radio channels

The first round of optimizations focuses on the transmitter side: due to the frequency response of the full opto-electonic system over the used 3 GHz band, the received 96 channels have different amplitudes and thus would give significantly different EVM on the received channels. Therefore, the transmitted amplitudes in the DSP domain were equalized using the approach described in section 3.2.3. The results are shown in Figure 3.14 for two different OPL values (25 and 29 dB). The black curve (with squares) reports the received EVM without any amplitude pre-emphasis equalization, *i.e.,* $\mathrm{EVM}_i^{out,no-pre}$ in Equations (3.21) and (3.22), showing an unacceptable variation among channels. For instance, a variation from EVM = 6% at lower frequencies to 11% at higher frequencies is shown in Fig. 2b. The pre-emphasis coefficients (k_i) to equalize the received SNR, and thus the EVM, are evaluated using Equation (3.21), where the $\mathrm{EVM}_{\mathrm{target}}^{out}$ value is computed using Equation (3.22). The blue curve (with circles) reports the EVM_i^{out} when the amplitude pre-emphasis equalization takes place. In both OPL cases, the functionality of the pre-emphasis technique is demonstrated, reducing the maximum EVM value from 8.3% and 11.5% to 6% and 7.5% for OPL = 25 and 29 dB, respectively. The effect of the pre-emphasis equalizer on flattening the EVM per channel distribution can also be observed.

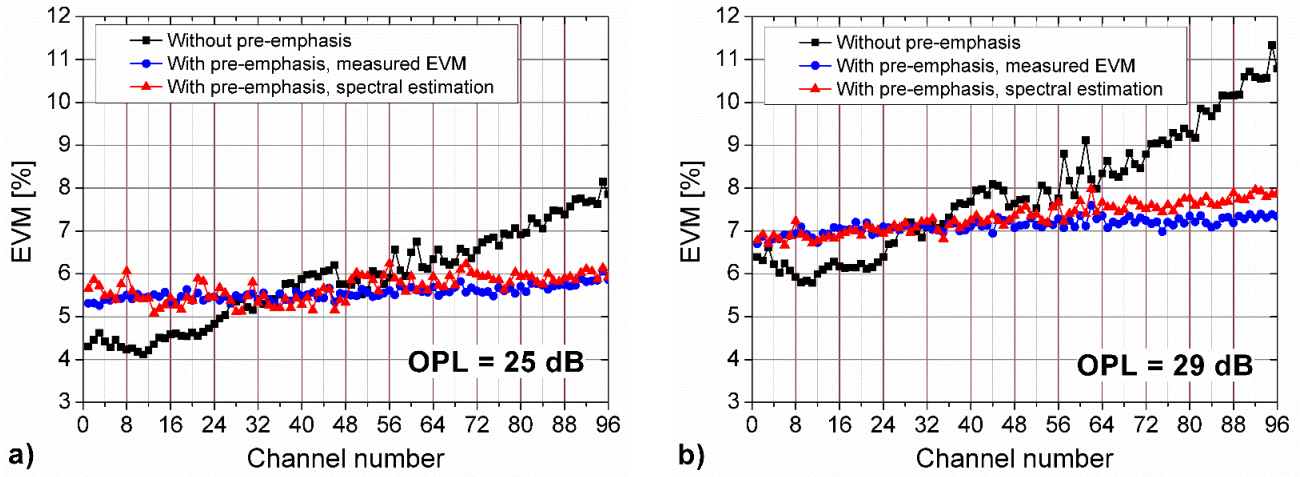

Figure 3.14 EVM of the 96 OFDM channels at a) 25 dB and b) 29 dB of OPL before and after equalization.

The EVM values presented in the blue curve of Figure 3.14 were measured on all channels at the output of a full OFDM receiver for each of the 96 channels. As discussed in section 3.2.4, this operation would likely be very complex in the RRH of a fronthauling architecture. For this reason, EVM results using our proposed simpler spectral estimation approach, described in section 3.2.4, are also presented with the red curves (with triangles) in Figure 3.14. As expected, no significant degradation between the blue and red curves can be observed. Moreover, in all cases the maximum EVM is maintained below the 8% target. As explained in section

3.2.4, since both approaches deliver similar results but the EVM measurement aided by OFDM receivers is simpler and faster when an off-line DSP approach is used, this alternative method will be used in the results reported in the rest of this Chapter. However, to the best of our knowledge, the spectral EVM estimation technique proposed and demonstrated here is a novel and useful contribution for real-time DSP implementations that enables the possibility of using equalization and compensation techniques that require a fast channel performance estimation, as the pre-emphasis and MZM nonlinearity compensation algorithms proposed and used here.

The next optimization, performed at the transmitter side, was related to the clipping and the nonlinearity compensation techniques, described in sections 3.2.1 and 3.2.2, respectively. The OPL is set to 15 dB, since for low OPL values the effect of nonlinear distortion in the performance is expected to be more notable as compared to the effect of SNR degradation. The average EVM was evaluated (over the 96 OFDM channels) as a function of both the clipping level ($CLIP_{TX}$), set at the AWG DAC following Equation (3.2), and the nonlinearity correction factor (CF_{TX}) of the pre-distortion function, given by Equation (3.5), that was imposed to the signal loaded in the AWG. The results are summarized in the contour graph shown in Figure 3.15.a. Thanks to this optimization procedure, the average EVM is reduced one order of magnitude, from about 4.7% (with no clipping and no correction factor) to about 3.7%.

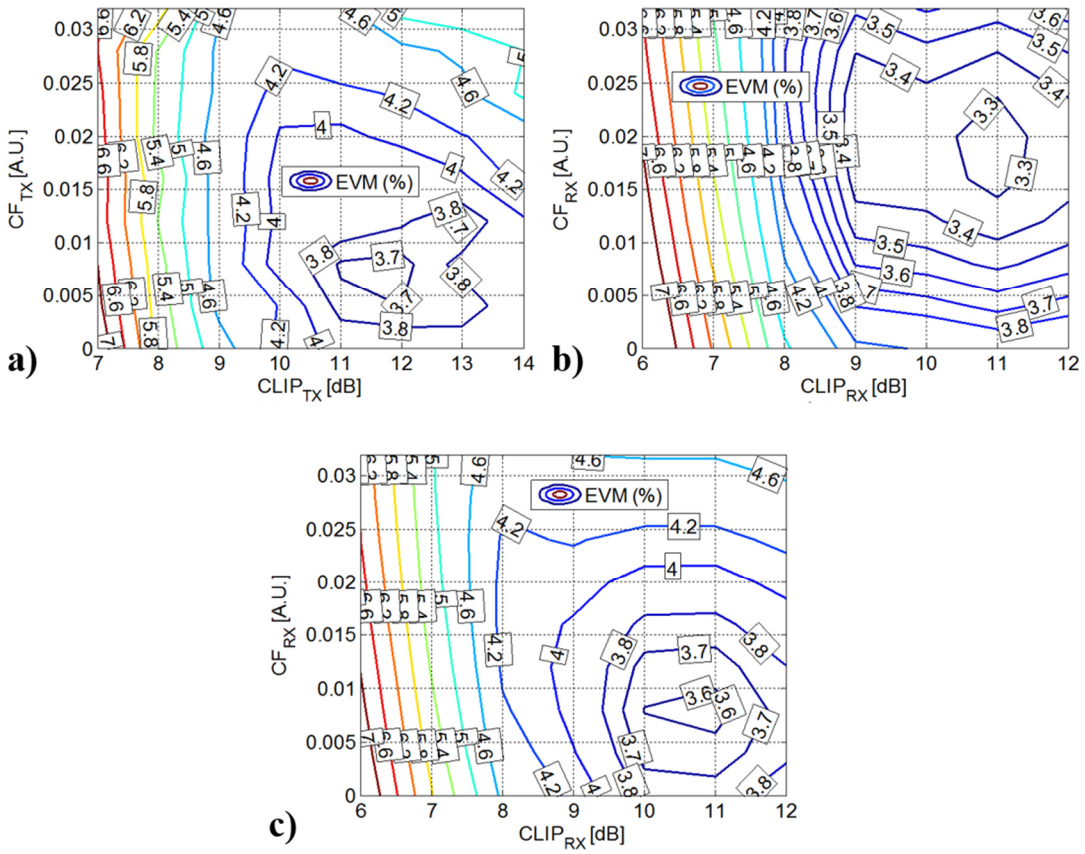

Figure 3.15 Average EVM of the 96 OFDM channels at 15 dB of OPL as a function of the clipping level and the compensation of the nonlinearity of the MZM electro-optic characteristic performed at (a) the transmitter side; (b) the receiver side; (c) at the receiver side setting the optimum parameters at the transmitter side.

The same optimization is then repeated at the receiver side, again at 15 dB of OPL. This time, the clipping level ($CLIP_{RX}$) is adjusted at the RTO ADC, while the nonlinearity correction factor (CF_{RX}) of the post-distortion technique is imposed at the receiver DSP stage. The results are presented in the contour graph shown in Figure 3.15.b, allowing us to assert that the receiver optimization provides better results than the transmitter one, since the lowest average EVM obtained in the best case is reduced to about 3.3%. When the nonlinear distortion compensation is applied at the transmitter side, the SSII generated at the modulator get reduced, which should be reflected in a system performance improvement. In contrast, when the nonlinear compensation is carried out at the receiver side, these SSII products are no longer reduced. Therefore, a better performance should be achieved applying the technique at the transmitter side, which anyway does not correspond with our findings. A hypothesis to explain this fact is outlined as follows. Both the clipping and the cubic transformation techniques employed to reduce nonlinear distortion end up modifying the spectrum of the signal, which can affect the performance of the system. This phenomenon could become strengthened in presence of CD and modulation chirp, resulting in a worse performance when the technique is applied at the transmitter side. According to our obtained results, the effect of spectrum distortion is then more pronounced that the effect of the SSII in the analyzed system.

The combination of both optimization alternatives was also investigated: the optimum parameters ($CLIP_{TX}$ = 12 dB and CF_{TX} = 0.008) are set at the transmitter side and the previous receiver optimization procedure is repeated. The results are depicted in Figure 3.15.c, from which it can be observed that the improvement with respect to the transmitter-only optimization case is minimal. By comparing the results of the three presented optimization scenarios, it can then be concluded that the receiver optimization provides the best results in terms of EVM improvement.

Finally, the EVM was evaluated as a function of the system OPL under three different conditions: i) without any transmitter or receiver optimization, ii) setting the parameters ($CLIP_{RX}$ = 11 dB and CF_{RX} = 0.02) resulting from the receiver optimization performed at 15 dB of OPL, and iii) evaluating and setting the best $CLIP_{RX}$ and CF_{RX} parameters for each OPL condition. The results are summarized in Figure 3.16, in which a wide range of OPL values, from 15 dB (which would be adequate for point-to-point fronthauling solutions) up to the OPLs required by PON standards, are spanned.

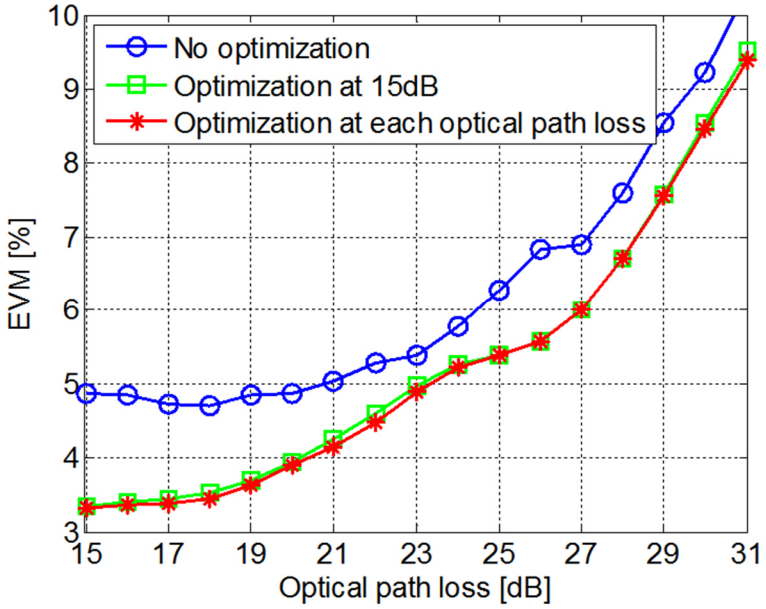

Figure 3.16 Comparison of the EVM vs. the OPL obtained with different optimization procedures.

Figure 3.16 depicts the main results of this section, showing how the performed optimization is valid over the full considered OPL range. In particular, it demonstrates the possibility of transmitting up to 29 dB, value required by PON in class N1, while satisfying the 8% ETSI requirements on 64-QAM. Moreover, we observe that the receiver's parameters optimization can be performed at any OPL value, since the difference between the two optimized curves is negligible. It is important to remark that, as expected, the combination of the clipping and nonlinear compensation techniques has a stronger impact on improving the performance for low OPLs (both nonlinear and SNR limited) than for high OPL values (mainly SNR limited).

Figure 3.17 shows a comparison between the results obtained with the nonlinear compensation technique based on our proposed cubic approach given by Equation (3.5) and those obtained using the exact inverse function

given by Equation (3.4), based on an arc cos transformation (see section 3.2.2). The figure shows curves of EVM as a function of the OPL for three different conditions: i) without any optimization (in blue with circles), ii) setting the best $CLIP_{RX}$ and CF_{RX} parameters for each OPL condition using the cubic based nonlinear compensation (in red with asterisks), and iii) setting the best $CLIP_{RX}$ parameter for each OPL condition using the arc cos based nonlinear compensation (in green with squares). By comparing the red and green curves, it could be observed that they match well for OPL values lower than 20 dB and higher than 26 dB, while a slight deviation is observed for OPL between 20 and 26 dB, in which the green curve outperforms the red one. From this results it can be concluded that the exact inverse function that linearizes the MZM power transfer function is slightly better than the cubic approximation in terms of performance. In contrast, in terms of complexity and hardware implementation, the cubic optimization should be preferred, especially for those OPLs where good matching between the arc cos approach and the cubic approach takes place.

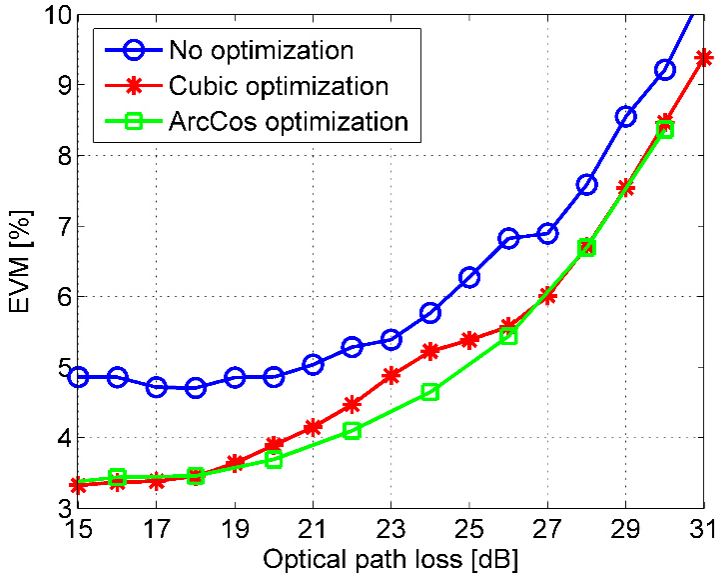

Figure 3.17 Comparison of the EVM as a function of the OPL obtained with different non-linear compensation procedures.

3.4.2 Results for WDM transmission of 192 radio channels per wavelength and mixed format transmission

In this Section, we present an experimental demonstration of a massive fronthauling transport. In particular, the WDM transmission of four wavelengths, each carrying 192 radio channels, is now analyzed. The optical channels were centered at 193.2 (Ch.1), 193.3 (Ch.2), Ch3=193.4 (Ch.3) and 193.5 (Ch.4) THz. The analyzed channel is Ch.3. The same optimization procedures, applied for the single-wavelength case reported in the previous section, were also applied to the WDM situation. Once applied the pre-emphasis technique, the $CLIP_{RX}$ and CF_{RX} parameters were optimized for each OPL. The average EVM of the 192 received radio channels, obtained for each OPL after optimization, is shown in Figure 3.18. It could be observed that a maximum OPL = 25.7 dB is achieved targeting an EVM < 8%. This OPL value is not compliant with the

minimum value required by PON in class N1 (OPL = 29 dB), therefore only point-to-point links could be considered for this transmission scenario.

One alternative to increase the maximum OPL of the system is decreasing the modulation order of the radio channels, or at least of some of them. It is well-known that by decreasing the modulation order, the received SNR (or EVM) requirements are relaxed. For instance, the maximum EVM required by ETSI for 16-QAM is 12.5% [114]. As a proof of concept experiment, the transmission of half of the channels with 64-QAM format and half of them with 16-QAM format is tested. The results are presented with the dashed blue curve in Figure 3.18. Care has been taken to outperform the EVM=12.5% limit for all the 16-QAM channels. For instance, for OPL = 15, 21 and 27 dB the maximum EVM when 64-QAM is used is 3.52%, 4.15% and 6.87 %, whereas for 16-QAM becomes 5.67%, 6.76% and 7.60%, respectively. By employing this approach, an OPL = 29 dB is now achieved targeting the required EVM ≤ 8% (64-QAM) and 12.5% (16-QAM). A gain of 3.3 dB of OPL is achieved. The drawback, however, is a loss in system capacity, particularly in the 16-QAM modulated channels. Each 20-MHz radio channel transmits 120 Mb/s when 64-QAM format is employed, then the overall raw capacity per optical channel is 23.04 Gb/s. If 16-QAM is used as modulation format, each radio signal reduces its capacity to 80 Mb/s. Then, for the case in which 50% of the channels are modulated with 64-QAM and the rest with 16-QAM, an overall raw capacity of 19.2 Gb/s is obtained. This translates into a reduction of 16.66% of the overall capacity, but the required increase in terms of the OPL. A trade-off between capacity and OPL is then evident.

The trade-off between maximum OPL and capacity was experimentally quantified for different EVM target values and the results are shown in Figure 3.18. The capacity per optical channel is expressed in terms of the 64-QAM/16-QAM channels ratio (*Cr*). The maximum capacity of 23.04 Gb/s corresponds to a *Cr* = 1 (all the channels modulated with 64-QAM). For a *Cr* = 0 (all the channels modulated with 16-QAM), a minimum capacity of 15.36 Gb/s is achieved. The EVM targets shown in Figure 3.9, namely 3.6%, 4.3%, 4.9% and 8%, corresponds to the 64-QAM modulation format. The corresponding EVM targets for 16-QAM modulation are 5.67%, 6.75%, 7.59% and 12.5%, respectively. For both modulation formats, the first three EVM targets were selected according to [113] in order to get a maximum EVM penalty of 1 dB, 1.5 dB and 2 dB, respectively, in the wireless segment due to the optical fronthaul segment and still fulfill the ETSI requirements at the output of the full system (composed of the fronthaul system in cascade with the wireless system).

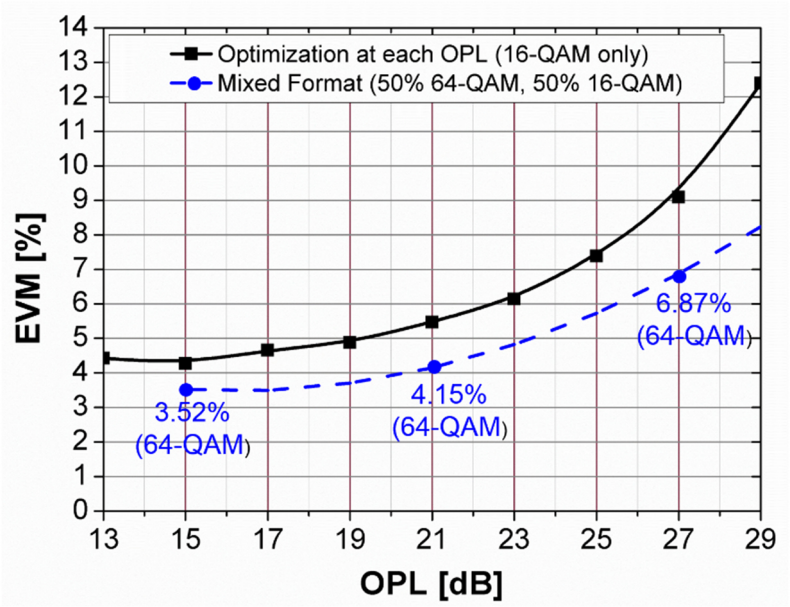

Figure 3.18 Comparison of the EVM versus the OPL obtained after optimization for two cases: i) All channels employing 64-QAM, and ii) Half of the channels employing 64-QAM and half of them employing 16-QAM.

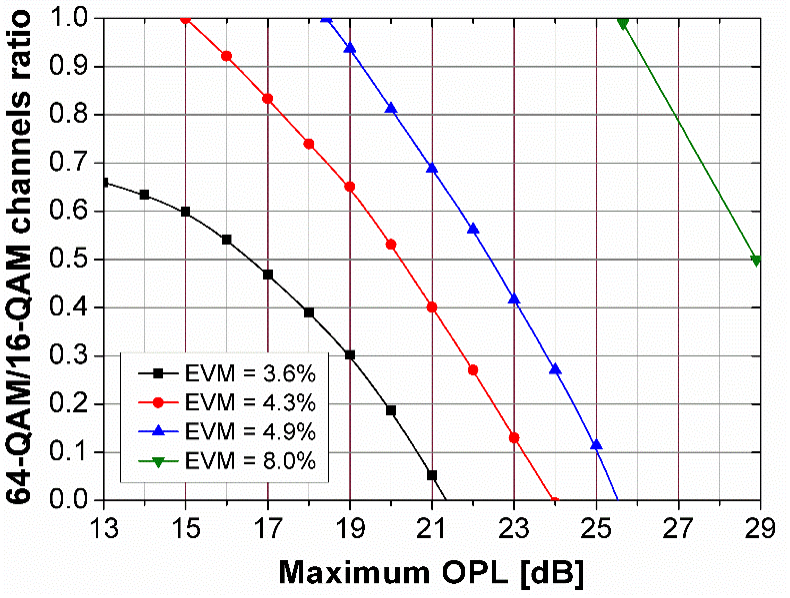

Figure 3.19 OPL as a function of the maximum capacity per channel expressed as the 64-QAM/16-QAM channels ratio, for different 64-QAM EVM targets.

3.5 Upstream optimization results

In this section, an analysis of the upstream link in optical fronthauling networks based on DSP-assisted channel aggregation is reported. The effect of both wireless and optical fiber transmission on the EVM is taken into account, and different statistical distributions of mobile terminals' positions within a radio cell are considered.

To date, and to the best of the author's knowledge, the DSP-assisted aggregation approach of several radio waveforms has been investigated for downstream purposes only. Most of the transmission experiments carried out so far foresee the transmission of a set of error-free channels (that is, EVM=0% at least in the DSP domain) over a fiber infrastructure, whose characteristics are determined for reaching, at the antenna sites, EMV values according to LTE standards.

For what concerns the upstream direction, the problem is reverted with respect to downstream, in the sense that the signal to be transmitted over the fiber path is already corrupted by the propagation through the wireless channel, as explained in section 3.2. In addition, mobile terminals are randomly distributed within the radio cell, and thus all electrical carriers reach the antenna, and then the electro-optical converters, with different EVM^{W} on a per-channel basis. Properly conditioning the aggregated signal then becomes the key aspect for dimensioning the optical link towards the BBU. Considering different distributions of the mobile terminals within a radio cell, our proposed pre-emphasis equalizer (presented in section 3.2.3) is applied to the signal transporting all the already noisy electrical carriers generated by the mobile terminals, and its functionality is experimentally tested.

Since we did not have access to a real radio distribution system on so many different radio channels, we reproduce in our laboratory some test condition in terms of the statistical distribution of the EVM^{W} of the signals reaching the antenna from the mobile terminals. In particular, we tested: a deterministic non-uniform distribution (sinusoidal), a random distribution and a uniform distribution. The sequences programmed in the AWG (see section 3.3) take then care of the distribution of EVM^{W} and of the related pre-emphasis equalization algorithm explained in section 3.2.3. Purpose of the experimental campaign is to receive, at the BBU site, all the different mobile carriers at the target EVM^{out} required for LTE standards. In particular, all experiments where performed with 96 LTE-like carriers employing 64-QAM as modulation format, targeting an EVM < 8%. The OPL was set to 20 dB, unless otherwise stated. It is important to clarify that according to the ETSI standard the EVM target in the upstream situation after the full transmission system can be much worse than 8% (extremely strong FEC codes are used on the radio channels, so that the actually received EVM can actually be very high). Purpose of this section is mainly to demonstrate the functionality of the proposed optimization procedures, *i.e.,* the pre-emphasis equalization, under the upstream conditions for a given arbitrary EVM target. Therefore, the EVM = 8% was just set as an indicative value to maintain the same target as in the downstream situation. The conclusions obtained here are independent of this target and can be generalized to any other value. In the following, the results of the experimental campaign are reported and discussed.

A deterministic EVM^{W} per channel distribution at the input of the fronthaul was analyzed as a first approach. Although deterministic distribution scenarios are unrealistic in real-world implementations, they are useful for testing purposes. A sinusoidal distribution (over two full periods, chosen arbitrarily) from 2% to 7.5% was imposed to the EVM^{W}, plotted in black with squares in Figure 3.20.a. The distribution was set to obtain one of the peaks of the EVM^{W} distribution at the highest frequency channel, which is the most affected by the low-pass response of the transmission system. This guarantees analyzing the worst-case scenario. At the output of

the fronthaul, an EVM^{out} distribution, plotted in blue with circles in Figure 3.20.a, with variations from 4% to unacceptable values of up to 10% is obtained when pre-emphasis equalization is not applied ($EVM^{out,no-pre}$ situation). The measured EVM^{W} and $EVM^{out,no-pre}$ per channel values are used to compute the optimum EVM^{out}_{target} following Equation (3.20). The corresponding constraint function G_{US} as a function of EVM^{out}_{target} is plotted in Figure 3.20.b. The optimum EVM^{out}_{target} value, that fulfills the constraint $G_{US}=1$, is 8.06%. By means of this optimum value, and the corresponding EVM^{W} and $EVM^{out,no-pre}$ per channel values, the pre-emphasis coefficients k_i are evaluated following Equation (3.15).

The results obtained when the pre-emphasis technique is applied are shown in red with triangles in Figure 3.20.a. The EVM^{out} per channel distribution now becomes more uniform, with all channels exhibiting an EVM below 8%. The functionality of the proposed pre-emphasis technique is clear in this case. It is worth to notice that when pre-emphasis is applied, the channels with the worst SNR (maximum EVM) at the input of the fronthaul are received at its output with a negligible SNR (EVM) penalty. A transparent transmission through the fronthaul is experienced by these channels since their power is enhanced to compensate for their lower SNR. This is performed at the expense of a strong degradation of the SNR (and EVM) of the best performing channels at the input of the fronthaul, due to a reduction of the power of these channels. For instance, channels 24 and 72 change their EVM from EVM^{W} = 2% at the input to EVM^{out} ~7.5% at the output, while before applying the pre-emphasis the EVM degradation was less sharp, obtaining an EVM^{out} of around 4% and 5.8%, respectively. Then, the pre-emphasis is exploited to compensate for the optical segment frequency response and, at the same time, to balance the LTE channels performance.

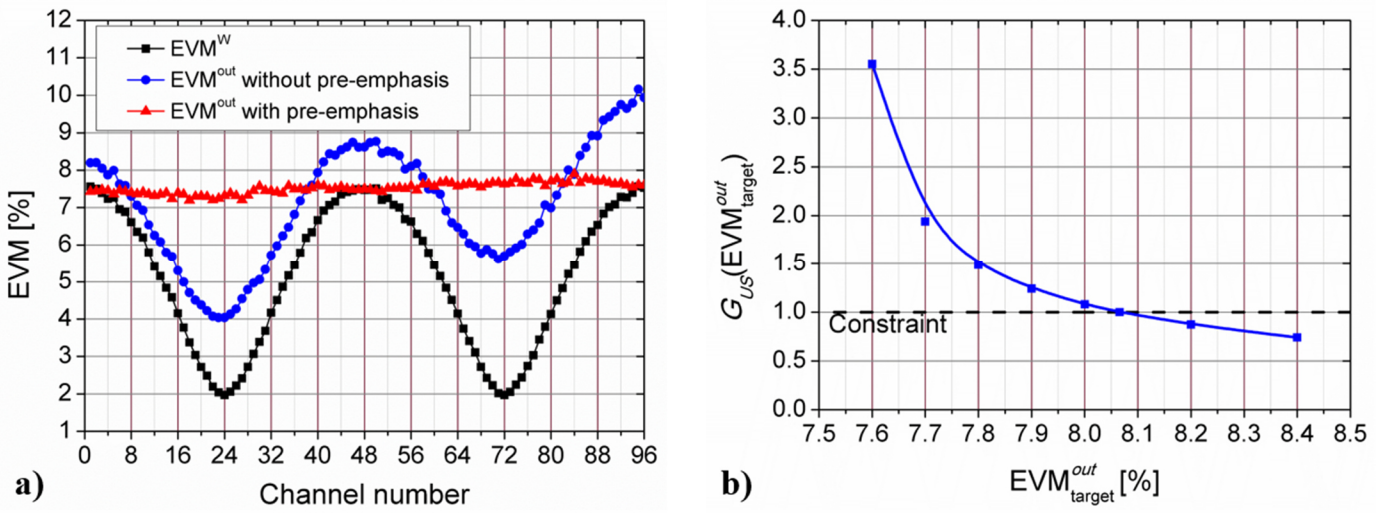

Figure 3.20 a) Performance per channel for a sinusoidal EVM^{W} distribution: at the antenna site and at the BBU site after 20 dB of OPL with and without pre-emphasis, and b) corresponding constraint function G_{US} versus EVM^{out}_{target}.

Another case where an EVM^{W} sinusoidal distribution is considered is depicted in Figure 3.21.a. In this case the minimum EVM^{W} is increased to 4% and the maximum is decreased to 7% with respect to the previous case. Although the EVM^{W} conditions were stressed, when pre-emphasis equalization is applied, the EVM^{out} target is still accomplished. The optimum EVM^{out}_{target} value is 7.687% ($G_{US}=1$). Figure 3.21.b shows EVM^{out} per channel curves when the pre-emphasis equalization is applied using different EVM^{out}_{target} values to compute the k_i coefficients. Note that the curve obtained using the optimum EVM target (solid red) outperforms the rest of the curves (dash curves) in terms of minimizing the maximum EVM^{out}, thus showing, for some exemplifying cases, a right EVM optimization process when using the analytically derived $G_{US}=1$ constraint.

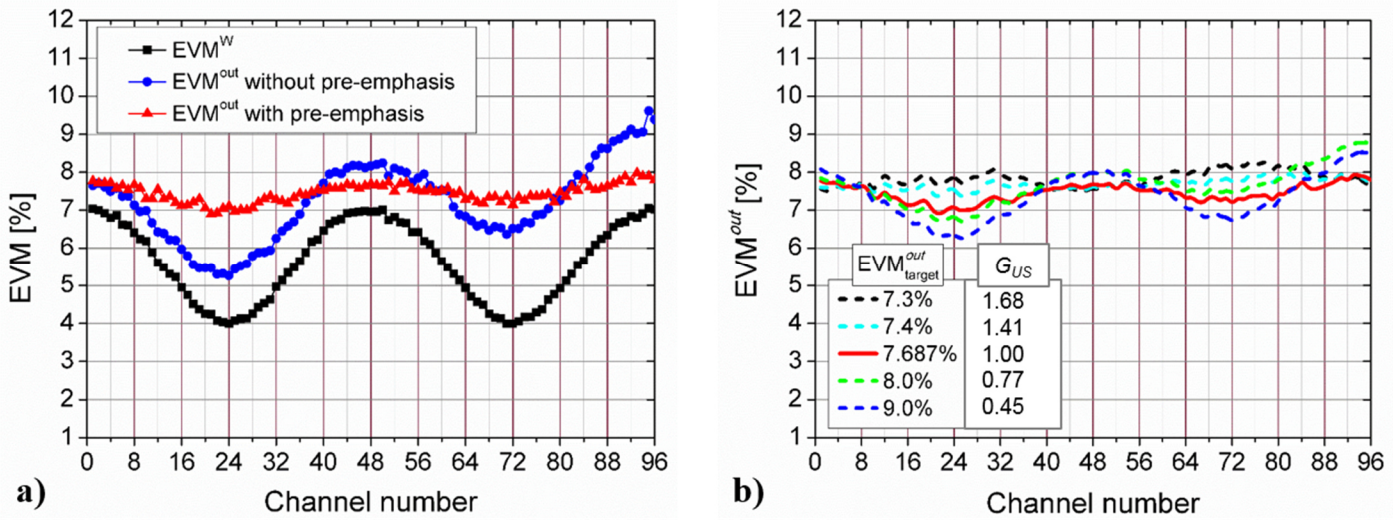

Figure 3.21 Performance per channel for a sinusoidal EVM^{W} distribution: a) at the antenna site and at the BBU site after 20 dB of OPL with and without pre-emphasis, and b) at the BBU site after 20 dB of OPL with pre-emphasis for different EVM^{out}_{target} values.

In order to test a more general situation, a random EVM^{W} distribution varying from 2% to 7.5% was enforced and the performance of the system was analyzed under these input conditions. Figure 3.22.a present the EVM^{W} (in black with squares) and the EVM^{out} without pre-emphasis (in blue with circles) per channel distributions corresponding to the random case. It is observed that several channels have an EVM^{out} higher than the chosen target.

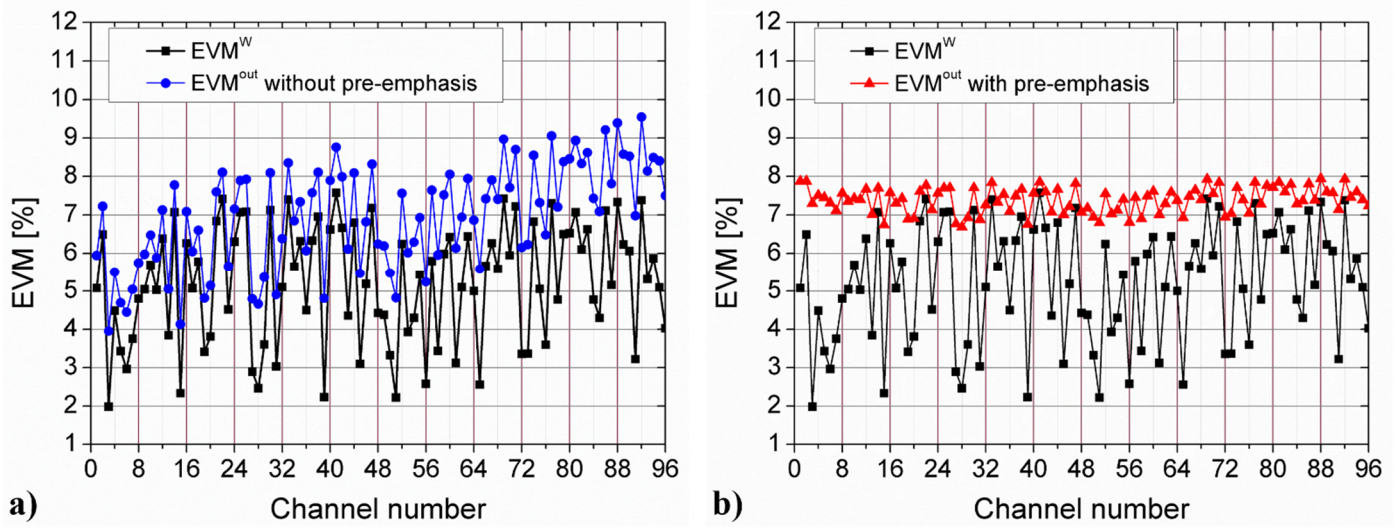

Figure 3.22 Performance per channel for a random EVM^{W} distribution: at the antenna site and at the BBU site after 20 dB of OPL with and without pre-emphasis.

Once the pre-emphasis technique is applied, the resulting EVM^{out} per channel distribution, shown in red with triangles in Figure 3.22.b, is flatten. All the channels outperform the EVM target. The functionality of the pre-emphasis equalization technique under a more general situation is then demonstrated.

Another random distribution situation, whose results are shown in Figure 3.23.a, was tested. A random EVM^{W} distribution with reduced variations from 4% to 6% was defined. However, this time the OPL was increased to 25 dB. By comparing the blue curve with circles and the red curve with squares, a much flatter EVM^{out} distribution is observed when the pre-emphasis technique is applied, as expected. Again, all the channels are below the chosen EVM target.

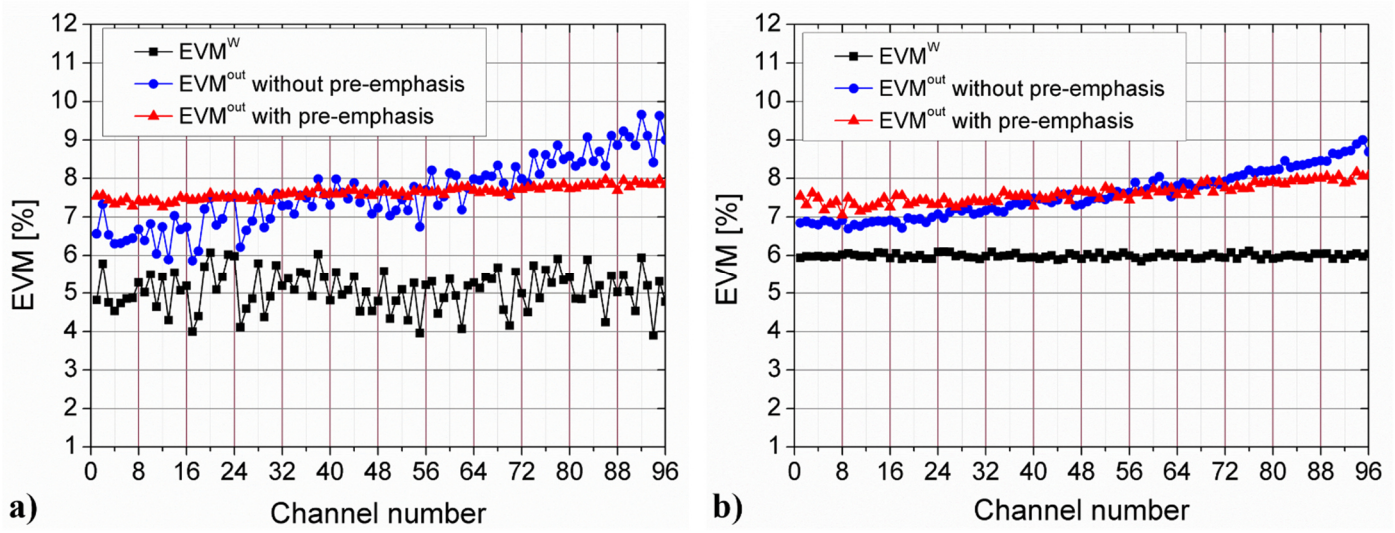

Figure 3.23 Performance per channel for (a) a random and (b) a uniform, EVM_i^W distribution: at the antenna site and at the BBU site after 25 dB and 20 dB of OPL, respectively, with and without pre-emphasis.

Finally, a uniform EVM_i^W distribution was analyzed. The resulting EVM^{out} values with and without applying the pre-emphasis technique are shown in Figure 3.23.b. In a real mobile network scenario, the EVM of the signals reaching the antenna from the mobile terminals (EVM_i^W) is far from being uniformly distributed over frequency. Nevertheless, we report this case because it represents the worst-case scenario for the upstream transmission because there is no SNR margin between channels, and all carriers worsen after optical propagation. In this case, the pre-emphasis is mainly needed to compensate for the optical link frequency response, as in the downstream situation. However, it is important to remark that the evaluation of the k_i coefficients is still different between this upstream uniform situation (in which $EVM_i^W = k_W$, being k_W a non-zero constant value) and the downstream one (in which EVM_i^W) (compare Equations (3.15) and (3.21)).

From this worst case scenario, it is shown that an EVM ≤ 8% at the BBUs can be achieved after up to 20 dB of OPL for all 96 LTE channels, provided that a maximum EVM_i^W as high as 6% is considered, irrespective of the EVM_i^W per channel distribution, and pre-emphasis is employed. If the maximum input EVM_i^W or the EVM^{out} target change, the OPL also changes. Therefore, since the maximum OPL value for the upstream direction can be different from that for the downstream direction, it is very important to dimension both directions of a link, the downstream and upstream, for a proper operation of the full system.

To finish this section, it should be clarified that although the pre-emphasis technique was demonstrated to work well under different scenarios for the downstream (see section 3.4.1) and the upstream cases, the EVM^{out} distribution is not completely flat in any of the analyzed situations. This slight deviation from an ideal flat case results from the difference between the assumed conditions to derive the equalization algorithm (see section

3.2.3) and the real conditions of the experiments. However, since this deviation is small in all cases, we could then consider our assumptions to be accurate enough.

3.6 The FDM DDO-OFDM system used as a high-speed optical interconnect

The overall maximum capacity of the four-wavelength FDM DDO-OFDM system analyzed in section 3.4.2 is 92.16 Gb/s (23.04 Gb/s per optical channel), for an OPL up to ~25 dB which includes the total attenuation of 25 km of SMF. This capacity is close to the 100 Gb/s data rate achieved by the fastest commercially available Ethernet transceivers over SMF for reaches of 10 and 40 km (with and without a semiconductor optical amplifier, respectively), based on a similar four wavelength WDM architecture, used as optical interconnect. If the OFDM generators/decoders, the FDM aggregators/de-aggregators and the optical transmitters/receivers are joint on the same device (see Figure 3.3 and Figure 3.13), the analyzed fronthaul system can be used as an optical transceiver that transforms a serial bit sequence with a data rate of 92 Gb/s into an analogue optical signal and vice versa. This transceiver could be used as an optical interconnect for short-reach applications. The graph of EVM as a function of OPL shown in Figure 3.18 for the case in which all channels are 64-QAM modulated, can be also represented as the BER vs received optical power (ROP) graph shown in Figure 3.24. The EVM to BER conversion is performed by means of the analytical expression reported in [115]. The ROP is evaluated by subtracting the OPL to the launch power into the fiber (+9 dBm). A receiver sensitivity of -16 dBm is then measured for a BER = $1x10^{-3}$. In order to improve the system performance to achieve the BER = $1x10^{-12}$, target of the 100 Gb/s Ethernet transceivers, the use of a high overhead FEC would be mandatory in this case. If a simpler low-overhead, low-power consumption and low-latency Reed-Solomon FEC scheme [116] is preferred, a more demanding pre-FEC BER target of $3.8x10^{-5}$ should be satisfied. For this BER value, a receiver sensitivity of -12.75 dBm is measured. Considering insertion losses of 6 dB for MUX and DEMUX devices, losses of 1 dB due to connector and splices, a total attenuation of 2 dB for 10-km of SMF operated in C-band, and a power penalty of 1 dB due to transmission, then the total losses of the system become 10 dB. A transmitted optical power per channel, measured at the output of the modulator, of -2.75 dBm is then needed, which is a value attainable with commercially available EMLs. Therefore, the EDFA used for fronthauling applications could be removed from the optical transceiver to reduce its size and power consumption. It is important to point out that negligible CD and cross-talk power penalties were measured in the analyzed system as reported in [113].

As compared to the 100 Gb/s Ethernet transceiver over 10-km of SMF, which operates using OOK format, the FDM DDO-OFDM transceiver is much more spectrally efficient (0.23 Gb/s/Hz vs 0.03125 Gb/s/Hz). In contrast, the electrical part of the transceiver is more complex, since the addition of digital OFDM, FDM and FEC blocks is needed. However, we consider these features as necessary to implement feasible optical transceivers beyond the 100 Gb/s capacity. In the next Chapter, a transceiver based on WDM and OFDM technologies is proposed and analyzed for the transmission of 400 Gb/s over 10-km of SMF. Since the system experimentally analyzed in this Chapter follows a similar DDO-OFDM approach, the discussion presented in this section becomes useful for the sake of comparing both systems.

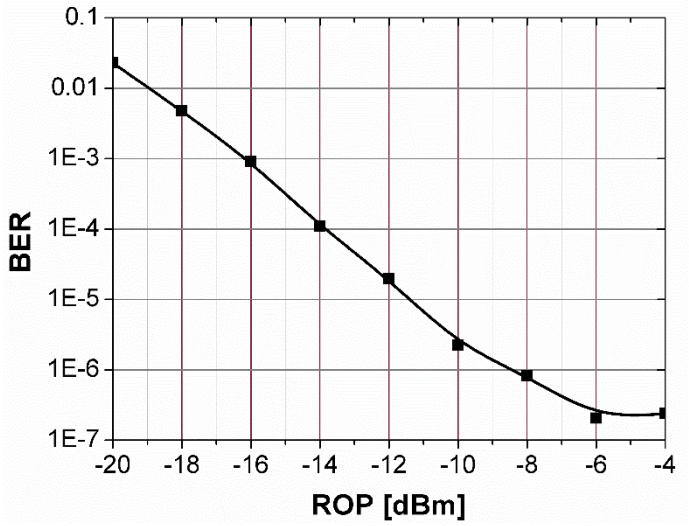

Figure 3.24 BER as a function of ROP graph of the optical channel 3 for the WDM transmission of 192 OFDM signals per optical channel, corresponding to an overall data rate of 92.16 Gb/s.

3.7 Conclusions of the Chapter

Some relatively simple digital techniques and optimization procedures for DSP-aggregated fronthauling, allowing improvements in the system performance while having a very little increase in DSP complexity, were experimentally demonstrated for both downstream and upstream directions.

Downstream transmission of up to 768 20-MHz LTE-like signals (192 per optical channel) each modulated with 64-QAM format, was demonstrated. For each optical channel, all 192 LTE signals outperform an EVM target of 8% for a maximum optical loss of 25.7 dB. The aggregated signal of each optical channel has a bandwidth of only 6 GHz. The current CPRI approach would have required a data rate of approximately 177 Gb/s per optical channel to transport the same amount of 20-MHZ LTE signals (without control words). A minimum ideal bandwidth of 88.5 GHz is required to transport 177 Gb/s using the OOK format employed in CPRI. Therefore, the system here analyzed requires ~15 times less bandwidth to transport the same amount of information than the current fronthauling technology.

An analysis of the upstream direction of the DSP-aggregated fronthauling architecture was performed here as well. An original pre-emphasis technique to equalize the received SNR, thus minimizing the maximum EVM per channel at the output of the fronthauling, was developed here for the upstream situation. The developed algorithm takes into account the EVM per channel values at the input of the fronthaul, called here EVM^{W}, which in the upstream case are different to zero and non-uniform among channels. The pre-emphasis technique was tested for different EVM^{W} distributions at the input of the fronthaul and its ability to equalize the EVM of all the channels at the output of the fronthaul was demonstrated for all the analyzed cases. It was shown that the maximum OPL value for the upstream direction can be different from that for the downstream direction. Therefore, the importance of dimensioning and optimize not only the downstream but the upstream direction of a link for proper operation of the full system, was demonstrated.

4. Chapter four: Numerical analysis of a 400 Gb/s optical intra-DCI based on WDM 4 x 100 Gb/s RF-IQ-DDO-OFDM Transceivers

In this Chapter the technical feasibility of an unamplified 4 x 100 Gb/s wavelength division multiplexed DDO-OFDM system that uses EAMs is numerically demonstrated for up to 10-km reach of SMF in both C- and O-bands for a BER target of 3.8×10^{-5}. Based on the use of specifications of currently available (realistic) components, error-free operation is achieved by finding optimum values for bias voltage and electrical gain in the modulator, and by employing a simple PAPR-reduction technique. A performance comparison with a Mach-Zehnder driven system is presented too. In section 4.6 a brief discussion about extending the analyzed system to a 16 x 100 Gb/s architecture for future 1.6 Tb/s optical interconnections is performed.

The architecture here put forward can be used as an alternative for next-generation 400 Gb/s Ethernet for high-speed intra-data center optical interconnects applications and adds on the value proposition of using multi-carrier modulation schemes for Ethernet and similar short-reach WDM schemes.

4.1 State-of-the-art and context

Ethernet is the most widely deployed technology to set up local area networks. In recent years, through the incorporation of optical transceivers to support higher data rates, its reach has been extended to also embrace metropolitan and short-reach data center interconnects. The most recent addition to the IEEE 802.3 (or Ethernet) standard was published in June 2010 [117]. It defines specifications for 40 and 100 Gb/s data rate links for several transmission distances. In particular, for applications up to 10 km, the physical medium dependent sublayer running at 100 Gb/s, termed 100GBaseLR4, uses a conventional SMF (CSMF) and WDM technology to transmit four wavelengths at 25 Gb/s raw data rate each. The optical channel plan follows the ITU-T G.694.1 recommendation for O band with 800 GHz channel spacing as follows: 1295.56, 1300.05, 1304.58 and 1309.14 nm. In the usual implementation approach [118], the four optical signals, each running at an actual rate of 25.78125 Gb/s, are wavelength division multiplexed into the fiber. For simplicity, NRZ is chosen as modulation format, because in this way, cost-effective EAMs can be used in the transmission side, and uninvolved direct-detection optical front-ends (OFEs), and corresponding 25 Gb/s electrical receivers, are employed in the receiver side. For the 100 Gb/s extended-reach (up to 40 km) physical medium dependent sublayer, termed 100GBaseER4, the transceiver architecture preserves the 100GBaseLR4 configuration, but a semiconductor optical pre-amplifier (SOA) is added to the design in order to extend the system power budget [118]. The first and second generations of 100 Gb/s Ethernet transceivers for 10 and 40 km reach, termed C Form-Factor Pluggable (CFP) and CFP2, respectively, are nowadays commercially available, while the third generation (CFP4) is still in beta version [119].

Due to the apparently unending bandwidth demand explosion, described in the Introduction section, in May 2014 the IEEE 400 Gigabit Ethernet (400 GbE) Task Force (TF) was established. Its mission so far has been

to lead the efforts of the research community to develop an Ethernet standard running four times faster than the current version. Different approaches have been considered to implement the physical medium dependent sublayer on CSMF for 2 and 10 km reach [120]. The simplest implementation approach consists in the use of 16 optical channels, each modulated at 25 Gb/s in NRZ format [121]. This solution, however, requires 12 more transceivers than its predecessor, with the corresponding increase in implementation cost and power consumption. An alternative architecture, attractive because it achieves an adequate trade-off between technical complexity and cost [122], is an 8 x 50 Gb/s WDM design using pulse amplitude modulation with four levels (PAM-4). This set up, however, still requires two times more transceivers than the 100GBaseLR4 implementation. Yet another approach to maintain the current optical component count, and therefore achieve the right balance between potential costs, power and port density, is to employ advanced modulation formats to set up a 4 x 100 Gb/s WDM design.

A single optical lane running at 100 Gb/s can be realized in several ways. The ITU, for instance, has recommended polarization-multiplexed QPSK modulation at 112 Gb/s to implement the OTU4 framing [123]. Unfortunately, this solution relies on intricate coherent technology, which could be excessively complex for 400 Gb/s intra-data center applications. Simpler alternatives based on direct detection such as: DMT, carrier-less amplitude phase modulation (CAP), and PAM with 4 or 8 amplitude levels, have been preferred and extensively investigated for this capacity and reach targets [12], [15], [17] , [91]. DMT has positioned as the best performing technology among them. However, the digital transmitter and receiver stages of DMT are more complex than that of PAM, therefore, the latter has been preferred for commercial purposes in the short-term.

DMT is a variant of IM-DDO-OFDM (see section 2.4.1) in which bit and power loading techniques are added to the digital OFDM transmitter and receiver in order to adjust the modulation order and the power of each *sub-carrier* according to its corresponding SNR penalty at the receiver side. An intermediate alternative between DMT and PAM in terms of digital complexity is proposed and analyzed in this work for the transmission of 100 Gb/s per optical lane. In contrast to DMT, the approach reported here, based on RF-IQ-DDO-OFDM (see section 2.4.2) using EAMs, avoids enforcing Hermitian symmetry to get a real-valued OFDM signal, as well as the use of bit and power loading techniques, thus decreasing the DSP complexity and halving the bandwidth requirements of the digital transmitter and receiver. Instead, the bandwidth requirements are moved to the *RF* and optical up and down conversion stages, namely, electrical oscillators and mixers and optical modulators and photodiodes. Based on the development and fabrication trends of electrical and optical devices, the availability of the required high-bandwidth technology in the mid-term can be foreseen. Indeed, experimental state-of-the-art devices that full-fit the high bandwidth requirements of some devices of the proposed architecture are reported in section 4.2.

Our proposed system to set up the 4 x 100 Gb/s Ethernet transceiver practically uses the same optical components employed in the aforementioned 4 x 25 Gb/s 100GBaseLR4 configuration. This makes it especially attractive to reduce development costs. Although the reuse of the DFB lasers and photodiodes is straightforward, the use of EAMs in a DDO-OFDM environment is limited by the narrow linear region of their

transmission function. Such shortcoming results in nonlinearity-induced SSII due to the normally high PAPR that OFDM driving signals exhibit [76]. For this reason, DDO-OFDM systems are normally implemented using MZMs. Nevertheless, EAMs present attractive features such as low drive voltages and power consumption, its bandwidth can reach >50 GHz, they can be integrated with the laser source in a compact structure and potentially lower cost as compared to MZMs [43]. Novel DSP-based techniques that perform SSII cancellation to increase the EAM operational region have recently been developed [70], [74], [76], [79]. However, these techniques increase the complexity of the transceivers at the digital stage, which is a characteristic to be avoided in short-reach applications. They are therefore aimed for 50 Gb/s, longer-reach applications.

Aided by a relatively simple random phase-shifting method to reduce the PAPR, described in section 4.2.4, and the use of optimization procedures to reduce the impact of the EAM nonlinearity, in this Chapter we numerically demonstrate the technical feasibility up to 10-km of a 4 x 100 Gb/s WDM architecture, prone to be used in 400 GbE, where each 100 Gb/s optical channel is implemented by means of RF-IQ-DDO-OFDM. This work adds on the value proposition of using multi-carrier modulation schemes for Ethernet and similar short-reach WDM scenarios. Our numerical research can also be considered relevant, not only because of the possible use of the proposed architecture for intra-data center Ethernet optical interconnects, but because the use of EAMs in high-speed DDO-OFDM systems has not been sufficiently investigated. In fact, this is, to the best of the author's knowledge, the first numerical analysis of the implementation of a 100 Gb/s DDO-OFDM channel that uses an EAM as optical transmitter, including its extension to the WDM domain.

4.2 Analyzed architecture and numerical setup

The system to be simulated, implemented on a VPI Transmission Maker^{TM} V9.2 co-simulation platform, is presented in Figure 4.1. It consists of four electrical RF-IQ-OFDM (eRF-IQ-OFDM) transmitters, as those described in section 2.4.2, each of which drives an EML composed of a distributed feedback laser (DFB) and an EAM. The four field-modulated optical OFDM channels are WDM multiplexed onto a CSMF. After demultiplexing, each channels is directly detected by an OFE and processed in its corresponding OFDM electrical receiver. The simulation steps and parameters are presented with more detail in the following sub-sections.

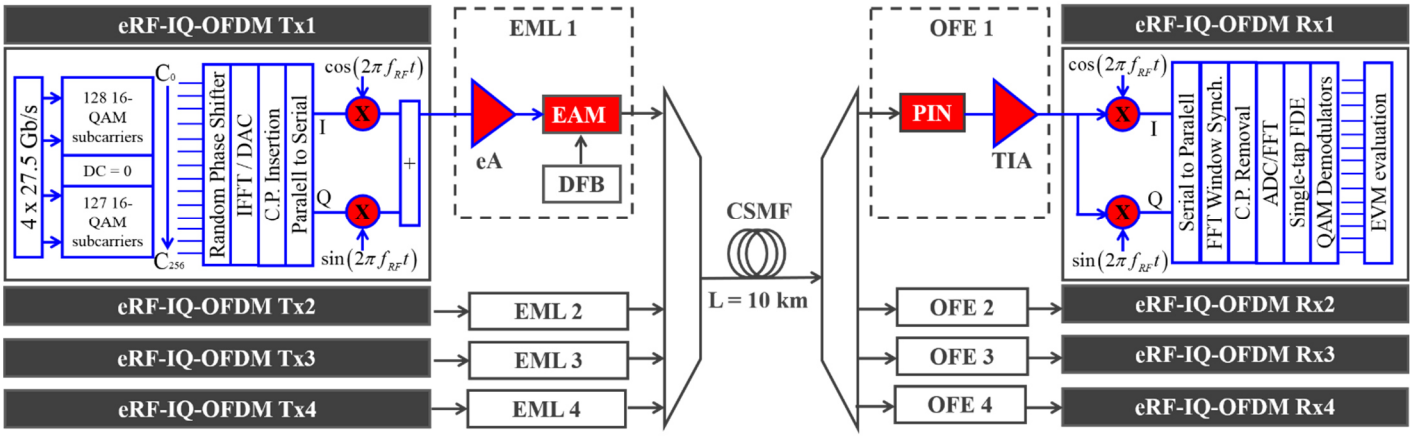

Figure 4.1 Schematic diagram of the WDM 4 x 100 Gb/s DD-OFDM transmission system. Electrical elements in blue. High-bandwidth elements in solid red.

4.2.1 Electrical OFDM Signal Generation

In each of the four electrical transmitters, a different pseudo-random bit sequence (PRBS), 2^{19} bits-long and running at 110 Gb/s, is mapped into 2^{17} 16-QAM symbols. Each OFDM symbol consists of 255 16-QAM symbols plus one symbol at the center of the data block (DC subcarrier) that is set to zero. The 110 Gb/s rate per optical channel results from including to the 100 Gb/s required in the MAC sublayer, the extra 3.125% data rate needed for PCS coding (assuming the same coding as for 100GBaseER4), 2.93% to allocate the CP for C-band transmission (2% in O-band), 3% overhead for FEC and 0.8% for the transmission of one pilot OFDM symbol every 512 symbols. Since high PAPR is known to be one of the main drawbacks of OFDM transmission, a random phase shift is added to every single 16-QAM symbol in the block to reduce it. This procedure, described in more detail in section 4.2.4, indeed reduces the PAPR, and therefore no signal clipping is applied. Each data block is then inverse-Fourier transformed via an iFFT algorithm. The digital to analog conversion of real and imaginary parts is simulated using zero-padding in the iFFT. A cyclic prefix of 272.7 ps for C-band operation (181.8 ps for O-band) over an optical fiber 10-km long is then added to supply enough guard time between OFDM symbols. The two analog electrical signals are mixed with the 0 and $\pi/2$ phases of a LO operating at f_{RF} = 41.25 GHz. Local oscillators operating at frequencies above 40 GHz have been reported in [124], [125], [126] and [127]. Besides, 26-40 GHz tuned voltage controlled oscillators are nowadays commercially available [128], [129]. The baseband to passband conversion creates a frequency guard band of 27.5 GHz between the optical carrier and the lowest frequency OFDM subcarrier (see Figure 4.8.a), thus preventing beating products due to direct detection to fall into the detection bandwidth (see section 2.4.5). The eRF-IQ-OFDM signal that drives each EML is finally produced by combining the two *RF-up-converted* signals. It must be mentioned that although the proposed design is based on the use of ultra-high speed RF electronics, recent advances in state-of-the-art silicon technology for millimeter wave frequencies have enabled the fabrication of the necessary complementary metal-oxide-semiconductor (CMOS) circuit blocks [130].For instance, RF up- and down-converters, which integrate a RF amplifier, a local oscillator and a mixer, operating at frequencies around 40 GHz and up to 60 GHz, have been reported in [33], [131], [132], [133], [134], [135], [136] and [137].

4.2.2 Optical Transmission and Detection

Each of the four eRF-IQ-OFDM signals drives an EAM which is fed using CW light derived from a DFB laser with OSNR = 40 dB, 1 MHz linewidth and output power of 14 dBm for C-band and 12 dBm for O-band [138]. The DFB frequencies for C-band grid are centered at 193.2, 193.3, 193.4 and 193.5 THz (1551.72, 1550.92, 1550.12 and 1549.31, nm), leading to a homogenously spaced, Ω = 100 GHz, channel plan. For the case of transmission over O-band, the same channel plan defined for 100GBaseLR4 using a Ω = 800 GHz was set: 228.2, 228.8, 230.6 and 231.4 THz (1309.14, 1304.58, 1300.05 and 1295.56 nm). In this case, the same lasers developed for 100 GbE transceivers could be reused. A narrower channel spacing for C-band operation was chosen to avoid excessive power penalties due to fiber dispersion at the expense of incurring on a small penalty due to linear cross-talk.

A well-known small-signal EAM model is employed to carry out the simulations (described in section 2.1.2). It is based on the use of voltage-dependent Taylor series of the transmission magnitude T(V(t)) and the linewidth enhancement (or chirp) factor α(V(t)), which relates the EAM change in absorption with the corresponding change in refractive index. The time-varying voltage signal is given by $V(t) = V_{bias}+V_m(t)$, V_{bias} is the DC bias voltage and $V_m(t)$ is the modulating voltage.

In order to guarantee predictions that are very close to reality, the transmission function coefficients used in the simulations for operation over C-band were determined through a fit process of the experimental curves of voltage-dependent output power and chirp factor of the quantum-well EAM presented in [139]. The graphs are shown in Figure 4.2 together with the corresponding fifth-order polynomial fits for the interval of interest. A CW input power of 0 dBm was assumed. The calculated values are $[T_0, T_1, T_2, T_3, T_4, T_5; \alpha_0, \alpha_1, \alpha_2, \alpha_3, \alpha_4, \alpha_5]$ = [-0.03, 4.20, 8.44, 14.25, 6.38, 0.88; 1.47, 2.00, 2.58, 2.63, 1.19, 0.20]. For completeness, Figure 4.2 also shows the calculated optical field magnitude at the EAM output. Additionally, in order to incorporate the EAM frequency response into the simulation model, a fifth-order Gaussian filter exhibiting a 3-dB bandwidth of 60 GHz was placed at the EAM electrical input port. This allowed us to reproduce the electro-optic small-signal frequency response characterization reported in [139]. Obviously, the experimental curve presented in [139] was derived from the same actual device used to carry out the transfer function fit mentioned before. For a V_{bias} = -1 V, the EAM bandwidth clearly exceeds 50 GHz. Therefore, the analyzed EAM fulfills the ultra-high speed requirements of the transmission system.

Measured characteristics of a typical EAM [140] that resulted in the following polynomial coefficients $[T_0, T_1, T_2, T_3; \alpha_0, \alpha_1, \alpha_2, \alpha_3]$ = [0, -2.75, -6.30, +1.5; 0.2, -0.3, -0.4, +0.1] are used for the O-band transmission analysis. The corresponding graphs of optical power, field and chirp-factor at the output of the modulator as a function of the driving voltage are shown in Figure 2.4 of section 2.1.2. The electro-optic frequency response was also modeled through a fifth-order Gaussian filter with a 3-dB bandwidth of 60 GHz.

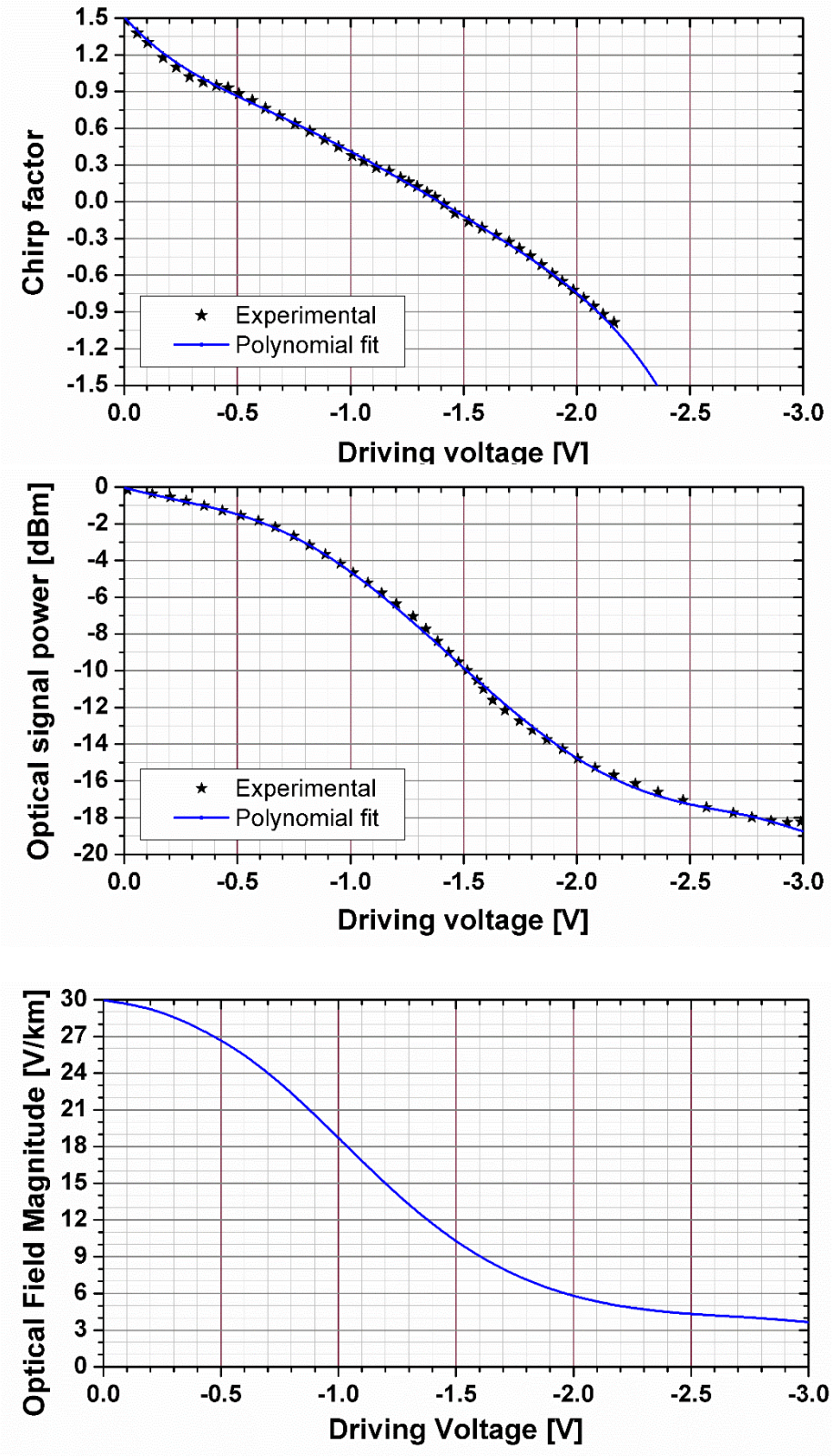

Figure 4.2 Transfer function characteristics of the EAM as a function of the driving voltage for a CW input power of 0 dBm. The experimental curves were extracted from [139].

The optical 4:1 MUX (DEMUX) was modeled via a third-order Gaussian bandpass filter with insertion losses of 3 dB and optimized FWHM bandwidth of 106.5 (81.5) GHz. The central frequencies of the MUX are f_1 + f_{RF} + N·Ω [GHz], where N = 0, 1, 2 and 3, and f_1 = 193,200 or 228,200 GHz, for C-Band or O-Band grid, respectively. The central frequencies of the DEMUX are shifted -14 GHz relative to those of the MUX. The MUX is also used to suppress the lower sideband (SB) of the optical signal and to optimize for each channel the carrier-to-SB power-ratio for minimum BER. An OSSB scheme was preferred over its ODSB counterpart because of the narrower spectral bandwidth that it exhibits, leading to a shorter chromatic dispersion-induced time delay and corresponding cyclic prefix. It also leads to a higher SNR at the receiver [59]. However, as mentioned in section 2.4.4, the most important reason for having chosen the OSSB scheme, is that it allows to simply compensate the fiber chromatic dispersion after square-law detection in the electrical domain. This is possible because the information of the relative arrival time of the various signal frequencies remains as part of the electrical output signal [69]. After multiplexing, the four OSSB waveforms plus carriers are launched into a CSMF whose characteristics at λ=1550 nm (1310 nm) are: attenuation of 0.2 (0.5) dB/km, chromatic dispersion of 17 (-0.02) ps/(nm·km), slope of 0.06 (0.09) ps/(nm^2·km), A_{eff} = 80 μm^2, nonlinear index of 26 x 10^{-21} m^2/W and PMD coefficient of 3.1623 x 10^{-15} s/√H. The SMF is modeled as described in section 2.3.After propagation along the fiber link and demultiplexing, each optical waveform is directly detected using a commercially available 50-GHz PIN photodiode whose responsivity is 0.65 (0.45) A/W for C-band (O-band) operation and that takes into account a dark current of 100 nA with shot noise and thermal noise of 10 pA/√Hz [141]. The OFE is complemented with a 60-GHz TIA [142]. Figure 4.3 presents the optical spectrum of the four multiplexed WDM channels after 10-km CSMF propagation over C-Band. The carriers and non-suppressed SBs are evident. The suppressing effect of the MUX can still be appreciated in the lowest frequency channel. Figure 4.3 confirms that a minimum of 100 GHz is an adequate choice for the C-band system channel spacing and demonstrates that although the numerical model takes into account the fiber nonlinear response, the corresponding effects, such as four-wave mixing, can be considered negligible.

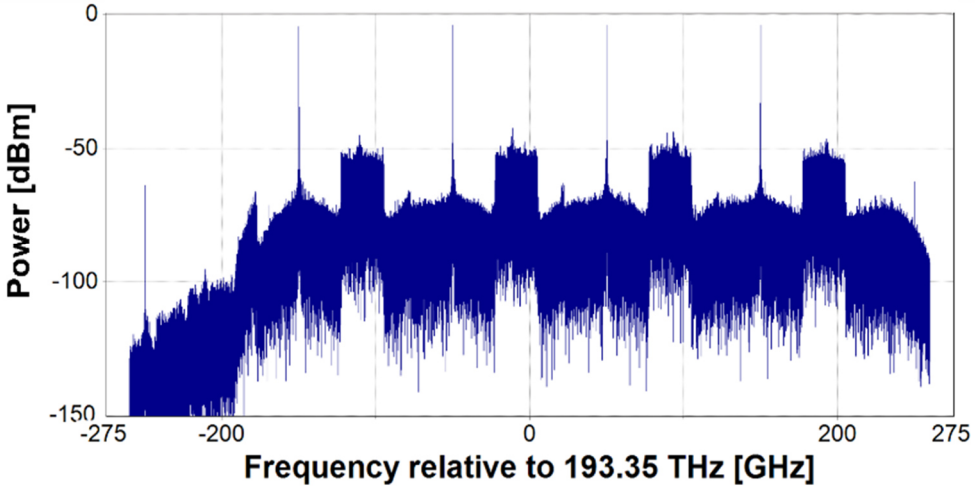

Figure 4.3 Optical spectrum of the WDM signal after 10-km CSMF propagation for a C-band grid.

4.2.3 Electrical OFDM Signal Reception

Once in the receivers, the inverse operations carried out at the transmitters are performed in reverse sequence (see Figure 4.1) aided by eight 56 GS/s ADCs [143] that digitize the signals. Before CP removal a FFT window synchronization technique is performed. This technique takes advantage of the use of pilot OFDM symbols in order to perform a cross-correlation between the expected and the received pilots to find the discrete time in which the cross-correlation is maximum. This discrete time corresponds to the transmission time delay and it is used to determine the start of the subsequent received symbols. The evaluated start time is used for CP removal and FFT window synchronization purposes. After Fourier-transformation, a single-tap FDE equalizer (described in section 2.4.4) is employed to compensate for phase and amplitude distortions, including the effect of fiber dispersion and, especially, the random phases introduced to reduce PAPR. The FIR coefficients are determined, for each optical channel, by estimating the phase and amplitude errors of every 16-QAM symbol that composes the first received (pilot) OFDM symbol of every 512 OFDM symbols transmission. The same filter, which is nothing but a complex multiplication, is then used to equalize the rest of the signal in an OFDM symbol-by-symbol basis. Following [115], the BER of the transmission system is theoretically estimated from the EVM that is measured at the constellation diagrams. Accurate theoretical predictions of BER values (in the order of 10^{-6}) for low EVM measurements are guaranteed from Fig. 2.b of [144], that shows, for a similar electrical OFDM setup used here, a very close match between theoretical estimations (solid) and actual BER measurements (circles) when transforming from EVM to BER. The theoretical approach used in this work is normally preferred because of its inherent reduction of simulation time. A low-overhead (3%) Reed-Solomon RS(528, 514) FEC scheme similar to the one standardized in IEEE 100GBaseKR4, exhibiting a latency ~100 ns and very low power consumption is assumed to guarantee a currently accepted free-error BER $\leq 1\text{x}\ 10^{-13}$ for a pre-FEC BER $\leq 3.8\text{x}10^{-5}$ [116], which is used as a target in the rest of this Chapter.

4.2.4 Peak-to-average power ratio (PAPR) reduction technique

An OFDM signal can be considered as the sum of many sinusoidal signals, whose amplitude and phase are dependent of the sequence of data symbols. The PAPR value of an OFDM signal is then determined by the amplitude and phase of the data symbols. Therefore, the PAPR value at every OFDM symbol changes if a phase shift to each data symbol that conforms the OFDM symbol is applied. This concept enables the possibility of PAPR reduction by properly choosing the phase shifts. Since the phase of the data symbols is a random value, the addition of a random phase block $\Theta=[\theta_1,\theta_2,...,\theta_N]$ to the phases of every block of data symbols, as shown in Figure 4.4, has been proved to be effective for PAPR reduction [145]. However, an optimum value of Θ must be found for every OFDM symbol. One distortion-less method to perform this is the selective mapping (SLM) technique. In a nutshell, SLM produces many Θ_i alternatives, $i=1,2,...,L$, each of which is applied to every block of data symbols to create *L* phase-shifted OFDM symbol candidates for every OFDM symbol. The candidate with the lower PAPR value substitutes the original OFDM symbol. The number *i* (called here the *finder*) of the corresponding Θ_i that phase-shifted the selected OFDM candidate should be transmitted as additional information. The receiver side knows the set of Θ_i alternatives used at the

transmitter, then the original symbol can be recovered at the receiver side by knowing the *i-finder* and then subtracting the corresponding phase-shifts $\left[\theta_{1,i},\theta_{2,i},...,\theta_{N,i}\right]$ to the received data symbols.

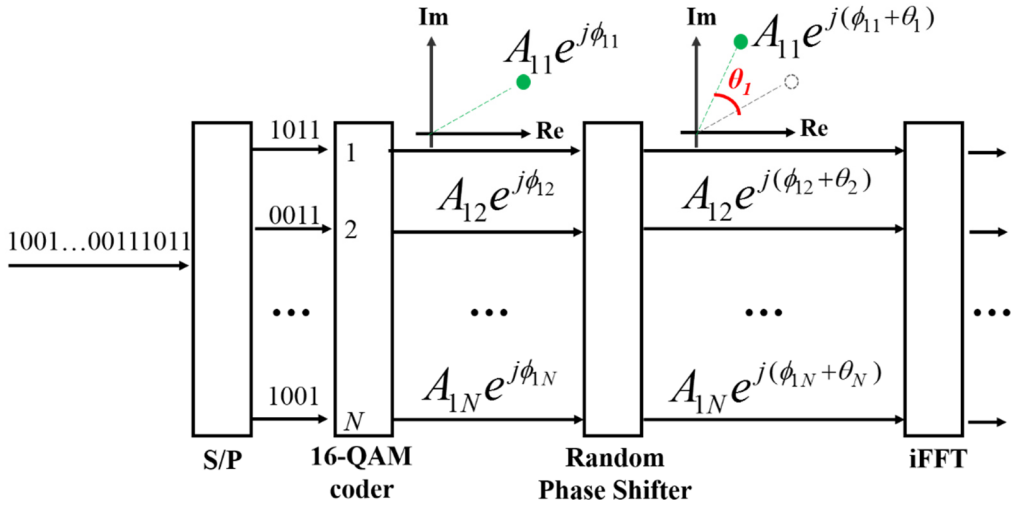

Figure 4.4 Schematic diagram of the operation of the random phase shifter block for a single optical channel. *N* stands for the number of OFDM subcarriers, $A_{mn}e^{j\phi_{mn}}$ represents the *n*-th 16-QAM symbol of the *m*-th OFDM symbol.

Although the SLM method effectively reduces the PAPR, its use increases the latency and complexity of the digital transmitter and receiver and decreases the spectral efficiency since the *i*-finder of the chosen Θ_i should be transmitted jointly with every OFDM symbol. The use of a less complex alternative was then explored.

The employed modulation format has a finite alphabet composed of 16 symbols. Then, the number of possible different OFDM symbols that can be generated for a given number of *sub-carriers*, although huge, is finite as well. Moreover, among all the possible combinations of 16-QAM symbols to conform an OFDM symbol, just some of them result in high PAPR. As discussed before, by introducing a different phase shift to every symbol of each of these combinations, the PAPR value can be reduced. However, finding a unique block of phase shifts that works for all the "high-PAPR" combinations while maintaining the PAPR of the "low-PAPR" combinations, is a difficult, but achievable task.

Based on this tenet, a simplified and empirical alternative to the SLM technique was here tested. Several Θ_i alternatives were generated and the resulting PAPR examined using many different sequences of data symbols. Few of them were found to work well for most of the sequences. After many repetitions, the Θ_0 block that resulted in the lowest PAPR for the majority of the tested sequences was selected. This Θ_0 was used as a fixed phase-shift block for PAPR reduction in our numerical analysis. As explained before, a pilot-aided digital equalizer corrects the phase distortion of each symbol at the receiver side, including these intentionally added phase shifts.

Since a trial-and-error methodology led to the Θ_0 block, which certainly is not the optimum one for every OFDM symbol, it is expected that the use of this method incurs in some penalty. However, this is certainly overcome by the fact that the method indeed does reduce the average PAPR of the whole transmitted OFDM signal while keeping the complexity, latency and data transmission efficiency of the system within acceptable limits. The functionality of the proposed method is demonstrated in section 4.3.3.

4.3 Optimization of the EAM operation

4.3.1 Results for O- band operation

In order to avoid nonlinear distortions originated at the transmitter side, a linear RF-to-optical (RTO) signal conversion is necessary for every optical OFDM implementation. Undesirably, the transmission function of an EAM has a narrow linear region compared to that of a typical MZM; therefore, maintaining the driving voltage within the linear regime of the EAM produces a low OMI, and the SB optical power becomes relatively low. The OMI of the signal can be increased at the expense of driving the EAM beyond its linear range, but this in turn increases the SSII. This inverse relation between OMI and SSII can be quantified in terms of the optical SB-to-noise-ratio (OSBNR). In order to explore the impact on the OSBNR and the performance of the system of driving the modulator in different regions of its transmission function, Figure 4.5 shows five representative cases. As mentioned before, the voltage of the driving signal is the sum of the EAM bias voltage (static) and the (dynamic) voltage of the modulating signal. The latter could be varied by changing the electrical gain (eG) of the electrical amplifier that is placed at the input of each EAM (see Figure 4.1). The five scenarios presented in Figure 4.5 are formed by combining pairs of eG and V_{bias} values. Each of the five subfigures that comprises Figure 4.5 provides the following graphical information: the electrical driving signal (composed by adding the bias voltage to the modulating signal), the corresponding operation region over the optical field transfer function, and the optical spectrum at the output port of the EAM (before lower SB suppression). The OSBNR is also displayed. The analysis is carried out on channel three of the WDM system.

For a fixed V_{bias} = 0.9 V, Figure 4.5.a1, Figure 4.5.a2 and Figure 4.5.a3 show results for eG = 1.0, 2.5 and 4.0, respectively. Note that V_{bias} = 0.9 V lies approximately in the middle of the linear region of the modulator. For eG = 1.0, the modulating signal has an RMS voltage of 0.14 V_{RMS} and maximum voltage excursions of ±0.6 V. For the EAM used in our investigation for O-band a linear RTO transformation is achieved for driving voltages between 0.2 and 1.4 V (see Figure 2.4), therefore, when eG = 1.0, the signal clearly drives the modulator within its linear regime. Nonetheless, a relatively low optical OSBNR of 19.3 dB is obtained. For eG = 2.5, the resulting amplified modulating signal has in this case a 0.35 V_{RMS} voltage with excursions in the order of ±1.0 V. Although some of the voltage peaks lie outside the linear range, most of the signal is linearly RTO transformed; in consequence, the OSBNR increases to 20.7 dB. For the third case (eG = 4.0), an electrical signal with RMS voltage of 0.56 V_{RMS} and excursions greater than ±1.5 V drives the modulator out of its linear operation regime, which results in an OSBNR = 19.5 dB. Regardless of the fact that the SB optical power increases by 10 dB when eG increases from 1.0 to 4.0, the resulting OSBNR exhibits a marginal change of only 0.2 dB. This occurs because the SSII also increases as a result of operating the EAM within its non-linear

region (see corresponding spectra in Figure 4.5.a1 and Figure 4.5.a3). The BER values obtained when eG = 1.0, 2.5 and 4.0 are $1.1x10^{-2}$, $1.5x10^{-5}$ and $1.3x10^{-2}$, respectively, which are consistent with the OSBNR value obtained in each case.

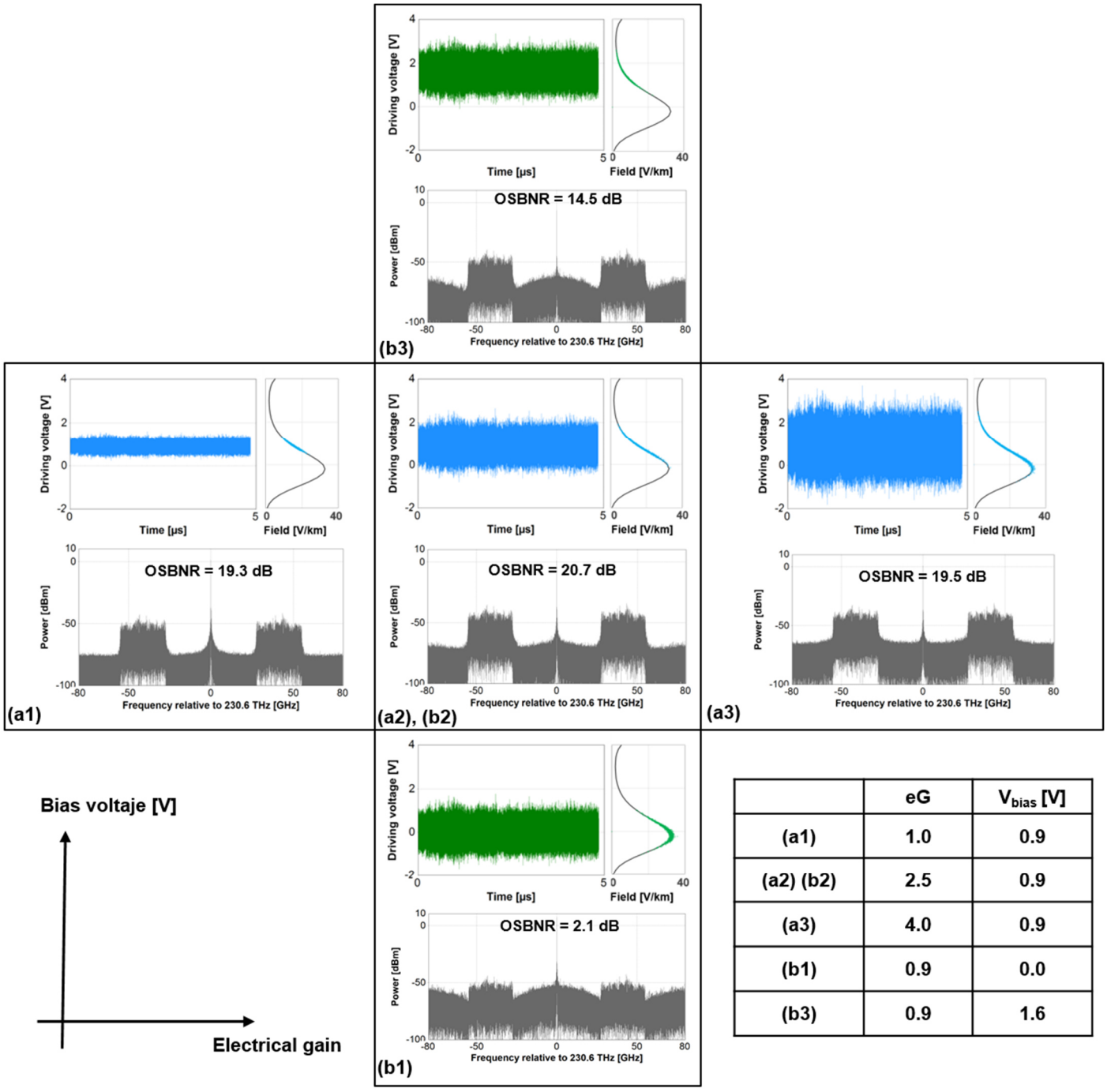

	eG	V_{bias} [V]
(a1)	1.0	0.9
(a2) (b2)	2.5	0.9
(a3)	4.0	0.9
(b1)	0.9	0.0
(b3)	0.9	1.6

Figure 4.5 Electrical driving signal at the input of the modulator, EAM region of operation on the transmission function, and corresponding optical spectrum at the output of the EAM for representative pairs of eG and V_{bias}. The OSBNR is measured at a resolution of 12.5 GHz.

Now, if the eG value is fixed to 2.5 and V_{bias} is set to 0 and 1.6 V, the graphs in Figure 4.5.b1 and Figure 4.5.b3, come up. The intermediate situation, V_{bias} = 0.9 V, has previously been analyzed (Figure 4.5.a2). For a fixed eG, the modulating signal remains the same in the three cases. However, a variation in V_{bias} shifts the EAM operation region, and in consequence the SSII value, keeping fixed the SB-optical power. For V_{bias} = 0 V, the signal drives the modulator under a strong non-linear regime. This results in a drastic increase of the SSII and a sharp reduction of the OSBNR (see the spectrum in Figure 4.5.b1), e.g. from 20.7 dB, for a reference V_{bias} = 0.9 V, to 2.1 dB. For a greater V_{bias} = 1.6 V, the operation regime lies again in the non-linear region and a low OSBNR of 14.5 dB is obtained. The poor BER values obtained for V_{bias} = 0 and 1.6 V are $1.5x10^{-1}$, and $3.8x10^{-2}$, again consistent with their corresponding OSBNR values.

The previous analysis shows that an adequate trade-off between OMI and modulator nonlinear distortion should then be found to obtain an optimum value of OSBNR that maximizes the system performance. Figure 4.6.a and Figure 4.6.b presents, for the 4 WDM channels, and after 10-km of fiber propagation, curves of BER versus eG for V_{bias}= 0.9 V and BER versus V_{bias} for eG = 2.5, respectively. The particular cases discussed in relation to Figure 4.5 are highlighted in Figure 4.6. It could be observed that, irrespective of the channel, there is an optimum eG (V_{bias}) of about 2.5 (0.9 V) that minimizes the BER. For these values all channels outperform the pre-FEC limit of 3.8×10^{-5}. For eG and V_{bias} values lower (higher) than 2.5 and 0.9 V, respectively, the BER performance decreases as a result of OMI (SSII) reduction (increase). The optimum values of eG and V_{bias} here derived were used to carry out the rest of the simulations corresponding to the O-band operation analysis.

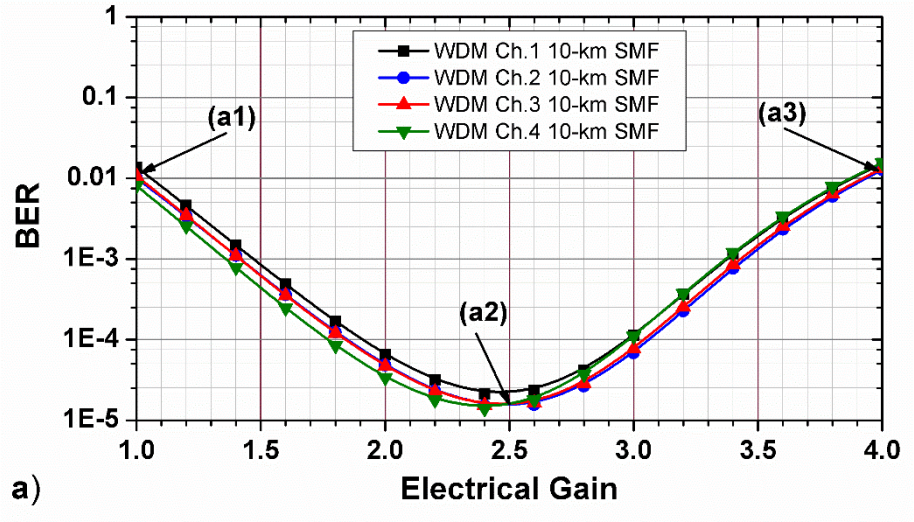

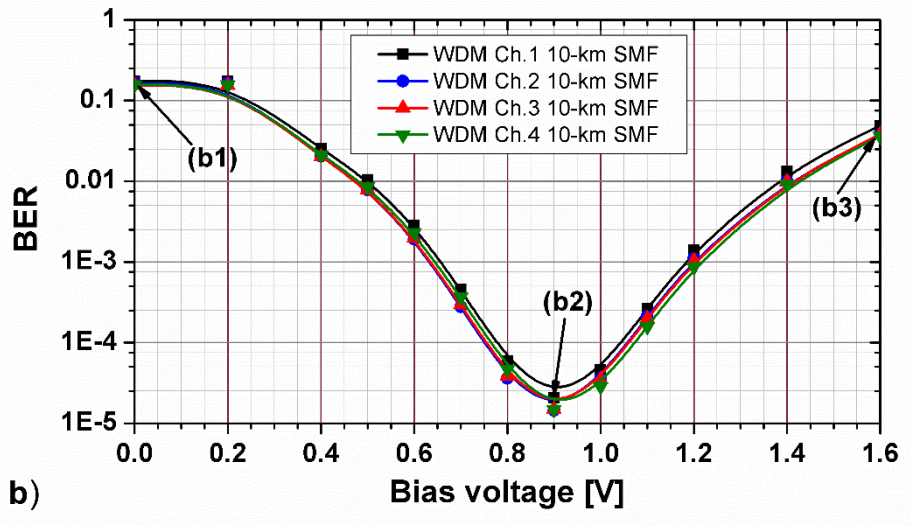

Figure 4.6 BER of the setup shown in Figure 4.1 operated in O-band after 10-km of fiber propagation as a function of a) the electrical gain of the amplifier placed at the input of the EAM, for a V_b = 0.9 and b) the bias voltage of the EAM for an eG = 2.5. The cases shown in Figure 4.5 are highlighted.

4.3.2 Results for C- band operation

For the EAM used for C-band operation a linear RTO transformation is achieved for driving voltages between -0.4 and -1.6 V (input dynamic range of 1.2 V) that also corresponds to low values of the chirp factor, varying between -0.3 and 0.8 (see Figure 4.2). As mentioned before, maintaining the driving voltage within the linear regime of the EAM produces a low OMI. For instance, when the eG of the eA that is placed at the input of each EAM (see Figure 4.1) is set to one, an electrical signal with RMS voltage of 0.14 V_{RMS} and maximum excursions of about ±0.6 V is generated by the eRF-IQ-OFDM transmitter (see Figure 4.8.b). This signal clearly drives the modulator within its linear regime, provided V_{bias}= -1 V. However, our simulations show that the resulting BER of any of the four channels after 10-km of fiber transmission remains above an unacceptable $3x10^{-4}$ since a relatively low OSBNR of 19 dB is also obtained. The trade-off between OMI and modulator nonlinear distortion is presented in Figure 4.7.a, which shows, for the 4 WDM channels, and after 10-km of fiber propagation, curves of BER versus eG for V_{bias}= -1.3 V. Again, there is an optimum eG of about 1.55 that minimizes the BER, irrespective of the channel. The resulting amplified driving signal has in this case an RMS voltage of 0.22 V_{RMS} and maximum voltage excursions of ±1.0 V. Despite some of the voltage peaks lie outside the linear range, most of the signal is linearly RTO transformed, and hence OSBNR and BER values of approximately 21 dB and up to $3.5x10^{-5}$, respectively, are obtained for the four channels. For eG values lower (higher) than 1.55, the BER performance decrease as a result of OMI (SSII) reduction (increase). The optimum V_{bias} for eG = 1.55 can be measured from Figure 4.7.b. It amounts to about -1.3 V, with minimum variation for all channels. A change in V_{bias} from its optimum value for a fixed eG, increases the SSII value while keeping fixed the SB-optical power. This in turn results in a reduction of the OSBNR, thus explaining the increase in BER values observed in the figure. The optimized eG and bias voltage values were used to carry out the rest of the C-band simulations, unless otherwise stated.

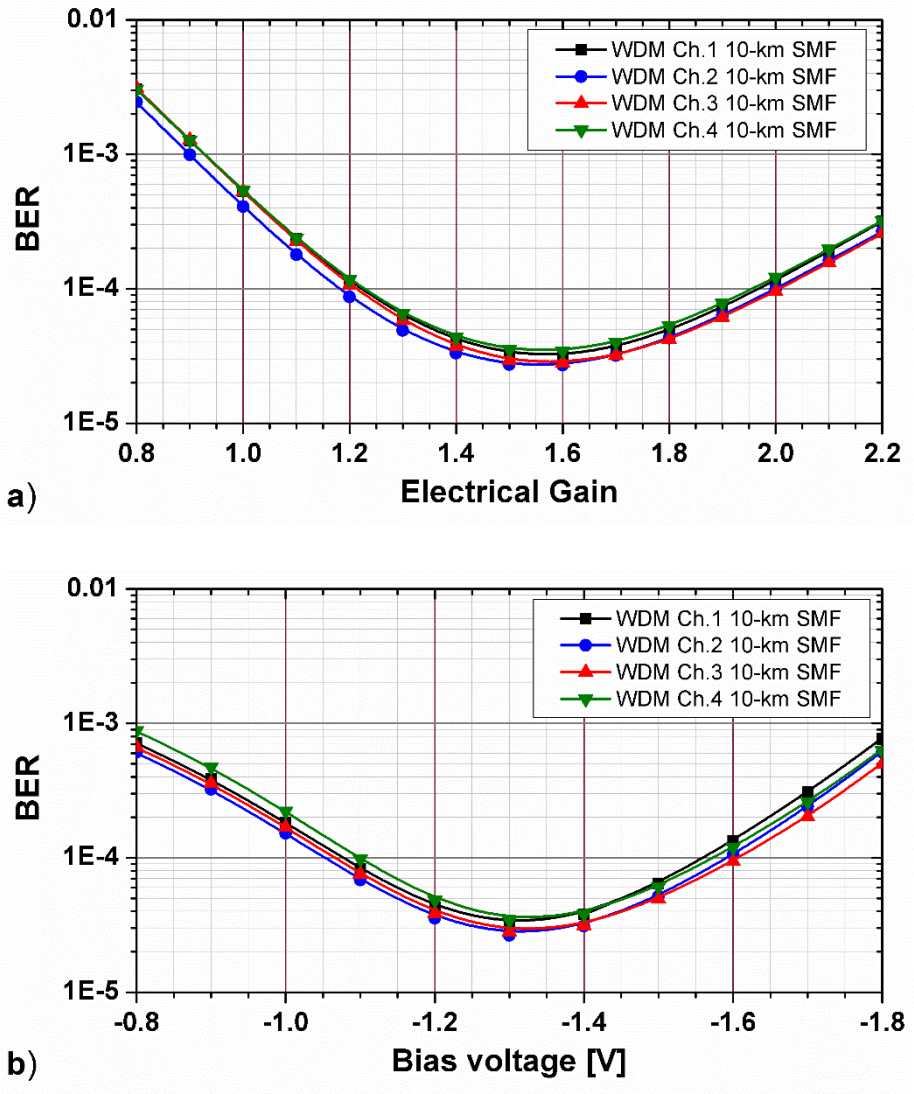

Figure 4.7 BER of the setup shown in Figure 4.1 operated in C-band after 10-km of fiber propagation as a function of a) the electrical gain of the amplifier placed at the input of the EAM and b) the bias voltage of the EAM.

4.3.3 Impact of PAPR reduction and frequency domain equalization

The effect of using the phase shifting technique, described in section 4.2.4, to reduce the PAPR of the eRF-IQ-OFDM signal, is shown in Figure 4.8. C-band operation is used as a matter of example. The graphs in Figure 4.8.b and Figure 4.8.c show a representation of 512 OFDM symbols in the time domain for an un-optimized eG = 1.0. The use of the phase shifting technique lowers the voltage maximum excursions from about ±2.2 V to a peak voltage $|Vp| < 0.6$ V. This, in turn, helps to reduce the PAPR value from 23.1 to 12.6 dB. For a single channel back-to-back (BtB) transmission this means a reduction in BER from 3.5×10^{-1} to 2.9×10^{-4} for the same ROP. The technique significantly improves the performance of the system, because, otherwise, the high peaks of the electrical signal would have driven the EAM into the strong non-linear operation regime, thus producing significant undesirable SSII products. Figure 4.8.a shows the optical spectrum at the output of

the EAM (before optical filtering) for the DFB (carrier) centered at the nominal frequency of Ch.3. The SSII products are evident when the phase shifting technique is not applied (light blue), whereas a higher OSBNR can be appreciated for the reduced PAPR case (dark blue).

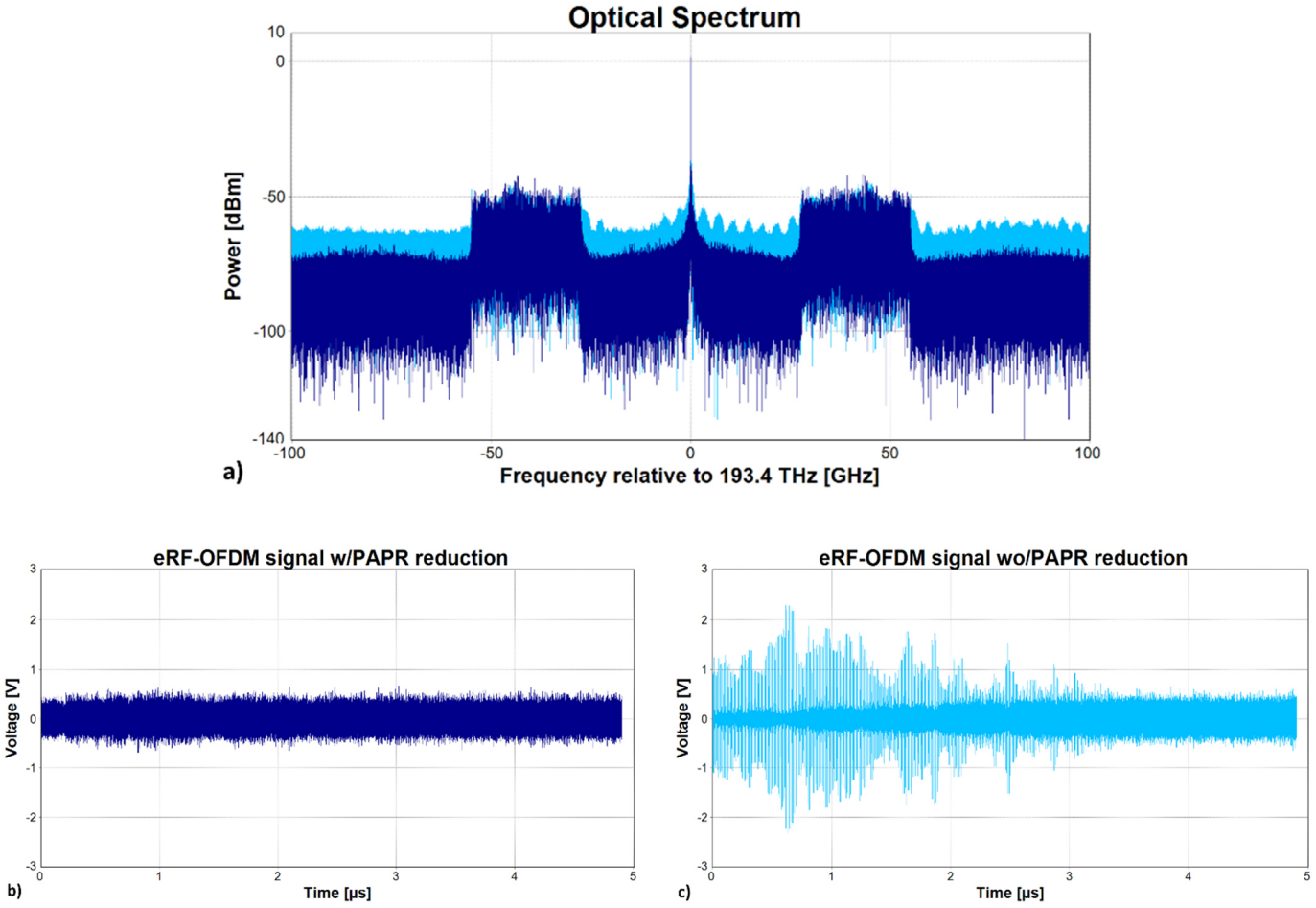

Figure 4.8 a) Optical spectra at the output of the EAM for single channel transmission (Ch. 3) and two different input eRF-IQ-OFDM signals: b) when the PAPR reduction technique is used (dark blue) and c) when it is omitted (light blue). The electrical gain eG = 1.0.

Despite the relatively short transmission length of the application under consideration, electronic dispersion compensation is critical to reach a BER < 3.8 x 10^{-5}. The relevance of the single-tap FDE used mainly as electronic dispersion compensator (EDC) can be demonstrated with the constellation diagram displayed in Figure 4.9.a, which shows the result of a 10-km single-channel transmission simulation when the EDC is absent from the receiver. Here the rest of the equalization scheme (to compensate, e.g., for the phase shift induced by the anti-PAPR technique) is maintained. Clearly, the phase shift induced by chromatic dispersion in the 16-QAM symbols severely deteriorates the system performance. When the EDC is included into the receiver, Figure 4.9.b is obtained. A BER of 3.4 x 10^{-5} can be measured from the constellation, hence demonstrating the significance of the compensator. Figure 4.9.c shows the constellation diagram for the BtB situation, where dispersion compensation is irrelevant. The resemblance with Figure 4.9.b confirms the correct operation of the

EDC. The spread in the received electrical subcarriers observed in both constellations is in general produced by the transmission/reception processes, but it can mainly be ascribed to optical modulation, where a residual nonlinearity-induced SSII is still present as well as a non-zero chirp, and to the noise generated at the laser and the photodiode.

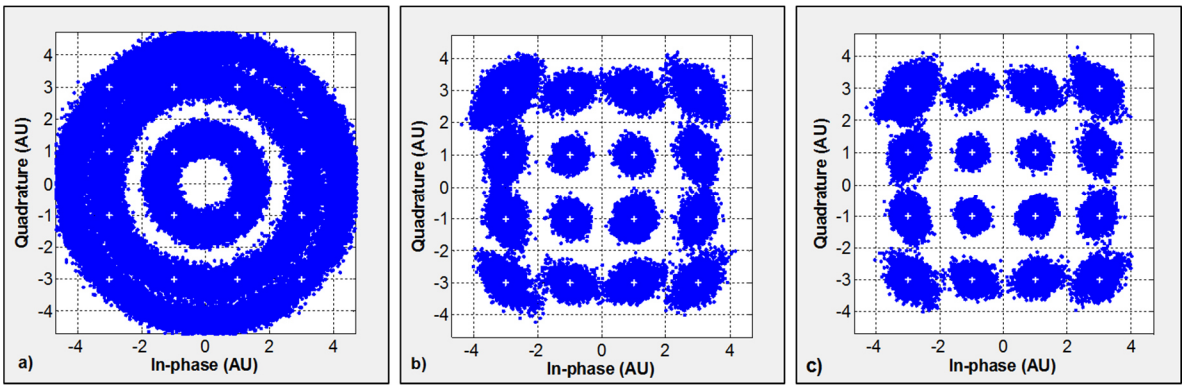

Figure 4.9 Single-channel (SCh 3) received constellation diagrams for different transmission schemes: a) after 10-km of fiber propagation where EDC is turned off, b) after 10-km of fiber propagation where EDC is turned on, c) back-to-back case.

4.4 Technical feasibility of the DDO-OFDM EAM-based system in C- and O-bands

The technical feasibility of the 4 x 100 Gb/s DDO-OFDM system for up to 10 km of fiber is now numerically demonstrated using the optimized EAM, for both C-band and O-band operation cases. Let us start the analysis of the system operated in C-band.

Figure 4.10 shows curves of BER as a function of ROP. Single-channel performance results, measured at Ch.3, are presented for the BtB (black curve with squares) and 10 km fiber transmission (blue curve with circles) cases. Sensitivities at BER = 3.8×10^{-5} of -7 dBm and -4 dBm are respectively measured, leading to a power penalty (PP) of 3.0 dB. This PP is mainly due to the interaction between chirp and dispersion and to the dispersion-induced phase mismatch between the optical carrier and the SB at the detection stage. Note that the 173 ps/nm chromatic dispersion is electronically compensated at the receiver. When the four channels are launched into the 10-km CSMF (red curve w/triangles), a sensitivity of -3.2 dBm is measured, which results in a PP of 0.8 dB with respect to the single channel case. This PP can be ascribed to linear cross-talk (XTPP). Since the system total losses amounts to 9 dB (6 dB for MUX and DEMUX, 1 dB for connectors and 2 dB for 10-km CSMF attenuation), a power budget analysis shows that a transmitter average output power of 5.8 dBm/Ch is necessary to reach the -3.2 dBm sensitivity level. According to our simulations, this corresponds to a DFB output power of 13.7 dBm, provided the optimized EAM is utilized. A slightly higher output power of 14 dBm was used to carry out our simulations, thus guaranteeing proper operation of all channels. This is a power attainable with current state-of-the-art lasers [138].

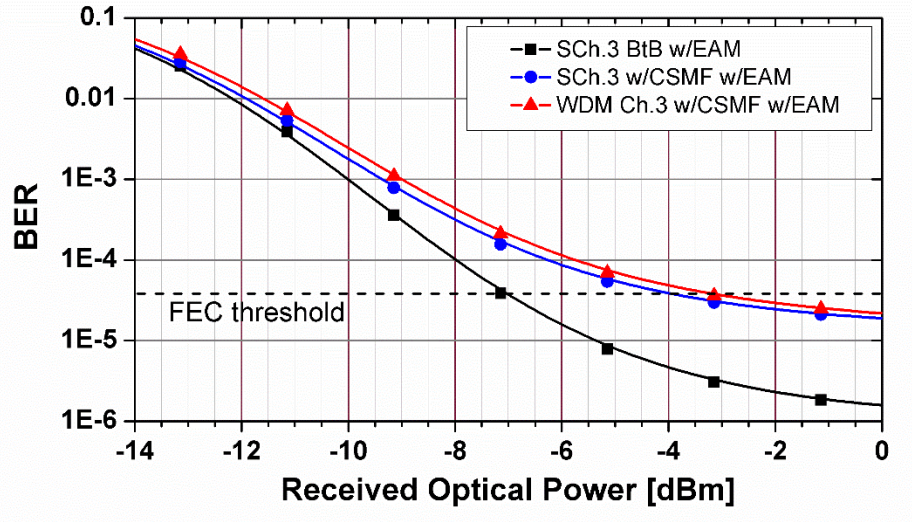

Figure 4.10 BER as a function of ROP of the system in Figure 4.1 operated in C-band for different transmission scenarios.

Table 1 shows the BER and EVM_{RMS} [%] of the system, and corresponding ROP, after 2 and 10 km of fiber transmission for a DFB output power of 14 dBm. For the transmission case where the fiber length, L, equals 2 km, the same transceiver parameters as for the L = 10 km case are used. Not even the cyclic prefix length is optimized. For L = 10 km, a BER $\leq 3.5 \times 10^{-5}$ is obtained for all channels, thus demonstrating the technical feasibility of the DD-OFDM set up as an alternative for the next-generation 10-km CSMF 400 Gb/s Ethernet standard. In addition, the numerical results presented in Table 4.1 demonstrate that the 10-km transceiver, without any extra tuning, can also be used to set up the 2-km CSMF version of the Ethernet standard.

Table 4.1 BER (and EVM_{RMS} [%]) for the WDM DD-OFDM system shown on Fig. 1 for L = 2 and 10 km reach.

Channel	Ch.1	Ch.2	Ch.3	Ch.4
EVM [%] @ L = 2 km	10.13	10.27	10.10	10.18
BER @ L = 2 km	3.8×10^{-6}	4.9×10^{-6}	3.5×10^{-6}	4.2×10^{-6}
ROP @ L = 2 km [dBm]	-1.51	-1.51	-1.53	-1.53
EVM [%] @ L = 10 km	11.38	11.26	11.29	11.42
BER @ L = 10 km	3.2×10^{-5}	2.7×10^{-5}	2.7×10^{-5}	3.4×10^{-5}
ROP @ L = 10 km [dBm]	-3.11	-3.11	-3.13	-3.13

The technical feasibility of the system operated on O-band is now analyzed. Figure 4.11 shows curves of BER versus ROP for this case. Sensitivities at BER = 3.8×10^{-5} of -7.8 dBm and -7.6 dBm are measured, for single-channel (measured at Ch.3) BtB (black curve with squares) and 10 km fiber transmission (blue curve with circles) cases, respectively. A relatively small FPP of 0.2 dB is obtained. The penalty due to fiber non-linear effects was also found to be negligible, as expected. When the four channels are launched into the 10-km CSMF (red curve w/triangles), a sensitivity of -7.5 dBm is measured, which results in a linear XTPP of 0.1 dB. Both penalties, FPP (0.2 dB) and XTPP (0.1 dB), are very low, and are the result of an adequate choice of the optical channel operating wavelengths. In the former case, all wavelengths are located very close to the fiber zero-dispersion wavelength, this results in low accumulated chromatic dispersion values. In the latter case, the difference between any two wavelengths (or channel spacing) can be considered wide enough to practically eliminate the effect of XT.

By comparing the aggregated penalty (FPP + XTPP) of the systems operating in different bands, a higher penalty of 3.5 dB is obtained for the C-band scheme. Note however, that all four channels in this scheme observe a lower CSMF attenuation value of about 0.2 dB/km, leading to total losses of 9 dB (6 dB for MUX and DEMUX, 1 dB for connectors and 2 dB for 10-km CSMF attenuation). In contrast, the total losses of the O-band system amounts to 12 dB. That is, 3 dB higher than in the C-band case. Therefore, the advantage in terms of FPP obtained in the O-band system is practically compensated by the gain in terms of lower attenuation in the C-band system. It thus results natural to think that if the C-band system is technically feasible, the O-band system should be feasible as well. A power budget analysis shows that as long as a transmitter average output power of 4.5 dBm/Ch is delivered to the fiber, the necessary -7.5 dBm sensitivity level for the WDM case could be achieved. According to our simulations, this corresponds to a DFB output power of 11.6 dBm, provided the optimized EAM is used. A power of 12 dBm was set to guarantee proper operation of all channels. Deploying the EAM-based OFDM system in O-band thus have the advantages over its C-band counterpart of consuming lower power per laser (2 dB) and exhibiting negligible linear cross-talk.

As part of the feasibility analysis, it is always important to bear in mind that although the optical link for the standard is in principle designed for the maximum reach, it is common practice among operators to deploy the same type of transceivers for interconnects of various lengths. Figure 4.12 shows, for each optical channel of the analyzed O-band system, curves of BER as a function of fiber length, varying from 0 to 20 km. The CP remains optimized for 10 km. It can be observed that for fiber lengths shorter than 10 km, all channels outperform the pre-FEC BER threshold of 3.8×10^{-5}. In other words, the transceivers, optimized for 10 km, work well at shorter distances. This includes the 2-km CSMF-standard under consideration by the 400 GbE TF. In the case of fibers longer than 10 km, either amplification or more powerful transmitters seem to be a must.

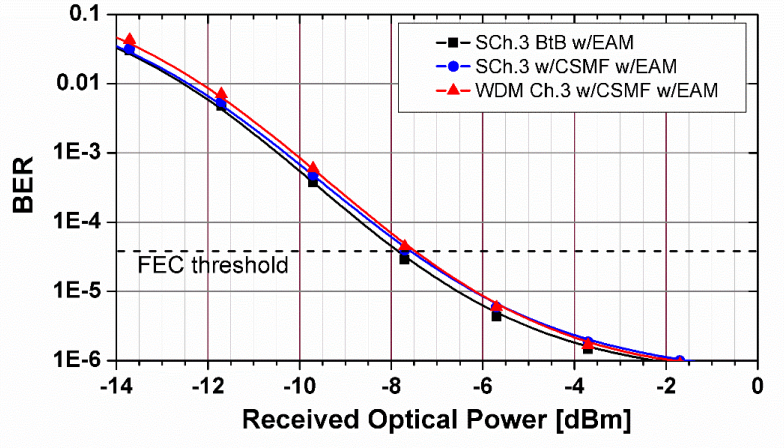

Figure 4.11 BER as a function of ROP of the system in Figure 4.1 operated in O-band for different transmission scenarios.

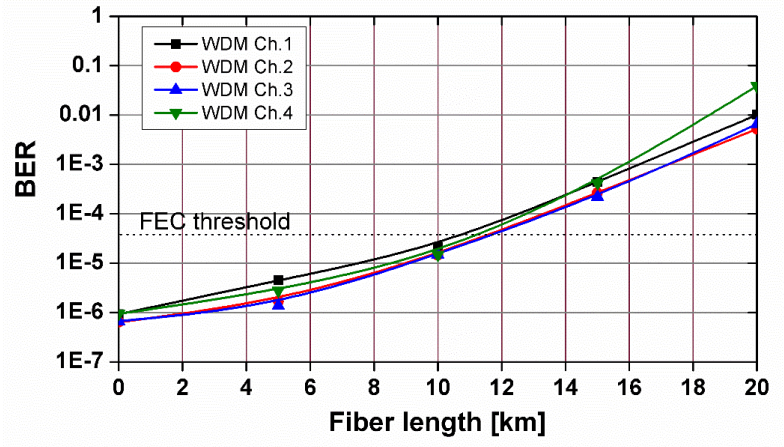

Figure 4.12 BER performance of each of the four channels of the system in Figure 4.1 operated in O-band as a function of fiber length.

4.5 Comparison with a DDO-OFDM MZM-based system

The previously analyzed DDO-OFDM system is now compared in terms of performance with the situation in which a MZM replaces the EAM. The MZM is modeled as described in section 2.1.1. The EAM used for C-band operation is considered. The rest of the setup and parameters of the system are maintained the same. The MZM has a DC and RF V_π of 5 V and an extinction ratio of 35 dB (the power splitting ratio is then $\psi_1 : \psi_2 = 51.8\% : 48.2\%$). Figure 4.13 shows curves of BER versus ROP for a BtB single channel configuration for different transmitter configuration cases: i) using an EAM with BW = 50 GHz and 16-QAM format (in black with squares), ii) using a MZM with BW = 50 GHz and 16-QAM format (in blue with circles), iii) using a MZM with BW = 40 GHz and 32-QAM format (in red with triangles). An optimum MZM bias voltage of 2.8 and 2 V was set for 16-QAM and 32-QAM, respectively. An optimum eG was also set in both cases.

The superiority of the MZM in terms of technical merits is evident when the same modulation format and modulator bandwidth are used. For instance, a sensitivity of -12 dBm for a target BER = 3.8 x 10^{-5} is achieved using a MZM with BW = 50 GHz and 16-QAM, whereas the corresponding sensitivity for the equivalent EAM is found at about -7 dBm. Also, the EAM-based system reaches a floor at BER ≈ 1 x 10^{-6}. In contrast, the MZM-based system can even reach the 400 GbE target BER of 1 x 10^{-13} with a sensitivity of -4 dBm without using any FEC scheme. Note, however, that state-of-the-art MZMs hardly reach bandwidths above 40 GHz. This bandwidth limit is insufficient to transmit 100 Gb/s using 16-QAM format and an RF-IQ-DDO-OFDM scheme, as shown in Figure 4.14. This figure shows the spectrum of a single optical channel at the output of a 40-GHz MZM when 32-QAM and 16-QAM digital modulations are employed in the RF-IQ-DDO-OFDM scheme. Clearly, the limited BW of the MZM degrades the signal high-frequency components, leading to an unacceptable BER value, after 10-km transmission, of 4.4x10^{-2} for the 16-QAM case. This confirms that, in contrast to EAMs, low-order digital modulation formats are unacceptable to set up 100 Gb/s optical channels in MZM-based RF-OFDM transmission systems.

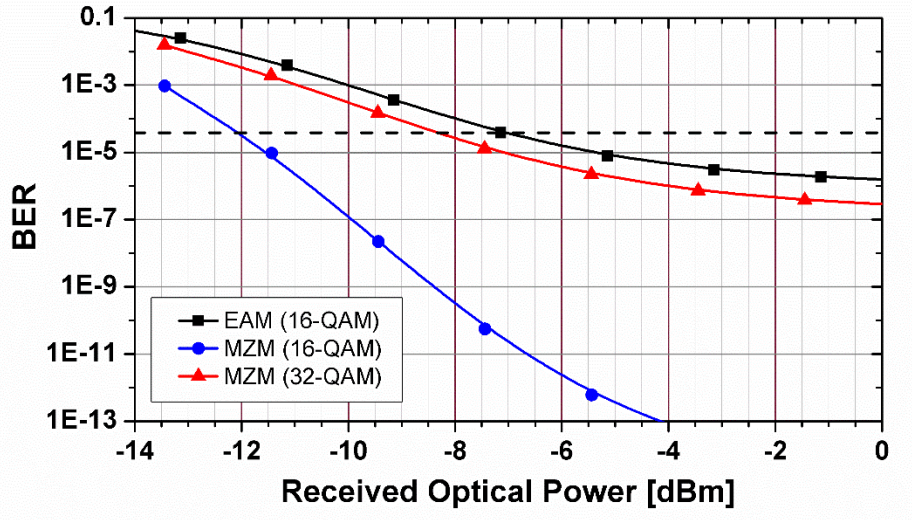

Figure 4.13 BER as a function of ROP for BtB single-channel transmission using an EAM and a MZM.

A steep reduction of the performance when passing from 16-QAM to 32-QAM could be observed by comparing the blue (with circles) and red (with triangles) curves of Figure 4.13. This is an expected result, since the received OSNR is the same in both cases, and it is well known that a higher received OSNR is required to achieve the same BER when the order of the modulation format is increased.

By comparing the red and black curves of Figure 4.13, it can be observed that the MZM-based system using 32-QAM format still outperforms the higher bandwidth EAM-based system. A ROP difference, or PP, of 1.5 dB between them at a BER = 3.8 x 10^{-5} is measured. However, some disadvantages of the MZM in terms of certain criteria that are relevant to the IEEE Task Force in charge of defining a future Ethernet standard, such as backward compatibility, integrability and economic feasibility, might balance the scale in favor of the EAM-based 400 Gb/s transmitter when deciding for a commercial product.

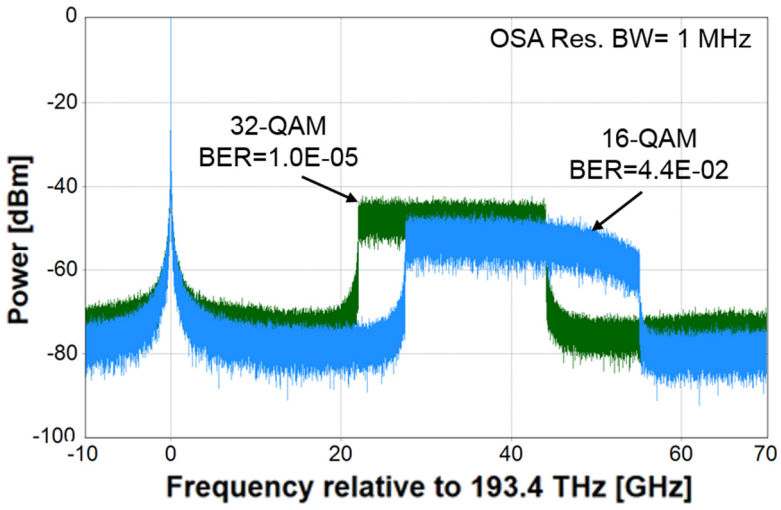

Figure 4.14 Optical spectra at the output of the 40-GHz BW MZM for an optical channel running at 100 Gb/s and digitally modulated with 16- and 32-QAM.

4.6 Beyond 400 Gb/s

Data rate targets of 800 Gb/s and 1.6 Tb/s have already been envisaged for forthcoming optical interconnection technology in the Ethernet roadmap for 2020+.

To implement a 1.6 Tb/s optical transceiver based on the RF-IQ-DDO-OFDM approach analyzed in this Chapter, sixteen optical channels must be multiplexed. This results in an increase of the total link losses since both the 1:16 multiplexer and the 1:16 de-multiplexer have insertion losses of at least 6 dB each. Then, a multiplexing power penalty of 6 dB between the four-channel and the sixteen-channel cases arises. This penalty must be somehow compensated by increasing the ROP per channel, so the performance target can be maintained.

If the system is operated in C-band with a 100 GHz channel spacing, a large fiber power penalty for the outer channels can be foreseen since, according to our results for the 400 Gb/s system, they experience a large accumulated chromatic dispersion. The use of a tighter channel plan to reduce this penalty is not recommended to avoid excessive cross-talk penalties. Therefore, if one considers the total power penalty that the system would incur due to multiplexing and fiber transmission, the hypothetical 16 x 100 Gb/s DDO-OFDM system does not seem to be a feasible option when operating in C-band.

In contrast, a very small fiber power penalty was measured in O-band for the 4 x 100 Gb/s system, even for the outer channels when using a wide channel spacing of 800 GHz. Therefore, if the 16 x 100 Gb/s DDO-OFDM system is implemented in the O-band with a channel spacing of 100 GHz, a negligible fiber power penalty could be guaranteed for all channels. However, due to channel spacing reduction, a cross-talk power penalty of at least 1 dB, assuming the same value measured for the 100 GHz four-channel system, must be

added to the total losses of the system. A 7 dB link penalty, considering multiplexing and cross-talk, then arises. This penalty could be compensated in the following manners:

- By reducing the reach of the system to only 2 km. This leads to a power saving of 4 dB. The remaining 3 dB must be provided by the lasers. The output power of each laser would then be a high 15 dBm.
- To maintain the reach of the system equal to 10 km, the use of a more complex FEC scheme or the addition of an optical amplifier seems to be a must, as detailed in the following paragraphs:
  - The BER target could be increased to ~1 x 10^{-3} by using a 20% overhead FEC scheme. From Figure 4.13, a sensitivity of -11 dBm at this BER is measured using a MZM and 32-QAM format for the single-channel situation. This represents a power saving of 4 dB with respect to the same situation using an EAM and a 7% overhead FEC. This power saving is the same as the one achieved by reducing the reach to 2 km, then lasers with a high output power of 15 dBm are also required. Undesirably, the use of a more complex FEC scheme increases the overhead, delay and power consumption of the transceiver.
  - For integration, power consumption and footprint reduction purposes, a SOA should be preferred over EDFA or Raman amplifiers. Typical SOAs operated in linear regime can provide a gain of around 20 dB, which would be enough to compensate for the 7 dB penalty. However, a SOA is a high non-linear device with a relatively high noise figure [118]. Therefore, power penalties due to nonlinear distortion, OSNR degradation and gain reduction at the output of the SOA, are expected to be high for the transmission of OFDM signals. For instance, according to Figure 4.11 a ROP = -7.6 dBm is needed to obtain a BER = 3.8 x 10^{-5}. Considering a XTPP = 1 dB for 100 GHz operation, a received power per channel of -6.6 dBm is required to get the same BER. Then, a total power of 11 dBm at the input of the DEMUX (considering insertion losses of 6 dB) is required. This value exceeds the output saturation power of typical bulk SOAs [118]. Therefore, gain clamping and nonlinear distortion power penalties are certainly expected, even if the SOA is operated as pre-amplifier.

In all the situations previously analyzed, the required laser output power turn out to be relatively high. Moreover, to set up a 10-km link, the complexity of the system must be increased. A longer reach target seems difficult to achieve, even using an optical amplifier. Furthermore, the power consumption and size of a sixteen channel transceiver with such power requirements are also restrictive factors for its implementation. If on top of that an extra optical amplifier or a more complex FEC scheme turns out to be necessary, the challenge becomes even greater.

To decrease the number of optical channels and therefore reduce cost, size and power consumption, an increase on the data rate per channel of the system seems to be the only solution. However, based on the current electro-optic technology, operation of the analyzed DDO-OFDM system (or even other approaches such as DMT, PAM or CAP, relying on direct detection) beyond 100 Gb/s per optical lane does not seem to be technically feasible. Based on the aforementioned arguments, a solution to achieve data rates from 800 Gb/s and up to 1.6 Tb/s is the use of coherent technology. This would most probably allow to substantially augment the system reach and reduce the number of optical channels without employing any kind of FEC scheme or optical

amplification. The feasibility of terabit optical systems for the metro-access space using this kind of advanced technology is the subject of the next Chapter.

4.7 Conclusions of the Chapter

The proposal of an unamplified 4 x 100 Gb/s WDM system over conventional SMF to be considered for next-generation Ethernet optical interconnects running at 400 Gb/s was presented. It is characterized by two main features: 1) each of the four optical channels is transmitted at 100 Gb/s through the use of RF-IQ-DDO-OFDM and 16-QAM modulation, 2) instead of typical, stand-alone Mach-Zehnder modulators, the system proposal employs potentially low-cost electro-absorption modulators.

An optimization procedure in terms of BER of the main modulator parameters (bias voltage and electrical gain) is carried out. A BER < 3.8×10^{-5} is demonstrated for up to 10-km of fiber transmission in both C- and O-bands by combining a simple, yet functional, PAPR-reduction technique with the optimum choice of bias voltage and electrical gain, thus leading to an acceptable trade-off between modulation index and nonlinear response of the optical modulator. It is then numerically demonstrated that the system runs error-free up to 10 km, provided that a low-overhead and power-efficient Reed-Solomon FEC scheme is assumed.

For single-channel back-to-back transmission, a receiver sensitivity of -7.0 and -7.8 dBm was measured for C- and O-band operation, respectively. The difference between the sensitivity values is due to the different total losses of the employed EAM in each case. Fiber and cross-talk power penalties of 3 and 1 dB are measured, respectively, for the 100 GHz spaced C-band grid. In contrast, the corresponding penalties in O-band with 800 GHz channel spacing, are very small. The higher fiber power penalty in C-band is fully compensated due to 3 dB less fiber attenuation for a 10 km transmission. Therefore, both C- and O-band schemes achieve the same performance with similar power laser requirements.

A back-to-back comparison between the same DDO-OFDM system using an EAM and a MZM was performed, which revealed that the performance using a MZM is notoriously better when 16-QAM format and the same 50-GHz modulator bandwidth is considered. However, unlike a state-of-the-art EAMs, the bandwidth of a state-of-the-art MZM does not exceed 40-GHz. To reduce the MZM required bandwidth to 40-GHz, the use of 32-QAM format is needed. In this case, the performance of the system is steeply reduced, but it is still slightly better than using a 50-GHz EAM and 16-QAM format. For instance, a penalty of 1.5 dB between them at a BER = 3.8 x 10-5 was measured. However, some disadvantages of the MZM in terms of certain criteria that are relevant in the intra-DCI space, such as integrability and economic feasibility, might balance the scale in favor of the EAM-based 400 Gb/s transmitter when deciding for a commercial product.

Although the DDO-OFDM proposed solution might be more technically complex and currently more expensive than an 8 x 50 Gb/s PAM-4 approach, we believe its cost will become reduced in the mid-term, as high-bandwidth electro-optic devices becomes more widely available. The simulation analysis presented here positions the proposed scheme as a technically feasible alternative to set up the physical layer for the next generation of Ethernet optical interconnects running at 400 Gb/s.

5. Chapter five: Numerical analysis of a 800 to 1600 Gb/s optical inter-DCI based on WDM multi-format coherent transceiver

Due to the exponential growth of the bandwidth demand, a permanent technological update of the physical infrastructure of the networks at all levels of coverage is necessary. To develop next-generation metro access and short-reach optical links, two approaches have mainly been considered. One of them is up-scaling from direct detection schemes developed for 400 Gb/s intra-DCI applications in order to preserve their inherent low cost, small footprint and low power consumption features. The second approach relies on down-scaling from coherent detection solutions aimed for long-haul links, betting for an imminent reduction of the cost, size and energy consumption of the required technology adapted to shorter-haul link requirements.

By following the second approach, in this Chapter an eight-channel multi-format coherent optical transceiver is proposed as an alternative to implement terabit metro inter-data center interconnects transmitting from 800 to 1600 Gb/s over CSMF. The maximum reach of the system as a function of transmitted power and overall capacity is numerically estimated for a BER target of $1x10^{-13}$, avoiding the use of optical amplification and FEC schemes. Design parameters of the main system devices were tuned up in order to find an adequate trade-off between system performance and their current availability in the market.

5.1 State-of-the-art and context

Due to the continuous emergence of new services and applications such as video-on-demand, server virtualization, cloud computing, grid computing and "the internet of things", bandwidth demand at the metropolitan and short-reach network level will steadily continue growing at least for the next few years [16], [146], [147]. As a response to this claim, the main drivers in the telecommunications community have joined forces to develop or extend technology and standards to augment the transmission data rates of the corresponding optical fiber-based systems. For instance, the 200 and 400 Gb/s Ethernet standards are expected to come up in the very near future [148] for optical interconnection within data centers. Notwithstanding, in order to cope with the bandwidth increasing demand, a technological leapfrog in the metro and short-reach space will soon be required. As for long-haul networks, in metro regional links the use of coherent optical communications systems have become predominant. In contrast, for shorter-haul applications, such as metro access and intra- and inter-data center interconnection [16], the use of direct detection technology is still preferred due to its simplicity and low cost.

Recent technological achievements to increase the speed and reach of current direct detection systems have focused on taking advantage of faster electronics to speed up the symbol or bit rate per wavelength channel, on increasing the optical channel count, or on employing more spectrally-efficient modulation formats [149], such as the extensively investigated PAM and DMT systems. Another direct detection alternative for the transmission of 400 Gb/s was presented in Chapter 4 of this thesis work and its technical feasibility was

demonstrated for a maximum reach of 10 km by means of numerical simulations. Although relatively uninvolved and cost-effective for intra-data center applications up to 400 Gb/s, direct detection unrepeated transmission systems exhibit serious limitations in terms of reach and data rate per wavelength channel, which make them unsuitable for the implementation of inter-data center terabit metro networks [4], [16]. In contrast, COCSs offer higher sensitivity and efficient use of the available spectrum. Moreover, they can deal with multi-level optical modulation (in power, phase and polarization), incorporate adaptive electronic equalization of transmission impairments, and add flexibility to the network (see section 2.5). The latter characteristic is important to adapt the network to changes in traffic demand on a cost-effective manner. It is therefore straightforward to envisage that, provided that the cost of key enabler components such as high-performance transceivers [150] sufficiently decreases (as normally happens), a migration of COCS from the long-haul realm to the metro or even the access space will eventually occur [151], [152]. In fact, COCSs have been proposed as an alternative to implement next-generation 400 Gb/s Ethernet over SMF [153]. Their use not only allows to extend the system's maximum reach from 10 to at least 40 km [154], serving inter-data centers, but also to halve the already agreed optical channel count [155]. Moreover, the Ethernet Alliance has already tentatively considered a bit rate of 1.6 Tb/s in its 2016 roadmap for a future Ethernet standard [156], which will most probably be based on the use of coherent transceivers assisted by digital signal processing, wavelength division multiplexing, and low cardinality advanced digital modulation formats, that is, QPSK and 16-QAM [157]. The performance analysis of 100 Gb/s PM-QPSK and 200 Gb/s PM-16-QAM transceivers with respect to relevant transmission characteristics have been presented in [154], [158] for metro access point-to-point links, and in [150] for a ROADM-based metro ring topology that relies on the use of optical amplifiers, FEC (i.e. BER$\leq$1 x10^{-3}) and a tightly spaced 144-channel Nyquist WDM grid. Also, Demonstrator 2 of the Horizon 2020 EU DIMENSION ongoing project focuses on an amplified COCS targeting link lengths between 10 and 80 km and considers the development of a power-efficient tunable 200 Gb/s optical transmitter [16]. However, further investigations are necessary to expand the already insufficient reported research in this topic, in specific, regarding the design and analysis of COCSs under shorter-haul links requirements rather than just transfer schemes and devices from the long-haul space.

Based on the aforementioned arguments, in this Chapter we propose and numerically investigate in terms of transmitted power, maximum reach and capacity, a COCS based on the use of flexible (with respect to bit rate and digital modulation format) transceivers that fulfil access network requirements, such as, lack of amplification and FEC (to minimize latency, power consumption and frame overhead), a relatively wide channel spacing to avoid pulse shaping through high-selective (Nyquist) optical filtering, low cardinality advanced digital modulation formats, and fabrication and operational characteristics that satisfy the more cost-conscious access/metro space. All these features set our systems apart from the frequently investigated COCS based on the use of advanced modulation formats. Therefore, our simulation analysis is not only different from more common approaches, but call for a high level of optimization (see section 5.3) to meet the demanding objective of BER $\leq$ 1x10^{-13}. The proposed CSMF-based architecture consists of a dual-polarization, eight WDM-channel scheme lying on C-Band (to diminish fiber attenuation and nonlinear effects) with 100 GHz channel-spacing and running at 100, 150, or 200 Gb/s per wavelength, respectively using QPSK, 8PSK and 16-QAM modulation, thus leading to a uniform raw data rate of 25 GBd that corresponds to an aggregated

transmission capacity of 800, 1200 and 1600 Gb/s. Following the most recent IEEE 802.3bs standard objectives, a target BER of $1x10^{-13}$ has been considered as error-free threshold. Having in mind the extended reach of a prospective physical medium dependent sublayer of an imminent Terabit Ethernet standard, an objective reach of at least 40 km for a maximum capacity of 1.6 Tb/s is pursued. Longer reaches, to cover different targets of the metro access space, can be achieved by decreasing the data rate by means of adapting the modulation format.

5.2 Analyzed architecture and numerical setup

The performance of the proposed architecture was analyzed using the well-tested VPI Transmission Maker™ V9.5 co-simulation suite. Care has been taken to select model parameters in accordance to specifications of commercial or close-to-market devices, thus guaranteeing reliable simulations. A general diagram of the 8-channel analyzed COCSs is shown in Figure 5.1. QPSK, 8PSK or 16-QAM can be chosen as modulation format of each optical channel by simply reconfiguring the electrical signals that drive each modulator and the DSP of the receivers, while leaving the entire optical architecture unchanged. Since the total symbol rate per optical channel is 28 GBd (25 GBd plus 12% of Ethernet overhead), the overall bit rate per optical channel becomes 112, 168 and 224 Gb/s when DP-QPSK, DP-8PSK or DP-16-QAM are selected, respectively. The transmitter (Tx) consists of eight DP-IQ modulators, each composed of two orthogonal pairs of single-drive MZMs [22], one for each polarization state, as described in section 2.5.1. Each optical transmitter makes use of a different seed to produce a distinctive pseudo-random bit sequence (PRBS), 2^{16} bits long [155], thus assuring inter-channel and inter-polarization data independence. The average dynamic losses of each optical IQ modulator were found to be 10.1 dB, 10.3 and 9.8 dB for QPSK, 8PSK and 16-QAM, respectively. Each of the four differential MZMs that conforms a DP-IQ modulator has static losses of 4 dB and a V_π dc and rf of 5 V. Their splitting ratio and 3-dB BW parameters are chosen according to the analysis presented in section 5.3.1. Identical CW DFB lasers act as light sources. The optical frequency grid was set in accordance to ITU-T G.694.1 recommendation for a channel spacing Ω = 100 GHz [155] and was centered at 193.45 THz (see Figure 5.5). C-band was preferred over O-band because of its lower loss and higher chromatic dispersion for the fiber of choice. The latter characteristic is important to reduce the impact of inter-channel nonlinear effects, especially considering that CD is electronically compensated at the receiver. The optical 8:1 MUX and 1:8 DEMUX, which are assumed to be arrayed waveguide gratings, were modeled with third-order Gaussian bandpass filters having insertion losses of 3 dB [159]. The central frequencies of these filters were set to match those of the lasers, while their BW is determined from the analysis presented in section 5.3.2.

After multiplexing, the optical waveforms are launched onto a CSMF, modeled as described in section 2.3, whose characteristics at λ=1550 nm are the following: attenuation of 0.23 dB/km, CD of 18 ps/(nm·km), slope of 0.06 ps/(nm^2·km), A_{eff} = 80 μm^2, polarization mode dispersion index of 0.1 ps/sqrt(km) and nonlinear index $n_2 = 236.82x10^{-22}$ m^2/W. At the receiver end, each demultiplexed optical channel is divided into orthogonally polarized components that are injected into conventional digital coherent receivers (described in section 2.5.1.), which are composed of 90° optical hybrids [160], [161], a local oscillator, balanced photodetectors (BPDs) , an analog-to-digital converter with 8-bits resolution and sampling at 2 Sa/symbol or 56 GSa/s [162], and a

digital signal processing stage. Each BPD comprises of two commercially available high-speed PIN photo-diodes with a responsivity of 0.8 A/W, a dark current of 100 nA with shot-noise and thermal-noise of 10 pA/sqrt(Hz) [163]. An electrical filter, modeled with fifth-order Bessel characteristics and an optimized BW for 16-QAM (see section 5.3.6) is placed at the output of the BPD to reduce noise. For CD compensation, an optical frequency domain equalizer [99] with FFT blocks of size equal to 512 and effective FFT blocks of size of 32, was employed, irrespective of the modulation format. The rest of the DSP algorithms, described in section 2.5.2, are as follows. For M-QPSK modulations: time domain equalization with constant modulus algorithm and multiple-input multiple-output of 11 taps, 50 iterations and error weight of $1x10^{-3}$ for polarization mode dispersion cancellation and cross-talk reduction [98], [102]; and a Viterbi-Viterbi-based algorithm for phase estimation and correction with a block size of 21 symbols [107], [108]. For 16-QAM modulation: TDE with multiple modulus algorithm and multiple-input multiple-output of 6 taps, 50 iterations and error weight of $1x10^{-2}$ for polarization mode dispersion and cross-talk reduction [98], [102], [109]; and a 16-QAM phase estimation and correction algorithm with a block size of 5 symbols [107], [109]. Following [164], the evaluation of the system performance is expressed in terms of BER and estimated directly from the EVM. This approach is normally preferred than direct bit counting because of its inherent reduction of computational resources.

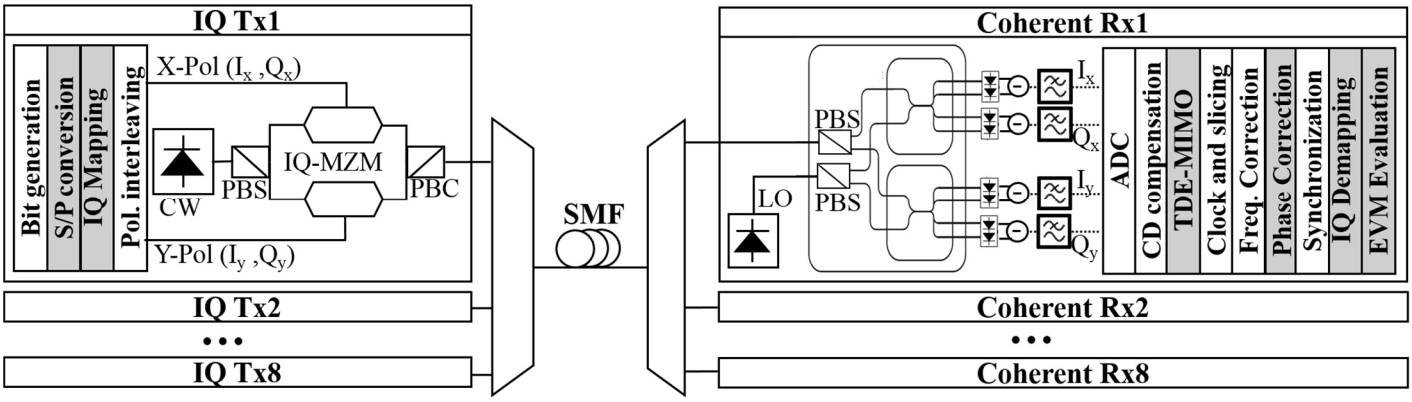

Figure 5.1 System setup of the proposed COCS. Electrical modulation format-dependent elements in gray.

5.3 Tuning of the main physical parameters for 16-QAM format

In this section, different system parameters are analyzed in order to define their optimum values that provide an adequate trade-off between the system performance and the current availability of the employed devices. Since it is well known that most of the system requirements increase as the modulation format increases, particularly regarding the received OSNR and optical power, the analysis of this section is performed using 16-QAM format. Moreover, the use of COCSs employing QPSK as modulation format has been much more investigated than those employing 16-QAM, thus turning the latter format into a more interesting one from a research standpoint. Besides, a 16-QAM-based analysis is more relevant because of its richness and especially, because of its potential use in terabit optical networks. A target reach of 40-km for an overall data rate of 1.6 Tb/s is pursued for the 16-QAM approach. The corresponding parameters found to fulfill this purpose are then

set as fixed values irrespective of the modulation format for the subsequent analyses presented in sections 5.4 and 5.5.

Unless otherwise stated, the parameter values used in the numerical simulations are those presented in Table 5.1. The performance analysis is carried out at the central channel centered at 193.4 THz. The BER is obtained from averaging the EVM of both polarizations.

Table 5.1 Standard Parameter Specifications

	Value	Units
MZM BW	40	GHz
MZM splitting ratio	51:49	%
Tx laser power (P_{Tx})	13	dBm
Tx laser OSNR ($OSNR_{Tx}$)	40	dB
Tx laser linewidth (LW_{Tx})	1	MHz
MUX and DEMUX BW	50	GHz
LO laser power (P_{LO})	10	dBm
LO laser OSNR ($OSNR_{LO}$)	40	dB
LO laser linewidth (LW_{LO})	1	MHz
Receiver electrical filter BW	16.8	GHz
Fiber length	40	km

5.3.1 MZM bandwidth and splitting ratio

Figure 5.2 shows the performance of the system as a function of the electro-optic bandwidth of the MZMs that comprises the IQ modulators, for different MZM extinction ratio (ER) values. The splitting ratio of the modulator is related to the ER parameter as:

$$\psi_1[\%]:\psi_2[\%] = 100\left(0.5+\varepsilon : 0.5-\varepsilon\right) \tag{5.1}$$

where

$$\varepsilon \approx \sqrt{\frac{1}{\mathrm{ER}_{linear}}} \tag{5.2}$$

An infinite ER value corresponds to a perfectly balanced MZM with a 50:50 splitting ratio. In practice, due to fabrication limitations, achieving a balanced 50:50 MZM Y-splitter is very difficult. Hence, imbalanced MZMs have a finite ER. The ER values (in dB) presented in Figure 5.2, namely $\mathrm{ER}[dB] = \{30, 35, 40, 45, 50\}$, correspond to splitting ratios of $\psi_1[\%]:\psi_2[\%] = \{53.2:46.8;\ 51.8:48.2;\ 51:49;\ 50.6:49.4;\ 50.3:49.7\}$. Unbalance of the MZM results in an undesired extra phase modulation which causes transmission penalties [165]. From Figure 5.2, it could be observed that a minimum ER of 40 dB is needed to outperform the system BER target. By setting an ER = 40 dB, a minimum MZM BW = 40 GHz is required. Commercial and

experimental IQ-MZMs having a BW ≥ 40 GHz have been reported in [166], [167], [168] and [169]. A MZM with a lower BW of 35 GHz can be accepted, provided that a MZM ER = 50 dB could be achieved, which represents an unfeasible (almost ideal) 50.3:49.7 splitting ratio requirement. In [170], a MZM with an ER = 47 dB has been reported. A MZM having a moderate ER = 40 dB and a BW = 40 GHz has been chosen to perform the rest of the simulation analysis. Figure 5.3 displays the optical spectrum of the X-polarized field at the output of the IQ-MZM. Different resolution values are shown.

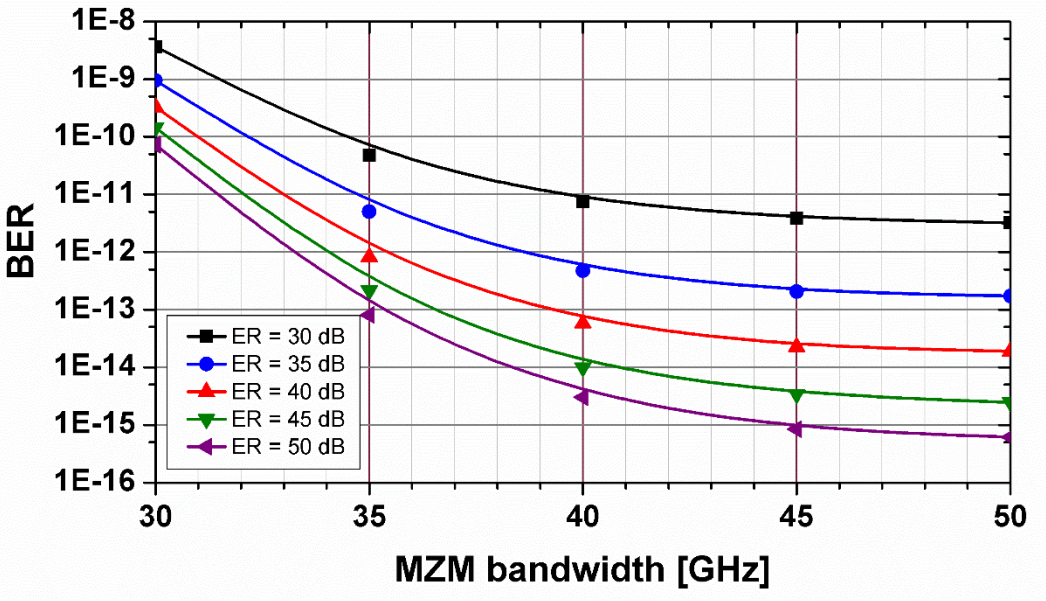

Figure 5.2 Simulated BER performance of the 40-km WDM system as a function of MZM bandwidth for different values of the MZM extinction ratio.

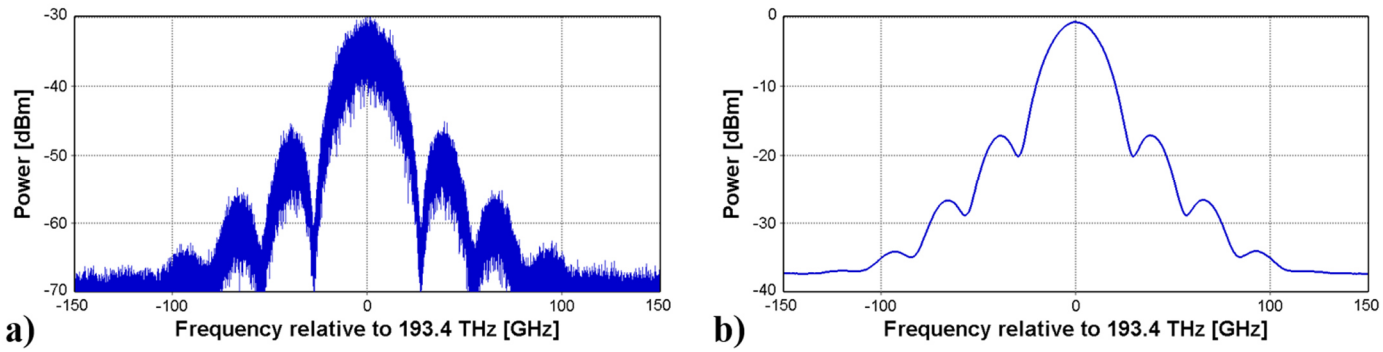

Figure 5.3 Optical spectrum at IQ modulator output, displayed with a) 5 MHz and b) 12.5 GHz (0.1 nm) resolution.

5.3.2 MUX and DEMUX bandwidth

Figure 5.4 shows the performance of the system as a function of MUX and DEMUX bandwidth. WDM simulations with 40 km of fiber and P_{Tx} = 13 dBm were carried out. Different combinations of MUX and

DEMUX BWs were tested, but it was found that the best results are obtained when MUX and DEMUX share the same BW value. According to the figure, the BER pronouncedly increases for filter BWs narrower than 28 GHz (sub-Nyquist cases). Since Nyquist pre-shaping is not considered in the analyzed transmission scheme, a minimum filter BW of 50 GHz was found to be necessary to reach a BER $\leq 1x10^{-13}$. Considering that this BW value has become a standard and the corresponding filters are readily available [159], a filter bandwidth for MUX and DEMUX of 50 GHz was then chosen. The resulting optical spectrum at the output of the MUX and input of the DEMUX after transmission through 40 km of fiber, where the channel spacing has been set to 100 GHz, are shown in Figure 5.5.a and Figure 5.5.b, respectively. Some satellite harmonics due to the presence of a moderate four-wave mixing effect are evident in Fig. 5.5.b. Their power ratio with respect to the main channels that convey the information exceeds 40 dB, and consequently, their effect can be neglected (see following section).

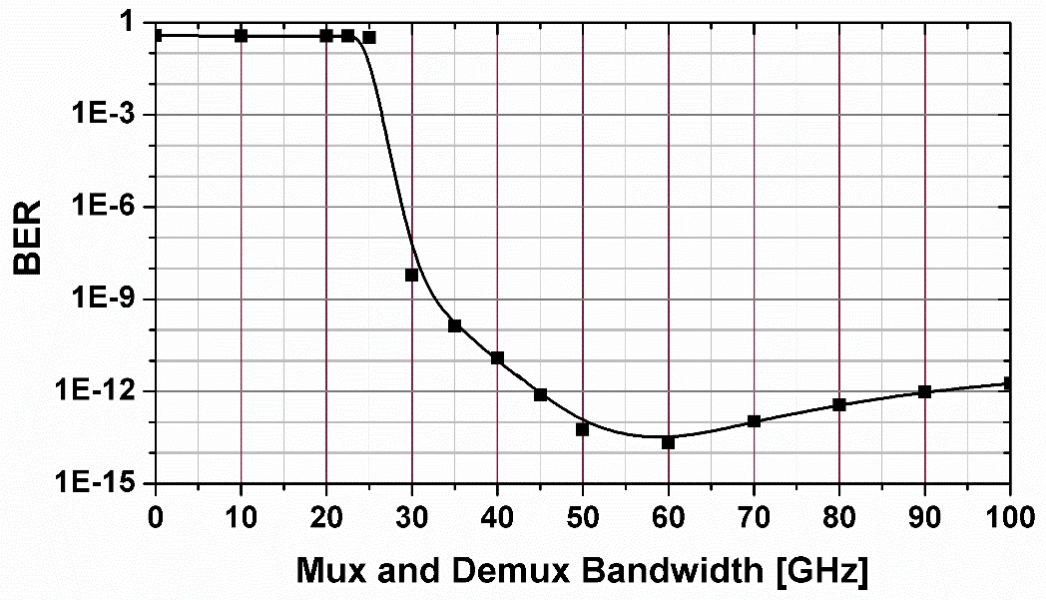

Figure 5.4 Simulated BER performance of the 40-km WDM system as a function of Mux and Demux filters BW.

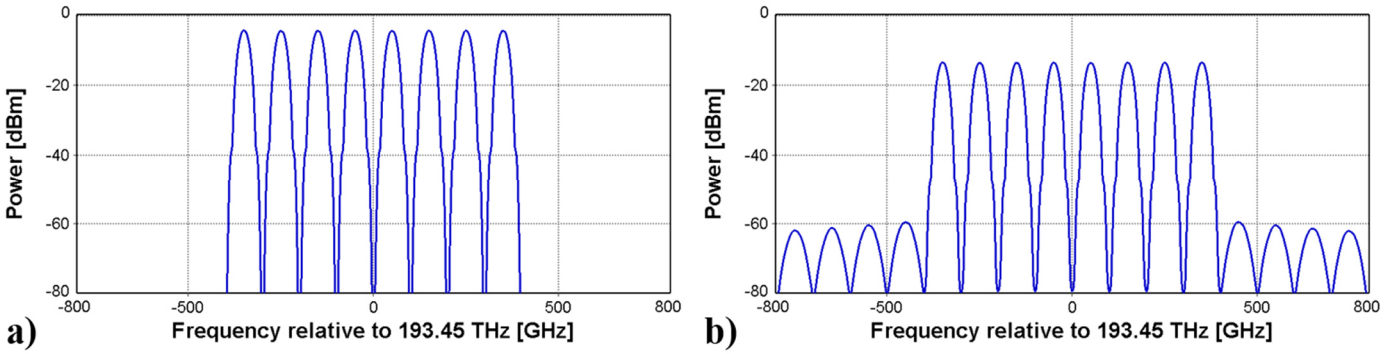

Figure 5.5 Multiplexed optical spectrum at fiber a) input, and b) output (40-km), displayed with 12.5 GHz (0.1 nm) resolution.

5.3.3 Power of the lasers

The effect of some key laser characteristics have a direct impact on the calculation of the power and OSNR budget, and hence the feasibility, of the proposed COCS. Figure 5.6 presents the results of varying the Tx laser (P_{Tx}) and local oscillator power (P_{LO}) on the systems performance. It can be observed that the variation of P_{Tx} has a stronger impact on the BER than the P_{LO} variation. This results in an asymmetry of the power pairs {P_{Tx}, P_{LO}} in terms of system performance. For example, for {+15,+7} dBm a BER slightly greater than $5x10^{-14}$ is obtained, but if the order is inverted to {+7,+15} dBm, a BER of about $1x10^{-9}$ is attained. This indicates that a higher power in the laser Tx (rather than in the local oscillator) should be preferred. Note, however, that P_{Tx} is constrained by the nonlinear response of the optical fiber. To quantify this, Figure 5.7 shows the behavior of BER as a function of total power injected into the fiber (P_{tot}). Curves (dashed) where the fiber nonlinearities are artificially turned off (i.e. $n_2 = 0$) are also displayed. The BER minimum is found at P_{tot} = +11.5 dBm (+2.47 dBm/ch). For higher values of P_{tot} the penalty due to nonlinearities is higher than the benefit of increasing the OSNR. It can be noted from the figure that the onset for fiber nonlinear response is located at about P_{tot} = +8.5 dBm (-0.53 dBm/ch). This value correspond to P_{Tx} = +13 dBm, and hence it sets a power upper bound to avoid nonlinear power penalties. Considering this constraint, Figure 5.6 indicates that the only feasible power pair is {+13,+10} dBm. They correspond to power values available from commercial laser diodes and are in agreement with reported experiments [171]. If a single laser is used to feed transmitter and receiver via a (lossless) splitter on an integrated device, the required power then becomes +14.76 dBm.

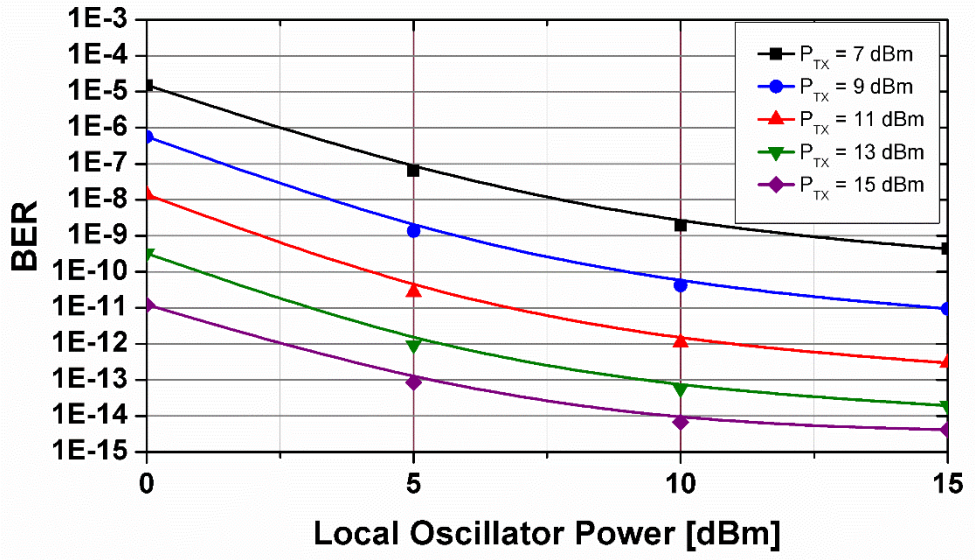

Figure 5.6 Simulated BER performance of the 40-km WDM system as a function of power delivered by the LO for different values of Tx laser power (P_{Tx}).

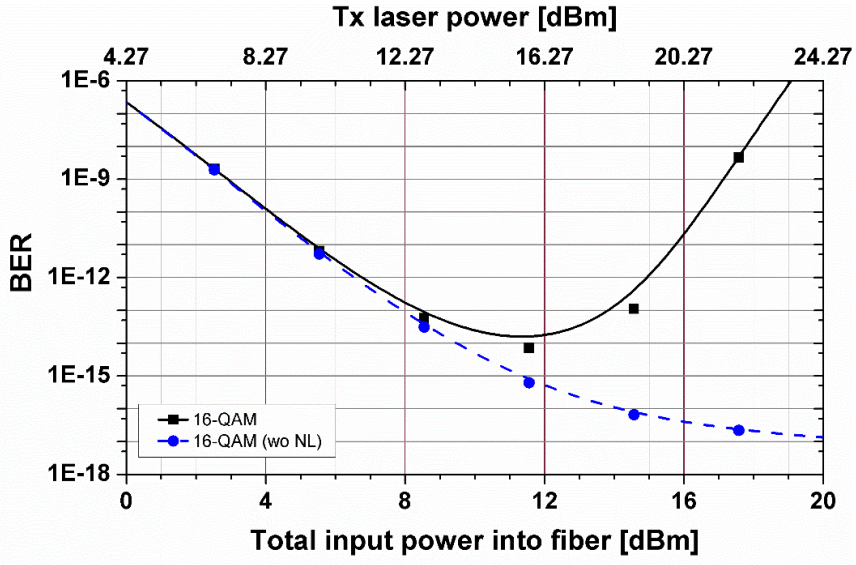

Figure 5.7 Simulated BER performance of the 40-km WDM system as a function of the total power injected into the fiber and the Tx laser power. The dotted line corresponds to simulations where the fiber nonlinear response is not considered.

5.3.4 OSNR of the lasers

The role of the OSNR is analyzed using Figure 5.8, which shows the calculated BER after 40-km transmission as a function of local oscillator OSNR ($OSNR_{LO}$) for different values of the transmitter laser OSNR ($OSNR_{Tx}$). From this figure it can be observed that the BER naturally decreases as $OSNR_{LO}$ or $OSNR_{Tx}$ increases. An $OSNR_{Tx}$ = 35 dB is insufficient to reach the BER target, and therefore only OSNR pairs with $OSNR_{Tx}$ values greater than about 40 dB fulfill the condition; {40,40} and {45,40} dB are examples. We have chosen as

operating OSNR values {40,40} dB, since they correspond to affordable commercial devices [16] and they are compatible with single laser transceiver designs.

Our choice of OSNR can be supported and our analysis extended employing the graphs of BER versus received OSNR presented in Figure 5.9. Simulation results for the back-to-back (BtB) WDM (solid) and the 40-km WDM transmission (dashed) situations are displayed. They are compared to both, an analytical approach [115], [172] (dotted lines) assuming a 28 GBd transmission over an AWGN channel, and BtB experimental results extracted from references [173] (diamonds) and [174] (triangles). The BtB-curves obtained with the simulator follow the trend shown by the analytical approach, but an OSNR overestimation of 12 dB for 16-QAM can be observed in the simulations for a BER = $1x10^{-13}$, which diminishes for higher BER values. The overestimation at BER = $1x10^{-3}$ is quite close to results reported for 16-QAM signals [173], [171], [174]. Our simulation results can hence be considered to be found in the demanding side, rather than focusing on favorable scenarios with relaxed tolerances. Figure 5.9 thus confirms that for 40 km SMF transmission, an $OSNR_{Tx}$ of 40 dB is necessary to attain a BER ≤ $1x10^{-13}$. Moreover, the results for the dashed curve agree with those presented in Figure 5.8 for the corresponding $OSNR_{LO}$ value. Our numerical analysis shows a 3 dB fiber transmission OSNR penalty, explained in more detail in section 5.5.

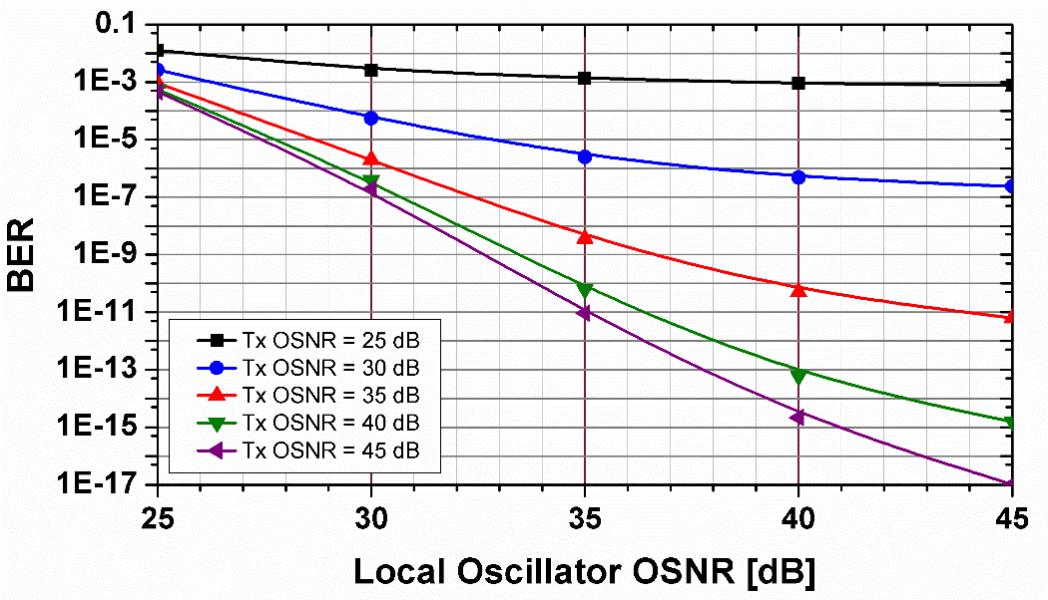

Figure 5.8 Simulated BER performance of the 40-km WDM system as a function of the OSNR at the LO output for different values of the OSNR at the Tx laser output.

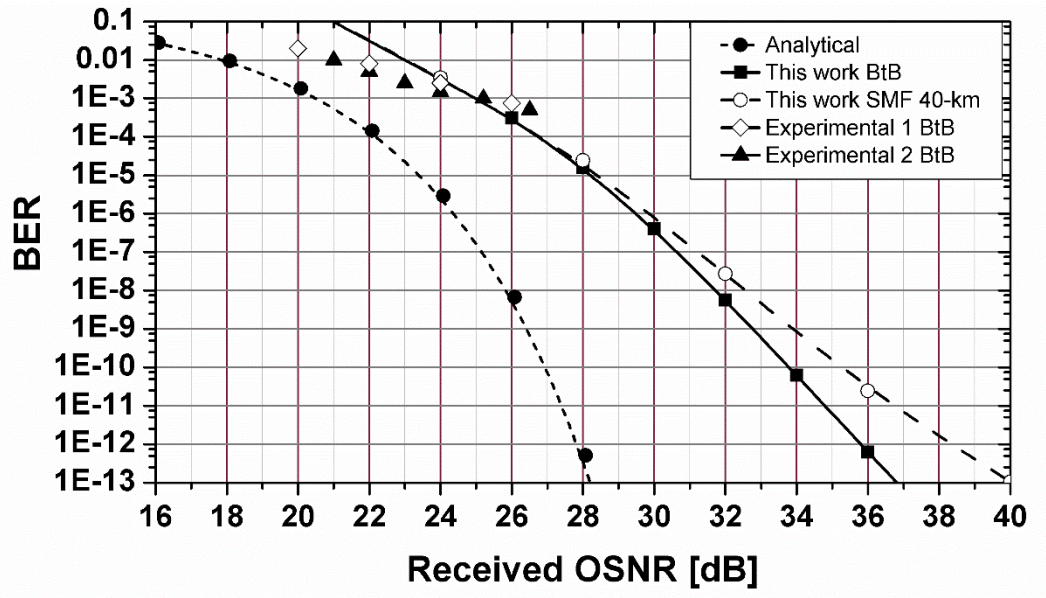

Figure 5.9 Simulated BER performance of the system as a function of the OSNR measured at the input of the coherent optical receiver for different scenarios. Dotted lines were analytically calculated [115], [172]. Diamonds [173] and triangles [174] correspond to back-to-back experimental measurements.

5.3.5 Linewidth of the lasers and frequency offset tolerance

For the sake of completeness, the influence of the lasers linewidth (LW) on the system performance has been also analyzed. Figure 5.10 shows the calculated BER after 40-km transmission as a function of the local oscillator linewidth for different values of the transmitter laser linewidth (Tx LW). In general, narrower LWs lead to better performance, while lasers having a LW broader than 1 MHz can be practically discarded from the proposal since they lead to overly high BER values. Note, however, that the use of lasers with a LW narrower than 1 MHz do not lead to a remarkable performance improvement either. Based on these remarks, and considering that in both COCS the desired BER performance is achieved with Tx and Rx lasers having a LW of 1 MHz, the lasers LW will be set to this value, especially because it corresponds to a parameter specification that is easily found nowadays on commercial state-of-the-art laser diodes.

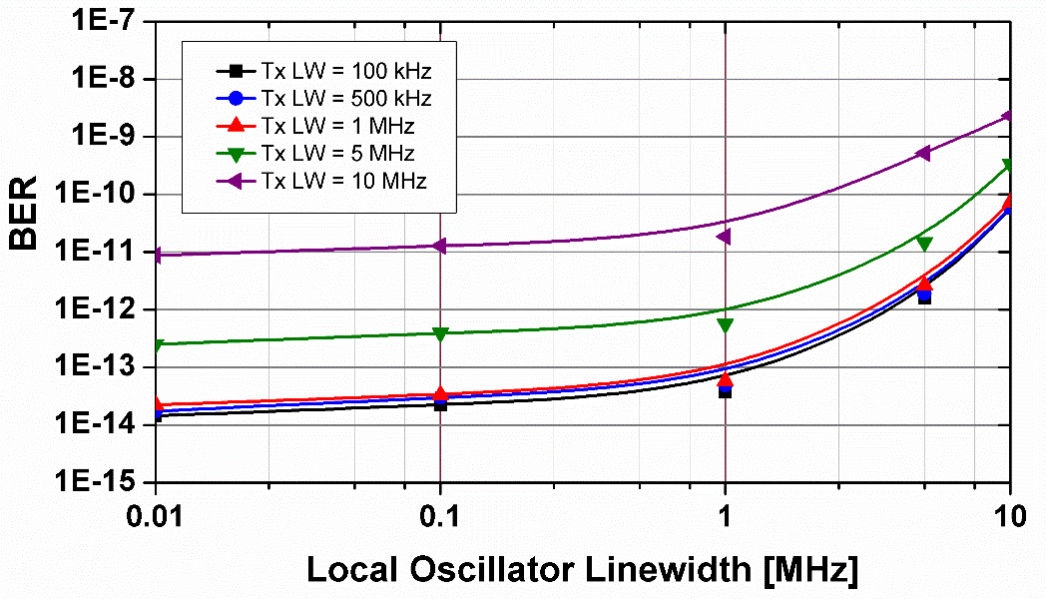

Figure 5.10 Simulated BER performance of the 40-km WDM system as a function of the LO linewidth for different values of the Tx laser linewidth (Tx LW).

For the results presented in Figure 5.10 (and in general, in all the results presented in this Chapter) coincidence in the operation carrier frequency of the transmitter and receiver lasers has been assumed. Since in reality this is not always the case, we carried out simulations to determine the maximum detuning (Δf_c) of the local oscillator carrier frequency with respect to the Tx laser frequency, with which the BER performance is maintained below $1x10^{-13}$. Our numerical analysis showed that using 16-QAM as modulation format a maximum Δf_c of 0.3 GHz fulfills the aforementioned condition (using QPSK this value becomes 0.61 GHz). However, this upper bounds can be extended provided that a carrier frequency recovery algorithm is included in the DSP block of the transmission link. For instance, when the frequency offset estimator introduced in [105] is applied to compensate the effect of Δf_c, a shift of the upper bounds to 3 GHz (QPSK) and 3.4 GHz (16-QAM) can be measured. The employment of this additional processing hence relaxes the physical tolerances of the optical sources, thus allowing for extra laser detuning due to aging or a moderate temperature drift.

5.3.6 Receiver electrical filter bandwidth

The last optimization procedure is performed to determine the bandwidth of the electrical filter placed at the output of each balanced photodetector at the receiver side. Figure 5.11 shows a curve of BER as a function of the receiver electrical filter bandwidth, measured at Ch. 4 (X polarization) after WDM propagation through 40 km of CSMF. An optimum value of 16.8 GHz, corresponding to 60% of the symbol rate, was found. For lower BW values, the BER is degraded due to filtering of useful spectral components, while for higher BW values the performance deteriorates because less noise is filtered out. An adequate trade-off between this two phenomena is found at the optimum value. The corresponding electrical spectrum at the output of the electrical filter is shown in Figure 5.12 for two resolution values.

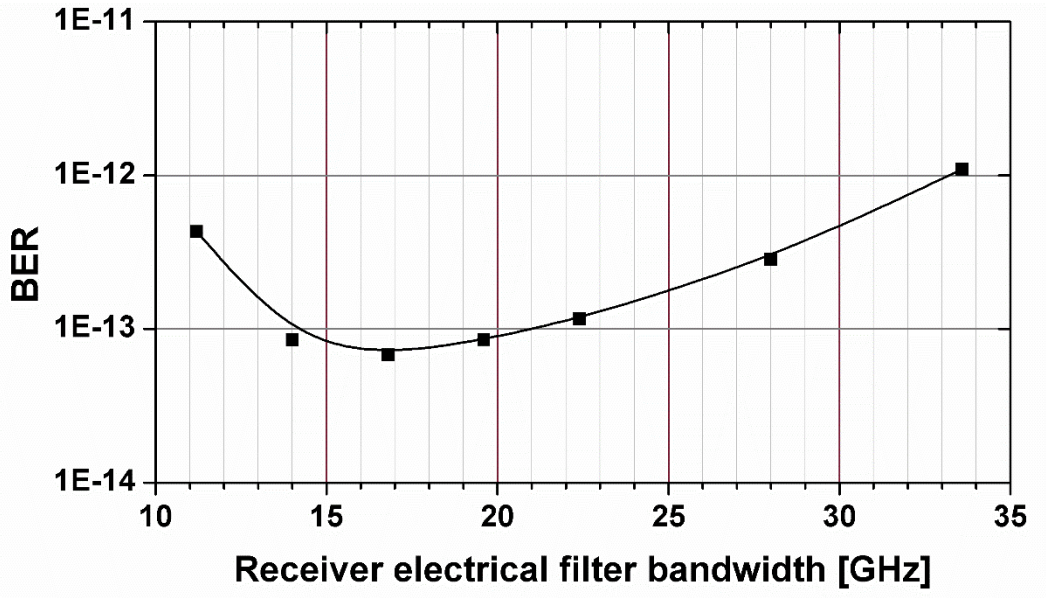

Figure 5.11 Simulated BER performance (measured at Ch. 4) of the 40-km WDM system as a function of the bandwidth of the electrical filter placed after balanced photodetector.

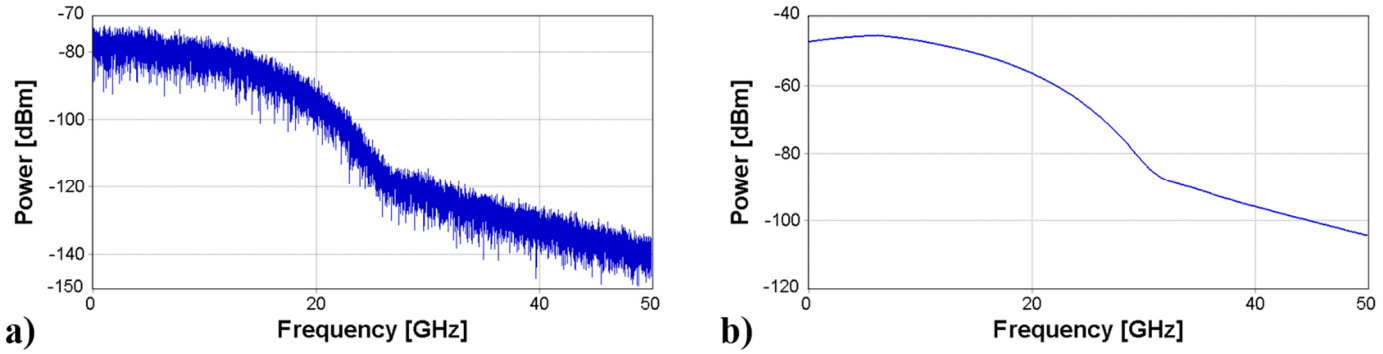

Figure 5.12 Electrical spectrum at receiver electrical filter output (after balanced photodetection), measured at Ch. 4, displayed with a) 5 MHz and b) 12.5 GHz resolution.

5.4 Maximum reach vs transmitted power and modulation format

Having determined the optimum design parameters of the system for 16-QAM modulation format and 40 km reach, Figure 5.13 shows curves of BER as a function of fiber link length for each of the three modulation formats. The laser power at the transmitter side (P_{TX}) is set to +13 dBm, a typical value achievable with commercial state-of-the-art lasers that still does not induce fiber nonlinear effects (see sections 5.3.3). The maximum reach of the system to target a BER = $1x10^{-13}$ is found to be 114, 81 and 40 km for QPSK, 8PSK and 16-QAM, respectively. Transmission at shorter fiber lengths for each modulation format presents no problem (BER < 10^{-13}). Note that the slope of the BER as a function of fiber length curve decreases as the order of the modulation format, and hence the transmitted data rate, increases.

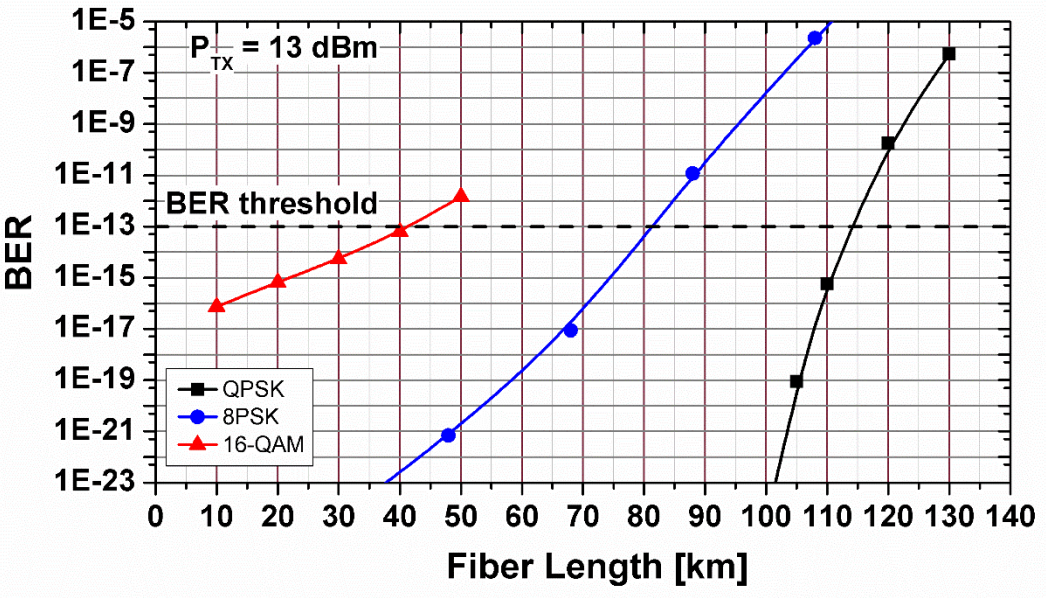

Figure 5.13 Reach of the system for each modulation format as a function of P_{TX} targeting a BER = $1x10^{-13}$.

It is well-known that the maximum reach of a fiber channel is constrained by its non-linear behavior. This is analyzed in Figure 5.14, which plots the reach of the system targeting a BER = $1x10^{-13}$ as a function of P_{TX} for each modulation format. Initially, the system reach linearly increases as a function of P_{TX} (in dB scale). The fiber response is linear. After reaching a maximum, the curves fall sharply. For very high P_{TX} values it is no longer possible to achieve the BER target, even at very short fiber lengths. This sets a maximum P_{TX} value in terms of fiber nonlinearities for each modulation format and confirms [173] that a higher tolerance to fiber nonlinear effects is exhibited by lower order modulation formats when transmitting at the same baud rate. Indeed, a maximum reach of 160, 112 and 44 km is calculated for a P_{TX} of +25, +22.5 and +17 dBm, when QPSK, 8PSK and 16-QAM are employed, respectively. These laser power values correspond to +20.4, +17.7 and +12.7 dBm (+11.4, +8.7 and +3.7 dBm) of total (per channel) power injected into the fiber. However, one must bear in mind that typical laser sources are constrained to deliver a power between +12 and +18 dBm [16], thus limiting the actual system reach to 135 and 102 km for QPSK and 8PSK, while for 16-QAM the limitation of about 44 km (at P_{TX} = +17 dBm) comes from the fiber nonlinear response. In this work the subsequent analysis is then carried out with P_{TX} = +13 dBm. This choice guarantees linear fiber response for all modulation formats and maintains the laser operation in the lower end of the aforementioned power interval, thus widening the choice for this component.

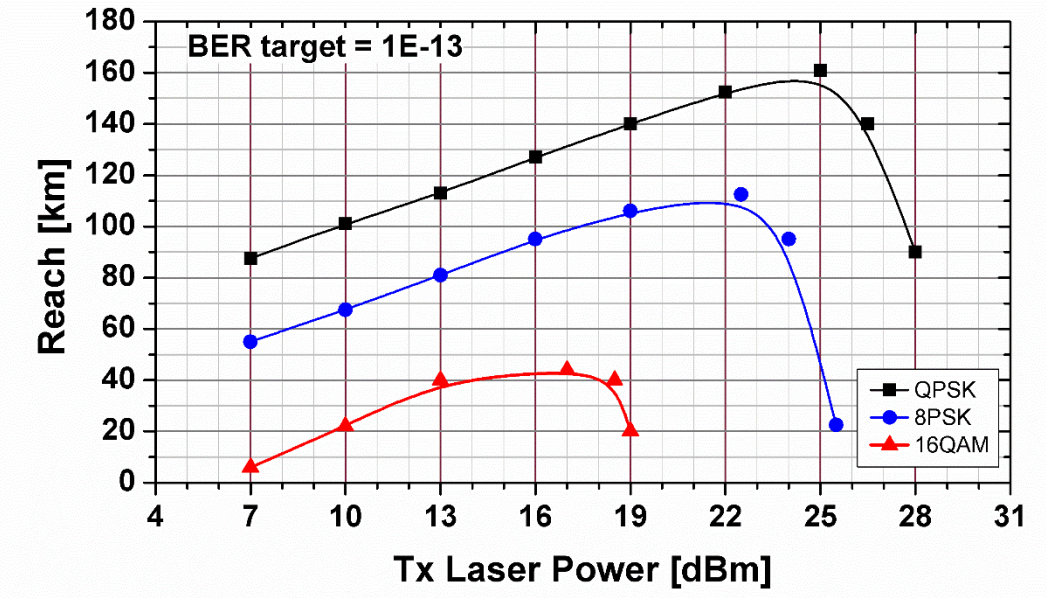

Figure 5.14 Simulated BER for each modulation format as a function of fiber length for a P_{TX} = +13 dBm.

5.5 Power and OSNR transmission penalties

Figure 5.15 shows, for each modulation format, curves of BER as a function of ROP. The dotted curves correspond to the BtB WDM situation, where no fiber is considered, whereas the solid curves correspond to WDM transmission through 114 (QPSK), 81 (8PSK) and 40 km (16-QAM) of SMF, which were found to be the maximum fiber lengths for P_{TX} = +13 dBm. BtB sensitivities at BER=1x10^{-13} of -30.6 for QPSK, -23.2 for 8PSK and -13.2 dBm for 16-QAM, were measured. The fiber transmission and BtB curves overlap regardless the employed modulation format. Therefore, a null fiber transmission power penalty (FTPP) is computed. Since for P_{TX} = +13 dBm the deleterious effects of the fiber nonlinearities are avoided, a negligible FTPP means that the dispersive effects of the fiber are completely compensated at the DSP stage of the receiver for such fiber lengths. In agreement with Figure 5.13, Figure 5.15 also shows that the slope of the BER versus ROP curves decreases as the order of the modulation format increases. Since the fiber nonlinear and dispersive effects were found to be negligible, the system performance degradation with fiber length can only be ascribed to the reduction of ROP caused by the total attenuation of the fiber, which proportionally increases with fiber length. Clearly, 16-QAM is less sensitive to the variations of received power than QPSK, but an overall higher ROP is required by the former modulation format to achieve the same performance level.

Figure 5.16 shows received constellation diagrams of each modulation format corresponding to WDM transmission through the corresponding maximum fiber lengths for a P_{TX} = +13 dBm, measured at the X polarization component of Ch.4. Very similar constellations were obtained for Y polarization components. In all cases the symbols are clearly distinguishable with high concentration around the ideal positions and only a few scattered points. The diagrams thus validate our results. From the figure it is observed that a less demanding EVM value is required to obtain the same BER target as the order of the modulation format decreases. For instance, constellations corresponding to QPSK and 8PSK cases are plotted on the same scale, however, the

received symbols are more dispersed from their ideal positions (*i.e.*, a higher EVM) in the QPSK case, while the BER measured in both cases is practically the same. Since the EVM value is inversely proportional to the SNR of the signal, this is an expected result, because it is well known that the SNR required to achieve a given performance level increases as the order of the modulation format increases.

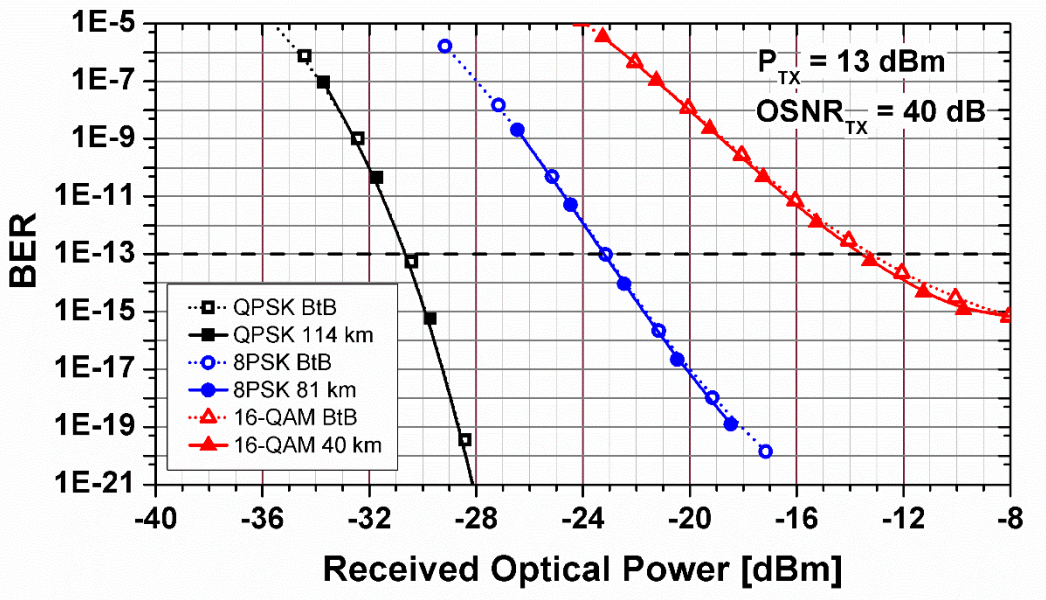

Figure 5.15 Simulated BER for each modulation format as a function of the ROP for a transmitter OSNR of 40 dB measured at the input of the coherent optical receiver for different scenarios.

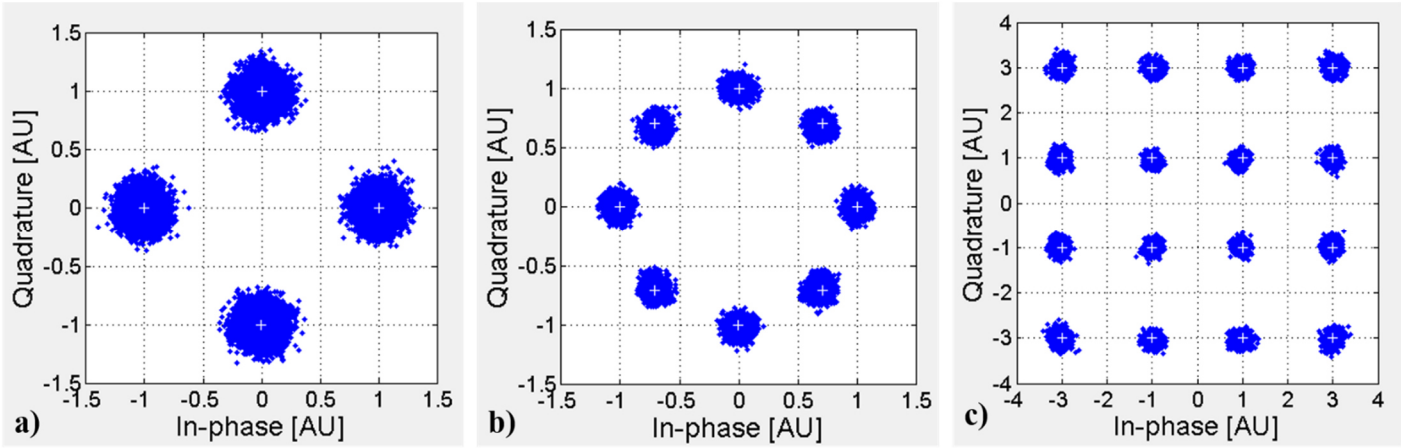

Figure 5.16 Received constellations at a) 114 km (QPSK), b) 81 km (8PSK) and c) 40 km (16-QAM), measured at the X-Pol of the fourth channel. Similar Y-Pol constellations were measured in all cases.

Graphs of BER as a function of received OSNR ($OSNR_{RX}$) are presented on Figure 5.17 for the same transmission distance (40 km); this allows a fair comparison among all modulation formats. Simulation results for the BtB WDM (dashed) and the 40-km WDM transmission (solid) situations are displayed. They are compared to the same analytical approach [115], [172] (dotted lines) as in section 5.3.4. The simulated BtB

curves follow the trend shown by the analytical approach, but an OSNR overestimation ($OSNR_{OE}$) of 0.5 dB for QPSK, 3.9 dB for 8PSK and 8.7 dB for 16-QAM can be observed in the simulations for a BER = $1x10^{-13}$. $OSNR_{OE}$ diminishes for higher BER values, especially in the QPSK case. The $OSNR_{OE}$ at BER = $1x10^{-13}$ is very low for QPSK, while significantly increases as the modulation format order increases. The $OSNR_{OE}$ can be considered a metric of the receiver quality. While the DSP algorithms proved to work well to compensate for fiber impairments (see Figure 5.15), other sources of noise (caused by lasers, photodiodes, DACs and ADCs) are not completely compensated, especially for 8PSK and 16-QAM formats. Our results in terms of $OSNR_{OE}$ for 16-QAM at high BER values (i.e. $1x10^{-3}$) nearly match experimental measurements [173], [171] [174]. We therefore trust in our calculations obtained under such uncommon, but relevant, conditions of very low BER values.

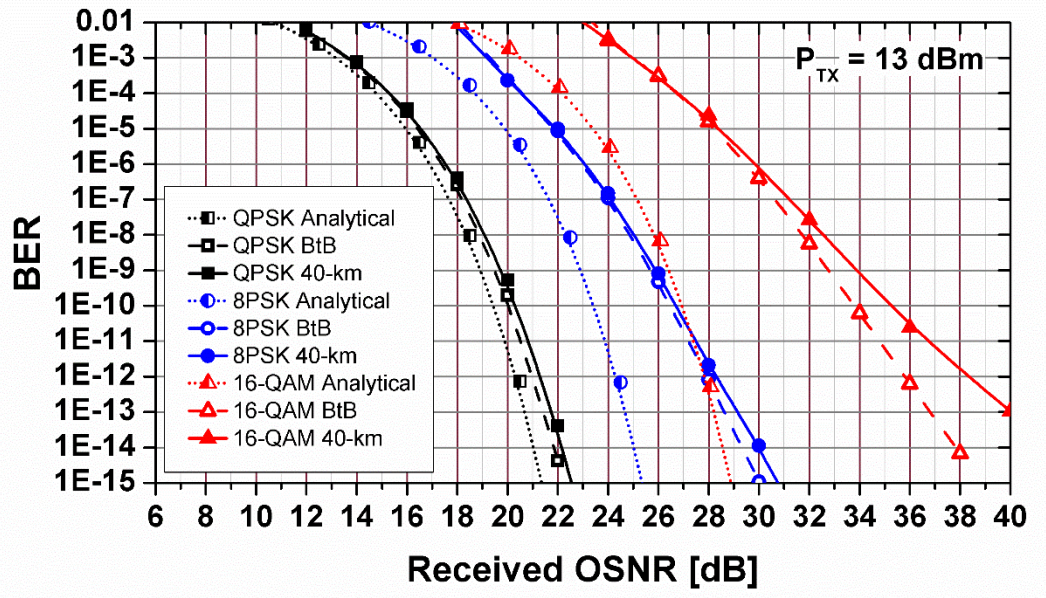

Figure 5.17 Simulated BER for each modulation format as a function of the OSNR measured at the input of the coherent optical receiver for different scenarios.

A comparison of the transmission and BtB curves leads to an OSNR penalty (Δ_{OSNR}). At BER = $1x10^{-13,}$ the penalty amounts to 0.3 (QPSK), 0.7 (8PSK) and 3.2 dB (16-QAM), and diminishes for higher BER values, until it completely vanishes. Since the fiber nonlinear and dispersive effects are negligible under the analyzed conditions, the calculated Δ_{OSNR} can only arise from the 9.2 dB difference in ROP between the BtB and the 40-km transmission case (Δ_{ROP}), caused by fiber attenuation (0.23 dB/km x 40 km). Δ_{OSNR} increases as the modulation format order increases and as the BER target decreases, even though Δ_{ROP} remains the same. Therefore, the OSNR requirements for COCS operating at low levels of BER (i.e. $1x10^{-13}$) are stricter than those of common COCS targeting higher BER values (~$1x10^{-3}$), especially as the modulation format order increases. Δ_{OSNR} could then be understood as the extra $OSNR_{RX}$ that is needed to compensate Δ_{ROP} for a set of given system conditions. For instance, let us first consider the 16-QAM case with P_{TX} = +13 dBm. In the BtB case, the ROP becomes -3.8 dBm, that comes from +13 dBm – 9.8 dB (modulator losses) – 6 dB (MUX & DEMUX IL) – 1 dB (connector losses). According to Figure 5.17, an $OSNR_{RX}$ = 36.8 dB is required to achieve

a BER = $1x10^{-13}$. In the 40-km transmission case, the ROP reduces to -13 dBm (-3.8 dBm – 9.2 dB) and the required $OSNR_{RX}$ is now 40 dB. Therefore, an extra Δ_{OSNR} = 3.2 dB is required to compensate for a Δ_{ROP} = 9.2 dB and still achieve the same BER target. Since for the link under analysis $OSNR_{RX}$ could be considered the same as $OSNR_{TX}$ (no optical amplification, linear operation and very low crosstalk), a minimum $OSNR_{TX}$ = 40 dB turns out to be necessary to achieve 40-km error-free transmission using a P_{TX} of +13 dBm with 16-QAM. Let us now consider the QPSK and 8PSK situations. According to Figure 5.17, the OSNR sensitivities in the BtB case amounts to 21.5 and 28.5 dB, respectively, whereas OSNR sensitivities of 40 dB are calculated for 114 km (QPSK) and 81 km (8PSK) transmissions (see Figure 5.15). The respective Δ_{OSNR} values then become 18.5 and 11.5 dB. They correspond to the extra OSNR at the transmitter that is needed to compensate for a fiber attenuation of Δ_{ROP} = 26.22 dB (QPSK) and 18.63 dB (8PSK). Our analysis makes it clear that the system maximum reach can then be adjusted by varying $OSNR_{TX}$. Since it is easier to tune P_{TX} rather than $OSNR_{TX}$, the latter parameter was considered to be fixed (40 dB) in our transceiver design. Nevertheless, had we employed an optical amplifier to extend the system reach, a compromise between ROP and OSNR should have been found, especially to achieve the OSNR-demanding BER target of $1x10^{-13}$.

5.6 Conclusion of the Chapter

After about a decade of the re-born of optical coherent systems, they will most probably become the universal transmission technology for dense WDM networks of all reaches. In the particular case of DCIs, our simulation work demonstrates that they can be employed for the development of 1.6 Tb/s unamplified Ethernet optical links ranging from 0 to 40 km without FEC. To achieve this, design parameters were here put forward for an 8 x 200 Gb/s coherent system running error-free at 28 GBd per optical channel using 16-QAM.

By employing the same parameters derived for 16-QAM modulation format, a multi-format 800 - 1600 Gb/s eight-channel coherent optical system aimed to deploy inter-data center interconnects was analyzed for a BER target of $1x10^{-13}$. A maximum reach of 114, 81 and 40 km was found for data rates of 800, 1200 and 1600 Gb/s when QPSK, 8PSK and 16-QAM were set as modulation formats, respectively, and the optical power at the lasers output was set to +13 dBm. No relevant transmission power penalties were found for the analyzed systems because they are fully compensated by electronic digital signal processing at the receiver. This is not the case for other noise sources generated at the transceivers. Additionally, moderate OSNR penalties due to fiber attenuation, that increase as the modulation format order increases and as the BER target decreases, were calculated.

In contrast to more common approaches, our research work stands out because it involves the use of a very low BER threshold. Under this condition, our simulations demonstrated that OSNR levels of about 40 dB are necessary for adequate system performance. Our investigations also showed that laser linewidths of at most 1 MHz should be specified, and that the transmitter laser characteristics play a more appreciable role than those of the receiver laser.

In conclusion, our research work demonstrates that transmission performance does not represent a constraint for the deployment of high bit-rate coherent systems at metro access level. Instead, power and cost-efficiency

should be the key consideration [16], [12]. The technological challenge that remains for high-speed short-reach coherent optical networks is hence to reduce power consumption and to achieve higher heat dissipation, mainly from the DSP and ADC/DAC components. An alternative worth exploring is the use of optical phase-locked loop-based homodyne receivers [175], injection locking schemes [176] or analog domain signal processing [158], whose power consumption is expected to be an order of magnitude lower than that of its digital counterpart. Miniaturization and photonic integration of the optical building blocks is also an issue to be tackled if a practical pluggable digital coherent transceiver is meant to be realized.

6. Chapter six: General conclusions and future work

Based on statistics and forecasts, the fundamental role that short-reach optical communication systems plays in the deployment of current and next generation high-speed telecommunication networks to cope with the exponential increase in data traffic demand was shown. Accordingly, three optical communication systems aimed for high-speed short reach applications, namely optical fronthauling, intra-data center and inter-data center optical interconnections, were proposed and analyzed.

The performance (in terms of maximum EVM) of a direct detection fronthaul system based on the recently proposed DSP aggregation approach was improved by the development and implementation of some low-complexity and low-latency DSP compensation techniques, and by performing some optimization procedures. The functionality of the referred techniques and optimizations was experimentally demonstrated in both downstream and upstream directions of the analyzed system.

Regarding the downstream case, the transmission of up to 4 x 192 20-MHz OFDM complex waveforms (~92 Gb/s using only 64-QAM) was experimentally demonstrated up to 25.7 dB of OPL. By setting 16-QAM in half of the channels, and 64-QAM in the other half, the transmission up to 29 dB of OPL was demonstrated, fulfilling the PON Class NI requirements, for a maximum capacity of 76.8 Gb/s. In order to achieve these results the following DSP techniques were implemented: clipping to reduce PAPR, time-domain MZM non-linear compensation and pre-emphasis SNR equalization. The optimum clipping level and cubic correction factor of the MZM non-linear compensation function were found and set. A reduction of the maximum EVM at the output of the fronthaul was experimentally demonstrated thus allowing to increase the maximum OPL.

For the upstream case, the maximum EVM at the output of the fronthaul was considerably reduced by flattening the EVM per channel distribution by means of a proposed and developed pre-emphasis equalization technique. Correct operation of this technique was experimentally demonstrated for different testing cases of the EVM per channel distribution at the input of the fronthaul, *i.e.* the EVM of the OFDM channels after wireless propagation, which in the upstream case are different to zero and non-uniform among channels. It was shown that the maximum OPL value that can be tolerated for the upstream direction can be different from that for the downstream direction regardless of using the same setup. Therefore, the importance of dimensioning and optimizing, not only the downstream, but the upstream direction of a link for proper operation of the full system was demonstrated.

The analyzed fronthaul system multiplexes in the frequency domain (FDM), using a DSP-based approach, several OFDM complex baseband signals, delivered to the fronthaul by an external system (the BBU or the mobile terminals, in the downstream and upstream cases, respectively). If the transmitter and receiver blocks of the fronthaul are integrated in addition with an OFDM complex baseband signals generator that transforms a serial binary sequence into several OFDM channels, and vice versa, the integrated system could be used as a high-speed optical transceiver for DCI applications, just like the rest of the analyzed systems in this thesis work. This optical transceiver system was termed here FDM DDO-OFDM.

For the sake of comparison, the main technical details and findings of each of the optical communications systems tackled in this contribution for DCI applications, are summarized on Table 6.1. A WDM 16 x 25 Gb/s system proposed as an alternative for 400 GbE and analyzed in our previous work reported in [121] and [177], is used as a reference for comparison purposes. This system is based on direct detection technology and OOK modulation format and represents a direct extension of the current commercial technology used to implement the 100 Gb/s Ethernet transceivers over SMF for intra-DCI applications.

Table 6.1 Technical comparison among the optical DCI systems analyzed in this thesis work and a system analyzed in a previous contribution reported in [121] and [177].

	Previous work	FDM DDO-OFDM	RF-IQ-DDO-OFDM		SC-COCS		
Application	Intra-DCI	Intra-DCI	Intra-DCI		Inter-DCI		
Bit rate per channel	25 Gb/s	23 Gb/s	100 Gb/s		100 Gb/s	150 Gb/s	200 Gb/s
Number of channels	16	4	4		8 (with dual-polarization)		
Overall bit rate	400 Gb/s	92 Gb/s	400 Gb/s		800 Gb/s	1.2 Tb/s	1.6 Tb/s
Modulation format	NRZ-OOK	64-QAM	16-QAM		QPSK	8PSK	16-QAM
Symbol rate per channel	25 GBd	3.84 GBd	25 GBd		25 GBd		
Optical modulator	EAM	MZM	EAM		DP-IQ-MZM		
3-dB Modulator BW	< 25 GHz	10 GHz	50 GHz		40 GHz		
Fiber length	40 km	10 km	10 km		114 km	81 km	40 km
Optical band	O	C	O	C	C		
Channel spacing	800 GHz	100 GHz	800 GHz	100 GHz	100 GHz		
Spectral efficiency	0.03125 b/s/Hz	0.23 b/s/Hz	0.25 b/s/Hz	1 b/s/Hz	1 b/s/Hz	1.5 b/s/Hz	2 b/s/Hz
Reception scheme	DD	DD	DD		DP-Coherent Detection		
Optical receiver per channel	1 PIN	1 APD	1 PIN		90° optical hybrid + four balanced photodetectors (8 PIN in total)		
BER target	1×10^{-12}	3.8×10^{-5}	3.8×10^{-5}		1×10^{-13}		
Sensitivty at BER target (Single channel BtB)	-12.5 dBm	-12.75 dBm	-7.8 dBm	-7 dBm	-30.6 dBm	-23.2 dBm	-13.2 dBm
Maximum dispersion power penalty	2.3 dB	~0 dB	0.2 dB	3 dB	~0 dB		
Electronic dispersion compensation	None	Yes	Yes	Yes	Yes		
Cross-talk power penalty	~0 dB	~0 dB	0.1 dB	1 dB	~0 dB		
Fiber nonlinearity penalty	Null	Null	Null	Null	Null		
Optical amplification	SOA	None	None		None		
Tx power per channel (at the modulator output)	+2.9 dBm	-2.75 dBm	+5 dBm	+6 dBm	+2.9 dBm	+2.7 dBm	+3.2 dBm
Required Tx power laser	+13 dBm	+8.2 dBm	+12 dBm	+14 dBm	+13 dBm (Tx) and +10 dBm (LO)		
Required Tx OSNR laser	38 dB	42 dB	40 dB	40 dB	40 dB		
Optical complexity	★☆☆☆☆	★☆☆☆	★★☆☆		★★★★		
Digital complexity	★☆☆☆☆	★★★☆	★★★☆		★★☆☆ (@Tx) ★★★★ (@Rx)		

Thanks to electronic dispersion compensation, the penalty due to chromatic dispersion was found to be negligible in all systems except for the 400 Gb/s RF-IQ-DDO-OFDM system operated in C-band. For this system a 3 dB fiber penalty was found. However, this penalty is attributed to the interaction of chirp, generated

at the EAM, and CD, and not only to CD itself. This fiber penalty was measured to be negligible in the same EAM-based system but operated in O-band since in this case the accumulated CD in any channel is very low. For this reasons, O-band operation of the RF-IQ-DDO-OFDM system should be preferred. In all the analyzed systems, the impact of PMD was found to be negligible. Note that the dual-polarization coherent system incorporates digital compensation of polarization impairments.

In the direct detection systems, the main impairments were found to be both the noise introduced by the devices, and the non-linear distortion induced by the modulator and the photo-detector square-root-law characteristics. In contrast, the DSP-powered coherent system was found to be only affected by the noise of the devices since a linear electrical-optical-electrical conversion was carried out by the IQ modulators and the coherent receivers.

A high laser output power of about +13 dBm, available with current state-of-the-art technology, was found to be needed in all systems to achieve their BER and reach targets. The only exception was the FDM DDO-OFDM system in which an APD instead of a PIN was employed, thus increasing the receiver sensitivity and then reducing the required transmitted power (to ~8 dBm). However, the impact of fiber nonlinearities for such laser output power (+13 dBm) was found to be negligible in all analyzed systems. Note, however, that for intra-DCI direct detection applications, the reach and BER targets are 10 km and 3.8×10^{-5}, respectively. In contrast, for the inter-DCI coherent system, maximum reaches of up to 110, 84 and 40 km targeting a very demanding BER of 1×10^{-13} for very high operational data rates of 800, 1200 and 1600 Gb/s, respectively, were achieved. The better performance of the coherent system in comparison to the directly detected systems is evident, but in contrast, its digital and optical complexity is higher. An extra laser (at the receiver), four times more photo-detectors, an optical 90° hybrid, a more sophisticated DSP stage, as well as twice the number of MZMs, are required per optical channel in the coherent approach as compared to the direct detection approaches. For this reason, the use of coherent systems in intra-DCI applications is currently restricted. Nonetheless, its use in feasible terabit metro networks seems to be a must. Moreover, we can envisage that just as the use of optical fiber has gained ground to copper wire in more and more shorter-reach networks, the use of coherent optical technology will be introduced more and more in shorter-reach applications.

The technical feasibility of a 400 Gb/s Ethernet transceiver for intra-DCI applications up to 10 km was numerically demonstrated by using a WDM 4 x 100 Gb/s RF-IQ-DDO-OFDM approach. Feasible operation was shown using both high-speed EAMs (with 16-QAM) in C- and O-bands as well as high-speed MZMs (using 32-QAM), which have been experimentally reported in state-of-the-art literature. The extension of this architecture to a 16 channel system with a data rate of 1.6 Tb/s that keeps the same performance and reach targets as well as the power requirements was found to be unfeasible. To attain data rates beyond 100 Gb/s per optical channel (per polarization state) with a fiber reach longer than 10 km without employing optical amplifiers and FEC schemes, the use of coherent technology seems to be a must with current state-of-the-art technology. Accordingly, the technical feasibility of a multi-format coherent optical transceiver able to transmit up to 1.6 Tb/s through 40 km of SMF for metro inter-DCI applications was numerically demonstrated. A maximum reach of 110 km for a maximum capacity of 800 Gb/s was numerically demonstrated using the proposed transceiver. In all cases, state-of-the-art lasers with OSNR of 40 dB, linewidth of 1 MHz and

transmitted optical power of +13 dBm were employed, as well as optical devices available with current experimental or commercial reported technology.

In conclusion, although for short-reach systems it is worth to look for alternatives to preserve the cost-effective and relatively simple direct detection scheme until exhausting its potentialities, the forecast of a strong trend to introduce the re-born coherent technology at all network levels to cope with the exponential traffic demand, motivates early analysis considering this imminent possibility. As aforementioned, both approaches were tackled in this contribution. The corresponding theoretical and experimental analyzes performed in this thesis work showed that our proposed systems are technically feasible to accomplish the proposed objective of providing alternatives to increase the capacity of currently available technology for different level applications.

6.1 Future work

In general, future work has to be done to experimentally validate the results obtained here via numerical simulations. Although our contributions are relevant, lack of the required very high-speed equipment did not allowed us to carry out this process in the present research work. Our work, therefore, opens a path to a fascinating set of experimental investigations. The development of new DSP algorithms to counteract physical impairments of the systems analyzed in this thesis is another interesting field for future research contributions. An excellent background in DSP technology together with a deep knowledge of optical system impairments are required to tackle this attractive field. Progress has been achieved in the compensation of fiber and other type of nonlinearities, but there are still trails to be explored.

In particular, a real-time validation of the spectral estimation technique, proposed in this work for fronthaul systems and validated via an off-line DSP approach, is needed to fully test its functionality. An analysis of the proposed pre-emphasis SNR equalization technique for fronthaul systems using real EVM per channel wireless distributions at the input of the system in the upstream direction is also worth to be carried out. The use of the FDM DDO-OFDM approach to implement high-speed optical transceivers could be proposed as an alternative for next generation 25 Gb/s PON systems. The feasibility of this system using more OFDM channels to transmit up to 100 Gb/s per optical channel using higher bandwidth components as an alternative for both 100 Gb/s PON or 400 Gb/s intra-DCIs is another interesting research topic. Similarly, the development of more powerful DSP algorithms to increase the receiver performance of the RF-IQ-DDO-OFDM system in order to enable the use of higher-order modulation formats, such as 64- or 128-QAM, to transmit the same 100 Gb/s per optical channel, but with narrow bandwidth requirements, is worth to be studied as well. Finally, regarding the SC-COCS, the development of both less-power-consuming DSP techniques for impairment compensation and cost-effective IQ modulators and coherent receivers, are utterly necessary to potentiate its adoption in shorter-reach optical systems.

Appendix A. Selected topics of signal theory

1. Complex baseband representation of a real-valued passband signal

Real world time-varying signals are real-valued signals. A modulated signal is a real-valued *passband* signal $x_{PB}(t)$ whose power spectral density ($S_{xx,PB}$ or simply *power spectrum*) is concentrated only in a frequency vicinity around a carrier frequency f_c [31].

$$S_{xx,PB}(f) \neq 0 \quad \forall f : 0 < f_c - \frac{B}{2} \leq |f| \leq f_c + \frac{B}{2} < \infty$$

The quantity B is called *bandwidth* of the signal. For real-valued signals, B is calculated only for positive frequencies. Since a *passband* signal $x_{PB}(t)$ is real, its *power spectrum* $S_{xx,PB}$ is symmetric about $f = 0$. Consequently, all of the information of the signal $x_{PB}(t)$ is contained in the positive half of its power spectrum $S_{xx,PB}$, defined as

$$S^{+}_{xx,PB}(f) = \sqrt{2} S_{xx,PB}(f) u(f) \tag{A. 1.1}$$

where $u(f)$ is the unit step function. The inverse Fourier transform of $S^{+}_{xx,PB}(f)$ is the complex signal

$$x^{+}_{PB}(t) = \frac{1}{\sqrt{2}} \left[x_{PB}(t) + jH\{x_{PB}(t)\} \right] \tag{A. 1.2}$$

where $H\{\cdot\}$ denotes the Hilbert transform operator. The signal $x^{+}_{PB}(t)$ is called the *analytical* signal of $x_{PB}(t)$. The factor of $\sqrt{2}$ in equation (A. 1.1) makes the signal $x^{+}_{PB}(t)$ to have the same energy as $x_{PB}(t)$. For simplicity this factor is omitted in other sections of this work since it is a constant amplitude factor that could be easily corrected at the receiver of the systems. By shifting the power spectrum $S^{+}_{xx,PB}(f)$ down to the origin we obtain

$$S_{xx}(f) = S^{+}_{xx,PB}(f + f_c)$$

whose inverse Fourier transform is the complex-valued *baseband* signal $x(t)$

$$x(t) = x_{PB}^{+}(t)e^{-j2\pi f_c t} \tag{A. 1.3}$$

The signal $x(t)$ is called the complex *baseband* representation or *complex envelope* of the real-valued *passband* signal $x_{PB}(t)$, and can be written in terms of its real and imaginary parts as

$$x(t) = x_I(t) - jx_Q(t) \tag{A. 1.4}$$

Where $x_I(t)$ and $x_Q(t)$ are real-valued *baseband* signals whose power spectral densities, $S_{xx,I}(f)$ and $S_{xx,Q}(f)$ respectively, are nonzero in a frequency interval around the DC f = 0.

$$S_{xx,I}(f) \neq 0, S_{xx,Q}(f) \neq 0 \quad \forall f : |f| \leq f_c + \frac{B}{2} < \infty$$

The signals $x_I(t)$ and $x_Q(t)$ are called the In-phase (I) and Quadrature (Q) components of $x(t)$. From equations (A. 1.2), (A. 1.3) and (A. 1.4) it can be obtained the *passband* signal from its *complex baseband representation* as follows

$$x_{PB}(t) = \mathrm{Re}\{\sqrt{2}x_{PB}^{+}(t)\} = \mathrm{Re}\{\sqrt{2}x(t)e^{j2\pi f_c t}\} \tag{A. 1.5}$$

$$x_{PB}(t) = \sqrt{2}\left[x_I(t)\cos(2\pi f_c t) + x_Q(t)\sin(2\pi f_c t)\right] \tag{A. 1.6}$$

Equation (A. 1.6) indicates a practical way to represent a real-valued *passband* signal aided by two real-valued *baseband* signals.

2. Condition of orthogonality among sub-channels in a multi-carrier system

A general diagram of a multi-carrier transmission systems is shown in Figure A.1. The complex representation (see Appendix A.1) of a MC transmitted signal $x_{MC}(t)$ is represented as

$$x_{MC}(t) = \sum_{i=1}^{N} \hat{x}_{IQ,i}(t) = \sum_{n=-\infty}^{\infty} \sum_{i=1}^{N} C_{in} \cdot p(t - n\hat{T}_s) \exp\left(j2\pi f_i t\right) \tag{A. 2.1}$$

where C_{in} is the *n*-th complex symbol of the *i*-th *sub-channel* $\hat{x}_{IQ,i}(t)$ that outputs an IQ modulator, f_i is the frequency of the *i*-th *sub-carrier* and $\hat{T}_s$ is the symbol period on each *sub-channel.*

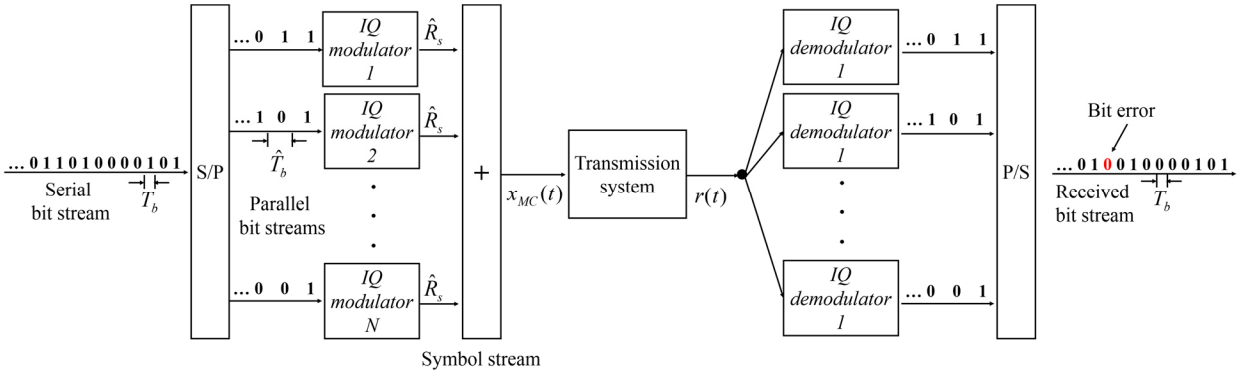

Figure A.1 Block diagram of a Multi-carrier transmission system

If two *sub-channels* are orthogonal to each other, then its correlation is zero. The correlation between any two *sub-channels* $\hat{x}_{IQ,p}(t)$ and $\hat{x}_{IQ,q}(t)$, for simplicity considering the transmission of only one symbol, is given by

$$\delta_{kl}(0) = \frac{1}{\hat{T}_s}\int_0^{\hat{T}_s} \hat{x}_{IQ,p}(t)\hat{x}^*_{IQ,q}(t)dt = \frac{1}{\hat{T}_s}\int_{-\hat{T}_s/2}^{\hat{T}_s/2} C_{pn}C^*_{qn}\exp\left(j2\pi\left(f_p - f_q\right)t\right)dt =$$

$$= \frac{C_{pn}C^*_{qn}}{\hat{T}_s}\left[\frac{\exp\left(j2\pi\left(f_p - f_q\right)t\right)}{j2\pi\left(f_p - f_q\right)}\right]_{-\hat{T}_s/2}^{\hat{T}_s/2} = \tag{A. 2.2}$$

$$= \frac{C_{pn}C^*_{qn}}{\hat{T}_s}\left[\frac{\exp\left(j\pi\left(f_p - f_q\right)\hat{T}_s\right) - \exp\left(-j\pi\left(f_p - f_q\right)\hat{T}_s\right)}{j2\pi\left(f_p - f_q\right)}\right] =$$

$$= \frac{C_{pn}C^*_{qn}}{\hat{T}_s}\left[\frac{\sin\left(\pi\left(f_p - f_q\right)\hat{T}_s\right)}{\pi\left(f_p - f_q\right)}\right]$$

From the above expression, it is clear that if

$$f_p - f_q = m\frac{1}{\hat{T}_s} \tag{A. 2.3}$$

where m is a natural number, $m \in \mathbb{N}$, then, any pair of *sub-channels* are orthogonal to each other (*i.e.* $\delta_{kl} = 0$), independently of the symbols that they are transmitting.

References

[1] Cisco, *The Zettabyte Era: Trends and Analysis,* June 2017.

[2] Cisco, *Visual Networking Index: Forecast and Methodology, 2016–2021,* June 6, 2017.

[3] Cisco, *VNI Forecast Highlights Tool, Mexico. [Online] Available at: http://www.cisco.com/c/m/en_us/solutions/service-provider/vni-forecast-highlights.html#,* June, 2017.

[4] E. Agrell, M. Karlsson, A. R. Chraplyvy, D. J. Richardson, P. M. Krummrich, P. Winzer, K. Roberts, J. K. Fischer, S. J. Savory, B. J. Eggleton, M. Secondini, F. R. Kschischang, A. Lord and J. Prat, "Roadmap of optical communications," *Journal of Optics,* vol. 18, no. 6, pp. 1-40, 2016.

[5] J. Hecht, "Great leaps of light," *IEEE Spectrum,* vol. 53, no. 2, pp. 28-53, 2016.

[6] N. Starosielski, The Undersea Network, Durham, NC: Duke University Press, 2015.

[7] H. D. Smith, J. L. S. d. Vivero and T. S. Agardy, Routledge Handbook of Ocean Resources and Managment, Earthscan from Routledge, 2015.

[8] V. Alwayn, Optical Network Design and Implementation, Cisco Press, 2004.

[9] OECD Broadband Portal, 2017.

[10] Cisco, *Visual Networking Index: Global Mobile Data Traffic Forecast Update, 2016–2021,* 2017.

[11] B. Lavallé, "Ciena. Experience. Outcomes," 31 May 2016. [Online]. Available: http://www.ciena.com/insights/articles/5G-wireless-needs-fiber-and-lots-of-it_prx.html. [Accessed 15 June 2017].

[12] X. Xu, E. Zhou, G. N. Liu, T. Zuo, Q. Zhong, L. Zhang, Y. Bao, X. Zhang, J. Li and Z. Li, "Advanced modulation formats for 400-Gbps short-reach optical inter-connection," *Optics Express,* vol. 23, pp. 492-500, 2015.

[13] R. Lin, High-Capacity Short-Reach Optical Communications, Stockholm, Sweden: KTH Royal Institute of Technology, 2016.

[14] I. Tomkos, "Super-sizing the data center," *Fibre Systems,* no. 11, pp. 22-25, 2016.

[15] K. P. Zhong, Y. W. X. Zhou, T. Gui, Y. Yang, J. Yuan, L. Wang, W. Chen, H. Zhang, J. Man, L. Zeng, C. Yu, A. P. T. Lau and C. Lu, "Recent Advances in Short Reach Systems," in *Optical Fiber Communication Conference, OSA Technical Digest (online) (Optical Society of America, 2017)*, Los Angeles, California USA, 2017.

[16] Directly Modulated Lasers on Silicon (DIMENSION) project, "Deliverable Report D 2.1 Report on system specifications," September 2016. [Online] Available: http://www.dimension-h2020.eu/wp-content/uploads/DIMENSION_Deliverable_Report_D2.1_v1.pdf.

[17] A. Dochhan, N. Eiselt, H. Griesser, M. Eiselt, J. J. V. Olmos, I. T. Monroy and J.-P. Elbers, "Solutions for 400 Gbit/s Inter Data Center WDM Transmission," in *ECOC 2016; 42nd European Conference on Optical Communication; Proceedings of*, Dusseldorf, Germany, 2016.

[18] Nokia, *Upscaling the metro. Application Note.,* 2016.

[19] M. Ilyas and H. T. Mouftah, The Handbook of Optical Communication Networks, CRC Press, 2003.

[20] N. Ghani, "Regional-Metro Optical Networks," in *Emerging Optical Network Technologies*, USA, Springer, 2005, pp. 75-108.

[21] C. Lin, Broadband Optical Access Networks and Fiber-to-the-Home: Systems Technologies and Deployment Strategies, John Wiley & Sons, 2006.

[22] E. Pincemin, J. Karaki, Y. Loussouarn, H. Poignant, C. Betoule, G. Thouenon and R. L. Bidan, "Challenges of 40/100Gbps and higher-rate deployments over long-haul transport networks," *Optical Fiber Technology,* vol. 17, no. 5, pp. 335-362, 2017.

[23] C. Xie, "Optical interconnects for data centers," in *2016 IEEE Photonics Conference (IPC)*, Waikoloa, HI, 2016.

[24] Cisco, *Visual Networking Index: Forecast and Methodology, 2014-2019 White Paper,* 2015.

[25] Cisco, *Global Cloud Index, 2015-2020 White paper.,* 2016.

[26] Bell-Labs, *Metro network traffic growth: an architecture impact study. White paper.,* 2012.

[27] Lightwave, "Sales of optical data center interconnect gear rise nearly 50%: IHS Markit," 28 March 2017. [Online]. Available: http://www.lightwaveonline.com/articles/2017/03/sales-of-optical-data-center-interconnect-gear-rise-nearly-50-ihs-markit.html. [Accessed 17 June 2017].

[28] A. Pizzinat, P. Chanclou, F. Saliou and T. Diallo, "Things You Should Know About Fronthaul," *Journal of Lightwave Technology,* vol. 33, no. 5, pp. 1077-1083, 2015.

[29] X. Liu, H. Zeng, N. Chand and F. Effenberger, "Efficient Mobile Fronthaul via DSP-Based Channel Aggregation," *Journal of Lightwave Technology,* vol. 34, no. 6, pp. 1556-1564, 2015.

[30] J. Bartelt, N. Vucic, D. Camps-Mur, E. Garcia-Villegas, I. Demirkol, A. Fehske, M. Grieger, A. Tzanakaki, J. Gutiérrez, E. Grass, G. Lyberopoulos and G. Fettweis, "5G transport network requirements for the next generation fronthaul interface," *Journal on Wireless Communications and Networking,* vol. 89, pp. 1-12, 2017.

[31] J. Proakis and M. Salehi, Digital communications, Fifth Edition ed., McGraw-Hill, 2007.

[32] J. Armstrong, "OFDM for optical communications," *Journal of Lightwave Technology,* vol. 27, no. 3, pp. 189-204, 2009.

[33] W. Shieh and I. Djordjevic, OFDM for Optical Communications, California, USA: Academic Press, 2010.

[34] S. B. Weinsten and P. M. Ebert, "Data transmission by frequency-division multiplexing using the discrete Fourier," *IEEE Transactions Communications,* vol. 19, pp. 628 - 634, 1971.

[35] J. Lee, F. Breyer, S. Randel, J. Zeng, F. Huijskens, H. P. v. d. Boom, A. M. Koonen and N. Hanik, "24-Gb/s Transmission over 730 m of Multimode Fiber by Direct Modulation of an 850-nm VCSEL Using Discrete Multi-Tone Modulation," in *Optical Fiber Communication Conference and Exposition and The National Fiber Optic Engineers Conference, OSA Technical Digest Series (CD) (Optical Society of America, 2007)*, California United States, 2007.

[36] F. Koyama and K. Iga, "Frequency chirping in external modulators," *Journal of Lightwave Technology,* vol. 6, no. 1, pp. 87-93, 1988.

[37] VPIphotonics, *Continuous Wave Laser (LaserCW). Version 9.5,* 2017.

[38] P. Hooijmans, Coherent Optical System Design, John Wiley & Sons, 1994.

[39] M. Seimetz, High-Order Modulation for Optical Fiber Transmission, New York, USA: Springer, 2009.

[40] VPIphotonics, *Control OSNR (SetOSNR). Version 9.5,* 2017.

[41] R. Alferness, "Waveguide electrooptic modulators," *IEEE Transactions on Microwave Theory Techniques,* vol. 30, pp. 1121-1137, 1982.

[42] VPIphotonics, *Modulator Differential MZ (Modulator DiffMZ_DSM). Version 9.5,* 2017.

[43] E. Chen and A. Murphy, Broadband Optical Modulators: Science, Technology, and Applications, Florida USA: CRC Press, 2011.

[44] J. S. Weiner, D. A. B. Miller and D. S. Chemla, "Quadratic electro-optic effect due to the quantum confined Stark effect in quantum wells," *Appl. Phys. Letters,* vol. 50, no. 13, pp. 842-844, 1987.

[45] VPIphotonics, *Modulator Electroabsorption Measured (ModulatorEA_Measured). Version 9.5,* 2017.

[46] F. Koyama and K. Iga, "Frequency chirping in external modulators," *Journal of Lightwave Technology,* vol. 6, no. 1, pp. 87-93, 1988.

[47] F. Dorgeuille and F. Devaux, "On the transmission performances and the chirp parameter of a multiple-quantum-well electroabsorption modulator," *Journal of Quantum Electronics,* vol. 30, no. 11, pp. 2565-2572, 1994.

[48] G. W. Lee and S. K. Han, "Linear dual electroabsorption modulator for analog optical transmission," *Microwave and Optical Technology Letters,* vol. 22, no. 6, p. 369–373, 1999.

[49] G. P. Agrawal, Fiber-Optic Communication System. Fourth Edition., Wiley, 2010.

[50] VPIphotonics, *Photodiode (Photodiode). Version 9.5,* 2017.

[51] R. Gutiérrez-Castrejón, "State-of-the-Art in Device and Network," in *WDM Systems and Networks*, Springer, 2011, pp. 63-97.

[52] VPIphotonics, *Fiber NLS Random Birefringence PMD Coarse Step (FiberNLS_PMD). Version 9.5,* 2017.

[53] C. D. Poole and R. E. Wagner, "Phenomenological approach to polarisation dispersion in long single-mode fibres," *Electronics Letters,* vol. 22, no. 19, pp. 1029-1030, 1986.

[54] G. P. Agrawal, Nonlinear Fiber-Optics, Fourth Edition, San Diego, California, USA: Academic Press, 2007.

[55] D. Marcuse, C. Menyuk and P. Wai, "Application of the Manakov-PMD equation to studies of signal propagation in," *Journal of Lightwave Technology,* vol. 15, no. 9, pp. 1735-1745, 1997.

[56] P. K. A. Wai, C. R. Menyuk and H. H. Chen, "Stability of solitons in randomly varying birefringent fibers," *Optics Letters,* vol. 16, no. 16, p. 1231–1233, 1991.

[57] H. Kogelnik, R. M. Jopson and L. E. Nelson, "Chapter 15. Polarization Mode Dispersion," in *Optical Fiber*, San Diego, USA, Academic Press, 2002, pp. 725-861.

[58] K. Kanonakis and e. al., "Results from the EU project ACCORDANCE on converged OFDMA-PON networks," in *2013 15th International Conference on Transparent Optical Networks (ICTON)*, Cartagena, 2013.

[59] J. C. B. Schmidt, A. J. Lowery and J. Armstrong, "Experimental Demonstrations of Electronic Dispersion Compensation for Long-Haul Transmission Using Direct-Detection Optical OFDM," *Journal of Lightwave Technology,* vol. 26, pp. 196-203, 2008.

[60] E. Giacoumidis, J. Wei, X. Jin and J. Tang, "Improved transmission performance of adaptively modulated optical OFDM signals over directly modulated DFB laser-based IMDD links using adaptive cyclic prefix," *Optics Express,* vol. 16, pp. 9480-9494, 2008.

[61] J. Tang and K. Shore, "30 Gb/s signal transmission over 40-km directly modulated DFB-laser-based single-mode-fibre links without optical amplification and dispersion compensation," *Journal of Lightwave Technology,* vol. 24, pp. 2318-2327, 2006.

[62] S. Iezekiel, Microwave Photonics: Devices and Applications, Chichester, UK: John Wiley & Sons., 2009.

[63] A. J. Lowery and J. Armstrong, "Orthogonal-frequency-division multiplexing for dispersion compensation of long-haul optic systems," *Optics Express,* vol. 14, pp. 2079-2084, 2006.

[64] W.-R. Peng, X. Wu, V. R. Arbab, K.-M. Feng, B. Shamee, L. C. Christen, J.-Y. Yang, A. E. Willner and S. Chi, "Theoretical and Experimental Investigations of Direct-Detected RF-Tone-Assisted Optical OFDM Systems," *Journal of Ligthwave Technology,* vol. 27, no. 10, pp. 1332 - 1339, 2009.

[65] N. Cvijetic, "OFDM for Next-Generation Optical Access Networks," *Jornal of Lightwave Technology,* vol. 30, no. 4, pp. 384-398, 2012.

[66] T. Schmidl and D. Cox, "Robust frequency and timming synchronization for OFDM," *IEEE Transactions Communications,* vol. 45, pp. 1613-1621, 1997.

[67] W. Shieh and C. Athaudage, "Coherent optical orthogonal frequency division multiplexing," *Electronics Letters,* vol. 42, no. 10, pp. 587-588, 2006.

[68] F. Buchali, R. Dischler and X. Liu, "Optical OFDM – A promising high-speed optical transpor technology," *Bell Labs Technical Journal,* vol. 14, no. 1, pp. 125-146, 2009.

[69] M. Sieben, J. Conradi and D. Dodds, "Optical single sideband transmission at 10 Gb/s using only electrical dispersion compensation," *Journal of Lightwave Technology,* vol. 17, no. 10, pp. 1742-1749, 1999.

[70] D.-Z. Hsu, C.-C. Wei, H.-Y. Chen, W.-Y. Li and J. Chen, "Cost-effective 33-Gbps intensity modulation direct detection multi-band OFDM LR-PON system employing a 10-GHz-based transceiver," *Optics Express,* vol. 19, no. 18, 2011.

[71] M. E. Chaibi and e. al., "Dispersion Compensation-Free IM/DD SSB-OFDM Transmission at 11.11 Gb/s Over 200 km SSMF Using Dual EML," *IEEE Photonics Technology Letters,* vol. 25, no. 23, pp. 2271-2273, 2013.

[72] H.-L. Cheng, W.-H. Chen, C.-C. Wei and Y.-J. Chiu, "Dispersion-tolerant single-sideband OFDM transmission in IM/DD systems using a single cascaded EAM," in *2015 Optical Fiber Communications Conference and Exhibition (OFC)*, Los Angeles, CA, 2015.

[73] D. J. G. Mestdagh, P. Spruyt and B. Biran, "Analysis of clipping effect in DMT-based ADSL systems," in *Communications, 1994. ICC '94, SUPERCOMM/ICC '94, Conference Record, 'Serving Humanity Through Communications.' IEEE International Conference on*, New Orleans, USA, 1994.

[74] C.-C. Wei, H.-L. Cheng, H.-Y. Chen, Y.-C. Chen, H.-H. Chu, K.-C. Chang, I.-C. Lu and J. Chen, "Analysis of Nonlinear Distortion and SSII Cancellation in EAM-Based IMDD OFDM Transmission," *Journal of Lightwave Technology,* vol. 33, no. 14, pp. 3069 - 3082, 2015.

[75] X. Zhang, Z. Li, C. Li, M. Luo, H. Li, C. Li, Q. Yang and S. Yu, "Transmission of 100-Gb/s DDO-OFDM/OQAM over 320-km SSMF with a single photodiode," *Optics Express,* vol. 22, pp. 12079-12086, 2014.

[76] D.-Z. Hsu, C.-C. Wei, H.-Y. Chen, Y.-C. Lu, C.-Y. Song, C.-C. Yang and J. Chen, "SSII cancellation in an EAM-based OFDM-IMDD transmission system employing a novel dynamic chirp model," *Optics Express,* vol. 21, pp. 533-543, 2013.

[77] C. C. Wei, "Small-signal analysis of OOFDM signal transmission with directly modulated laser and direct detection," *Optics Letters,* vol. 36, no. 2, pp. 151-153, 2011.

[78] W. R. Peng, B. Zhang, K. M. Feng, X. Wu, A. E. Willner and S. Chi, "Spectral Efficient Direct-Detected OFDM Transmission Incorporating a Tunable Frequency Gap and an Iterative Detection Techniques," *Journal of Lightwave Technology,* vol. 27, no. 24, pp. 5723-5735, 2009.

[79] C. Ju, X. Chen, N. Liu and L. Wang, "Subcarrier to subcarrier intermixing interference cancellation in vestigial-sideband orthogonal frequency division multiplexing systems," *Optical Engineering,* vol. 53, no. 9, pp. 1-6, 2014.

[80] W. O. Popoola, Z. Ghassemlooy and B. G. Stewart, "Pilot-Assisted PAPR Reduction Technique for Optical OFDM Communication Systems," *Journal of Lightwave Technology,* vol. 32, no. 7, pp. 1374 - 1382, 2014.

[81] J. A. L. Silva, A. V. T. Cartaxo and M. E. V. Segatto, "A PAPR reduction technique based on a constant envelope OFDM approach for fiber nonlinearity mitigation in optical direct-detection systems," *Journal of Optical Communications and Networking,* vol. 4, no. 4, pp. 296-303, 2012.

[82] D. Gupta and D. Dhawan, "A Study of Various PAPR Reduction Techniques for Optical OFDM Systems," *International Journal of Computer Applications,* vol. 115, no. 15, pp. 26 - 29, 2015.

[83] R. L. Nadal, *Performance analysis of optical OFDM transmission systems using PAPR mitigation techniques and alternative transforms,* Barcelona: Universitat Politècnica de Catalunya, 2012.

[84] C. Ju, N. Liu, X. Chen and Z. Zhang, "SSBI Mitigation in A-RF-Tone-Based VSSB-OFDM System With a Frequency-Domain Volterra Series Equalizer," *Journal of Lightwave Technology,* vol. 33, no. 23, pp. 4997-5006, 2015.

[85] O. Omomukuyo, M. P. Thakur and J. E. Mitchell, "Experimental demonstration of digital predistortion for linearization of Mach-Zehnder modulators in direct-detection MB-OFDM ultra-wideband over fiber systems," in *2012 Asia Communications and Photonics Conference (ACP)*, Guangzhou, 2012.

[86] A. Cartaxo and V. Vujičić, "Predistortion technique for mitigating the Mach-Zehnder modulator nonlinearity effect in DD-OFDM-UWB optical transmission systems," in *2011 13th International Conference on Transparent Optical Networks*, Stockholm, 2011.

[87] Y. Shen, B. Hraimel, X. Zhang, G. E. R. Cowan, K. Wu and T. Liu, "A Novel Analog Broadband RF Predistortion Circuit to Linearize Electro-Absorption Modulators in Multiband OFDM Radio-Over-Fiber Systems," *IEEE Transactions on Microwave Theory and Techniques,* vol. 58, no. 11, pp. 3327-3335, 2010.

[88] T. H. Nguyen, T. B. Nguyen, T. H. Bui, N. T. T. Trang and T. T. Le, "Novel technique for nonlinearity postcompensation of Mach-Zehnder modulator in an analog-optical link," in *2014 International Conference on Advanced Technologies for Communications (ATC 2014)*, Hanoi, 2014.

[89] P. Yang, H. Shi and X. Chen, "EAM-based multiband OFDM systems incorporating PAPR reduction and SSII cancellation," *Optics & Laser Technology,* vol. 78, no. Part B, p. 50–55, 2016.

[90] L. Mehedy, M. Bakaul, A. Nirmalathas and E. Skafidas, "OFDM versus single carrier towards spectrally efficient 100 Gb/s transmission with direct detection," *Journal of Optical Communications and Networking,* vol. 4, no. 10, pp. 779-789, 2012.

[91] K. Zhong, X. Zhou, T. Gui, L. Tao, Y. Gao, W. Chen, J. Man, L. Zeng, A. P. T. Lau and C. Lu, "Experimental study of PAM-4, CAP-16, and DMT for 100 Gb/s Short Reach Optical Transmission Systems," *Optics Express,* vol. 23, pp. 1176-1189, 2015.

[92] M. H. Eiselt, N. Eiselt and A. Dochhan, "Direct Detection Solutions for 100G and Beyond," in *Optical Fiber Communication Conference, OSA Technical Digest (Optical Society of America, 2017)*, Los Angeles, California USA, 2017.

[93] A. Barbieri, G. Colavolpe, T. Foggi, E. Forestieri and G. Prati, "OFDM versus Single-Carrier Transmission for 100 Gbps Optical Communication," *Journal of Lightwave Technology,* vol. 28, pp. 2537-2551, 2010.

[94] P. Zhu, J. Li, Y. Chen, Y. Xu, N. Zhang, B. Guo, Z. Chen and Y. He, "Comparison of coherent optical single-carrier and multi-carrier superchannel with FDM and FDE," *Optical Fiber Technology,* vol. 20, no. 5, p. 453–460, 2014.

[95] A. Lobato, M. Kuschnerov, A. Diaz, A. Napoli, B. Spinnler and B. Lankl, "Performance comparison of single carrier and OFDM in coherent optical long-haul communication systems," in *2011 Asia Communications and Photonics Conference and Exhibition (ACP)*, Shanghai, 2011.

[96] G. Bosco, A. Carena, V. Curri, P. Poggiolini and F. Forghieri, "Performance Limits of Nyquist-WDM and CO-OFDM in High-Speed PM-QPSK Systems," *Photonics Technology Letters,* vol. 22, no. 15, pp. 1129-1131, 2010.

[97] A. Diaz-Souto, Comparison of OFDM with Single Carrier in high-data rate optical communication systems, Barcelona: Universitat Politecnico de Catalunya, 2011.

[98] S. J. Savory, G. Gavioli, R. I. Killey and P. Bayvel, "Electronic compensation of chromatic dispersion using a digital coherent receiver," *Optics Express,* vol. 15, no. 5, pp. 2120-2126, 2007 .

[99] R. Kudo, T. Kobayashi, K. Ishihara, Y. Takatori, A. Sano and Y. Miyamoto, "Coherent Optical Single Carrier Transmission Using Overlap Frequency Domain Equalization for Long-Haul Optical Systems," *Journal of Lightwave Technology,* vol. 27, no. 16, pp. 3721-3728, 2009.

[100] S. J. Savory, "Digital Coherent Optical Receivers: Algorithms and Subsystems," *Journal of Selected Topics in Quantum Electronics,* vol. 16, no. 5, pp. 1164-1179, 2010.

[101] R. Raheli and G. Picchi, "Synchronous and fractionally-spaced blind equalization in dually-polarized digital radio links," in *Proc. IEEE Int. Conf. Commun., 1991 (ICC), Conf. Record*, 1991.

[102] S. J. Savory, "Digital filters for coherent optical receivers," *Optics Express,* vol. 16, no. 2, pp. 804-817, 2008.

[103] H. Louchet, K. Kuzmin and A. Richter, "Improved DSP algorithms for coherent 16-QAM transmission," in *Proc. IEEE ECOC`08*, 2008.

[104] VPIphotonics, *Digital Signal Processing Library (DSP_Lib). Version 9.5,* 2017.

[105] M. Selmi, Y. Jaouen and P. Ciblat, "Accurate digital frequency offset estimator for coherent PolMux QAM transmission systems," in *Proc. 35th Eur. Conf. on Opt. Commun. (ECOC)*, Vienna, Austria, 2009.

[106] Y. Wang, E. Serpedin and P. Ciblat, "Optimal blind carrier recovery for MPSK burst transmissions," *IEEE Transactions on Communications,* vol. 51, no. 9, pp. 1571-1581, 2003.

[107] A. J. Viterbi and A. M. Viterbi, "Nonlinear estimation of PSK-modulated carrier phase with application to burst digital transmission," *IEEE Transactions on Information Theory,* vol. 29, no. 4, pp. 543-551, 1983.

[108] S. Tsukamoto, K. Katoh and K. Kikuchi, "Coherent demodulation of optical multilevel phase-shift-keying signals using homodyne detection and digital signal processing," *IEEE Photonics Technology Letters,* vol. 18, no. 10, pp. 1131-1133, 2006.

[109] H. Louchet, K. Kuzmin and A. Richter, "Improved DSP algorithms for coherent 16-QAM transmission," in *2008*, Brussels, 2008 34th European Conference on Optical Communication (ECOC).

[110] E. G. Larsson, O. Edfors, F. Tufvesson and T. L. Marzetta, "Massive MIMO for next generation wireless systems," *IEEE Communications Magazine ,* vol. 52, no. 2, pp. 186-195, 2014.

[111] CPRI Specification V6.1, Common Public Radio Interface (CPRI); Interface Specification, 2014.

[112] ITU-T Recommendation Series G, Supplement 55, "Radio-over-fibre (RoF) technologies and their applications," , 2015.

[113] M. Befekadu, S. Straullu, S. Abrate and R. Gaudino, "Experimental Optimization of DSP-Aggregated Front-hauling Transmission for up to 4x96 LTE radio waveforms," in *42th European Conference and Exhibition on Optical Communication (ECOC)*, Dusseldorf, Germany, 2016.

[114] ETSI Technical Specification 136 104 V12.6.0 (2015-02), 2015.

[115] R. A. Shafik, M. S. Rahman and A. R. Islam, "On the Extended Relationships Among EVM, BER and SNR as Performance Metrics," in *2006 International Conference on Electrical and Computer Engineering*, Dhaka, 2006.

[116] P. Anslow, "FEC performance on multi-part links," in *IEEE P802.3bs Task Force*, San Antonio, TX, 2014.

[117] IEEE 802.3ba, IEEE Std., 2010 [Online]. Available: http://standards.ieee.org/about/get/802/802.3.html., 2010.

[118] M. Duelk and R. Gutiérrez-Castrejón, "4 x 25-Gb/s 40-km PHY at 1310 nm for 100 GbE using SOA-based preamplifier," *Journal of Lightwave Technology,* vol. 26, pp. 1681-1689, 2008.

[119] CFP Multi-Source Agreement documents are available at http://www.cfp-msa.org./, 2017.

[120] All the IEEE 400 GbE TF contributions are publicly available at http://www.ieee802.org/3/bs/public/., 2017.

[121] R. Gutiérrez-Castrejón and P. Torres-Ferrera, "Design and technical feasibility of next 400 GbE 40-km PMD based on 16 x 25 Gbps Architecture," *Journal of Lightwave Technology,* vol. 31, pp. 2386-2393, 2013.

[122] D. Dove and X. Song, "Considering 2 km and 10 km Architectural Alternatives," in *IEEE 802.3 400 GbE SG*, Indian Wells, USA, 2014.

[123] E. Lach and W. Idler, "Modulation formats for 100G and beyond," *Optical Fiber Technology,* vol. 17, pp. 377-386, 2011.

[124] D. M. Pozar, Microwave engineering 3rd Edition, John Wiley and Sons, Inc., 2005.

[125] L. M. Franca-Neto, R. E. Bishop and B. A. Bloechel, "64 GHz and 100 GHz VCOs in 90 nm CMOS using optimum pumping method," in *IEEE International Solid-State Circuits Conference, Vol. 1 of Digest of Technical Papers (IEEE, 2004)*, 2004.

[126] F. Ellinger, T. Morf, G. Buren, C. Kromer, G. Sialm, L. Rodoni, M. Schmatz and H. Jackel, "60 GHz VCO with wideband tuning range fabricated on VLSI SOI CMOS technology," in *Vol. 3 of IEEE MTT-S International Microwave Symposium Digest (IEEE, 2004)*, 2004.

[127] M. Ercoli, D. Dragomirescu and R. Plana, "High performance local oscillator signal driver for 60-GHz I/Q systems in 65nm CMOS technology," in *Progress in Electromagnetics Research Conference*, 2013.

[128] Norden Millimeter, "26.5 – 40 GHz Up-Converter", 2015.

[129] National Instruments, "VTO-33500-40L 27 to 40 GHz Voltage Tuned Oscillator", 2015.

[130] C. H. Doan, S. Emami, A. M. Niknejad and R. W. Brodersen, "Millimeter-wave CMOS design," *IEEE Journal of Solid-State Circuits,* vol. 40, pp. 144-155, 2005.

[131] F. Zhang, E. Skafidas and W. Shieh, "60 GHz double-balanced up-conversion mixer on 130 nm CMOS technology," *Electron. Letters,* vol. 44, pp. 633-634, 2008.

[132] S. Emami, C. H. Doan, A. M. Niknejad and R. W. Brodersen, "A Highly Integrated 60GHz CMOS Front-End Receiver," in *Proceedings of IEEE Solid-State Circuits Conference (IEEE, 2007)*, 2007.

[133] B. Razavi, "A 60-GHz CMOS receiver front-end," *IEEE Journal of Solid-State Circuits,* vol. 41, pp. 17-22, 2006.

[134] M. Kraemer, M. Ercoli, D. Dragomirescu and R. Plana, "A wideband single-balanced down-mixer for the 60 GHz band in 65 nm CMOS," in *Proceedings of Asia-Pacific Microwave Conference (IEEE, 2010)*, 2010.

[135] J. H. Tsai, P. S. Wu, C. S. Lin, T. W. Huang, J. G. J. Chem and W. C. Huang, "25–75 GHz Broadband Gilbert-Cell Mixer using 90-nm CMOS Technology," *IEEE Microwave and Wireless Components Letters,* vol. 17, no. 4, pp. 247-249, 2007.

[136] C. S. Lin, P. S. Wu, H. Y. Chang and H. Wang, "A 9–50-GHz Gilbert-Cell Down-Conversion Mixer in 0.13-nm CMOS technology," *IEEE Microwave and Wireless Components Letters,* vol. 16, no. 5, pp. 293-295, 2006.

[137] J. H. Tsai, "Design of 40–108-GHz Low-Power and High-Speed CMOS Up-/Down-Conversion Ring Mixers for Multistandard MMW Radio Applications," *IEEE Transactions on Microwave Theory and Techniques,* vol. 60, no. 3, pp. 670-678, 2012.

[138] P. Mazurek, H. d. Waardt and J. P. Turkiewicz, "Towards 1 Tbit/s SOA-based 1310 nm transmission for local area network/data centre applications," *IET Optoelectronics,* vol. 9, no. 1, pp. 1-9, 2015.

[139] Y. Miyazaki, H. Tada, S.-y. Tokizaki, K. Takagi, T. Aoyagi and Y. Mitsui, "Small-chirp 40-Gbps electroabsorption modulator with novel tensile-strained asymmetric quantum-well absorption layer," *IEEE Journal of Quantum Electronics,* vol. 39, no. 6, pp. 813-819, 2003.

[140] M. Jamro and J. Senior, "Chirp Control of an Electroabsorption Modulator to be used for Regeneration and Wavelength Conversion at 40 Gbit/s in All-Optical Networking," *Phot. Net. Comm.,* vol. 10, no. 2, pp. 267-268 , 2005.

[141] Finisar, "50 GHz Photodetector XPDV2320R Datasheet,", 2014.

[142] K. W. Kobayashi, "State-of-the-Art 60 GHz, 3.6 K-Ohm Transimpedance Amplifier for 40 Gb/s and beyond," in *IEEE Radio Frequency Integrated Circuits (RFIC) Symposium (IEEE 2003)*, 2003.

[143] I. Dedic, "56GS/s ADC: enabling 100 GbE," in *Optical Fiber Communication Conference Vol. 1 of 2010 OSA Technical Digest Series (Optical Society of America, 2010)*, 2010.

[144] S. O. Vázquez, P. Torres-Ferrera, R. Gutiérrez-Castrejón and I. Tomkos, "Unamplified 10-km transmission using direct-detection optical OFDM superchannel at 100 Gbps," in *Latin America Optics and Photonics Conference, Vol. 1 of 2014 OSA Technical Digest Series (Optical Society of America, 2014)*, Cancun, Mexico, 2014.

[145] Y. Handali, I. Nizan and D. Wulich, "On channel capacity of OFDM with SLM method for PAPR reduction," in *2006 IEEE 24th Convention of Electrical & Electronics Engineers in Israel*, Eilat, Israel, 2006.

[146] CISCO White Paper, "The Zettabyte Era: Trends and Analysis," June, 2016. [Online] Available: http://www.cisco.com/c/en/us/solutions/collateral/service-provider/visual-networking-index-vni/vni-hyperconnectivity-wp.html.

[147] IEEE 802.3 Ethernet Working Group, "IEEE 802.3™ Industry Connections Ethernet Bandwidth Assessment". July, 2012. [Online] Available: http://www.ieee802.org/3/ad_hoc/bwa/BWA_Report.pdf.

[148] J. D'Ambrosia, *IEEE P802.3bs Baseline Summary,* 2015.

[149] S. Gringeri, E. B. Basch and T. J. Xia, "Technical considerations for supporting data rates beyond 100 Gb/s," *IEEE Commun.Mag.,* vol. 50, no. 2, p. S21–S30, 2012.

[150] W. Forysiak and D. S. Govan, "Progress toward 100-G digital coherent pluggables using InP-based photonics," *Journal of Ligthwave Technology,* vol. 32, no. 16, pp. 2925-2934, 2014.

[151] M. Artiglia, R. Corsini, M. Presi, F. Bottoni, G. Cossu and E. Ciaramella, "Coherent systems for low-cost 10 Gb/s optical access networks," *Journal of Lightwave Technology,* vol. 33, no. 15, pp. 3338-3344, 2015.

[152] H. Rohde, E. Gottwald, A. Teixeira, J. D. Reis, A.Shahpari, K. Pulverer and J. S. Wey, "Coherent ultra dense WDM technology for next generation optical metro and access networks," *Journal of Ligthwave Technology,* vol. 32, no. 10, pp. 2041-2052, 2014.

[153] R. Hirai, M. Kono, S. Tsusumi, H. Toyoda and N. Kikuchi, "Initial thought about modulation format & FEC for long-reach 400GbE," in *Presented at the IEE 802.3 400 Gb/s Ethernet Study Group Meeting*, Geneva. Switzerland, 2013.

[154] W. C. Ng, A. T. Nguyen, C. S. Park and L. A. Rusch, "Reduction of MIMO-FIR taps via SOP-estimation in Stokes space for 100 Gbps short reach applications," in *Proceedings of The European Conference on Optical Communication (ECOC 2014)*, 2014.

[155] M. A. García-Yáñez and R. Gutiérrez-Castrejón, "Technical feasibility of a 400 Gb/s unamplified WDM coherent transmission system for Ethernet over 40 km of single-mode fiber," in *Proceedings of the 12th International Conference on Electrical Engineering, Computing Science and Automatic Control (CCE 2015)*, 2015.

[156] Ethernet Alliance, "The 2016 Ethernet Roadmap", [Online] Available: http://www.ethernetalliance.org/roadmap/.

[157] C. R. Cole, "100-Gb/s and beyond transceiver technology," *Optical Fiber Technology,* vol. 17, no. 5, pp. 472-479, 2011.

[158] N. Nambath and S. Gupta, "Low power terabit /second optical interconnects for data centers," in *Proceedings of the International Conference on Signal Processing and Communications (SPCOM 2014)*, 2014.

[159] Enablence 100 GHz Wavelength Division Multiplexer/Demultiplexer specification sheet. Mod. APMUX1100/APDMX1100. [Online] Available: http://www.enablence.com/media/mediamanager/pdf/18-enablence-datasheet-ocsd-awg-standard-100ghzmultidemulti.pdf.

[160] M. Seimetz and C. M. Weinert, "Options, feasability, and availability of 2x4 90° hybrids for coherent optical systems," *Journal of Lightwave Technology,* vol. 24, pp. 1317-1322, 2006.

[161] Kylia 90° Optical hybrids specification sheet. Mod COH24-X, XOH28-X. [Online] Available: http://kylia.com/wp-content/uploads/2015/02/datasheet-COH-V1.2.pdf.

[162] I. Dedic, "56GS/s ADC: enabling 100 GbE," in *Optical Fiber Communication Conference Vol. 1 of 2010 OSA Technical Digest Series (Optical Society of America, 2010)*, 2010.

[163] Finisar 70 GHz Balanced Photodetector specification sheet. Mod. BPDV3120R. [Online] Available: https://www.finisar.com/sites/default/files/downloads/bpdv3120r_70ghz_balanced_photodetector_product_brief_reva1_0.pdf.

[164] R. Schmogrow, B. Nebendahl and M. Winter, "Error vector magnitude as a performance measure for advanced modulation formats," *IEEE Photonics Technol. Letters,* vol. 24, pp. 61-63, 2012.

[165] C.-T. Lin, J. Chen, S.-P. Dai, P.-C. Peng and S. Chi, "Impact of Nonlinear Transfer Function and Imperfect Splitting Ratio of MZM on Optical Up-Conversion Employing Double Sideband With Carrier Suppression Modulation," *Journal of Lightwave Technology,* vol. 26, no. 15, pp. 2449-2459, 2008.

[166] G. Letal, K. Prosyk, R. Millett, D. Macquistan, S. Paquet, O. Thibault-Maheu and J.-F. Gagné, "Low loss InP C-band IQ modulator with 40GHz bandwidth and 1.5V Vπ," in *2015 Optical Fiber Communications Conference and Exhibition (OFC)*, Los Angeles, CA, 2015.

[167] K. Prosyk, A. Ait-Ouali, C. Bornholdt, T. Brast, M. Gruner, M. Hamacher and D. Hoffmann, "High performance 40GHz InP Mach-Zehnder modulator," in *Optical Fiber Communication Conference and Exposition (OFC/NFOEC), 2012 and the National Fiber Optic Engineers Conference*, Los Angeles, CA, 2012.

[168] Oclaro, "400G Lithium Niobate Modulator".

[169] G. Wang, J.-P. Fortier and C. Paquet, *Inp IQ Modulators for Applications Beyond 100G,* Teraxion, 2015.

[170] Y. Ogiso, Y. Tsuchiya, S. Shinada, S. Nakajima, T. Kawanishi and H. Nakajima, "High Extinction-Ratio Integrated Mach–Zehnder Modulator With Active Y-Branch for Optical SSB Signal Generation," *IEEE Photonics Technology Letters,* vol. 22, no. 12, pp. 941-943, 2010.

[171] J. K. Fischer, R. Ludwig, L. Molle, M. Nölle, A. Beling, C. C. Leonhardt, A. Matiss, A. Umbach, R. Kunkel, H.-G. Bach and C. Schubert, "Integrated Coherent Receiver Modules for 100G Ethernet and Beyond," in *12 ITG Symposium Proc. of Photonics Networks*, 2012.

[172] R. J. Essiambre, G. Kramer, P. J. Winzer, G. J. Foschini and B. Goebel, "Capacity Limits of Optical Fiber Networks," *Journal of Lightwave Technology,* vol. 28, no. 4, pp. 662-701, 2010.

[173] R. Freund, M. Nölle and M. Seimetz, "Higher-Order Modulation Formats for Spectral-Efficient High-Speed Metro Systems," in *SPIE Proceedings Vo. 7959: Optical Metro Networks and Short-Haul Systems III*, 2011.

[174] S. Chandrasekhar, X. Liu, P. J. Winzer, J. E. Simsarian and R. A. Griffin, "Compact All-InP Laser-Vector-Modulator for Generation and Transmission of 100-Gb/s PDM-QPSK and 200-Gb/s PDM-16-QAM," *Journal of Lightwave Technology,* vol. 32, no. 4, pp. 736-742, 2014.

[175] H. C. P. M. Lu, E. Bloch, A. Sivananthan, J. S. Parker, Z. Griffith, L. A. Johansson, M. J. W. Rodwell and L. A. Coldren, "An integrated 40 Gbit/s optical costas receiver," *Journal of Lightwave Technology,* vol. 31, no. 13, pp. 2244-2253, 2013.

[176] Y. Xydas, C. Ressopoulos and A. Bogris, "Numerical analysis of 50 Gbaud homodyne coherent receivers relying on line-coding and injection locking in lasers," *Optical Fiber Technology,* vol. 26, pp. 184-189, 2015.

[177] P. Torres-Ferrera and R. Gutiérrez-Castrejón, "Impact of channel-spacing on next 400 Gb/s Ethernet 40-km PMD based on 16 x 25 Gb/s WDM architecture," *Optical Fiber Technology,* vol. 20, pp. 177-183, 2014.